

AD 692 500

VOLUME 1

OAR 69-0011

AD 692500

proceedings  
of the  
**OAR**

# RESEARCH APPLICATIONS CONFERENCE



sponsored by

THE OFFICE OF AEROSPACE RESEARCH ★ UNITED STATES AIR FORCE  
Arlington, Virginia

**Best  
Available  
Copy**

**Proceedings of the  
OAR RESEARCH APPLICATIONS CONFERENCE**

**13 March 1969**



**Office of Aerospace Research ★ United States Air Force  
Arlington, Virginia**

Agencies of the Department of Defense, qualified contractors  
and other Government agencies may obtain copies from the

Defense Documentation Center  
Cameron Station  
Alexandria, Virginia 22314

This document has been released also to the

CLEARINGHOUSE  
U.S. Department of Commerce  
Springfield, Virginia 22151

for sale to the public.

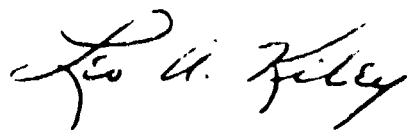
THIS DOCUMENT HAS BEEN APPROVED FOR PUBLIC RELEASE AND SALE; ITS  
DISTRIBUTION IS UNLIMITED.

## FOREWORD

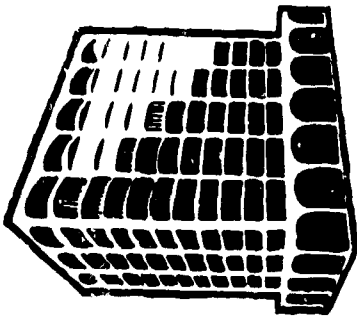
As in past years, the 1969 OAR Research Applications Conference has again produced a number of suggestions for the technological exploitation of OAR's research program. The presentations included in these *Proceedings* demonstrate the possible applications of this research, even though the full impact of the ideas may not be felt until some time in the future.

OAR, as the prime research agency of the United States Air Force, conducts and sponsors a broad program of fundamental research aimed at advancing Air Force technology. This program encompasses a search for new scientific knowledge in OAR's own laboratories, as well as in universities and technical institutions at home and abroad.

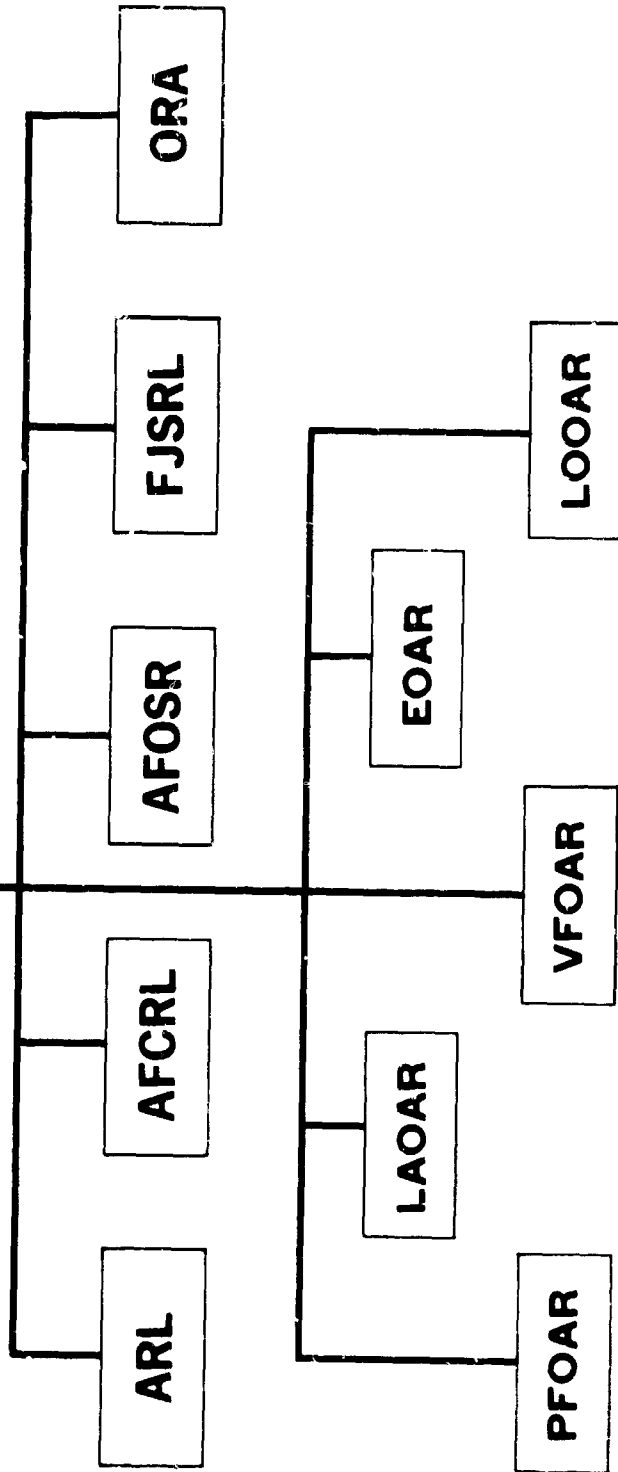
The dissemination of the results of research is also part of OAR's mission. Although it is often difficult to predict where research will lead, OAR channels its work into fields of interest that offer the greatest promise for meeting current and future Air Force operational needs.



**LEO A. KILEY**  
**Brigadier General, USAF**  
**Commander**



**HQ OAR**



**AIR FORCE CAMBRIDGE RESEARCH LABORATORIES**  
**L. G. Hanscom Field, Bedford, Mass.**

Does research in the physical, engineering and environmental sciences, and conducts specifically assigned exploratory-development efforts involving the physical, engineering, and environmental sciences. Contracts for research and development work which closely supports and extends in-house efforts.

**AIR FORCE OFFICE OF SCIENTIFIC RESEARCH**  
**Arlington, Va.**

Through contracts and grants, supports programs of extramural research designed to provide new scientific knowledge and understanding. Areas of research include the physical, engineering, environmental and life sciences.

**AEROSPACE RESEARCH LABORATORIES**  
**Wright-Patterson AFB, Ohio**

Conducts research in the physical and engineering sciences, and contracts for research which closely supports and extends in-house efforts.

**THE FRANK J. SEILER RESEARCH LABORATORY**  
**USAF Academy, Colo.**

Conducts research in chemistry, applied mathematics, and aerospace mechanics. Fosters, encourages, and supports related research by the USAF Academy faculty and cadets.

**OFFICE OF RESEARCH ANALYSES**  
**Holloman Air Force Base, N. Mex.**

Conducts mission analyses to identify future aerospace missions; conducts systems analyses to determine technical validity, operational feasibility, and cost-effectiveness of future Air Force systems; and conducts research analyses to identify promising opportunities for relevant research programs.

**EUROPEAN OFFICE OF AEROSPACE RESEARCH**  
**Brussels, Belgium**

Secures in Free Europe, the Near East, Middle East (including India, Burma and Ceylon), and Africa, scientific research and development efforts in support of the programs of Air Force organizations, and provides scientific liaison which fosters mutually beneficial relations among the United States and the scientific communities of those areas. (In December 1968, EOAR will initiate its relocation to London, England, where it will be collocated with comparable activities of the Army and Navy. This relocation move, scheduled to be completed by midsummer 1970, will involve a shift of EOAR's mission from one which is procurement-oriented to one which emphasizes more of a scientific interface with the foreign research community.)

**LATIN AMERICAN OFFICE OF AEROSPACE RESEARCH**  
**Rio de Janeiro, Brazil**

Administers research efforts in South America.

**PATRICK FIELD OFFICE**  
**Patrick Air Force Base,**  
**Fla.**

**LOS ANGELES**  
**FIELD OFFICE**  
**Los Angeles, Calif.**

**VANDENBERG FIELD OFFICE**  
**Vandenberg Air Force Base,**  
**Calif.**

These three field offices above support the aerospace research effort by maintaining liaison among the scientists, the launch teams, and the contractors. This permits small scientific experiments to be installed on rockets fired for other purposes, thus insuring that the Air Force receives maximum pay-load utilization.

## INTRODUCTION

The aim of this 1969 OAR Research Applications Conference has been to emphasize the continuing efforts of researchers, both in-house and at universities in the U.S. and abroad, to solve some of the current practical problems of the Air Force. The useful solutions stemming from these efforts have helped to further the technological progress of both the Air Force and the DOD as a whole.

Some of the current or potential applications resulting from OAR research are included in this volume. Although they do not reflect all facets of the broad OAR research program, they do provide a meaningful spectrum of Air Force interests, and demonstrate the need to sustain a healthy DOD research program.

# CONTENTS

	<u>Page</u>
Foreword	iii
Introduction	vii
Application of High Magnetic Fields Benjamin Lax, D. Bruce Montgomery, and Henry H. Kolm Francis Bitter National Magnet Lab Massachusetts Institute of Technology	A-1
• New Developments in Supersonic Combustion Research J. Swithentank Department of Fuel Technology and Chemical Engineering • University of Sheffield, England	B-1
Negative Ion Reactions of Significance to the Atmosphere Dr. Thomas O. Tiernan and Dr. B. Mason Hughes Chemistry Research Laboratory Aerospace Research Laboratories	C-1
New Atomic Spectroscopic Methods for Trace Analysis J. D. Winefordner Department of Chemistry University of Florida	D-1
Plan Shear Indicator for Real-Time Doppler Radar Identification of Hazardous Storm Winds Graham M. Armstrong and Ralph J. Donaldson, Jr. Meteorology Laboratory Air Force Cambridge Research Laboratories	E-1
• Stress Corrosion Cracking of 6-4 Titanium Alloy Major William E. Craven Metallurgy and Ceramics Research Laboratory Aerospace Research Laboratories	F-1
The Spectrum-Analysis Radar J. L. Poirier Microwave Physics Laboratory Air Force Cambridge Research Laboratories	G-1

	<u>Page</u>
Nondestructive Evaluation of Metal Fatigue R. Barton, W. Lyle Donaldson and F. N. Kusenberger Division of Electronics and Electrical Engineering and Applied Economics Southwest Research Institute	H-1
Application of the Statistics of Ionospheric Scintillation to VHF and UHF Systems Richard S. Allen Ionospheric Physics Laboratory Air Force Cambridge Research Laboratories	I-1
Electrochemical Behavior of a Molten Aluminum- Chloride/ Sodium-Chloride Electrolyte Major L. A. King and Major D. W. Seegmiller The Frank J. Seiler Research Laboratory	J-1
The Magnetic Wind-Tunnel-Model Suspension and Balance System Eugene F. Covert Aerophysics Laboratory Department of Aeronautics and Astronautics Massachusetts Institute of Technology, and Fred.L. Daum Fluid Dynamics Facilities Research Laboratory Aerospace Research Laboratories	K-1
Research in Electrofluid-dynamic Power Generation Captain John A. Decaire and Maurice O. Lawson Energetics Research Laboratory Aerospace Research Laboratories	L-1
The Isentropic-Compression Tube F. J. Stoddard Aerodynamic Research Department Cornell Aeronautical Laboratory, Inc.	M-1
Supersonic Compressor Research Captain Ronald L. Haugen and Dr. Arthur J. Wennerstrom Fluid Dynamics Facilities Research Laboratory Aerospace Research Laboratories	N-1

**CONFERENCE PAPERS**

APPLICATION OF HIGH MAGNETIC FIELDS

Benjamin Lax, D. Bruce Montgomery and Henry H. Kolm

Francis Bitter National Magnet Laboratory

Massachusetts Institute of Technology

Cambridge, Massachusetts

## APPLICATION OF HIGH MAGNETIC FIELDS

Benjamin Lax, \* D. Bruce Montgomery and Henry H. Kolm

Francis Bitter National Magnet Laboratory<sup>†</sup>  
Massachusetts Institute of Technology  
Cambridge, Massachusetts

### ABSTRACT

This paper presents a number of scientific and device applications of high magnetic fields. Scientific applications include research in superconductivity, nuclear magnetic resonance in chemical and biological systems, and in submillimeter spectroscopy. Device applications include quantum electronic devices, electron beam devices, synchrotron radiation devices, plasma source devices and thermomagnetic devices. Other areas discussed include the medical applications of catheter guidance, heart pace-making and measurement of the weak fields of the heart and brain, and the application of high fields to electromagnetic proof-loading of bonded aircraft structures and to magnetic ore separation.

---

\*Also Physics Department, Massachusetts Institute of Technology.

<sup>†</sup>Supported by the U. S. Air Force Office of Scientific Research.

## APPLICATION OF HIGH MAGNETIC FIELDS

Benjamin Lax, \* D. Bruce Montgomery and Henry H. Kolm

Francis Bitter National Magnet Laboratory<sup>†</sup>  
Massachusetts Institute of Technology  
Cambridge, Massachusetts

### I. INTRODUCTION

In the five years since its establishment by the Air Force, the MIT National Magnet Laboratory has clearly demonstrated the tremendous versatility of high magnetic fields as a tool for fundamental research. Although the principal application of high magnetic fields has been to research in such areas as spectroscopy, plasma physics, low temperatures, solid-state, and superconductivity, this basic work has resulted in considerable practical fall-out. Although many of these applications are still only conceptual ones, many have great future potential, and already there have been a number of achievements.

High magnetic fields have now become very important tools in such applied areas as magneto-hydrodynamic generators, fusion experiments, bubble chambers, ore separators, and metal forming. In addition, the use of high magnetic fields promises to be of equal or greater importance in future projects such as radiation sources, high energy accelerators, electron beam devices, solid state detectors, transportation, shielding, and even in the testing of aircraft structures.

### II. SCIENTIFIC APPLICATIONS

#### A. The Hybrid Magnet, A Unique New Concept.

A unique concept in magnet design is now being implemented at the Laboratory. Very high power, high field, water-cooled coils are being combined with large superconducting coils to make hybrid magnet systems which will provide more intense fields than are possible by either technique alone. [1, 2]

The hybrid concept has only recently become feasible due to advances in superconducting magnet technology. The attractiveness of combining the two techniques becomes evident when one considers the assets and liabilities of each system

---

\*Also Physics Department, Massachusetts Institute of Technology.

<sup>†</sup>Supported by the U. S. Air Force Office of Scientific Research.

by itself. As shown in Fig. 1, the water-cooled section is used at the center of the magnet where it makes most effective use of the dc power input and where the field exceeds the critical field of any known superconducting material. The superconducting coil is the outer concentric section where the field is within the superconducting range and where large amounts of dc power would be required to produce an equivalent field in a water-cooled structure. The central field then can be far higher than could be generated by the superconductor alone, and higher than could be generated by the core alone under a given limitation of power.

To couple the two systems together requires the use of a cryostat of novel design as shown in Fig. 2. The liquid helium cryostat containing the superconducting coil must have room temperature access for the water-cooled core, and in addition, special provision must be made to support the very large mechanical forces developed by the magnetic interactions of the two systems. The first hybrid prototype system is now under construction at the Laboratory, and will be the first of a series of such systems.

While the first hybrid system will use only a 60 kilogauss (kG) superconducting coil, the next generation of hybrids will incorporate superconducting sections giving fields twice that high. Such a 120 kG field superconducting magnet is the practical economic limit at present, but would be sufficiently high to allow the generation of steady fields over 300 kG in a hybrid system with 10 megawatts dc power input, 250 kG with 5 megawatts and 200 kG with 2.5 megawatts representing a four-fold increase in the number of magnets operating above 200 kG. The hybrid concept, then, can lead to a very significant augmentation of high magnetic field capabilities for both basic experiments and applications.

#### B. High Field Superconductors.

Since the advent of high field superconducting materials, most manufacturers have made exploratory measurements in the steady state high field water-cooled magnets at the Laboratory. In fact, the two highest field superconductors known today, vanadium gallium and niobium germanium aluminum, have been under study here, the first by Dr. K. Tachikawa [3] of the National Research Institute for Metals, Tokyo, and the second by the staff of the Laboratory using material supplied by Dr. B. Matthias and his colleagues at the University of California, La Jolla, and Bell Telephone Laboratories. [4] (Fig. 3). In the future, when higher magnetic fields up to 300 kG are available with hybrid magnets, the measurements on these and other new materials can be readily extended. Although preliminary measurements are sometimes made with pulsed magnets, these results are neither complete nor fully reliable. For example, the measurement of magnetic susceptibility, critical currents and other fundamental properties requires dc techniques. In addition the large volume water-cooled magnets permit the measurements of small test coils of such materials, thus simulating the realistic conditions of high magnetic fields, i.e., forces and pressures which will exist in future magnets made completely of superconductors, the small test coil representing the inner elements of the coil subjected to the most critical conditions.

With the inevitable advances in high magnetic field superconductors and related closed cycle refrigerators, such systems will become mobile both for airborne and ground systems and because they can be used for shielding electronic equipment and personnel from high energy particles, may play an important role in

space exploration.

### C. Nuclear Magnetic Resonance in Chemical and Biological Systems.

High field nuclear magnetic resonance (NMR) measurements offer one of the most unique and promising opportunities for fundamental contributions to the future understanding of biological and organic systems, owing to the uniquely direct information which they give on the electronic structure of molecules. The power of the method depends on two characteristic interactions: the chemical shift and the indirect spin-spin interaction. The chemical shift refers to the screening of the nucleus by currents induced in the extranuclear electron cloud by the external fields. The indirect spin-spin interaction ("J-coupling") refers to electron spin polarization by the nuclear magnetic moment, which communicates the quantum state of that moment to nearby states in the electron cloud.

Both of these interactions represent very small shifts and splittings of the Larmor frequency – typically less than 1 ppm for protons. The development of useful spectrometers has thus depended heavily on the development of magnets having effective homogeneity over the sample as well as time stability, considerably better than 1 ppm.

The NMR signal to noise ratio, other factors being constant, is roughly quadratic with the applied field strength. Thus there is a great premium on the development of stronger fields having the requisite homogeneity. Moreover, the chemical shifts increase linearly with field strength, thus giving spectra taken at higher field strengths a simpler, better separated, and more easily interpreted form. This is particularly important in the study of large molecules (e.g., proteins) which give such overlapping spectra at lower field strengths as to be nearly useless. Recent work [5] has shown that increasing the field strength from 24 to 52 kG provides a significant step forward in what can be done on such systems. Further increases in field strength will be rewarded by further order-of-magnitude increases in the power of the NMR method.

The importance of these measurements and the difficulty of producing the magnetic fields with sufficient homogeneity and stability make the development of high field NMR instruments a natural project for a major national laboratory. The development of the magnetic fields of 100 kilogauss and higher, homogeneous and stable to one part in  $10^9$  requires the type of engineering approach which had led to the design and construction of modest accelerators and radio astronomy installations. Its construction and exploitation for basic measurements will require a team approach involving engineers, physicists, chemists, and biologists.

We are proposing a development project which will ultimately culminate in an NMR magnet producing 200 kG homogeneous and stable to 1 part in  $10^9$ . This goal will be approached in two major steps, the first being the construction of a 5 cm bore superconducting magnet producing 150 kG, uniform and stable, to 1 part in  $10^9$  over  $1 \text{ cm}^3$  of volume. This magnet would itself represent a three times increase in the fields available for NMR work and would be of inestimable benefit to biologists and organic chemists.

A field of 150 kG is the highest field that can be expected from superconducting magnets in the foreseeable future, but this need not limit the ultimate goal. The

hybrid-magnet concept, already being implemented, can be used to extend the range. In this case a 100 kG, 40 cm bore superconducting magnet producing a highly homogeneous field of 100 kG would be combined with a high homogeneity copper water-cooled insert to produce a combined field of 200 kG, again homogeneous to 1 part in  $10^8$ . Time stability would be achieved by means of a superconducting shield of high critical field but which need carry only vanishingly small currents. This last step, that of the hybrid magnet, is clearly the more difficult, but it is also capable of the more unique contributions.

#### D. Submillimeter Spectroscopy.

During the last two decades microwave and millimeter resonance spectroscopy has been exploited as a powerful technique for a wide variety of studies in solid state physics and chemistry. Such studies required modest magnetic fields supplied by commercial electro-magnets. However, the same techniques have not been possible in the short millimeter and submillimeter regions until recently because fields of sufficient magnitude were not available. Today there are three classes of magnets possible, superconducting, water-cooled or hybrid, and synchronous pulsed magnets, and these should extend resonance spectroscopy from 1 millimeter well into the submillimeter regions. The hybrid magnets which will be capable of providing fields in excess of 300 kG continuously are beautifully matched to the cyanide laser which emits radiation at 337 microns or  $3/10$  of a millimeter. With this system a high resolution, high precision spectrometer can be made available for studying magnetic resonance, cyclotron resonance, spin resonance, etc. The synchronous pulse system, whose design is now being studied, will provide 500 kG pulses of a millisecond duration once every second and should extend submillimeter spectroscopy to even higher frequencies. Although the pulse will result in some loss of resolution, it will nevertheless provide a very important and effective tool in conjunction with submillimeter and far infrared lasers.

#### E. Electronic Devices.

A great many electronic phenomena in solids, gases and vacuum tube devices arise only if a steady magnetic field is first applied to a semiconducting or magnetic crystal or to an electron plasma or stream. This age of modern electronics has come to depend heavily on phenomena such as cyclotron resonance in semiconductors, ferromagnetic resonance, antiferromagnetic resonance, paramagnetic phenomena for maser operation, the magnetic properties of electron plasmas for helicon wave propagation and finally, the creation of magneto-acoustic waves which are a new combination of magnetic spin waves and sound waves in solids. These are several areas in electronics where one can foresee these combined field and device systems playing an important part.

Perhaps the best example of a clear impact in the immediate future is in millimeter and submillimeter wave systems. Here we need the new cyclotron resonance electron beam radiation source, as well as travelling wave masers, ferrimagnetic isolators and circulators and, finally, fast sensitive solid state detectors, all of which require large steady magnetic fields. This submillimeter wavelength range is one of the few remaining undeveloped sections of the electromagnetic spectrum from the applications point of view.

## 1. Quantum Electronic Devices.

The area known as quantum electronics involves the use of lasers, masers, and related devices as useful sources of radiation or as sensitive detectors of this radiation. Basic work in magnetospectroscopy has naturally led to the conception of a number of detecting devices involving magnetic fields. Tunable infrared detectors using low-gap semiconducting materials and high magnetic fields are particularly suitable as tunable monochromatic sensors in the submillimeter, near infrared and far infrared regions of the spectrum. These detectors would use both cyclotron resonance and interband transitions between quantized magnetic levels for this purpose and would significantly extend the range of present detectors.

Parametric effects involving nonlinear phenomena both in magnetic and electron systems in the presence of a magnetic field could be used both as detectors and as tunable sources in the far infrared and submillimeter regions. Some of this work has already begun with high power gas lasers such as the CO<sub>2</sub> laser in electron systems using nonparabolic phenomena in semiconductors in magnetic fields.

One potential device in quantum electronics is a tunable local oscillator for a potential CO<sub>2</sub> laser radar system. Here a semiconductor such as lead-tin-telluride would be tuned with a magnetic field in an automatic frequency control mode. The feasibility of this has already been demonstrated.

Another type of detector or source that high magnetic fields would make available is the use of the maser in the submillimeter or far infrared region. A CW gas laser such as the cyanide or water-vapor laser would be used as a pumping source for exciting a 3 or 4 level maser either in a magnetic or electric dipole transition. This is analogous to the low noise masers that have been developed in the microwave and millimeter region. Such devices, of course, require high magnetic fields for operation.

Some of the most exciting quantum electronics phenomena are those associated with the analogous behavior of high energy free electrons and their interaction with laser beams or hot electrons in solids. One can make use of the quantum limit of the resultant inverted population in both semiconductors or semimetals.

Finally, the tunability of solid state and gaseous lasers in high magnetic fields offers a high resolution scanning system. This then can act as an ultra-sensitive tool for resolving fine structure in optical, infrared, and ultraviolet spectroscopy.

## 2. Electron Beam Devices.

It is known from electrodynamic calculations that energetic electron beams in high magnetic fields will emit radiation in the submillimeter regions as well as harmonics which extend into the far infrared. In a recent experiment [6] a broad band electron beam device of this type was operated and swept from a 6 mm wavelength to 0.7 mm by employing a magnetic field up to 150 kG, emitting substantial power from the fundamental transition. This unprecedented range gives great encouragement for continued research in this area. Crossed electric

and magnetic field devices of the magnetron variety can also be investigated for their properties as radiation sources in high magnetic fields not only in the millimeter and infrared region, but at higher frequencies as well. Such electron beam devices with a pulsed magnetic field employing a combined betatron-magnetron configuration should be an excellent source of pulse synchrotron radiation in a very compact device.

### 3. Synchrotron Radiation Sources and Accelerators.

Beams of electrons, injected from pulsed synchrotrons and orbited in storage rings can be unique sources of strong radiation in the ultraviolet, X-ray and gamma ray regions of the spectrum. [7] The concept of high magnetic field storage rings for use in synchrotron radiation sources was first discussed at the Francis Bitter National Magnet Laboratory in 1963 and has generated considerable enthusiasm and resulted in an actual experimental system at the University of Wisconsin which is now operable. Use of pulse fields and high field superconducting magnets in suitable combinations would result in devices more efficient and vastly more compact than the adaptation of existing accelerators. The existence of these strong continuous high resolution sources would revolutionize spectroscopy in this region of the spectrum.

High energy physicists have not utilized high magnetic fields for accelerators because of the excessive radiation loss involved at maximum energy. Therefore they usually have resorted to systems with large diameter at lower magnetic fields. For the purpose of radiation devices, accelerators and storage rings can be built out of high field superconducting magnets or pulsed magnets making them considerably more compact and smaller in size. Furthermore, for these purposes there is an important trade-off between energy and magnetic field to achieve the same or greater performance in terms of spectral limits and intensities. For example, the Cambridge Electron Accelerator with a 6 BeV beam and approximately 10 kG magnetic field and a diameter of about 30 meters has an upper emission frequency of about  $1 \text{ \AA}$  as a synchrotron radiation source. In terms of a radiation source the same upper frequency and even greater intensity could be achieved by increasing the field 10-fold with a superconducting magnet and thereby reducing the diameter of the device to a modest 3 meters. In fact, such an accelerator combined with a similar high field compact storage ring can be made to produce  $\gamma$  rays with a total power output of the order of megawatts. Such an intense  $\gamma$  ray source would represent a tremendous tool for a variety of industrial and military projects.

In addition to their function as sources, these devices themselves would be studied in regard to the interaction of photons with intense electron beams and for stimulated emission of electrons accelerated in a magnetic field. See Fig. 4. For example, a high power laser radiating into these high current, high field storage ring configurations will produce many more gamma ray photons by the inverse Compton effect than the present low current beam accelerators. In addition, enhanced radiation can also be obtained by stimulating emission downward by beaming the laser, or the synchrotron radiation, in the same direction as the motion of the electron beam rather than against it. These problems are of great practical and theoretical interest. Stimulated synchrotron radiation, which is an entirely new subject, might be utilized to produce extremely intense incoherent and possibly coherent sources at very high frequencies which could be used as natural

pumps to pump lasers at much lower frequencies.

Development of the superconducting magnet technology for high field storage rings, development of the pulse field cyclotron, synchrotron or betatron injection devices, as well as the possibility of employing the spectral output of such a device, make this area a natural one for the exploitation of high magnetic fields.

Another application of high magnetic field accelerators is for heavy particles, i.e., protons or alpha particles, where radiation is not a serious limitation to energy. The high field accelerators could be considerably reduced in size.

#### 4. Plasma Source Device.

The behavior of dynamic electron plasma devices in magnetic fields in excess of 100 kG have as yet not been explored. Such devices constitute very efficient radiation sources through the electromagnetic spectrum. It will be very important to study not only the dynamic behavior of such plasmas as a basic problem, but also the radiation capability in the presence of high magnetic fields.

Such devices can be compact tubes in dc or pulse magnetic fields of relatively small volume, somewhat larger devices involving several cubic centimeters, or devices in the order of 1 to 2 orders of magnitude larger. Again the regions of interest are the submillimeter, infrared, and ultraviolet regions where there is great need for strong efficient sources.

#### 5. Thermomagnetic Devices.

Recent theoretical work [8] has demonstrated the importance of high magnetic fields in enhancing the efficiency of thermomagnetic devices using solid state materials. The demonstration of this enhancement for energy conversion represents an important basic physics problem. If the material with the optimum theoretical properties can be found, thermomagnetic devices can be a highly practical and promising development. The converse of this device, a solid-state thermo-electric refrigerator appears to be much more promising and will receive a good deal of theoretical and experimental attention in the next five years. The importance of such devices for certain cooling applications is obvious.

### III. OTHER APPLICATIONS

#### A. Medical Applications of High Magnetic Fields.

There are a number of potential medical applications of magnetic fields. These include magnetically induced forces for the guidance of catheters through body cavities, the control of muscles or valves, the removal of ferromagnetic foreign bodies, magnetic forces to guide and localize ferrite powders for X-ray diagnostics or for use as carriers of medication, the inductive coupling of energy into implanted devices and for direct pace-making or defibrillation of the heart, and finally, the monitoring of blood flow and the measurement of heart and brain wave electrical activity. The Laboratory is active in several of these areas, specifically the magnetic guidance of catheters, magnetic pace-making and defibril-

lation of the heart, and the magnetic measurement of heart and brain wave electrical activity.

An external magnet system capable of guiding a ferromagnetic-tipped catheter through vessels in the body would greatly facilitate many medical treatments by providing access to parts of the body otherwise inaccessible except by major surgery. Such guided catheters could be used both in diagnosis and in clinical treatments. Neurological applications, for example, would include blocking feeded vessels of certain intracranial vascular malformations, and the local injection of high concentrations of radio-opaque medium or chemotherapeutic agents.

The external magnet system for catheter guidance must be capable of exerting forces sufficiently strong and continuously adjustable in magnitude and orientation. Magnetic field gradients in the order of 1 kG/cm are required for full utilization of the technique, and this requirement for very large field gradients opens up a potentially very important new application of superconducting magnets in the medical area. The feasibility of this technique has already been demonstrated with a "cardiovascular navigator" developed in the Laboratory in collaboration with Massachusetts General Hospital [9] which uses the water-cooled electromagnet shown in Fig. 5. A system utilizing a superconducting magnet could be vastly more effective and could open up an entirely new area of medical treatment.

A superconducting magnet system for neurosurgical use consisting of three orthogonal pairs of coils has been proposed [10] and designed by the Laboratory and would be capable of producing a gradient of 1 kG/cm in any direction by adjusting the currents in the three sets of coils. The proposed system is shown in Fig. 6.

In a second medical area, we have recently begun work in pace-making the heart by means of magnetically induced voltages. If a magnetic field is changed sufficiently rapidly ( $10^5$  -  $10^7$  gauss/sec), voltages can be induced in muscle tissue of sufficient magnitude to fire the muscle. A preliminary small system is being built for the University of Vermont for animal studies and may very likely prove to be the forerunner of systems for use in intensive care units where automatic emergency pace-making and defibrillation are current important unsolved problems.

We have also recently become involved in a closely related area, that of the measurement of the weak magnetic fields arising from various natural current sources within humans. The following measurements [11] have been made by Dr. David Cohen of the Laboratory at his facility at the University of Illinois at Chicago: (1) the ac magnetic field arising from the same ac heart ion currents which produce the electrocardiogram, with a field maximum of  $\sim 5 \times 10^{-7}$  gauss; (2) the ac magnetic field arising from the same ac alpha-rhythm ion currents which produce much of the electroencephalograph, with a maximum of  $\sim 1 \times 10^{-9}$  gauss; (3) the dc magnetic field arising from a dc current near the abdomen, of undetermined source, with a maximum of  $\sim 5 \times 10^{-7}$  gauss. A new magnetically shielded room, essential for this work, is now being built and the study continued by Dr. Cohen.

One reason that surface magnetic measurements are potentially useful in medical research and diagnosis is the limitation of surface voltage measurements,

which cannot uniquely determine the internal charge (or excitable tissue) distribution. The combination of surface voltage and magnetic measurements, while still not producing uniqueness, does give more internal information than voltage measurements alone.

#### B. Electromagnetic Proof-Loading of Bonded Aircraft Structures.

The first application of high field technology to the aircraft industry was made in 1960, when the Francis Bitter National Magnet Laboratory assisted the Convair Division of General Dynamics in the development of a method for swaging turnbuckles and clevis fittings to control cables, as well as torque actuating tubes to splined connectors, by the use of a pulsed magnetic field instead of a mechanical swaging die. [12] Since the induced eddy current force always complies with the irregular shape of the cable, magnetic swaging proved to be substantially more reliable than mechanical swaging and the technique has been adopted throughout the industry. The "Magnaform Division" organized by General Dynamics to supply the apparatus to other aircraft manufacturers was recently sold to the Gulf Corporation.

In this swaging process, as well as in other magnetic forming applications developed subsequently, the metal is subjected to a pulsed magnetic field. Induced eddy currents flow in such a way as to oppose the change in field, or to prevent the field from penetrating into the metal. In reacting against the field which induces them, these eddy currents repel the metal from the pulsed field coil. The method has two basic limitations: there is no way to control the direction of the force; it is always repulsive. Moreover, the method is very inefficient; since the instantaneous eddy current is proportional to the rate of change of the magnetic field, the current maximum precedes the field maximum. The induced force, being proportional to the vector product of current and field, is therefore substantially weaker than it could be if the phase lag were somehow eliminated.

Recognition of this circumstance led to the invention of a more sophisticated method of magnetic forming which makes use of two separately controlled pulsed fields: a slowly pulsed field which penetrates into the metal, and a fast-rising pulse which does not penetrate but induces a substantial skin current. The two pulses can be timed and oriented so as to produce the desired force, which may be repulsive or attractive. Eight years later, in September 1968, a new requirement of the aircraft industry presented an opportunity to apply this new principle. We were approached by the Boeing Company with a request for assistance in solving a problem.

The advent of modern adhesives has made it possible to use bonded structures in aircraft design which are superior to the traditional riveted structures in several important respects. They eliminate stress concentration in skin-stressed structures, they possess inherent damping against fluttering and vibration, and they allow the incorporation of honey comb laminations for stiffening and distributed reinforcement. Unfortunately the use of bonded structures has been precluded by lack of a non-destructive testing method. Testing would involve applying a traction of several thousand psi to an aircraft skin. Boeing wondered whether it was possible to apply such a proof-loading force electromagnetically, and by means of a technique applicable during construction as well as in-service inspection of

complete aircraft. With support from Boeing, we were able to demonstrate the feasibility of a proofloading device based on the double pulse method.

In these preliminary tests, the background field is provided by a six inch caliber Bitter solenoid magnet which accommodates an oval traction coil. Supplied with energy from a capacitor discharge of six microsecond duration, this traction coil induces the skin current which generates the proofloading force by interaction with the continuous magnetic field. The traction force acts on opposite surfaces of a bonded test panel inserted into the coil, thereby raising a visible blister wherever a known flaw has been introduced into the bonding layer. Experiments now being performed with this laboratory device are intended to determine the parameters needed to design a prototype industrial testing machine. Obviously this machine will make use of a traction coil designed to generate an external field so that the proofloading force can be applied to fuselage, empennage and wing surfaces of aircraft.

Figure 7 is a photograph of the laboratory device, operating in conjunction with the Bitter solenoid magnet which provides the background field. Associated diagnostic equipment is located on a balcony above the magnet and does not appear in the photograph.

Figure 8 is a simplified sketch which illustrates operation of the experimental system. The traction coil is connected by means of low inductance co-axial tubes to the fast bank, a 2 microfarad, 50 kilovolt energy storage capacitor. The system is highly under-damped, and a free discharge would therefore oscillate or "ring" for a large number of cycles. Since proofloading requires a uni-directional force, it is necessary to terminate or "crowbar" the discharge after completion of the first half-cycle. This is accomplished by means of a double spark gap housed in a monolithic, heavy-walled cylinder of lucite submerged in transformer oil. The gap housing must obviously withstand a considerable shock wave since the plasma is expected to conduct peak currents of 50 to 100 kiloamperes. The cavity in the lucite cylinder is pressurized with nitrogen to permit control of the breakdown voltage and contains three spherical electrodes in addition to two tungsten trigger needles. The oil-filled circuit box which surrounds the main gap also contains two primary trigger gaps with all associated pulse transformers, voltage dividers and pulse forming circuitry. Only the primary, low voltage control circuits are housed in a separate, remotely located chassis.

Operation of the system is very simple in principle. The central spherical electrode, which is connected to the capacitor, is flanked by two other spheres, one connected to the traction coil and the other to ground. A pulse of several hundred kilovolts supplied to the appropriate tungsten trigger needle initiates a discharge through the coil. At the instant the discharge current begins to reverse, a suitably timed second trigger pulse initiates a second discharge to the grounded sphere. The current waveform observed without and with crowbar operation are sketched in the figure. Reliable operation requires careful adjustment of gap spacings and nitrogen pressure, as well as suitable filtering and shielding against radio frequency pickup and magnetic induction. It is believed that with some modifications this basic system can be made sufficiently reliable for plant operation by inexperienced personnel.

Before bonded structures can be used with confidence, it will be necessary to

establish dynamic (i.e., impact) as well as static test criteria for bond quality. We intend to assist Boeing and possibly the A.S.T.M. in perfecting criteria for ultimate adoption as industry standards.

### C. Magnetic Ore Separation.

The force which can be exerted magnetically on a magnetic particle is proportional to three quantities: the gradient of the applied magnetic field, the size of the particle, and the magnetization of the particle (whether permanent or induced by the applied field). In cases involving relatively large particles which are highly ferromagnetic a force adequate for separation can be achieved by simple means, and magnetic separators are commonly used to remove such particles from a non-magnetic medium in the form of a wet slurry or suspension, a fluidized (gas-supported) bed, or a simple dry aggregate. However, there are many cases of considerable interest in which magnetic separation has never been possible on an industrial scale, due primarily to the very rudimentary state of the art. Such cases involve particles which are either too small in relation to commonly achievable gradients, or too difficult to magnetize in relation to commonly achievable field intensities. There may also be more subtle difficulties.

The Francis Bitter National Magnet Laboratory has responded to several requests for assistance in solving magnetic separation problems, and even this casual and purely informal contact with the industry has led to at least one new industrial process. There is no question that a great deal of economic and even strategic value can be achieved by applying more sophisticated methods of magnet design to magnetic separation. Ironical though it may seem, it is likely that superconducting magnets, in their present state of development, are ready to make a substantial contribution in the one area which has never been mentioned in any of the numerous speculations concerning superconducting applications: ore separation.

Our most successful intervention in magnetic separation has been in the purification of kaolin for use in paper coating. This involves the removal of particles which are very small (colloidal and sub-colloidal), very weakly magnetic (they only contain trace amounts of iron in the form of stain), and which must be removed to a very complete degree for the process to be of any value. Fortunately these difficulties are offset by a very substantial advantage: the cost of the separation need not be borne by the very small fraction of magnetic material which is removed, but may be allocated to the bulk of the feed which is thereby purified. Thus a cost figure which is prohibitive in dollars per gram removed becomes very attractive in dollars per ton purified. We succeeded in developing a magnetic separator capable of outperforming the chemical separation process used previously, and even utilizing grades of kaolin not previously amenable to economic purification. The device makes use of magnetized stainless steel wool to achieve a large volume of high field gradient, and a magnetizing field somewhat higher than can be achieved in commonly used industrial separators. The first production capacity separator is now under construction.

There is a rather interesting scientific by-product of this application: kaolin was once ocean bottom sediment, and magnetic impurities contained in it may be expected to have collected and trapped magnetic monopoles incident with the cosmic radiation for geological periods of time. The clay mining company, in gratitude

for our assistance, has agreed to make their magnetic tailings available to be searched for magnetic monopoles.

A second application we have been working on informally for some time involves the removal of non-sulfide molybdenum and tungsten from what is now the tailing flow from the Climax Molybdenum Company's operation. Only molybdenum sulfide can be recovered economically by present means. The loss of non-sulfide molybdenum represents an estimated \$20,000 per day. Unfortunately the situation in this case is the converse of the kaolin situation: the cost of the separation must be borne by the very small fraction of material which is removed, and in terms of dollars per gram no process they have tried looks very promising on economic grounds. There is one ameliorating circumstance: the removal need not be complete, as in the kaolin case. On the other hand, the process must accommodate enormous quantities of slurry at a high flow rate. Our tests so far have indicated that the method applied to kaolin will work in principle but fails to achieve practical through-put rates. It also requires the prior removal of coarse components. Results obtained so far suggest another promising approach: a continuous flow process using a quadrupole gradient. We have modified an existing magnet to experiment with this technique, but have not as yet been able to fit the work into our schedule.

A third project, begun only recently, is being conducted in cooperation with a large copper mining company. It is aimed at developing a technique for magnetically classifying ores obtained from ocean bottom sediment.

#### D. Transportation.

During the last few years a number of scientists have seriously proposed the use of superconducting magnets in conjunction with high speed transportation. [13] The basic concept involves the location of a series of high field magnets at the base of a train with the magnetic field oriented vertically. At sufficiently high speed this magnetic field produces eddy currents in the track bed which contains loops of conducting copper or aluminum. The eddy currents so induced set up a field which opposes those of the superconducting magnet, thereby lifting the train several inches above the ground. In this way the only friction that opposes the motion of the train is that of the air. With a proper magnetic configuration and suitably designed track beds, the train could be confined and reach speeds of the order of 300 mph.

The important contribution of this Laboratory would be in the design of a wide variety of configurations for high field magnets and to related problems of supporting large volume superconducting magnets that are subjected to large external forces. This problem is not unlike that faced in the construction of the hybrid magnet.

## REFERENCES

1. D. B. Montgomery, J. E. C. Williams, N. T. Pierce, R. Weggel, and M. J. Leupold, "A High Field Magnet Combining Superconductors with Water-Cooled Conductors," Advances in Cryogenic Engineering, Volume 14 (1969) (to be published).
2. "The Hybrid, A Unique New Concept," OAR Progress (1968).
3. K. Tachikawa, S. Fukuda and Y. Tanaka, Cryogenic Engineering (Haywood-Temple Industrial Publications).
4. S. Foner, E. J. McNiff, B. T. Matthias and E. Corenzwit, "Critical Fields of  $Nb_3Al_{1-x}Ge_x$  Alloys in Liquid  $H_2$ ," 1968 Applied Superconductivity Conference, to be published in J. Appl. Phys. (April 1969); "Properties of High Superconducting Transition Temperature  $Nb_3Al_{1-x}Ge_x$  Alloys," Proc. LT-11, 1968 (to be published, 1969).
5. R. C. Ferguson and W. D. Phillips, Science 157, 257 (1967).
6. I. B. Bott, Proc. Inst. Elec. Engrs. 52, 330 (1964).
7. K. Codling and R. P. Madden, J. Appl. Phys. 36, 380 (1965).
8. J. M. Honig and B. Lax, J. Appl. Phys. 39, 3549 (1968).
9. S. B. Yodh, N. T. Pierce, R. J. Weggel and D. B. Montgomery, J. Medical and Biological Engineering 6, 143 (1968).
10. D. B. Montgomery, R. J. Weggel, M. J. Leupold, S. E. Yody and R. L. Wright, "A Superconducting Magnet System for Intravascular Navigation," 1968 Applied Superconductivity Conference, to be published in J. Appl. Phys. (April 1969).
11. D. Cohen, Science 156, 652 (1967); Science 161, 784 (1968).
12. U.S. Patents 2,976,907 and 3,383,890.
13. J. R. Powell and G. R. Danby, ASME-66-WA/RR-5; F. C. Chilton, P. T. Coffey and T. W. Barbee, Jr., "A Magnetic Suspension System," 1968 Applied Superconductivity Conference, to be published in J. Appl. Phys. (April 1969).

## FIGURE CAPTIONS

- Fig. 1. Overall view of the 225 kilogauss (kG) hybrid water-cooled and superconducting magnet system. The external helium storage vessel is at the left and supplies helium to the magnet cryostat. The 8 kW power supply is shown between the cryostats. A small refrigerator is shown mounted on top of the magnet cryostat and is used to hold the magnet at  $20^{\circ}\text{K}$  between scheduled operations. The magnet cryostat is mounted on heavy springs to allow relative motion between the two coil systems under fault conditions.
- Fig. 2. Fourteen-inch room temperature bore hybrid magnet cryostat for the 60 kG superconducting coil showing the cable type of suspension used to support the large interaction forces between the superconducting magnet and the copper insert. The helium cryostat is surrounded by a nitrogen cryostat and access for electrical leads and cryogenic fluids is provided by the 3 inch tube.
- Fig. 3. Comparison of critical field vs. absolute temperature for a number of high field superconductors tested at the Francis Bitter National Magnet Laboratory. At a given temperature, the new NbGeAl alloy has a much higher critical field than any of the previous materials and at  $14^{\circ}\text{K}$  the critical field is measured as 200 kG. The transition temperature is  $20.7^{\circ}\text{K}$ . The dashed curve below  $14^{\circ}\text{K}$  is an extrapolation assuming the physical parameters derived above  $14^{\circ}\text{K}$ . Although the critical field may be as high as the extrapolation indicates, measurements will require very high dc fields.
- Fig. 4. Universal synchrotron radiation source for a broad spectral range from the near ultraviolet to the X-ray region. Intense  $\gamma$ -rays produced by inverse Compton effect of interaction of laser radiation with electrons.
- Fig. 5. Five kW electromagnet for catheter guidance which permits horizontal translation and rotation about three axes.
- Fig. 6. Proposed superconducting magnet system for catheter guidance in neurosurgical applications. Three orthogonal sets of coils can generate a gradient in any direction in space as high as 1000 gauss/cm.
- Fig. 7. Experimental electromagnetic proof-loading apparatus installed in 6 inch Bitter magnet at the Francis Bitter National Magnet Laboratory.
- Fig. 8. Schematic diagram of experimental electromagnetic proof-loading apparatus.

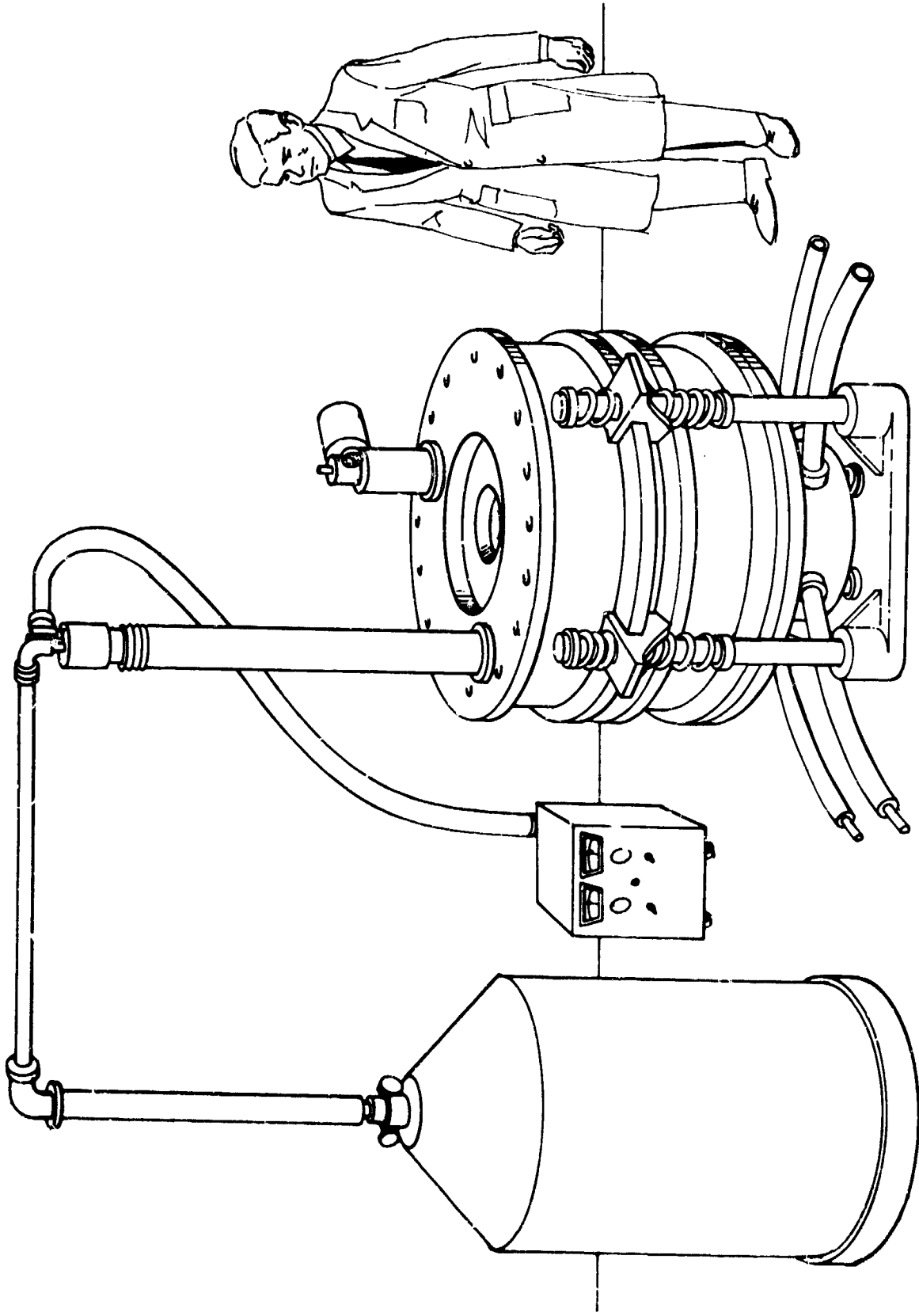


Figure 1

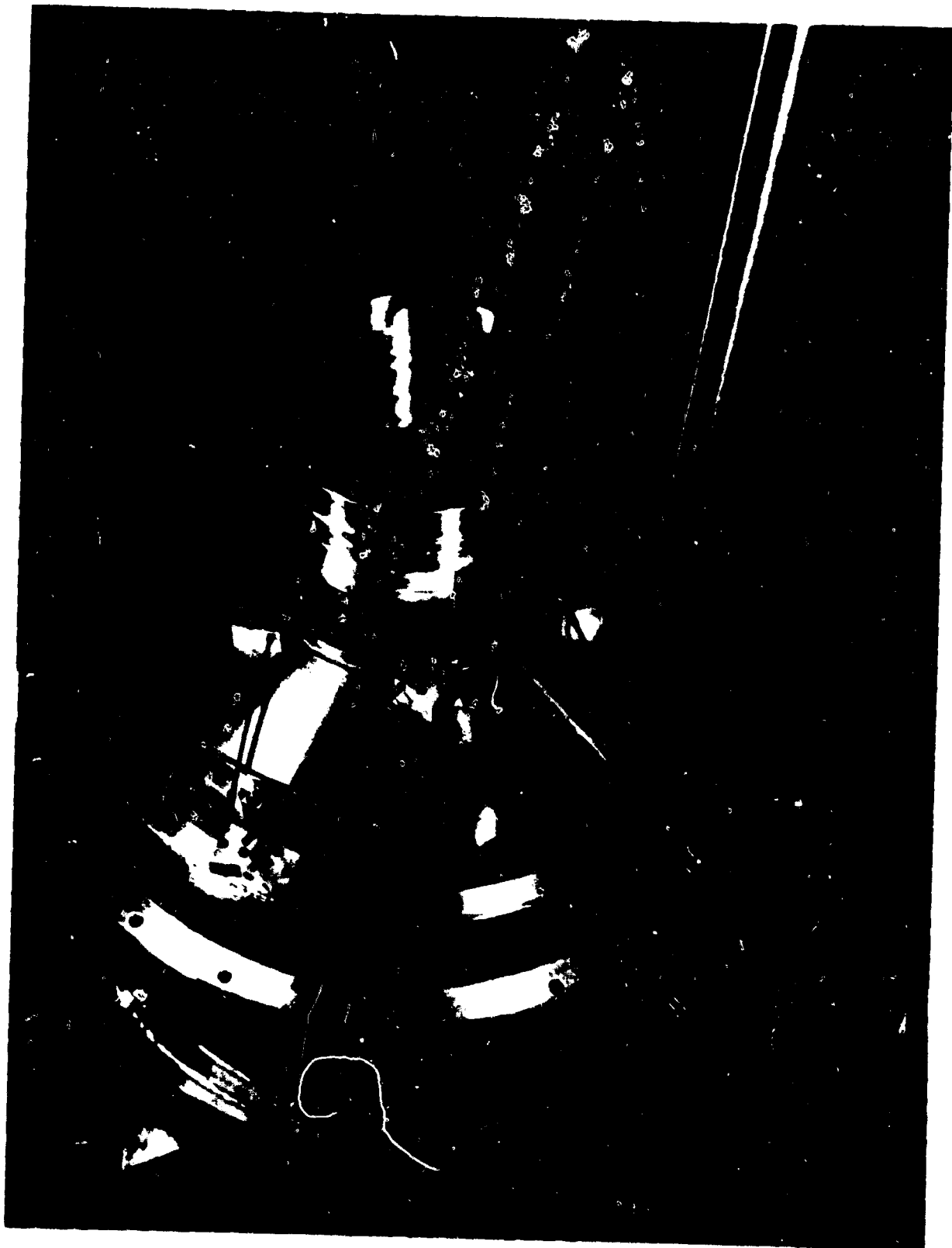


Figure 2

A-17

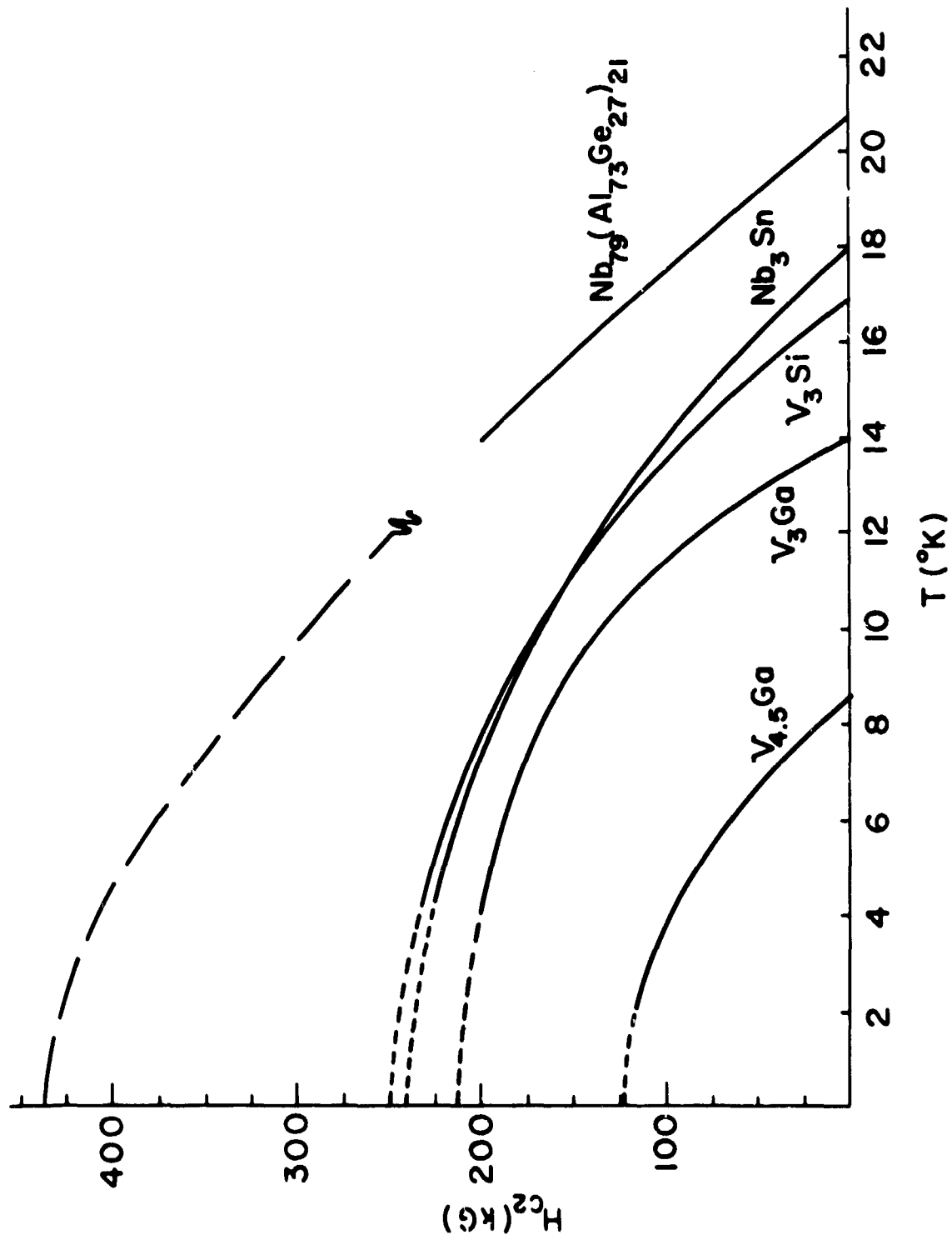


Figure 3

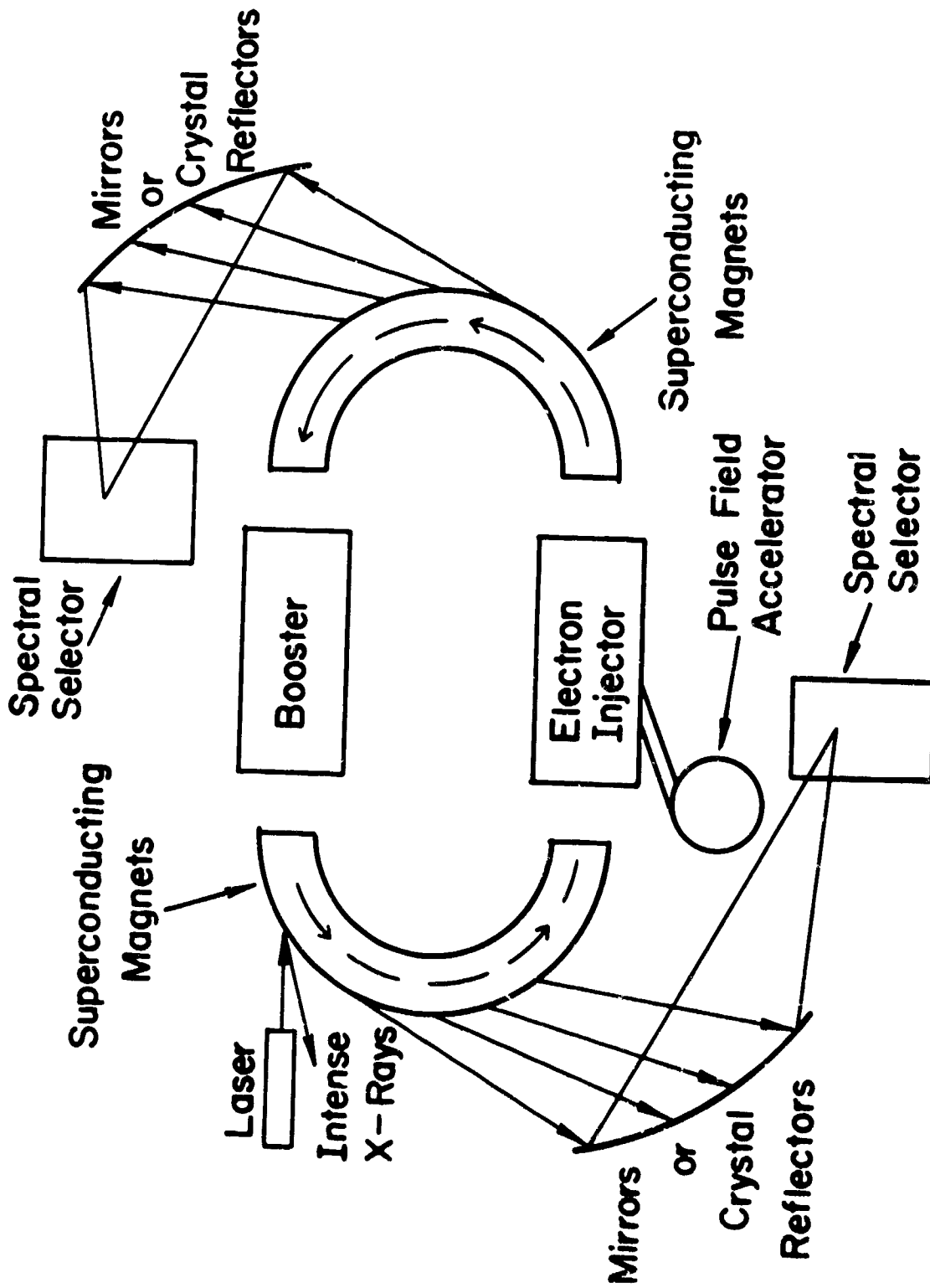


Figure 4



Figure 5

A-20

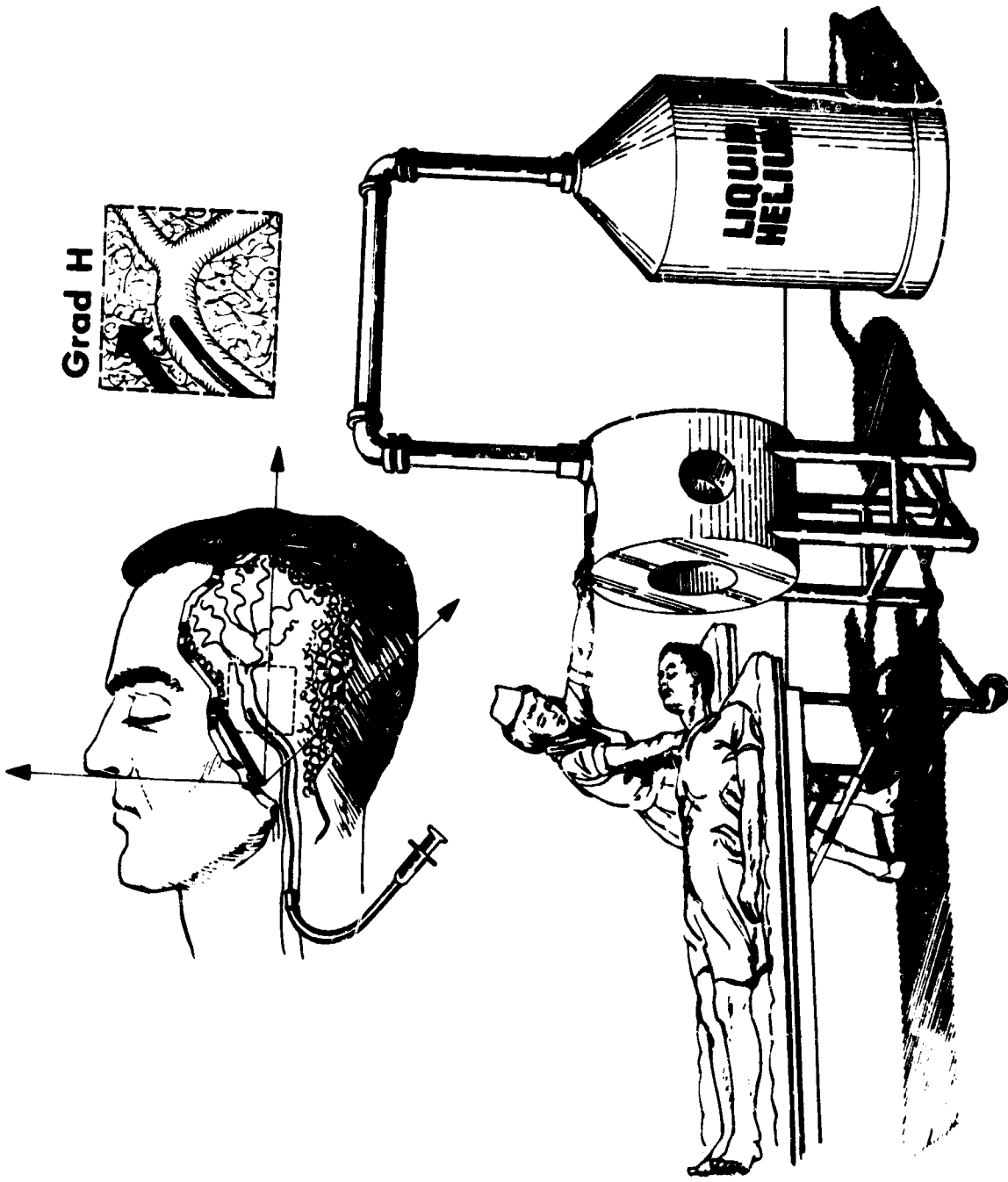
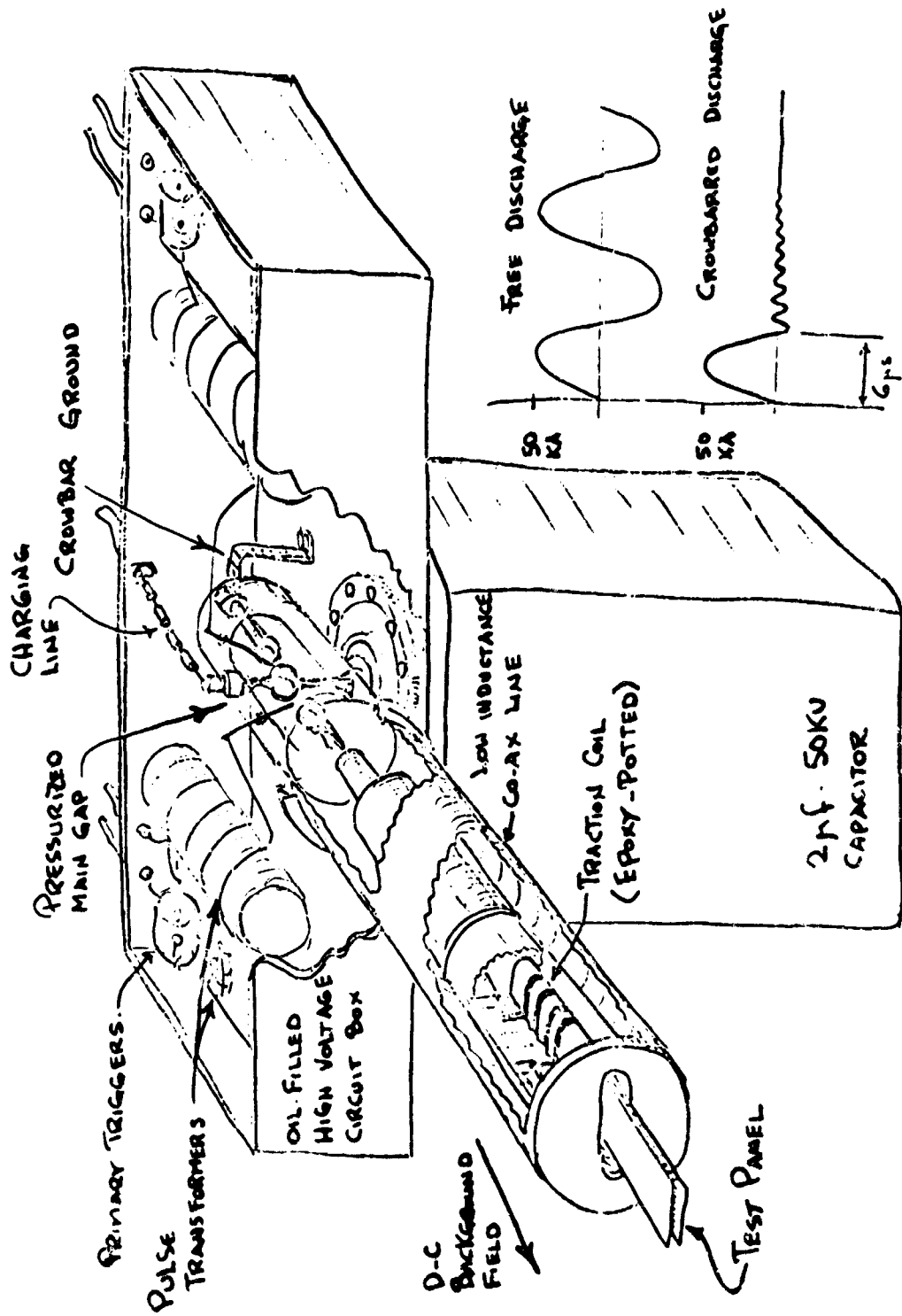


Figure 6



Figure 7



EXPERIMENTAL ELECTROMAGNETIC PROOFLOADING APPARATUS  
 DEC 1968 - KOLM

Figure 8

NEW DEVELOPMENTS IN  
SUPERSONIC COMBUSTION RESEARCH

J. Swithenbank

Department of Fuel Technology and Chemical Engineering  
University of Sheffield

## New Developments in Supersonic Combustion Research.

J. Swithenbank.

Department of Fuel Technology and Chemical Engineering.  
University of Sheffield.

### Abstract.

This research programme is aimed at detailed understanding of the supersonic combustion process relevant to scramjets and hybrid engines. The work is particularly directed at the hydrogen/air system and flight Mach numbers  $>10$ . A 150 mm. hypersonic shock tunnel is used to provide the high stagnation pressures and temperatures (up to 500 bars and  $8000^{\circ}$  K) which are required, and the tunnel nozzle is directly connected to the supersonic burner. A typical combustion chamber is 75 mm. x 75 mm. x 1 metre long, and operates at an entry Mach. number of 3.5. Since the test section static pressure is much higher than in conventional hypersonic shock tunnels, special operating techniques have been evolved which eliminate the expensive highly evacuated dump tank which is usually used.

Novel instrumentation has been developed as follows:-

1. A high speed gas sampling valve and probe can be used to monitor the gas composition in the test section. This has shown that oxygen deficiency and contamination of the test gas (air) by the driver gas (helium) are significant factors, and due allowance must be made in the interpretation of supersonic combustion results.
2. A hypersonic velocity meter based on an open circuit electro-magnetically induced voltage is used to determine the velocities in the supersonic burner.
3. A low cost magnetic drum recording system has been developed which can give a large bandwidth capacity on hundreds of channels for 40 milliseconds. The information can be recovered as a stationary oscilloscope trace or fed to a tape punch.

A theoretical study of the turbulent fuel/air mixing process has revealed a simple principle by which optimum mixing and combustion systems may be designed. In the case of supersonic systems, this approach reveals that mixing losses are much larger than has been hitherto assumed and result in a severe performance penalty at the higher speeds. When applied to subsonic systems the theory indicates the design of very low pressure loss self proportioning gas turbine burners and low pollution carburation systems for piston engines. In particular it may be applied to dual-mode scramjet burners.

## Introduction.

This paper presents a summary of the research studies sponsored at Sheffield University by the OSR and highlights some of the practical applications.

The present generation of aeronautical propulsion systems has attained a performance plateau, which will only be surpassed by the introduction of new devices. In the case of the gas turbine/ramjet engine, the most promising new unit (1) is the scramjet (supersonic combustion ramjet); whilst in the case of the rocket, a new hybrid unit involving air augmentation appears advantageous. In order to exploit these advanced concepts, detailed research on the fundamental aerodynamics, mixing and chemical reactions is required. Since these fields of study are so vast, it is important that the research is confined to the relevant areas if maximum progress is to be made at minimum cost. Thus the first requirement is that we correctly simulate the important flight parameters in our laboratory studies.

Figure 1a shows the flight corridor of an advanced vehicle, and the corresponding stagnation pressures and temperatures are given in Figures 1b and 1c. It may be shown (2) that a maximum speed of about Mach 15 is likely for cruise missions, whilst for boost acceleration missions, speeds up to Mach 20 are conceivable. We are therefore interested in stagnation pressures and temperatures up to 5000 Bars, 8000°K and  $10^5$  Bars, 14000°K for ultimate cruise and boost missions respectively.

If we now turn our attention to the scramjet engine as shown in Figure 2, we see that this consists of an intake, combustor and nozzle, which must all be integrally mounted with the airframe to form a satisfactory vehicle. Parametric studies (2) indicate that for optimum engine performance, the combustor entrance flow should be subsonic below a flight Mach number  $\approx 4.5$ , and supersonic at the higher Mach numbers. We thus require the combustion system to operate both subsonically and supersonically (i.e. dual-mode) if we are not to have a multiplicity of engines fitted to a hypersonic vehicle. The subsonic combustion aspect of the combustor design will be discussed later in the paper. During supersonic combustion conditions, the combustor entrance Mach number is approximately one third of the flight Mach number, and therefore falls in the range 2 to 5. The corresponding combustor static pressure is in the range 0.2 to 4 Bars (Figure 3a) and the static temperature is 1000 to 2000°K (Figure 3b). The high overall engine performance

potential is indicated in Figure 3c as a function of Flight Mach number.

The important phenomena to be studied in a scramjet combustor are the turbulent mixing of fuel and air, with simultaneous chemical reaction, and the interaction of the resulting pressure gradients with the duct geometry. Fortunately sufficient is now known about supersonic combustion that the critical parameters can be identified, and it is found that the major problems can be studied without duplicating the maximum flight stagnation conditions. At speeds above Mach 10, the combustion time is sufficiently short that the system is mixing controlled, and the pressure and temperature can be reduced with little loss of accuracy of simulation. It is therefore concluded (4) that for flight speeds above Mach 10, connected supersonic combustion testing can be adequately covered by stagnation temperatures of 5000°K and stagnation pressures of 200 Bars. (Note. The total pressure loss in the intake does not have to be supplied.)

#### The Sheffield University Shock Tunnel.

In 1963 a 150mm shock tunnel was built to study supersonic combustion for scramjet operation above Mach 10, and a general view of the facility is given in Plate 1.

The main disadvantage of the shock tunnel arises from the short testing time of a few milliseconds. However, since the residence time in the combustor is < 0.5 m.sec. testing times in excess of one millisecond are adequate to study the combustion process. The tailored interface reflected shock tunnel gives the longest running time for a given length of driven tube, and the capability of such a facility is shown on Figures 4a and 4b as a function of primary shock Mach number. It can be seen that air stagnation temperatures of 5000°K as required for engine tests, can be produced with combustion heated helium driver gases.

Hot helium is used following the technique developed by General Electric in which a mixture of 70% helium and stoichiometric hydrogen: oxygen, is ignited by eight high energy discharge igniters (5). The combustion results in a smooth six to seven fold pressure rise over a period of about 10 millisecc., after which time the diaphragm opens. The maximum driver pressure is repeatable within 3%, and is usually about 20% greater than the final air stagnation pressure.

### High Speed Gas Sampling.

Recent studies have shown that contact surface interactions may curtail the useful running period, in addition to the familiar limitation due to the arrival at the nozzle of the tail or reflected head of the expansion wave from the diaphragm. Theoretical studies(6) have indicated that two phenomena may arise, namely contact surface instability, and shock bifurcation caused by shock interaction with the boundary layer. This latter process results in annular jets of driver gas penetrating the shock heated gas in the stagnation region, and diluting the test gas flowing through the nozzle. The theoretical onset of these two mechanisms usually occurs just above the tailoring Mach number. However, due to the importance of gas composition in our studies, we have investigated this phenomena experimentally (7). A high speed sampling valve fitted with a sampling probe was mounted at the exit of the tunnel nozzle. (Plate 2.) A flow of argon through the valve was passed directly to a gas chromatograph for analysis, and one sample could be taken on each tunnel firing. The valve was operated by discharging a capacitor through the solenoid coil, and the opening time was about 1.5 milliseconds. Some results are illustrated in Fig. 5 and it can be seen that driver gas (helium) appeared in almost every sample. Although it is felt that a shock tunnel could be designed to minimize or eliminate the contamination, our immediate approach is to make allowance for this dilution effect in the interpretation of our supersonic combustion test results. Measurements of oxygen concentration both with and without hydrogen fuel injection have also been made with the sampling valve, and these are reported in Refs. 7 and 8.

### Starting Transients in the Supersonic Combustor.

Although the test section static pressure is usually close to atmospheric, much higher pressures can be built up in the starting shock system. Fig. 6a shows that the starting shock Mach number in the test section is about Mach 5 for all test Mach numbers. The corresponding minimum starting pressure ratio to eliminate the overpressure is shown in Fig 6b together with the running pressure ratio, and it can be seen that the latter is about an order of magnitude smaller. Thus the test section must be evacuated to about one tenth to one thirtieth of the test static pressure prior to firing. It will be noted that this is a much lower vacuum than is used on conventional shock tunnels, also the dump tank can be

replaced by a simple blast tube to atmosphere which further reduces the facility costs.

#### The Measurement of Gas Velocity by Electromagnetic Induction.

When the ionized test gas is passed between the poles of a magnet, so that the magnetic field is perpendicular to the velocity vector, then the orthogonal induced voltage is equal to the product of the velocity and field strength. Since the latter is known, velocity can be determined. As shown in Plate 3, our supersonic combustion test section is fitted with a magnet and up to 150 volts is produced at the electrodes. Some test results are illustrated on Fig 7 and they show that the gas impedance is  $10^5 \rightarrow 10^6 \Omega$ , which is in accordance with the calculated equilibrium value (Refs 9 and 10). It appears likely that the technique can be used widely in aeronautical testing facilities such as pebble bed heated hypersonic wind tunnels.

The high electrical conductivity of the gas has been confirmed by an electrodeless meter based on the dissipation of energy in a 20 MHz field induced in the gas.

#### Low Cost Magnetic Drum Recording System.

The operation of a shock tunnel facility for engine testing requires a large bandwidth (d.c.  $\rightarrow$  10 KHz ) on many channels ( $>$  20) for a short time ( $<$  40 milliseconds.) The only commercial instrument which can meet this requirement is the oscilloscope and camera at a cost in excess of \$1000 per channel. We have, therefore, developed (Ref 11) a low cost system based on a magnetic drum in which the information is recorded on separate tracks each having a response of  $\sim$  1 MHz. In order to obtain a response down to zero frequency, f.m. recording is used, although instruments such as ionization gauges may be recorded in direct mode. In addition to low cost, the system has several other advantages:

- a) Since the signal is retained for 40 m.secs., the decision to retain the test data does not have to be made until after the test - rather than before as in the case of the oscilloscope/camera system.
- b) One oscilloscope can be used to display all channels in turn after the firing, and a stationary pattern is obtained.

- c) One counter timer can be used to measure all time intervals.
- d) By counting cycles through a gating circuit and operating a tape punch, the data can be easily fed into a computer for analysis.
- e) Our present drums have a capacity of 370 channels each, although we only use a few channels at present. Plate 4.

Theoretical Studies.

A theoretical study of the fuel/air mixing and combustion process has been made based upon a new interpretation of turbulence theory. The application of turbulence theory to the solution of internal flow problems is still in an early stage of development, due to mathematical complexity, and in many cases only an order of magnitude solution can be obtained. In our treatment, the system is regarded as a classical stirred reactor, and energy balance principles are used to calculate the minimum input pressure energy required to generate the necessary stirring (i.e. turbulence intensity).

In general the low-wave number end of the turbulent-energy spectrum depends on the geometry of the turbulence-producing device, while the high-wave number region of the spectrum is almost isotropic, and independent of the source of eddy formation. The smaller eddies are very important in the turbulent mixing and combustion process in which fuel, air and combustion products are stirred together to the molecular level. Since the high wave-number eddies contain about 80% of the total turbulence energy, the ability of different systems to achieve mixing will depend largely on the total turbulence energy in each system. Now:-

$$\text{Kinetic energy of turbulence} = \int_0^{\infty} \rho E(k) dk \approx \frac{3}{2} \rho u'^2$$

- where
- k is the wave number.
  - E(k) is the energy spectrum function.
  - ρ is the density.
  - u' is the root mean square turbulence velocity.

In general, turbulence is generated from the mean motion of a stream by the shear stress and velocity gradient. In free turbulence (i.e. jets and wakes), all the velocity energy of the mean motion that is lost, appears first as kinetic energy of turbulence and is later viscously dissipated as heat.

The source of the energy necessary to provide the turbulent kinetic energy is then the pressure (or velocity) energy of the stream. In the case of baffle or bluff body mixers, as in gas turbine engines, industrial burners, etc., the turbulence produced can be calculated by the energy balance.

$$\frac{3}{2} \rho u'^2 = \Delta P = \zeta \frac{1}{2} \rho U^2$$

where  $\zeta$  is the pressure loss factor.  
 $\Delta P$  is the total pressure loss.  
 $U$  is the stream Velocity.

In the case of co-axial jet mixing systems, such as are proposed for scramjet burners, the hydrogen fuel jet carries negligible kinetic energy due to its low density, and practically all the mixing energy comes from the air stream. The fuel jet, therefore, acts very much like a bluff body and in principle, fuel injection into the wake of a suitably designed stirrer can result in a more rapid release of the turbulence, and hence a shorter supersonic burner, than is obtained with a co-axial jet system. (Plate 5) Such a bluff based body will also operate as a subsonic flame stabilizer for dual-mode operation.

The important parameter in the design of a mixing-combustion system is, therefore, the turbulence intensity, which is very approximately equal to the width/length ratio per fuel injection unit. In order to minimize the friction drag on the walls of the combustor, it should be made as short as possible, and this implies that we should use the highest possible turbulence intensity. If we postulate that non-linear dissipation effects would inhibit the formation of supersonic relative motion of the eddies, then the intensity of turbulence would be limited to  $1/M$ . Thus we are unlikely to be able to operate a supersonic combustion system at high turbulence levels, and turbulence intensity will generally fall in the range 15-40%. At hypersonic flow conditions we can then write the energy balance

$$\frac{3}{2} \rho u'^2 = \frac{1}{2} \rho_3 U_3^2 - \frac{1}{2} \rho_M U_M^2$$

$$\therefore U_M/U_3 = \left( 1 - 3(u'/U)^2 \right)^{\frac{1}{2}} = 1 - (3/2)(u'/U)^2$$

Thus when  $u'/U = 0.2$ ,  $U_M/U_3 = 0.94$  giving a 6% loss in velocity !

To show what this means in terms of loss of specific impulse, we can write approximately.

$$\Delta I_f = \frac{W \Delta U}{g W_f} \approx \frac{U_1}{g} \left( \frac{3}{2} \left( \frac{u'}{U} \right)^2 \right)$$

This function is plotted in Fig. 8 and the large loss in specific impulse-amounting to a few hundred seconds - is apparent. In order to carry out exact calculations, a kinetic energy efficiency  $\eta_T$  for the turbulent mixing process may be defined, thus

$$\eta_T = (H - h_{ms}) / (H - h)$$

where  $H$  is the total enthalpy

$h$  is the static enthalpy

$h_{ms}$  is the static enthalpy in the mixed region when

expanded isentropically to the initial pressure.

In the case of constant pressure mixing, this would reduce to

$$\eta_T = (U_M/U)^2 = 1 - 3(u'/U)^2$$

The kinetic efficiency parameter  $\eta_T$  can then be incorporated into engine cycle calculations in the usual manner.

This theory can be readily extended to lower speed systems such as gas turbine burners or industrial high intensity combustors. In these, the turbulence velocity is approximately equal to the mean velocity, hence the length of the initial combustion zone is approximately equal to the diameter. It also follows that the scale of the turbulence should be an order of magnitude smaller than the diameter of the burner. We can, therefore, calculate the geometry of a high intensity burner as follows:

Inserting  $u'/U = 1$  into the energy balance equation gives:-

$$\Delta P / \frac{1}{2} \rho U^2 = \zeta = 3$$

Thus a pressure loss of three dynamic heads across the flame stabilizer will give a minimum well stirred combustor. The pressure loss can be expressed in terms of Mach number ( $M$ ) as:-

$$\Delta P / \rho = 3\gamma M^2 / 2 = 2.1 M^2$$

In the case of a gas turbine burner operating at Mach 0.1 this indicates that an optimum combustor will have ~ 2.1% total pressure loss, if the energy to stir the combustor is taken from the air stream. Similarly for an industrial high intensity burner operating at 30 metres/sec, we find that the fan must provide 2100 N/m<sup>2</sup> (8.5"H<sub>2</sub>O) for the stabilizer pressure drop, plus a similar pressure for the mixing region (if mixing and combustion are separate) plus whatever exit velocity head is required from the flame. In addition, friction losses and the fundamental pressure loss due to heat addition must be overcome by the fan, but these can be made small.

The blockage of a baffle type stabilizer (combustion can) giving three dynamic heads of pressure loss can be shown to be about 60% of the combustor area (12), and this baffle should be streamlined on its upstream surface. The requirement that the scale of turbulence should be an order of magnitude smaller than the dimensions of the combustion chamber can be achieved by distributing the open area of the baffle between orifices, whose individual dimensions are an order of magnitude smaller than the chamber dimensions. Of course, the boundary velocity gradient to prevent flashback may provide a limitation on the range of satisfactory operation if mixing and combustion are separate.

When gaseous fuel is available at high pressure, it is possible to use the fuel pressure as the source of energy to stir the combustor (Plate 6). In this case only a small quantity of fuel is available to stir a large quantity of mixture, and the energy balance equation must be modified to calculate the fuel pressure, thus:

$$\Delta P = 3\gamma \rho M^2 / 2\alpha$$

where  $\alpha$  is the fuel/air ratio.

For the primary region of a gas turbine can operating at altitude, the required fuel pressure is, therefore, about 0.7 bar (10 psi). In order to stir the primary and dilution zones, fuel pressures about five times larger are required (i.e. proportional to W secondary/W primary). However, in larger gas turbines a cool layer of secondary air along the nozzle guide vanes is desirable, hence full secondary stirring is not always necessary. The potentialities of such a gas turbine burner are:

- a) An increase in aircraft range or payload of about 1%.
  - b) A burner with a self proportioning primary zone. This follows since the primary air flow is determined by the fuel momentum, and the difference in air flow will automatically pass to the secondary region.
  - c) Reduced pollution. The vaporized fuel will follow the same path at all operating pressures, thus eliminating the rich core, which can cause smoke at low altitude.
- N.B. (The disadvantage is, of course, the requirement for a flash boiler or heat exchanger to vaporize the fuel. It will be noted that pumping liquid fuel to a high pressure requires comparatively little power, whereas compressing the air to provide combustor stirring energy requires a large amount of power.)

These same principles may be readily applied to the mixing process in an automobile carburettor. This process normally requires a pressure drop of about  $2500 \text{ N/m}^2$  ( $10'' \text{ H}_2\text{O}$ ), and reduces the maximum engine power by about 5%. A vaporized high pressure fuel system used as indicated above should recover this power, and also reduce pollution due to the elimination of large droplets.

### Conclusion.

1. A tailored interface hypersonic shock tunnel is a suitable facility for connected testing of scramjet combustion systems. It can easily produce stagnation temperatures  $> 5000^\circ\text{K}$  and pressures  $> 200 \text{ bar}$  for a few milliseconds.
2. Supersonic combustor static pressures are about equal to atmospheric, however the test section must be evacuated to about  $1/30$  of atmospheric pressure, if the test section is not to be damaged by the starting transients. A simple blast tube can also be used in place of the conventional dump tank.
3. Contamination of the test gas by the driver gas has been shown to be a problem, and a high speed gas sampling instrument is essential for the interpretation of combustion results from shock tunnels.

4. An electromagnetic velocity meter has been developed for use with high temperature test facilities. It appears that the gas conductivity is in accordance with the theoretical value.
5. A low cost multi-channel magnetic drum recording system has been developed, which is ideally suited for use with shock tunnels and other intermittent testing facilities.
6. Theoretical studies of the turbulent fuel/air mixing process have provided a fundamental technique by which pressure losses due to mixing may be calculated. These losses are surprisingly large for scramjet systems.
7. This theoretical analysis can also be used to design short dual mode supersonic combustors, novel gas turbine combustors, carburation systems, etc.

#### Acknowledgment.

This paper presents some of the work which has been supported jointly by the U.S.A.F. O.S.R., Ministry of Technology and the Science Research Council. This support is gratefully acknowledged. The work of the many colleagues, who have also contributed to these studies is also acknowledged, in particular Mr. R.J. Parsons, Mr. J.K. Richmond and Dr. D.S. Taylor have carried out experiments which are discussed herein.

## References.

1. Mordell, D.L. and Swithenbank, J. "Hypersonic Ramjets". Second International Congress of the Aeronautical Sciences. p.p. 831-848. Pergamon Press, N.Y. 1960.
2. Swithenbank, J. "Hypersonic Air-Breathing Propulsion". Progress in Aeronautical Sciences Vol,8. (E.D.Kuchemann). p.p. 229-294. Pergamon Press, 1966.
3. Curran, E.T. and Swithenbank, J. "Really High Speed Propulsion by Scramjets." Aircraft Engineering, January, 1966. p.p. 36-41.
4. Wood, M.P. "The Shock Tunnel as a Supersonic Combustion Test Facility." Fuel Society Journal, 1966, p.p. 50-60.
5. Wood, M.P. Ph.D. Thesis, University of Sheffield, 1968.
6. Davies, L. "The Interaction of the Reflected Shock with the Boundary Layer in a Shock Tube and its influence on the Duration of Hot Flow in the Reflected Shock Tunnel, Parts I & II" A.R.C. Current Papers Nos. 880-881. H.M.S.O. London, 1967.
7. Richmond, J.K. and Parsons, J. "Application of Rapid Sampling Techniques to Supersonic Flows of Gas Mixture in a Shock Tunnel". Report No. HIC 118. Dept. of Fuel Technology and Chemical Engineering, Sheffield University, 1968.
8. Richmond, J.K., Parsons, R.J., and Swithenbank, J. "On Shock-Tunnel simulation of Scramjet Combustion Chamber Performance". Presented at the AIAA, 7th. Aerospace Sciences Meeting, January, 1969, New York.
9. Swithenbank, J, and Parsons, R.J. "Experimental Techniques for Supersonic Combustion Research in a Shock Tunnel". 30th. AGARD Propulsion and Energetics Panel Meeting, Munich, September 1967.
10. Parsons, R.J. Ph.D. Thesis, University of Sheffield, 1969.

11. Taylor, D.S. and Swithenbank, J. "Proposed design for a High-Frequency Magnetic Drum Recording System", Dept. of Fuel Technology and Chemical Engineering, Report No. HIC 112, July, 1968.
12. Swithenbank, J. and Chigier, N.C. "Vortex mixing for Supersonic Combustion", 12th. International Symposium on Combustion". Poitiers France Sept. 1968.

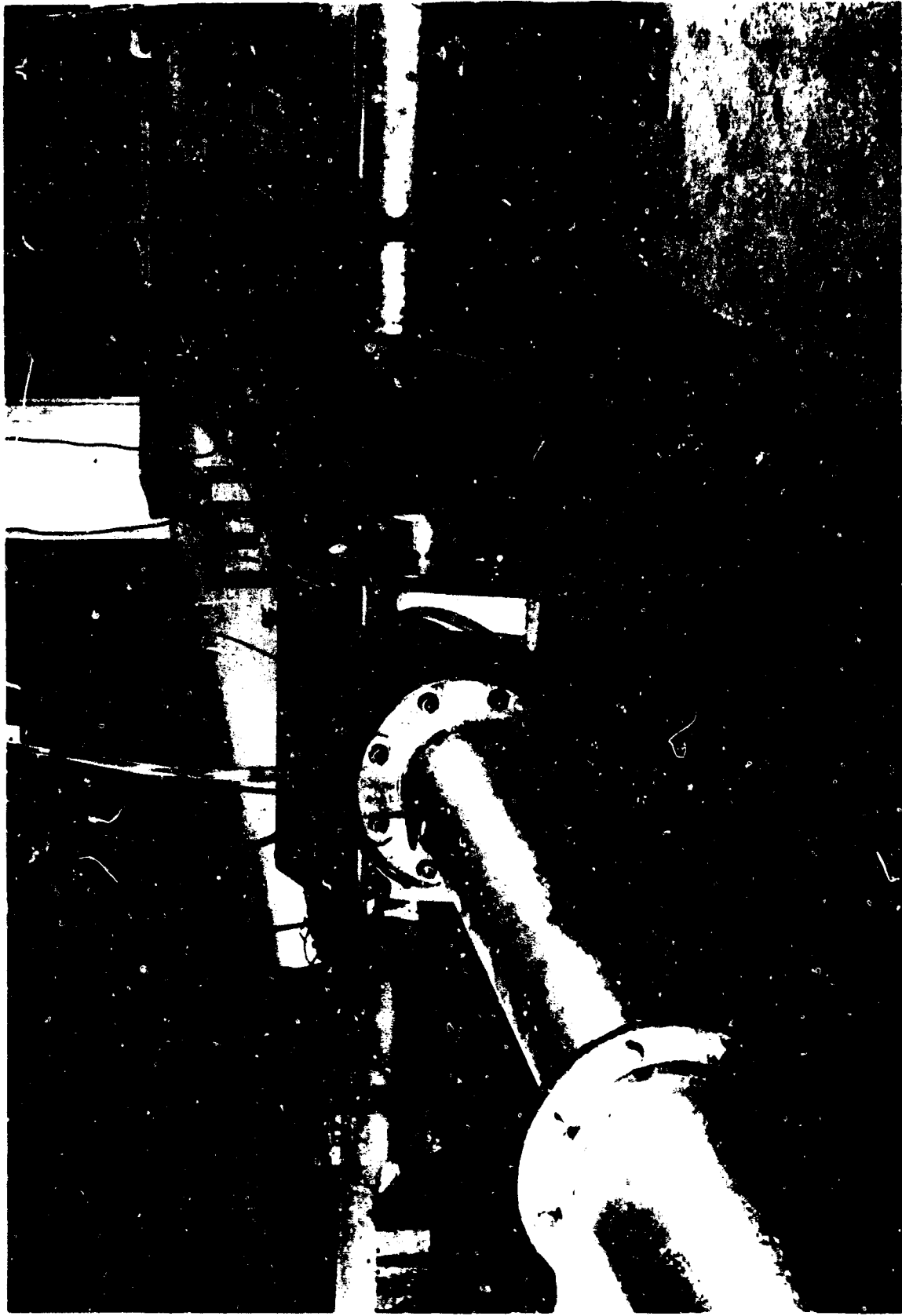


Plate 1



Plate 2

B-15



Plate 3

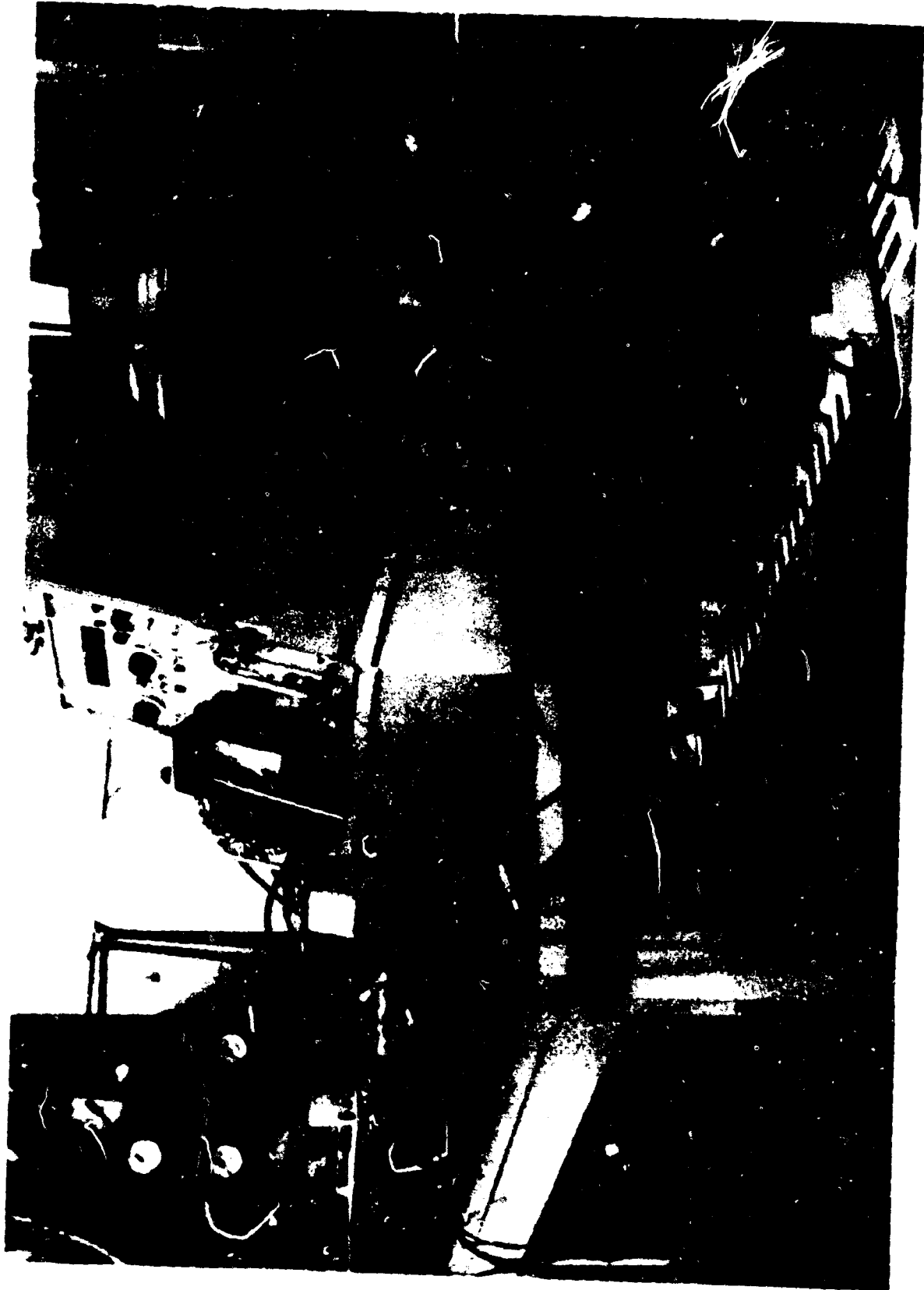


Plate 4

B-17



Plate 5

B-18



Plate 6

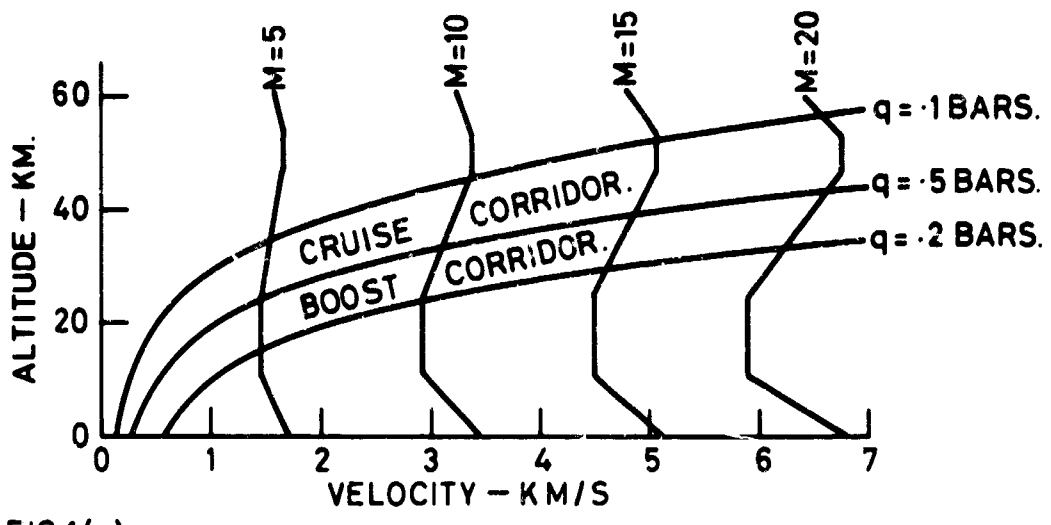


FIG.1(a)

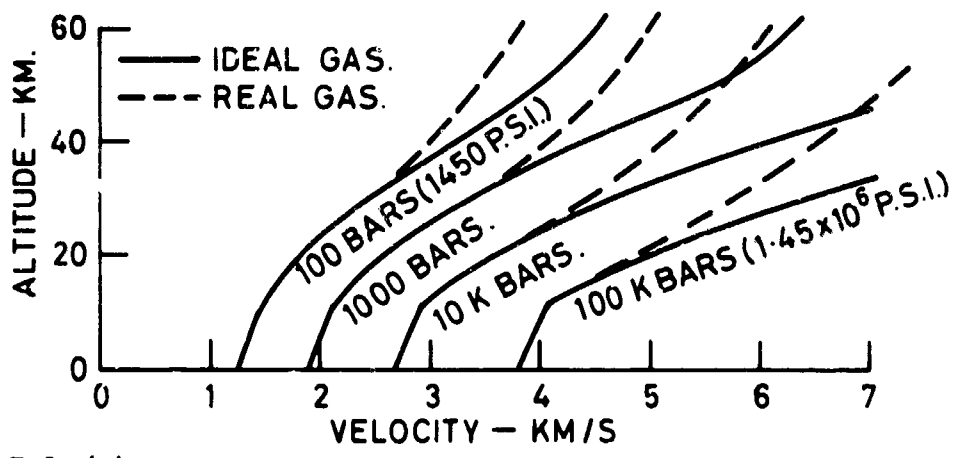


FIG.1(b)

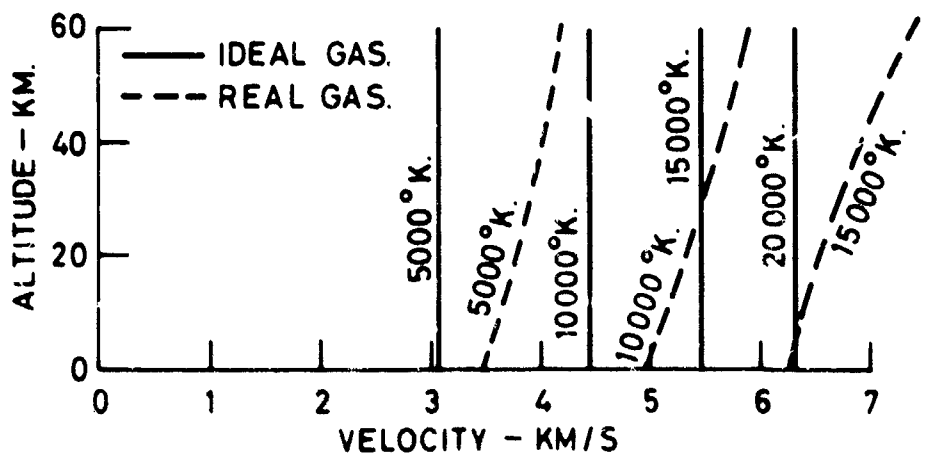


FIG.1(c)

FLIGHT STAGNATION CONDITIONS.

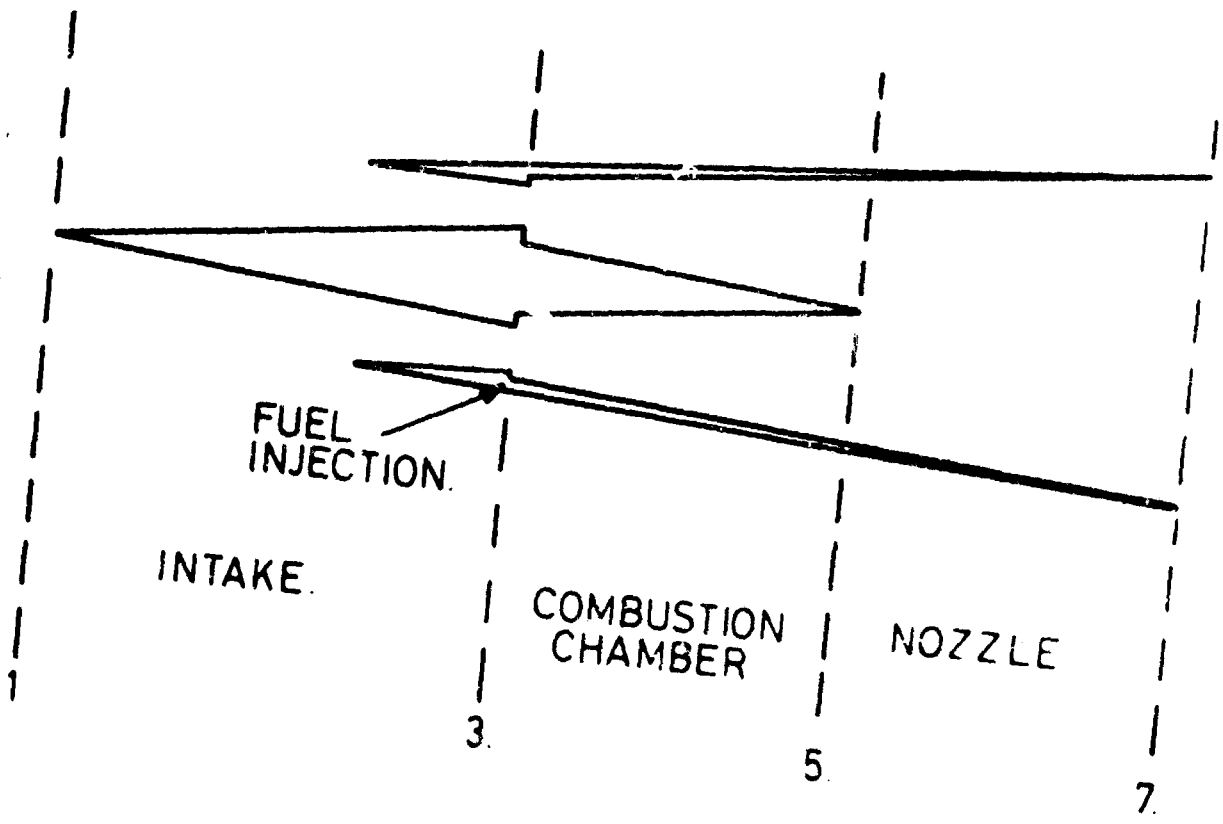
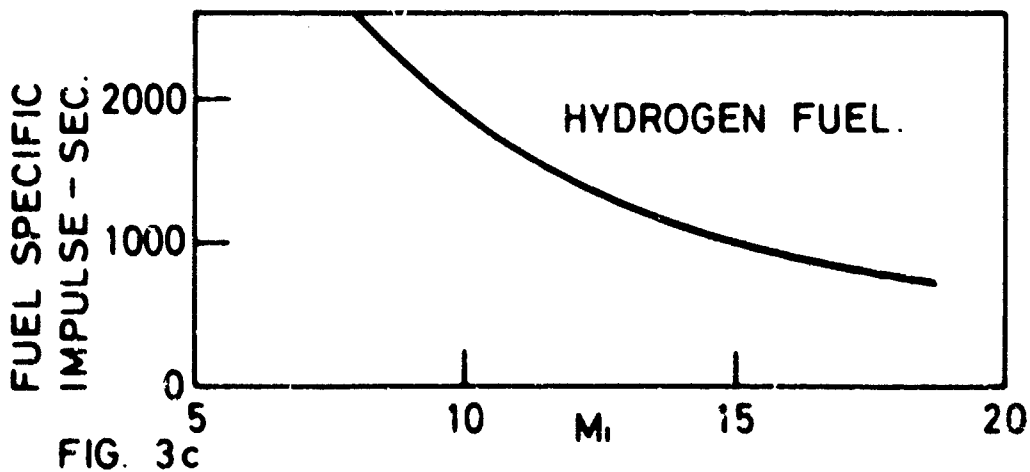
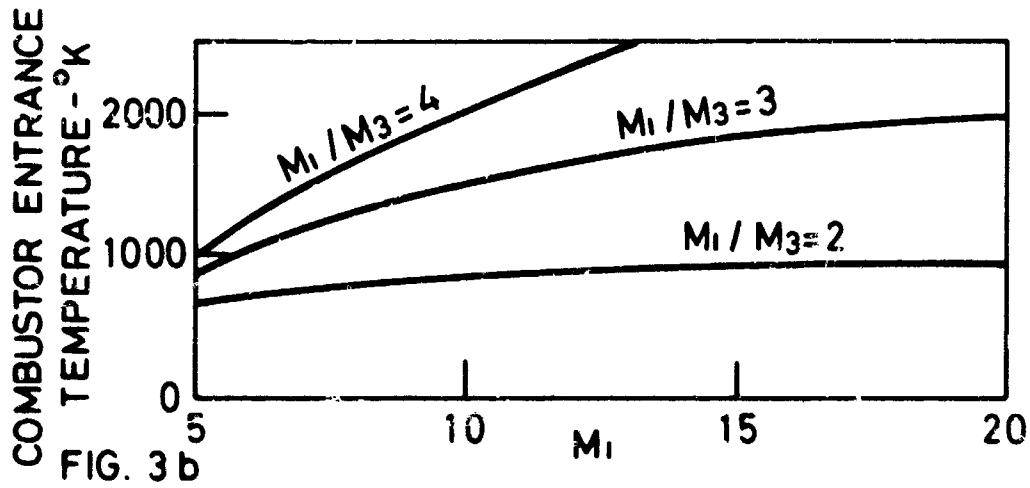
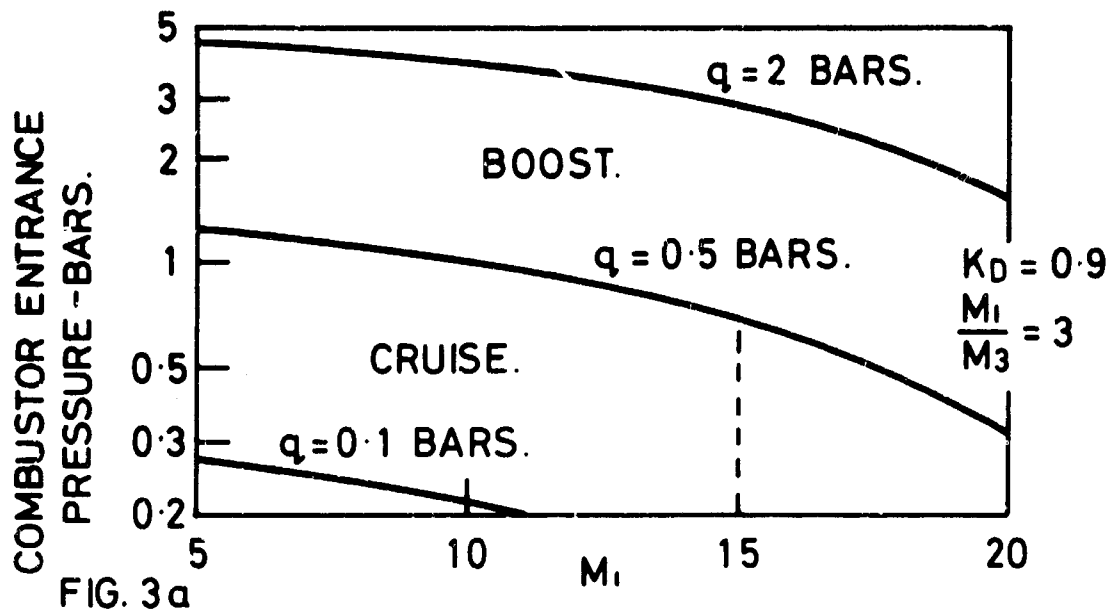


FIG.2 ENGINE STATIONS.



SCRAMJET OPERATING CONDITIONS.

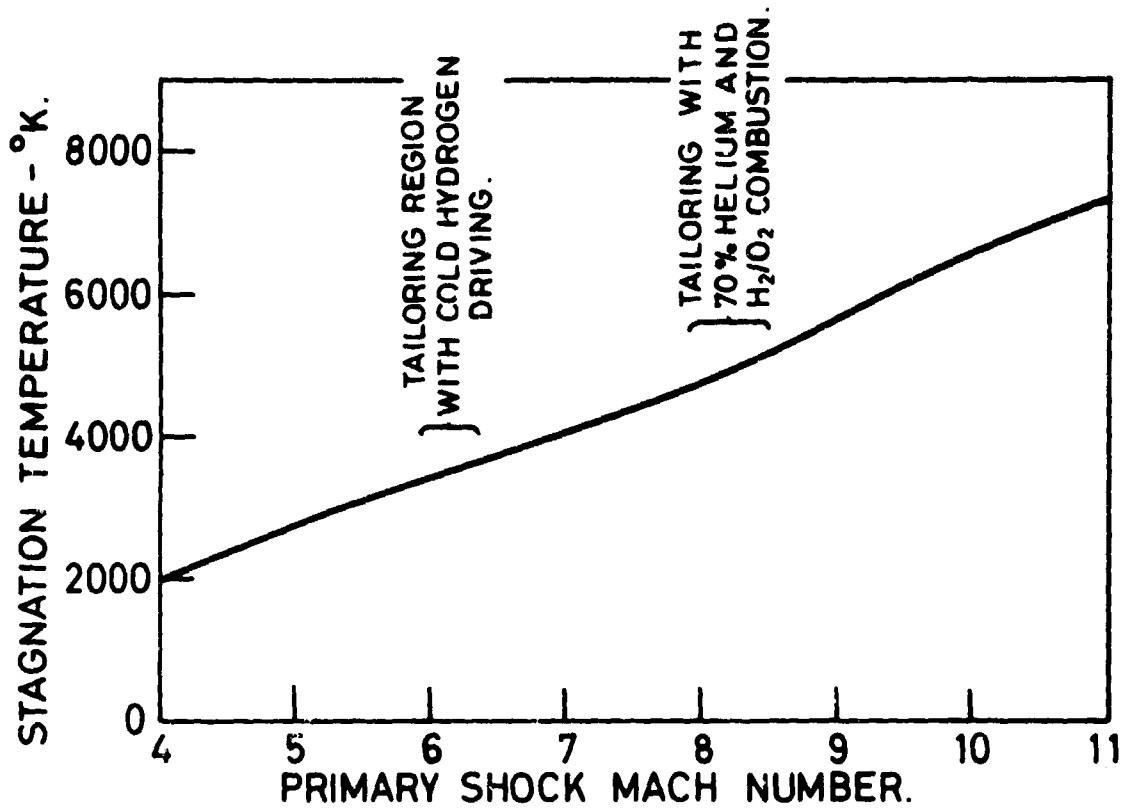


FIG. 4a

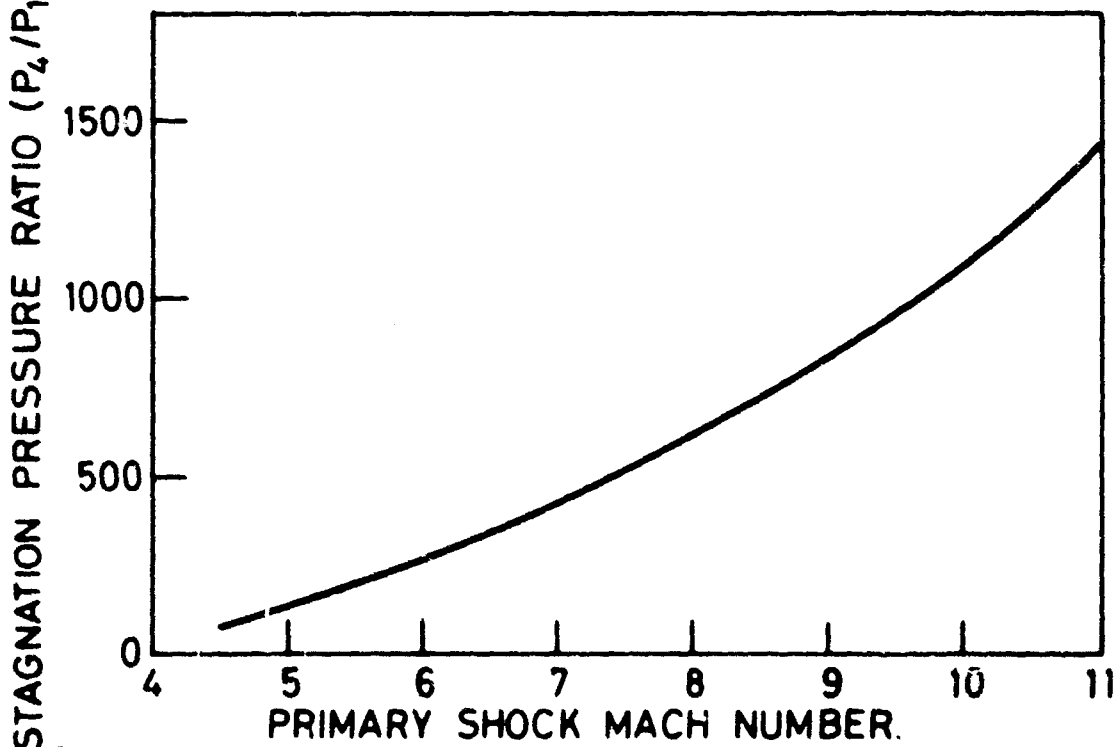


FIG. 4b

SHOCK TUNNEL PERFORMANCE.

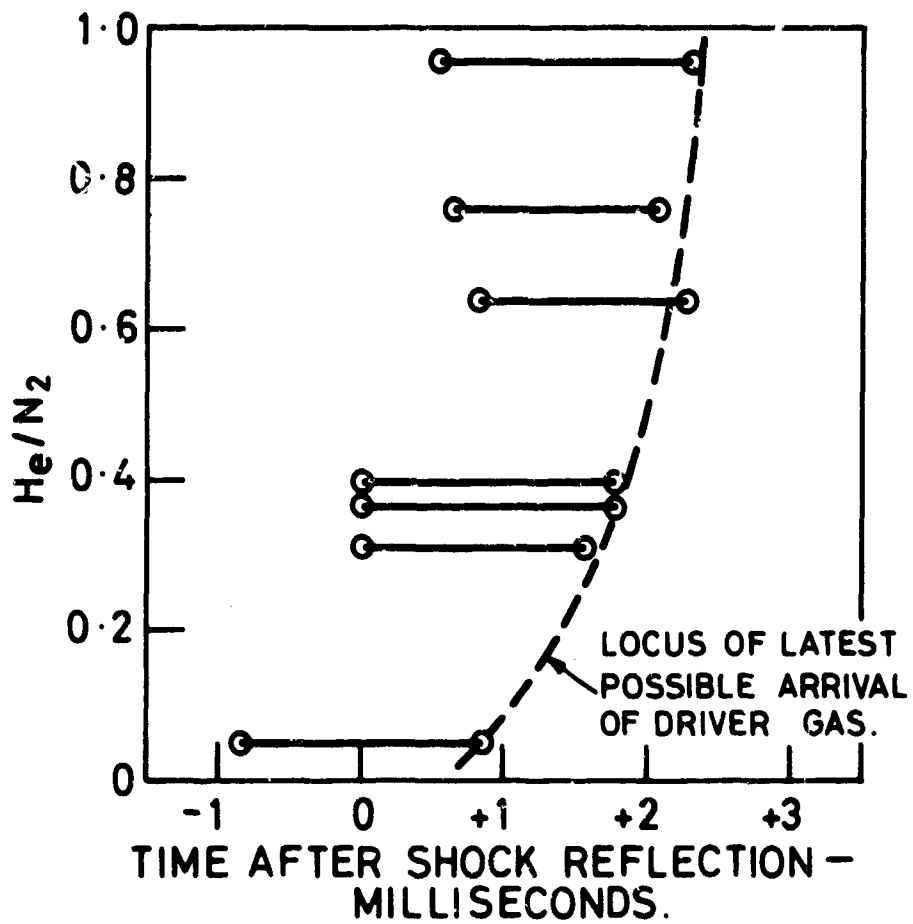


FIG. 5. GAS SAMPLING RESULTS.

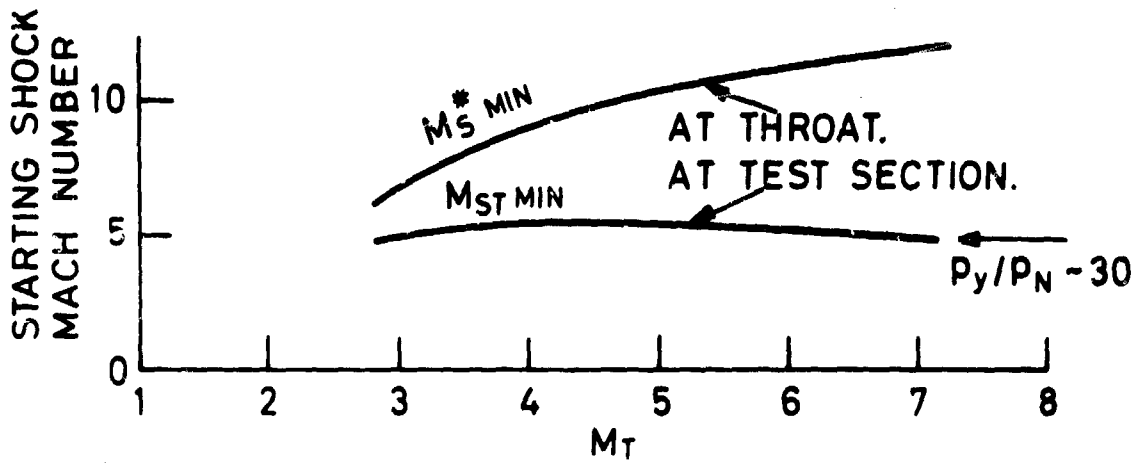


FIG. 6 (a)

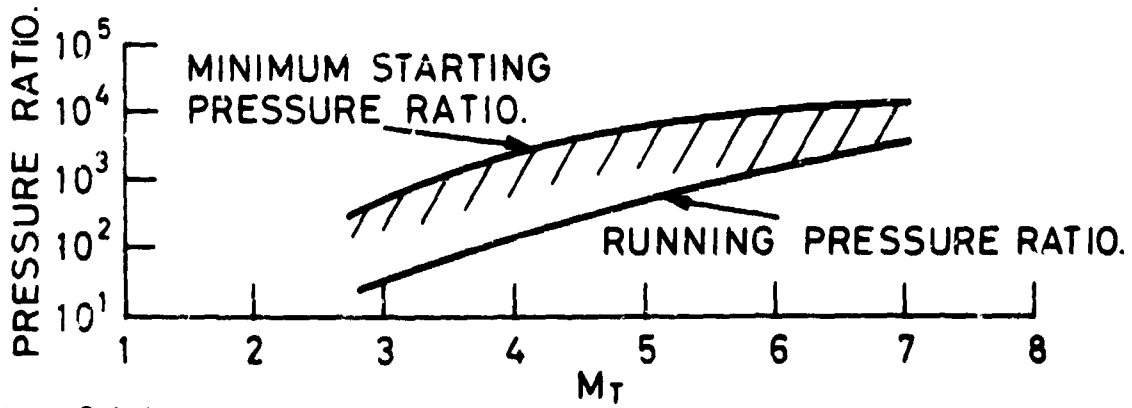
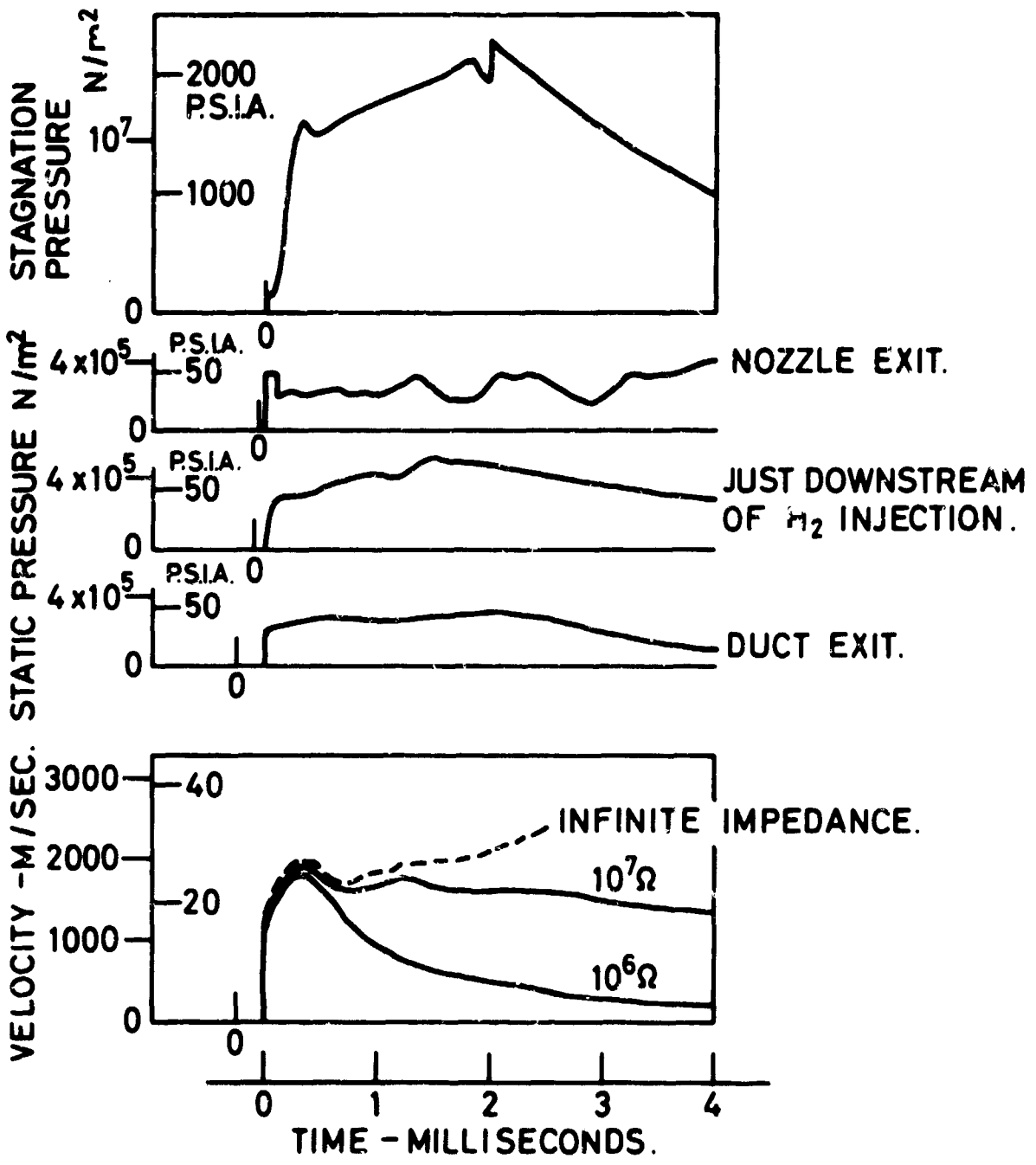


FIG. 6 (b)

TUNNEL STARTING.



**FIG. 7. RESULTS FROM ELECTRO-MAGNETIC INDUCTION VELOCITY METER.**

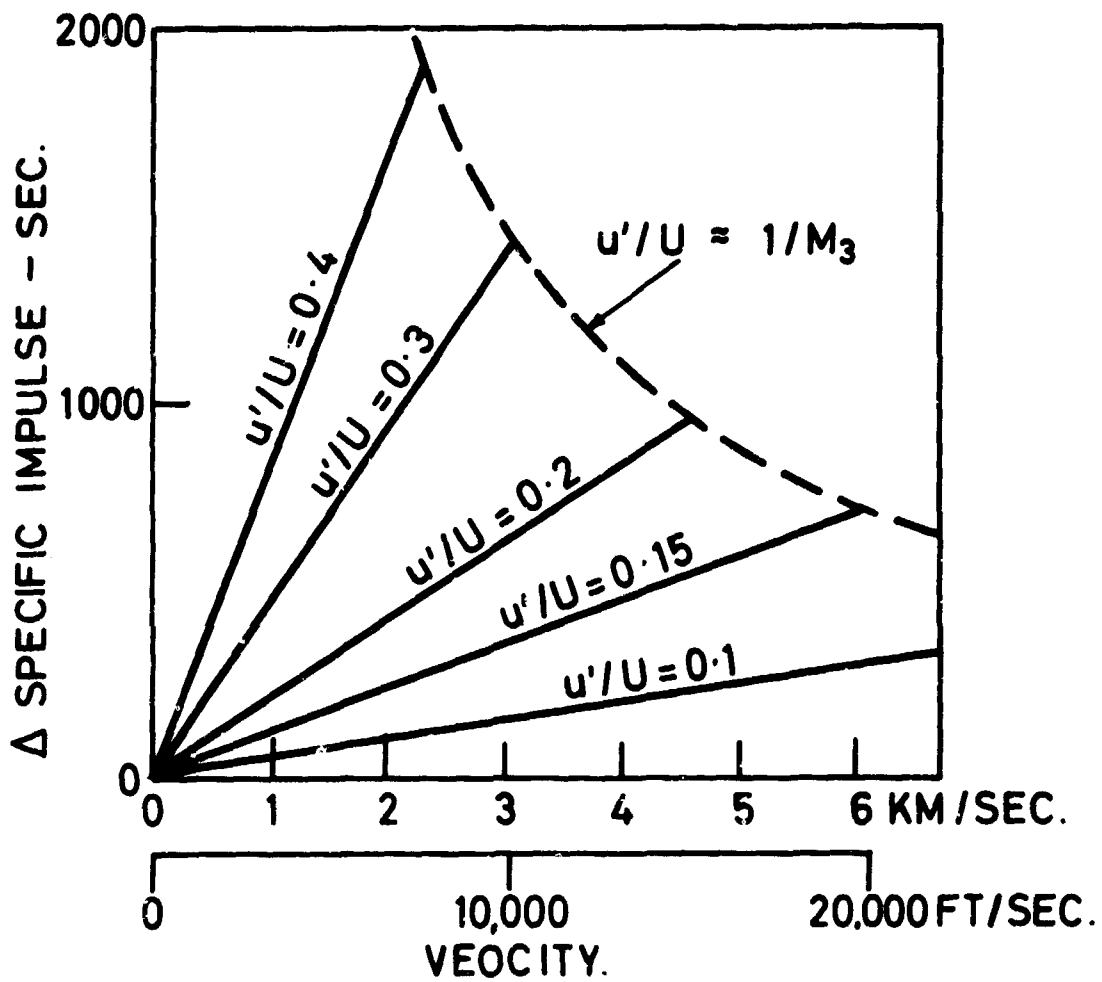


FIG. 8. SPECIFIC IMPULSE LOSS DUE TO TURBULENT MIXING.

NEGATIVE ION REACTIONS OF  
SIGNIFICANCE TO THE ATMOSPHERE

Dr. Thomas C. Tiernan and Dr. B. Mason Hughes

Chemistry Research Laboratory  
Aerospace Research Laboratories

## Negative Ion Reactions of Significance to the Atmosphere

Dr. Thomas O. Tiernan and Dr. B. Mason Hughes  
Chemistry Research Laboratory  
Aerospace Research Laboratories

### ABSTRACT

Measurements of the ionic composition of the ionosphere by rocket probes have established the presence of several prominent negative ionic species. Very little information has been available concerning either the source of these ions or their possible interactions with other atmospheric constituents. Recent experiments in our laboratory, using mass spectrometric techniques, have examined the reactions of negative ions such as  $O^-$ ,  $O_2^-$ ,  $NO^-$ , and  $OH^-$ , with a large number of selected neutral molecules, with particular attention to natural atmospheric gases. In several cases, rate determinations for these reactions have been made, and insight into the detailed reaction mechanisms has been derived by using isotopically substituted reactants. These studies provide information which is vital to the establishment of reliable atmospheric models and the understanding of deionization phenomena. These laboratory measurements have important implications for such topics as atmospheric perturbations by nuclear detonations.

### Introduction

The ionosphere, that region of the earth's atmosphere which is electrically charged, extends from the earth's surface to the boundary between the earth's magnetic field and outer space. This region includes ions of many types, created largely by impact of high energy photons, ( $\gamma < 1027\text{\AA}^2$ ), from the sun and also by secondary photoelectrons ejected by the initial impact process but which are sufficiently energetic to cause further ionization before reaching thermal equilibrium. Thermalized electrons also constitute a large part of the ionospheric medium and these survive essentially as free electrons until they undergo recombination reactions with positive ions. Such recombinations usually result in dissociation if the positive ion is diatomic, thereby creating atomic species which are also highly reactive.

The earliest information about the ionosphere was obtained from observations of the reflectivity which free electrons in this region show for radio waves. From such measurements it has proved possible to derive in considerable detail the electron density as a function of altitude. More recently, sounding rockets and satellites have yielded data on the actual ionic and neutral composition of the ionosphere. The multitude of ions shown to be present by such measurements could conceivably involve a

large number of interactions. Therefore, to aid in resolving the chemistry and physics of the ionosphere and in drawing conclusions about the dominant reaction processes occurring there, it has been necessary to resort to laboratory studies in which various experimental techniques are employed to study reactions of isolated ions and other reactive intermediates. While considerable progress has been made in the identification of positive ionic reactions of relevance to the ionosphere by such laboratory methods,<sup>1</sup> much less data has been obtained at this point regarding the interactions of negative ionic species.

Negative ion reactions are particularly important for that region of the ionosphere below 90 kilometers, the so-called "D region". In this region, the concentration of neutral molecules (that is, the atmospheric density) is sufficiently large that  $O_2^-$  ions formed by electron attachment to oxygen molecules, which would normally dissociate, are stabilized by further collisions with molecules which remove some of the excess energy. Such three-body attachment processes have been well-known for some time as a consequence of their demonstration in the laboratory.<sup>2</sup> Although these  $O_2^-$  species are presumably neutralized either by photodetachment of electrons or associative detachment reactions in the daytime, their lifetime at night in the ionosphere is considerably longer and they are potentially reactive. Similarly, dissociative electron attachment to ozone molecules present in the ionosphere creates  $O^-$  ions which must also be considered in any postulated reaction scheme.

One of the earlier studies of negative ion reactions<sup>3</sup> in atmospheric gases utilized an afterglow discharge mass spectrometer to examine pure atmospheric components and appropriate gaseous mixtures. Significantly,  $CO_3^-$  and  $NO_3H_2^-$  were observed as important negative ion products. The role of ions such as  $O_2^-$  and  $NO_2^-$  was also considered. Quite recently, Fehsenfeld et al.<sup>4</sup> have applied a flowing afterglow technique to determine rate constants for various ionic reactions of  $O^-$ ,  $O_2^-$ ,  $O_3^-$  and  $CO_3^-$ . On the basis of their data, these workers proposed two reaction chains which would result in the production of  $NO_2^-$  and  $NO_3^-$  as the dominant negative ion species in the D-region. And, indeed, recent sampling probes of the ionosphere<sup>5</sup> have identified, among others, ions corresponding in mass to  $NO_2^-$  and  $NO_3^-$ .

The ion chemistry of the "ionosphere" is still very poorly understood, however. The concentration of neutral constituents such as  $O_3$ ,  $NO$ ,  $H_2O$ ,  $N_2O$ , etc. in this region is yet a major uncertainty. Also, the reactions of ions such as  $O^-$  and  $O_2^-$  with several of these atmospheric components have still not been adequately probed. In view of these facts, we have attempted to apply mass spectrometric techniques, such as we have recently employed so successfully in our studies of a variety of positive ion-molecule processes,<sup>6-8</sup> to the examination of selected negative ion reactions. It is notable that there have been virtually no negative ion mass spectrometric studies reported in which a beam instrument such as ours was utilized. Our success in accomplishing such studies depends in large part on novel experimental techniques devised in our laboratory which will be described in the following section.

### Experimental

The instrument utilized for the negative ion-molecule reaction studies reported here is the dual-stage ARL tandem mass spectrometer, which has been described in some detail in previous publications.<sup>9,10</sup> A schematic diagram of this research mass spectrometer is shown in Figure 1 and Figure 2 is a pictorial representation of the instrument. It consists essentially of two mass spectrometers of Mattauch-Herzog geometry coupled by an intermediate collision chamber. Thus a mass and energy analyzed ion beam can be selected in the first stage spectrometer and impacted on the target gas of choice in the collision chamber. The resulting ionic products from the reaction are then analyzed and detected in the second stage mass spectrometer. The unique feature of this ARL instrument is its capability to provide ion beams of experimentally useful intensity over the range 0.3-100 eV with an energy spread of only 0.3 eV. Since negative ion-molecule interactions in the atmospheric environment are expected to occur at near-thermal energies, the low energy capability of the ARL tandem mass spectrometer is particularly desirable if reasonable analogies are to be drawn between laboratory experiments and actual ionospheric processes. The low energy limit of the ARL tandem instrument is made possible because of the unique retarding "slot" lens which degrades the ion beam energy from its value of about 180 eV, with which the beam exits from the  $\beta$ -slit, to the desired impacting energy. Because of the relatively low intensities of ionic products from ion-neutral interactions in the instrument, it is necessary to utilize an electron multiplier detector and to employ pulse counting techniques.

While the tandem mass spectrometer described above has been successfully applied to positive ion molecule reactions for some time, it is only recently that modifications were accomplished to permit observations of negative ion processes. An important consequence of these modifications was the development in our laboratory of a new ion source and a mode of source operation with which it is possible to realize negative ion beams in the tandem spectrometer of intensities of  $10^{-8}$  amp or higher, measured at the  $\beta$ - or energy defining slit (Figure 1). The source is displayed schematically in Figure 3 and is in most respects a conventional electron impact source. It is distinctive, however, in that the anode or electron trap is not isolated from the impact chamber as is customary but is actually within this region. Under the conditions to be noted below, this source operates by ejecting relatively large quantities of secondary electrons from the anode which have low energies in the region appropriate for electron capture by molecules ( $\sim 0-10$  eV). The necessary operating conditions are as follows: 1) A rather high impacting electron energy is required, typically 100-200 eV. The optimum primary electron energy can be selected by consulting available data<sup>11</sup> on the energy distribution of reflected secondary electrons from metal surfaces, taking into account the metal used for the anode and the energy dependence of electron capture for formation of the negative ion species in question. Much of the latter information is also available in the literature.<sup>12</sup> 2) The anode must be at ground potential. Using a potential attractive for electrons traps secondary electrons before they can escape the anode surface. 3) High anode currents result in maximum negative ion yields, as would be expected.

The mode of operation described improves the efficiency of negative ion formation by about a factor of 1000 over that possible when negative ions are formed directly by impacting the source molecules with low energy electron beams for which beam collimation and penetration into the ionization chamber are significant problems. Moreover, the newly designed source can be operated at considerably higher pressures than would be possible otherwise, and this in turn increases the probability of three-body capture processes which are frequently necessary for the formation of negative species.

The high efficiency negative ion source outlined here will be described in detail in a forthcoming publication.<sup>13</sup>

### Results and Discussion

Preliminary data have been obtained on the reactions of  $O^-$ ,  $O_2^-$ ,  $NO^-$  and  $OH^-$  with a large number of neutral molecules. The discussion here will be limited to reactions with simple inorganic gases which are known atmospheric constituents.

Rate Constant Determinations. The ARL tandem mass spectrometer is restricted in operation to collision chamber pressures below about 50 microns, owing to pumping system restrictions. While this is quite sufficient to observe products from a single ion-neutral collision, it is not, except in rare instances, adequate for the detection of higher order processes. Some of the ion-molecule processes observed in the tandem spectrometer for the reactions of  $O^-$ ,  $O_2^-$  and  $NO^-$  are shown in Table I,

Table I

<u>Reaction</u>	<u>Rate Constant, k (<math>\times 10^9</math> cm<sup>3</sup> molecule<sup>-1</sup> sec<sup>-1</sup>)</u>
(2) $O^- + H_2 \rightarrow OH^- + H$	0.28
(3) $O^- + H_2O \rightarrow OH^- + OH$	0.10
(4) $O^- + N_2O \rightarrow NO^- + NO$	0.14
(5) $O_2^- + NO_2 \rightarrow NO_2^- + O_2$	0.76
(6) $NO^- + O_2 \rightarrow O_2^- + NO$	0.35
(7) $NO^- + NO_2 \rightarrow NO_2^- + NO$	0.23

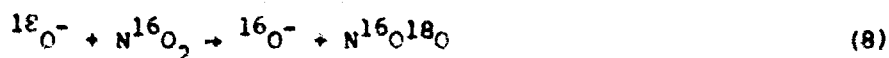
along with the rate constants derived for these reactions. Rate constants were obtained by normalizing cross-sections measured in the tandem instrument to the rate constant for the charge transfer reaction,



for which  $k = 1 \times 10^{-9} \text{ cm}^3 \text{ molecule}^{-1} \text{ sec}^{-1}$  was reported by Paulson.<sup>14</sup> No reactions of  $\text{OH}^-$  with simple inorganic molecules could be observed in the tandem instrument at the relatively low collision chamber pressures used. Also, no apparent reactions of  $\text{O}^-$  with  $\text{CO}_2$ ,  $\text{CO}$ ,  $\text{O}_2$ ,  $\text{NO}$ , or  $\text{NO}_2$  were detected under these conditions. The failure in our case to observe complex ions such as  $\text{CO}_3^-$ ,  $\text{O}_3^-$ , and  $\text{NO}_3^-$  from such reactions is not surprising in light of the above discussion since previous observations of these species involved experiments conducted at much higher pressures.<sup>3,15</sup> Under these conditions, such complexes are formed in three-body processes, as is now well established.

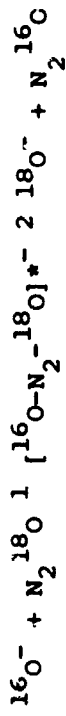
Reaction Mechanisms. It is of fundamental interest to consider the mechanisms of some of the negative ion-molecule reactions which have been observed. Considerable insight into these reaction mechanisms can be obtained from experiments in which isotopically substituted reactants are used. As an example, the application of such techniques for reaction (4) will be illustrated. The  $\text{NO}^-$  product from this reaction could conceivably be produced by several mechanisms. Thus it might be formed by dissociative charge transfer, by a discrete particle transfer or through an intermediate ion-neutral complex at the low relative energies involved. Table II shows the isotopic product distribution from the reactions of  $^{16}\text{O}^-$  with  $\text{N}_2^{18}\text{O}$  and of  $^{18}\text{O}^-$  with  $\text{N}_2^{16}\text{O}$ . As can be seen, the  $\text{NO}^-$  product from both reactions consists of approximately equal components of  $\text{N}^{16}\text{O}^-$  and  $\text{N}^{18}\text{O}^-$ . Also interesting is the fact that  $\text{O}^-$  is actually formed as a product in this reaction. The tandem mass spectrometer is an "in-line" type instrument in which ionic products are detected in the same direction as the impacting ion beam. It is evident therefore that this back-reaction product would not be detected except in an isotopic experiment, because a product ion of the same mass as the reactant is obscured by the latter which is of much larger magnitude. However since the oxygen atom which appears in the  $\text{NO}^-$  product apparently comes from either the ion or the neutral with about equal probability, it is reasonable to assume that both  $^{16}\text{O}^-$  and  $^{18}\text{O}^-$  are actually formed as products from either of the reactions shown in Table II. On this basis, it seems apparent that the reaction involves formation of an intermediate  $(\text{N}_2\text{O}_2)^*$  complex in which the energy is distributed among the various degrees of freedom in random fashion.

Similar experiments show that the reaction of  $\text{O}^-$  with  $\text{NO}_2$  is quite different from that discussed above. Thus, when  $^{18}\text{O}^-$  is impacted on  $\text{N}^{16}\text{O}_2$ , the reactions observed are,



The relative rates for these reaction channels are in the order  $k_8/k_9/k_{10} = 0.17/0.76/0.07$ . Clearly, the major charge transfer product  $\text{N}^{16}\text{O}_2^-$  is not isotopically mixed and therefore must result principally from a long range interaction rather than from the orbiting complex usually assumed for low energy ion-neutral reactions. Again, there is a back-reaction yielding

Table II



<u>Relative Product Distribution for</u>		<u>Relative Product Distribution for</u>	
<u>Reaction 1</u>		<u>Reaction 2</u>	
<u>NO<sup>-</sup> Product</u>	<u>Total Products</u>	<u>Total Products</u>	<u>NO<sup>-</sup> Product</u>
52.2	15.6	18.0	51.1
47.8	14.2	17.3	48.9
---	a	64.7	
70.2		---	a

a. Product ion of same mass as reactant cannot be observed.

$O^-$ , although in this case it is relatively minor.

As in the case of  $N_2O$ ,  $O^-$  ions apparently react with water molecules chiefly through formation of an intermediate complex. In this instance, the observed product distribution from the isotopic studies is,



where  $k_{11}/k_{12}/k_{13} = 0.022/0.020/0.96$ .

Conclusions. It is appropriate to consider the negative ion reactions observed in the present study in relation to currently held reaction schemes for the ionosphere. Dalgarno<sup>16</sup> suggested some time ago that the associative detachment reactions,



might provide an important mechanism by which these ions are lost from the ionosphere. More recently, Fehsenfeld et al.<sup>4</sup> have measured rate constants for these processes as  $k_{14} = 1.9 \times 10^{-10} \text{ cm}^3 \text{ sec}^{-1}$  and  $k_{15} = 3.3 \times 10^{-15} \text{ cm}^3 \text{ sec}^{-1}$  respectively, using the flowing afterglow technique. The relatively large magnitude of these rate constants indicates that such associative detachment processes would dominate photodetachment in the ionosphere. However, the rate constants given in Table I for reactions of  $O^-$  and  $O_2^-$  are in some instances larger than those for associative detachment of these ions with O atoms. It would seem, therefore, that it will be necessary to consider reactions such as those shown in Table I in formulating a realistic reaction scheme for the ionosphere. This may well require some modifications to the sequence proposed by Fehsenfeld et al.<sup>4</sup> Ultimately such considerations will rest on reliable determinations of the concentrations of the various inorganic gases in the ionosphere.

The preliminary mass spectrometric investigations described here illustrate the value of this technique for negative ion-molecule studies. In contrast to less definitive drift tube or discharge studies, these methods provide detailed information on the specific reactions of individual ions without prior knowledge of these processes. Moreover, reliable kinetic data is readily obtained by a much less tedious experimental procedure than required in non-mass spectrometric methods.

#### Future Work and Applications

In future investigations, high pressure mass spectrometric techniques will be applied to study various atmospheric negative ion reactions. At higher pressures, it will be possible to observe short-lived negative ion

complexes and to follow their sequential reactions. It should be possible to ultimately arrive at a reliable estimate of the overall reaction schemes for various regions of the ionosphere by considering competitive reaction kinetics and the relative concentrations of neutral and ionic reactants.

Apart from their obvious significance for clarifying the physics and chemistry of the upper atmosphere, studies of negative ion processes have importance for a variety of topics. Among these are the explanation of deionization phenomena following the creation of bursts of electrons in the atmosphere by nuclear detonations, for example, and related problems such as radar and communications blackout.

#### Bibliography

1. E. E. Ferguson, F. C. Fehsenfeld and A. L. Schmeltekopf, in "Space Research", Vol. VII, p. 135, Ed. R. L. Smith-Rose, North-Holland Publishing Co., Amsterdam (1967).
2. L. M. Chanin, A. V. Phelps, and M. A. Biondi, Phys. Rev. 128, 219 (1959).
3. W. L. Fite and J. A. Rutherford, Discussions of the Faraday Society, 37, 192 (1964).
4. F. C. Fehsenfeld, A. L. Schmeltekopf, H. I. Schiff and E. E. Ferguson, Planet. Space Sci. 15, 373 (1967).
5. R. S. Narcisi, A. D. Bailey and L. Della Lucca, "Negative Ion Composition Measurements in the Lower Ionosphere", Symposium on Physics and Chemistry of the Upper Atmosphere, Defense Atomic Support Agency, Waltham, Mass., 12-13 June (1968).
6. T. O. Tiernan and J. H. Futrell, J. Phys. Chem. 72, 3080 (1968).
7. J. H. Futrell and T. O. Tiernan, J. Phys. Chem. 72, 158 (1968).
8. T. O. Tiernan and B. M. Hughes, Advances in Chemistry, "Radiation Chemistry--II", 92, 113 (1966).
9. J. H. Futrell and C. D. Miller, Rev. Sci. Instr. 37, 1521 (1966).
10. T. O. Tiernan, "A Significant Advance in the Study of Ion-Molecule Reactions", OAR Research Review, VII, No. 1, p. 16, January (1968).
11. O. Hachenberg and W. Brauer, "Secondary Electron Emission from Solids", in Advances in Electronics and Electron Physics, Ed. L. Marton, Vol. XI, p. 413, 1959.
12. D. Rapp and D. D. Briglia, "Total Cross Sections for Negative Ion Formation in Gases by Electron Impact", Lockheed Missiles & Space Co., Report IMSC-6-74-64-40.

13. T. O. Tiernan, C. D. Miller and B. M. Hughes, to be published.
14. J. F. Paulson, "Some Negative Ion Reactions in Simple Gases", in *Advances in Chemistry Series*, 58, "Ion-Molecule Reactions in the Gas Phase", Ed. P. Ausloos, p. 28, 1966.
15. J. L. Moruzzi and A. V. Phelps, *J. Chem. Phys.* 45, 4617 (1966).
16. A. Dalgarno, *Ann. Geophys.* 17, 16 (1961).

### List of Figures

Figure 1. Schematic of ARL tandem mass spectrometer.  $\beta$  is the energy-resolving slit and M1 is the magnet of the ion gun spectrometer. D1 is ion detector monitor for ion gun. QL is quadrupole lens, EC is movable electrometer for total ion-current measurement, M2 is mass analyzer of second stage, and D2 is final detector for product ion analyzer.

Figure 2. Front view of the ARL tandem mass spectrometer.

Figure 3. High efficiency negative ion source. Gas enters source chamber through inlet, GI, where it is ionized. Electrons emitted by filament, F, pass through source chamber and strike electron trap, T. Secondary electrons emitted from surface of T, are reflected into chamber where they are captured by molecules, yielding negative ions. Negative ions are driven out of source through exit aperture, IE, by a repulsive potential applied to repeller electrodes, R. Collimation of the electron beam is accomplished by the field impressed by magnet, M. S is shield for filament.

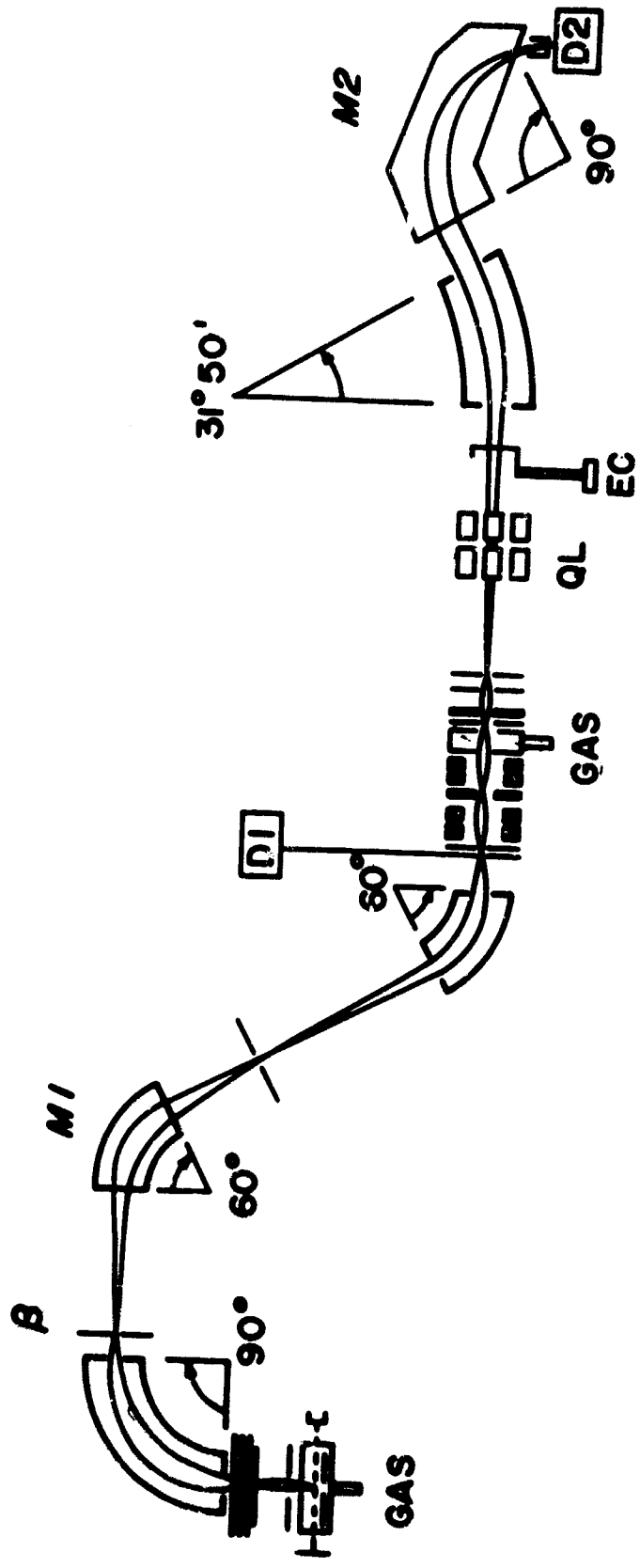


Figure 1

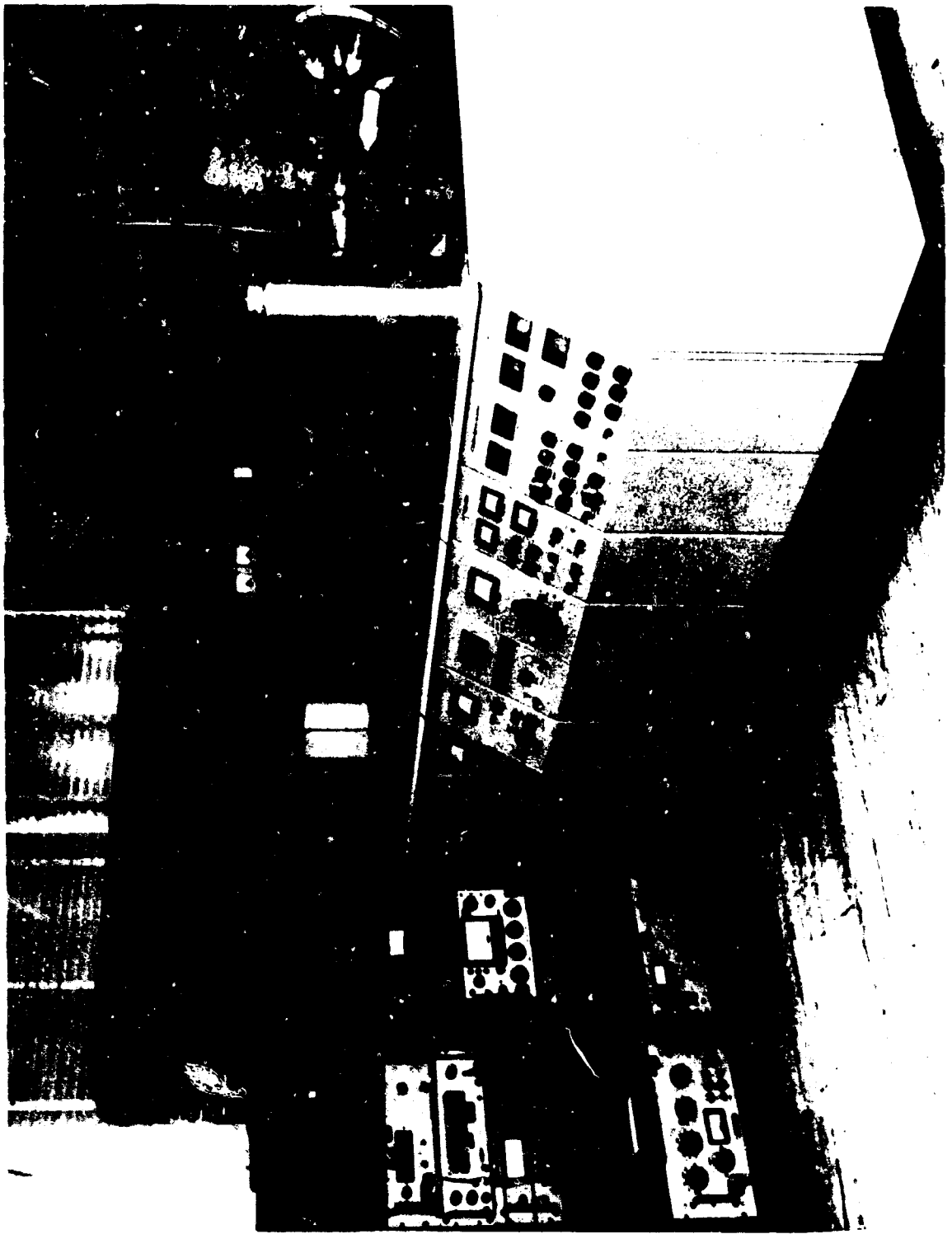


Figure 2

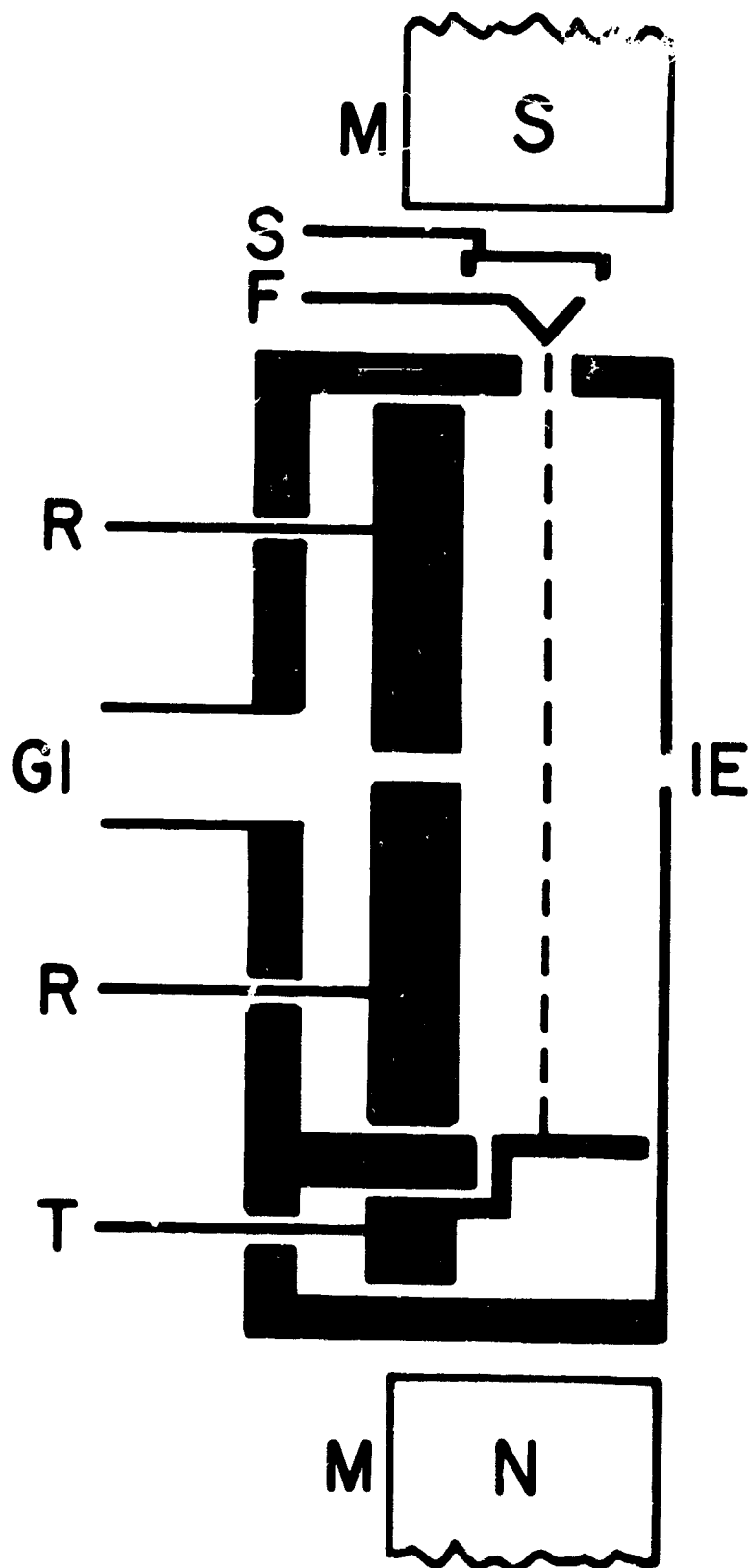


Figure 3

NEW ATOMIC SPECTROSCOPIC  
METHODS FOR TRACE ANALYSIS

J. D. Winefordner  
University of Florida, Department of Chemistry  
Gainesville, Florida

## NEW ATOMIC SPECTROSCOPIC METHODS FOR TRACE ANALYSIS

J. D. Winefordner

University of Florida, Department of Chemistry  
Gainesville, Florida 32601

Improved methods are being developed for measuring trace amounts of elements in small quantities of complex materials.

Amounts ranging from  $10^{-15}$  to  $10^{-6}$  grams may be measured in volumes of one milliliter or less of such materials as lubricating oils, biological fluids and tissues, foods, water and air. In particular, trace metals\* may be detected in lubricating oils used in jet and other engines and gear boxes. Methods are being developed to give more reliable, faster and less expensive methods of analysis of trace wear metals in oils than are now being used in the Air Force SOAP (Spectrometric Oil Analysis Program), directed toward detecting incipient, catastrophic mechanical failures.

Techniques under development involve (1) selection and preparation of a solution sample, (2) introduction of the sample solution into an atomizer to form an aerosol and (3) measurement of the emission, absorption or fluorescence of radiation by the atoms of the species of concern. Since the intensity of the emitted, absorbed, or fluoresced radiation is usually proportional to the concentration of the species of concern, measurement of the resulting intensity by a monochromator-photodetector system can therefore be directly used for quantitative analysis of the elemental species.

The studies are directed toward understanding the fundamental aspects of the methods and of the effect of the instrumental, spectral and sampling parameters of the instrumental signal and signal-to-noise ratio. The objectives are speed and simplicity, together with the following factors:

---

\* Aluminum, chromium, copper, iron, lead, magnesium, silicon, tin, titanium, manganese, vanadium, cadmium, zinc, cobalt, barium, sodium and calcium.

## BIOGRAPHY

Dr. James D. Winefordner, Professor of Chemistry at the University of Florida, has been an AFOSR grantee since 1964. He has authored more than 100 papers and chapters on such topics as atomic and molecular emission, absorption, and fluorescence in flames and other hot gases; development of sensitive, selective, and accurate methods of trace analysis of metals and molecules in materials; and development of sensitive, selective gas and liquid chromatographic detectors.

Dr. Winefordner received his Ph.D. from the University of Illinois in 1958. He also received an M.S. in 1955 and a B.S. in 1954 from the same university. He was a research associate there until becoming an assistant professor at the University of Florida in 1959.

He is a member of the American Chemical Society, and the American Association for the Advancement of Science. He is also a member of the Advisory Board of Analytical Chemistry and the editorial board of Chemical Instrumentation.

## ABSTRACT

The importance of trace metal determinations in biological fluids, air and water pollution samples, and in lubricating fluids is well-known. The Spectrochemical Analysis Group at the University of Florida has been especially concerned with trace metal determinations in synthetic samples by using newly developed spectrochemical methods. The techniques which have been and are being used include: (1) atomic fluorescence flame spectrometry, (2) atomic fluorescence spectrometry with a graphite furnace and (3) atomic absorption spectroscopy with a graphite furnace. In the first two methods, a sample is atomized and the resulting atoms are excited by a light source. The light emitted when the atoms become de-excited is measured and is directly related to the number of atoms excited. In the absorption method, the sample is atomized and the resulting atomic vapor is measured by a standard light absorption method. In the first technique, a flame is used to atomize the sample, whereas, in the latter two techniques a graphite furnace at about 2000°C is used. By using those techniques, it is possible to selectively and accurately measure such small amounts as  $10^{-10}$  grams of some metals in small amounts of solution (0.01 milliliter). The advantages and disadvantages of these techniques will be stressed, particularly for monitoring wear metals in lubricating fluids as a means of indicating improper engine operation or predicting engine malfunctions in diesel, reciprocating and jet engines.

1. sensitivity: detection of lowest concentration or amount of species of concern
2. selectivity: measurement of the species of concern in the presence of many other potential interferences
3. accuracy: small systematic errors
4. precision: small random errors

To obtain the best possible results in a spectroscopic measurement, we are interested not only in the final application of the technique to specific problems but also in improving well established techniques by a better understanding of the theoretical and instrumental aspects and in developing new techniques and methodology. As a result of this approach, we have measured fundamental spectral parameters of elements, such as quantum efficiencies of atoms in flames, collisional cross sections of atoms and molecules in flames, and collisional energies of diatomic molecules in flames. These measurements have resulted in more optimum experimental conditions for analysis and even in development of new analytical methods. We have also developed new instrumentation, such as light detection devices, new sources of light, and new methodology as a result of this approach.

The current SOAP program has been very successful in predicting impending failure of a component in a jet engine. In fact, when the analyst has in the past recommended a jet engine overhaul, the mechanics found in 90 percent of the cases worn parts which might have resulted in losses of lives and equipment if the aircraft had not been grounded for engine overhaul. In another 5 percent of the cases, parts were beginning to wear, and the engine would have needed an overhaul in the near future. In the final 5 percent there was no apparent wearing of parts. The two techniques now used for SOAP are (1) emission spectroscopy in which oil is sampled using a rotating graphite disc. Excitation is by a spark discharge. (2) Atomic absorption spectroscopy is carried out by aspirating an oil sample after dilution into a flame to produce an atomic vapor. The fraction of light from an external light source absorbed by the atomic vapor is measured. The first technique gives rapid and simultaneous results on all metals concerned but involves expensive equipment, fussy calibration, and gives marginal accuracy. The second technique gives more reliable results on single metals at one time and is less expensive, but it is much slower than the first method and gives marginal results for some elements.

## Spectroscopic Methods Under Study

The experimental systems used in atomic absorption, atomic emission, and atomic fluorescence flame spectrometry are very similar, as can be seen in Figure 1. In all three methods the sample is atomized, forming an atomic vapor of the sample in an appropriate manner, as by means of a flame, arc, or a graphite furnace, since atoms are required. In all three methods, the intensity of light emitted, absorbed or fluoresced is measured by (1) a monochromator or filter, which is used to selectively isolate the radiation of concern from radiation of possible interferents, (2) a photodetector, which converts the desired radiation passing through the monochromator into an electrical signal, and (3) an amplifier-readout system which is used to display an electrical signal proportional to the intensity of light emitted, absorbed or fluoresced.

In all three methods the resulting electrical signal is also proportional to the concentration of the emitters, absorbers, or fluorescences, which is the basis of quantitative analysis. In atomic emission spectrometry, the resulting atomic vapor is excited either by means of an independent system, such as a high frequency-discharge. A portion of the excited atoms (excitation is mainly by collisions with energetic species) undergoes radiational deactivation, called emission (see Figure 4 for mechanism of process), which is measured as described above. In atomic absorption spectrometry, radiation from an external source, such as a hollow cathode discharge tube, an electrodeless discharge tube, or a xenon arc lamp (Figure 3), is passed through the resulting atomic vapor and the intensity absorbed, or the fraction of radiation absorbed is measured as described above. In this case, the source radiation, which is of the correct wavelength (energy), causes the atom to be excited from the groundstate to an excited state (absorption process), which causes the source intensity passing through the atomic vapor to decrease (Figure 2). In atomic fluorescence spectrometry, radiation from an external source (Figure 3) is again allowed to fall upon the resulting atomic vapor, just as in the atomic absorption case. However, in this case, radiation (called fluorescence) results from the deactivation of the atoms excited by the external light. This fluorescence is measured by a photoelectric cell. (The mechanisms of excitation and de-excitation are shown in Figure 2). In all three methods, the wavelength (energy) of the emitted, absorbed, or fluoresced light is characteristic of the atom of concern. Since the emitted, absorbed, or fluoresced spectral lines are of narrow wavelength, for example 0.1 Angstrom, and the spectral range over which such transitions occur is very great, for example, about 8,000 Angstrom, extremely great selectivity is obtained in these three spectroscopic methods. Minimal interference occurs due to overlap of spectral lines.

The optical system, which is used only to isolate the emitted, absorbed, or fluoresced spectral line from other lines, consists of either a grating or prism monochromator, or possibly filters. The detector system consists of either a d.c. electrometer or an a.c. amplifier if the

emitted, absorbed or fluoresced light is modulated. We are currently evaluating a number of detection systems to determine the optimum one for atomic absorption, absorption, and fluorescence spectroscopy. For example, we are currently involved in developing a photon counting system for atomic fluorescence spectroscopy. Such a system should yield far greater signal-to-noise ratios and thus allow greater sensitivity of analysis.

The source of excitation of atoms in atomic emission spectroscopy is also the method of forming atoms. For example, the most common method is to aspirate the sample solution into a flame to produce an atomic vapor. The sample may, for instance, be sprayed directly into the flame. This is convenient and safe but results in a distribution of large droplets, many of which do not have time to evaporate before leaving the flame gases, particularly in turbulent flames. Or the sample may be introduced into a chamber to produce a fine aerosol and then introduced into the flame. Usually the flames are premixed, resulting in a more efficient conversion of sample vapor into an atomic vapor. This is less convenient than the first method, and also the flame system is susceptible to flashbacks. The resulting atomic vapor is then excited via collisions with thermally excited molecules in the flame. This technique is commonly called atomic emission flame spectrometry or just flame photometry. It has been used for years in the measurement of elements, such as sodium and potassium in blood, and calcium and magnesium in soils. We have developed theoretical expressions for the instrumental signal and signal-to-noise ratio to allow the analyst to select the optimum experimental conditions and to even predict the range of useful concentrations which can be measured by this technique. We are also calculating the flame-gas temperatures and compositions to aid in the selection of the optimum flame type for atomic emission as well as atomic absorption and atomic fluorescence flame spectrometry. By such calculations, we can estimate the number of atoms of concern per unit volume of flame gases and thus determine the feasibility of carrying out a practical determination.

The external sources of excitation (Figure 3) used are generally hollow cathode discharge lamps, or electrodeless discharge tubes in atomic absorption and electrodeless discharge tubes or xenon arc lamps in atomic fluorescence. Hollow cathode discharge tubes (HCDD) produce very sharp, fairly intense spectral lines. The basic structure (Figure 3) consists of a tungsten wire to support the cathode containing the element of concern and another wire to serve as the anode; the tubes contain an inert gas, such as argon, at about one mm pressure. A voltage of about 250 volts is applied between the electrodes resulting in a glow discharge within the cathode. The glow discharge accelerates positive ions toward the cathode causing sputtering of the cathode material; the resulting atoms collide with other positive ions and are excited to emit characteristic radiation. Electrodeless discharge tubes (EDT) have considerably higher intensities than HCDD's and also are simpler to construct.

They consist of a quartz bulb containing a small amount of the metal or the metal iodide of the species of concern and a pressure of about one mm of an inert gas such as argon. Upon initiation by a Tesla coil when placed in a high frequency (microwave) field, electrons are accelerated by the electric field resulting in excitation and/or ionization of the inert gas. Collisions of the energetic species result in heat, vaporizing the metal of concern, and producing excitation of the metal of interest. The xenon arc lamp (XE) is a continuous radiation source which has been used in many scientific instruments, as well as in street lighting and motion picture projectors. Sources for atomic fluorescence spectrometry must be extremely intense, since the measured signal depends directly on the source intensity. My group is one of the leaders in development of extremely intense, stable light sources such as electrodeless discharge tubes for atomic fluorescence spectroscopy. Elements for which electrodeless discharge tubes have been prepared are shown in Figure 4. Such sources are now being accepted as the optimal ones for atomic fluorescence spectroscopy and are also being used rather than hollow cathode discharge in many atomic absorption studies.

The method of producing an atomic vapor (Figure 5) of the species of concern is probably the most critical step in atomic emission, atomic absorption, and atomic fluorescence spectroscopy. Most workers have preferred to use the flame for all three methods and thus the names, atomic emission flame spectrometry, atomic absorption flame spectrometry, and atomic fluorescence flame spectrometry. The flame ( $H_2-O_2$ ,  $H_2$ -air,  $C_2H_2-O_2$ ,  $C_2H_2-N_2O$ , etc.) can be used to atomize most metals in the periodic table. It is a simple, precise means of producing an atomic vapor. However, most non-metals and some metals, such as W, Mo, Tc, Re, Ru, Os, Rh, Ir, Ta, Wb, Al, Sn, Sb, Bi, Ge, Se, and Te, as well as the rare earth elements, can not be detected reliably at low concentrations. To measure such species, it is necessary to use a more efficient atomizer such as a graphite furnace, which consists of a graphite tube containing the sample, heated to about  $2000^{\circ}K$  by electrical current. Such a system has been shown to be extremely efficient in producing atoms even for non-metals and is currently being studied. We have also derived expressions for determining the optimum experimental conditions to achieve the maximum instrumental signals and signal-to-noise ratios for atomic absorption and atomic fluorescence flame spectrometry. We are also considered the inventors of atomic fluorescence flame spectrometry as an analytical tool and are leaders in the use of graphite furnaces for atomic absorption and atomic fluorescence spectrometry.

## Sensitivity of Analysis

The sensitivity of analysis of an element by any method is indicated by the limit of detection. This is defined as that concentration or amount of that specific element which produces an instrumental signal which can be just measured above the noise level of the instrument. Table I shows limits of detection for a number of elements, measured by atomic emission spectrometry with a flame atomizer and exciter and with a graphite furnace atomizer and Rf excitation. Table II shows the limits of detection for a number of elements measured by atomic absorption spectrometry with a flame atomizer, and with a graphite furnace atomizer. Table III shows the limits of detection for a number of elements measured using atomic fluorescence flame spectrometry. Studies currently in progress include: atomic emission spectrometry using a graphite furnace atomizer and microwave excitation, to give improved limits of detection for many elements listed in Table I, particularly the non-metals; atomic absorption spectrometry using a unique graphite furnace, to give improved limits of detection for many of the elements listed in Table II; atomic fluorescence spectrometry using a graphite furnace atomizer, which could be especially suited to wear metals in oils; and atomic fluorescence spectrometry using extremely intense pulsed sources, which could produce lower limits of detection for all elements listed in Tables I, II and III.

### Analysis of Wear Metals In Lubricating Oils

Silver, copper, magnesium, and iron in jet engine lubricating oils were analyzed by means of atomic fluorescence flame spectrometry. The method required considerably less time than methods currently used by SOAP, and the results are comparable to those obtained in the SOAP studies (Table IV). Because of poor sensitivity for elements, such as titanium, chromium, silicon, aluminum, and tin, these elements could not be measured using the present system. However, studies are now in progress, in which hotter flames such as  $H_2-N_2O$  and  $C_2H_2-N_2O$ , and graphite cells, are used in the atomic fluorescence studies. It is not unreasonable to expect that all trace wear metals in oils could be measured with no more than five to ten percent relative errors and within a matter of minutes.

Table I. Approximate Limits of Detection (ng. grams) By Atomic Emission Spectrometry

Element	Flame Emission <sup>a,b</sup>	High Frequency Emission <sup>c</sup>
Ag	300	0.01
Al	200	
As	50000	
Au	4000	
B	30000	15
Ba	30	0.1
Bi	40000	4
Ca	5.0	
Cd	6000	
Ce	10000	
Co	1000	0.3
Cr	100	0.01
Cs	8.0	
Cu	100	
Dy	100	
Er	300	
Eu	3.0	
Fe	700	
Ga	70	
Gd	2000	10
Ge	600	
Hf	75000	
Hg	40000	
Ho	100	
In	30	0.5
Ir	100000	
K	3.0	
La	1000	
Li	0.003	0.8
Lu	200	5.0
Mg	200	
Mn	100	0.04
Mo	30	
Na	0.1	
Nb	1000	
Nd	1000	
Ni	600	0.1
Os	10000	
Pb	3000	
Pd	1000	
Pt	40000	
Rb	2.0	
Re	1000	
Rh	3000	
Ru	3000	
Sb	20000	
Sc	70	
Si	5000	

Table I continued

Sm	600	
Sn	4000	
Sr	4.0	0.008
Ta	18000	
Tb	1000	
Te	200000	
Th	150000	6.0
Ti	500	
Tl	90	
Tm	200	
U	10000	
V	300	
W	4000	
Y	300	
Yb	50	
Zn	50000	5.0
Zr	50000	

---

- a. Limits of detection are for aspiration of 1.0 ml. of solution into flame. If volume could be reduced 10-fold, then absolute limits in table would also decrease by 10-fold.
- b. Data taken in part from Koirtoyann, S. R.; paper presented at The Mid-American Symposium in Spectroscopy, Chicago, Illinois, 1967.
- c. Data taken from Svoboda, V., Anal Chem., submitted paper.

Table II. Limits of Detection (in nanograms) by Atomic Absorption Spectrometry

Element	Flame Absorption <sup>a,b</sup>	Graphite Cell Absorption <sup>c</sup>
Ag	10	0.0008
Al	100	0.54
As	500	0.6
Au	100	
B	15000	
Ba	100	
Bi	20	0.2
Ca	3.0	0.5
Cd	10	0.002
Co	7.0	
Cr	5.0	
Cs	50	
Cu	5.0	0.01
Dy	200	0.2
Er	200	0.04
Eu	200	
Fe	10	0.02
Ga	70	
Gd	4000	
Ge	2000	
Hf	15000	
Hg	200	0.2
Ho	300	0.3
In	50	
Ir	4000	
K	5.0	
La	80000	
Li	5.0	0.03
Lu	50000	
Mg	5.0	
Mn	5.0	0.008
Mo	100	
Na	5.0	0.007
Nb	20000	
Nd	2000	
Ni	10	0.07
Pb	10	0.01
Pd	500	
Fr	6000	
Pt	500	
Rb	5.0	
Re	1500	
Rh	30	
Ru	300	
Sb	200	0.1
Sc	200	
Se		2.0
Si	200	
Sm	5000	

Table II continued

Sn	100	0.2
Sr	10	
Ta	6000	
Tb	2000	
Te	300	
Ti	100	
Tl	200	0.04
Tm	100	
U	12000	
V	100	
W	3000	
Y	300	
Yb	40	
Zn	2.0	0.0008
Zr	5000	

---

- a. Limits of detection are for aspiration of 1.0 ml. of solution into flame. If volume could be reduced 10-fold, then absolute limit in table would also decrease by 10-fold.
- b. Data taken in part from Koirtoyann, Sr, paper presented at Mid American Symposium on Spectroscopy, Chicago, Illinois, 1967.
- c. Data taken from Massman, H. Spectrochem. Acta 23B, 215 (1968) and from Woodriff, R., Stone, R. W., and Held, A.M., Appl. Spectr. 22, 408 (1968).

Table III. Limits of Detection (in nanograms) In Atomic Fluorescence Spectrometry

Element	Flame Fluorescence <sup>a</sup>	Graphite Cell <sup>b</sup>
Ag	0.1	0.0015
Al	25000	
Au	50	
Be	2000	
Bi	100	
Ca	20	
Cd	0.001	0.00025
Co	40	
Cr	5000	
Cu	1.0	0.45
Fe	100	3.0
Ga	500	
Hg	2.0	
In	100	
Mg	4.0	0.0035
Mn	6.0	
Mo	2000	
Ni	3.0	
Pb	20	0.035
Pd	500	
Pt	50000	
Rh	3000	
Sb	400	0.2
Sc	10000	
Se	150	
Sn	100000	
Sr	30	
Te	50	
Ti	5000	
Tl	8.0	2.0
Zn	0.04	

a. Data taken from Winefordner, J. D. et.al. papers.

b. Data taken from Massmann, H., Spectrochim. Acta 23B, 215 (1968) and from Woodriff, R., Stone, A. W., and Held, A. M., Appl. Spectr. 22, 408 (1968).

Table IV. Determination of Wear Metals in Correlation Jet Engine Oil Samples  
 Using Atomic Absorption Flame Spectrometry (AA), Atomic Emission (AE)  
 With Spark Spectrometry, and Atomic Fluorescence Flame Spectrometry (AF)<sup>a</sup>

Sample	Concentration , $\mu\text{g/ml}$											
	Ag			Cu			Fe			Mg		
	AF <sup>a</sup>	AE <sup>b</sup>	AA <sup>c</sup>	AF	AE <sup>d</sup>	AA <sup>e</sup>	AF	AE <sup>f</sup>	AA <sup>g</sup>	AF	AE <sup>h</sup>	AA <sup>i</sup>
67-2	0.71	0.9	0.7	7.9	8.5	5.6	23	30.1	28.3	4.7	2.4	3.0
67-3	0.66	0.8	0.5	15.0	16.2	10.6	20	15.8	19.1	2.1	0.8	1.1
67-6	0.44	0.3	0.7	8.4	9.6	6.0	16	16.3	17.0	2.1	2.2	2.1
67-9	0.46	0.1	0.4	6.2	9.3	4.1	34	27.5	28.7	10.8	11.4	10.1
67-10	0.32	0.4	0.4	9.5	8.3	4.7	26	27.5	25.6	4.3	3.6	3.8
67-11	1.14	0.9	1.1	3.8	3.0	3.0	13	9.3	9.5	1.6	2.1	2.2
67-12	0.46	0.5	0.5	3.2	4.7	2.7	33	27.5	22.7	2.6	1.7	2.5
68-2	0.87	0.6	0.9	17.3	15.5	15.9	24	15.0	21.5	2.6	0.8	2.8
68-3	0.59	0.6	0.6	4.1	4.6	2.8	43	22.6	29.0	3.2	1.0	2.0
68-4	0.40	0.4	0.4	2.0	2.9	1.5	75	80.7	58.1	3.7	3.1	2.5

a. Data taken from paper by R. Smith, C. M. Stafford, and J. D. Winefordner  
Canad. J. Spectr., in press.

## FIGURE CAPTIONS

Figure 1. Schematic Diagram of Experimental Systems Used in Atomic Emission, Atomic Absorption, and Atomic Fluorescence Spectrometry.

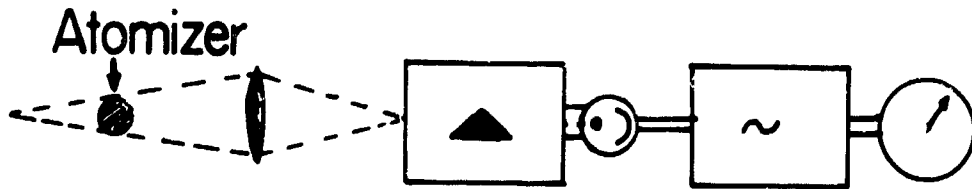
Figure 2. Mechanism of Excitation and De-excitation of Atoms in Atomic Emission, Atomic Absorption, and Atomic Fluorescence Spectrometry.

Figure 3. Sources of Excitation for Atomic Absorption and atomic Fluorescence Spectrometry.

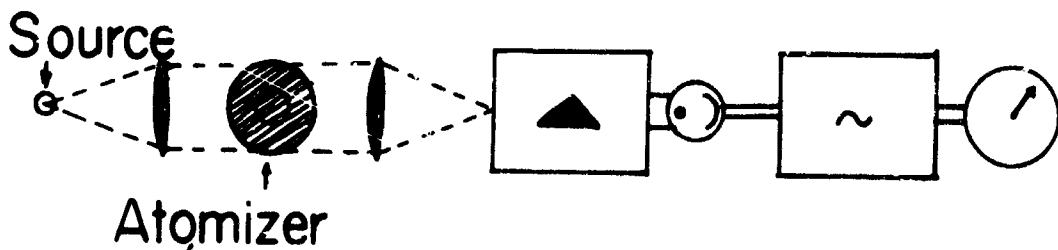
Figure 4. Elements for Which Hollow Cathode (HCDT) and Electrodeless (EDT) Discharge Tubes Have Been Prepared.

Figure 5. Methods of Production of An Atomic Vapor.

# ATOMIC EMISSION



# ATOMIC ABSORPTION



# ATOMIC FLUORESCENCE

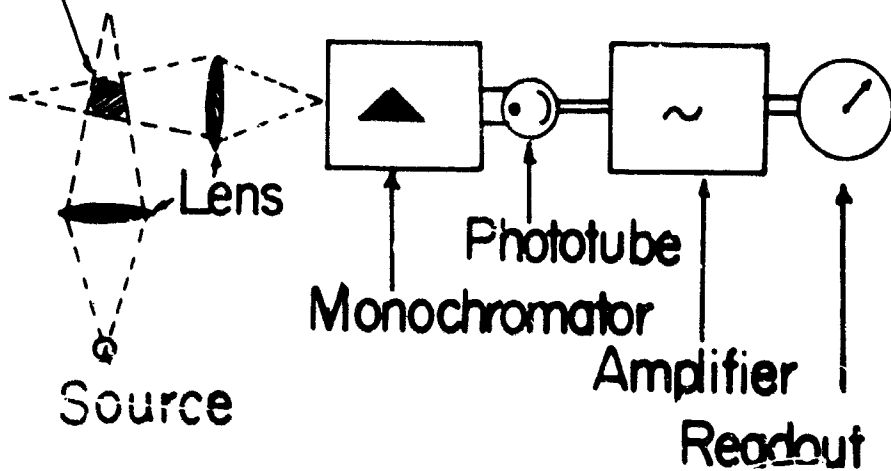


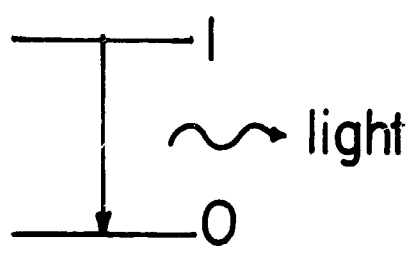
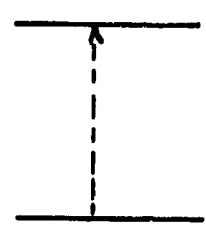
FIGURE 1

# ATOMIC EMISSION

Excitation

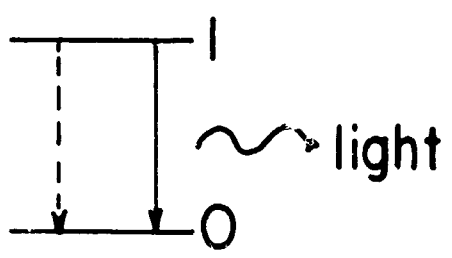
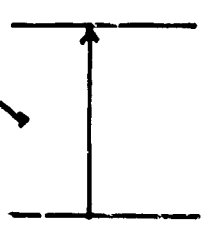
Deexcitation

via collisions



# ATOMIC ABSORPTION

light



# ATOMIC FLUORESCENCE

light

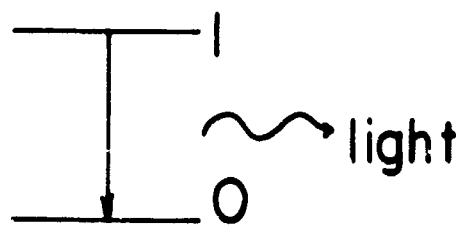
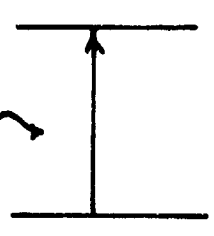


FIGURE 2

# HCDT

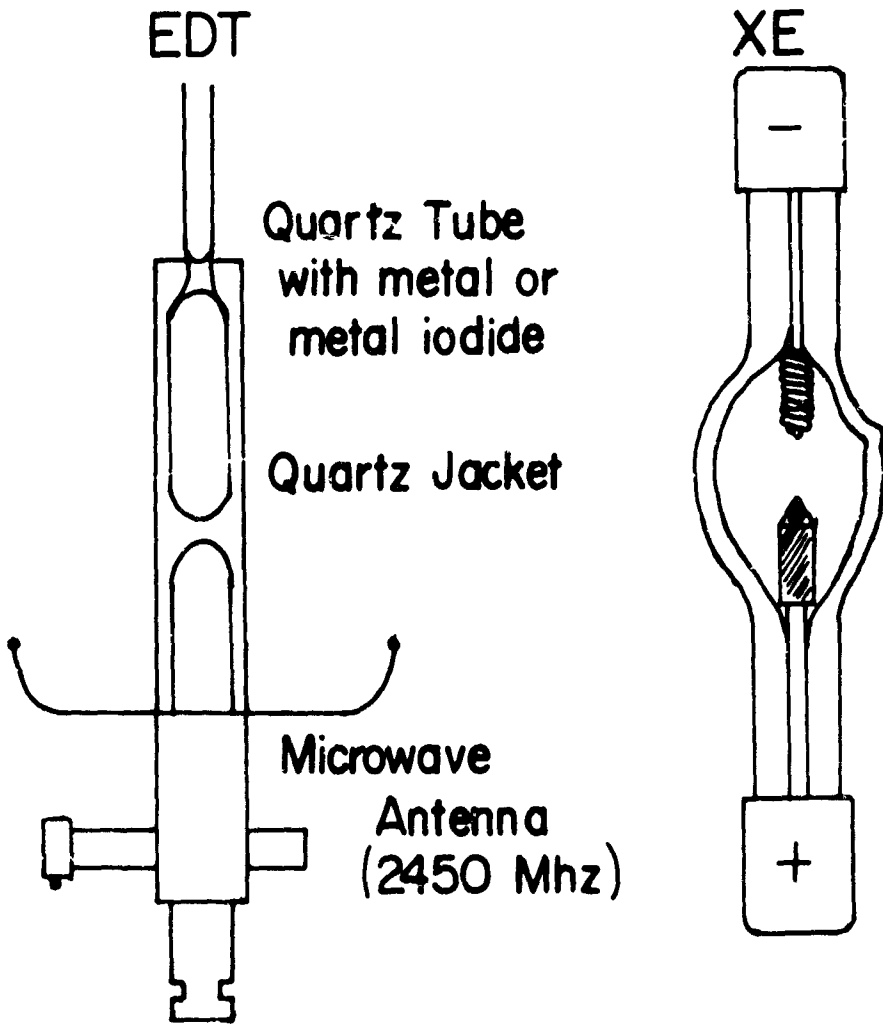
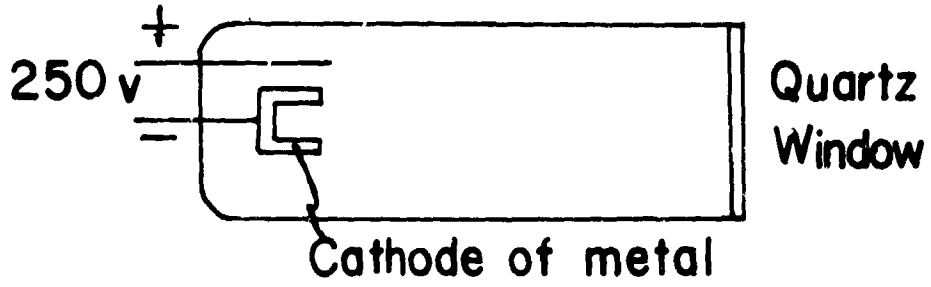


FIGURE 3

HCDT 

EDT 

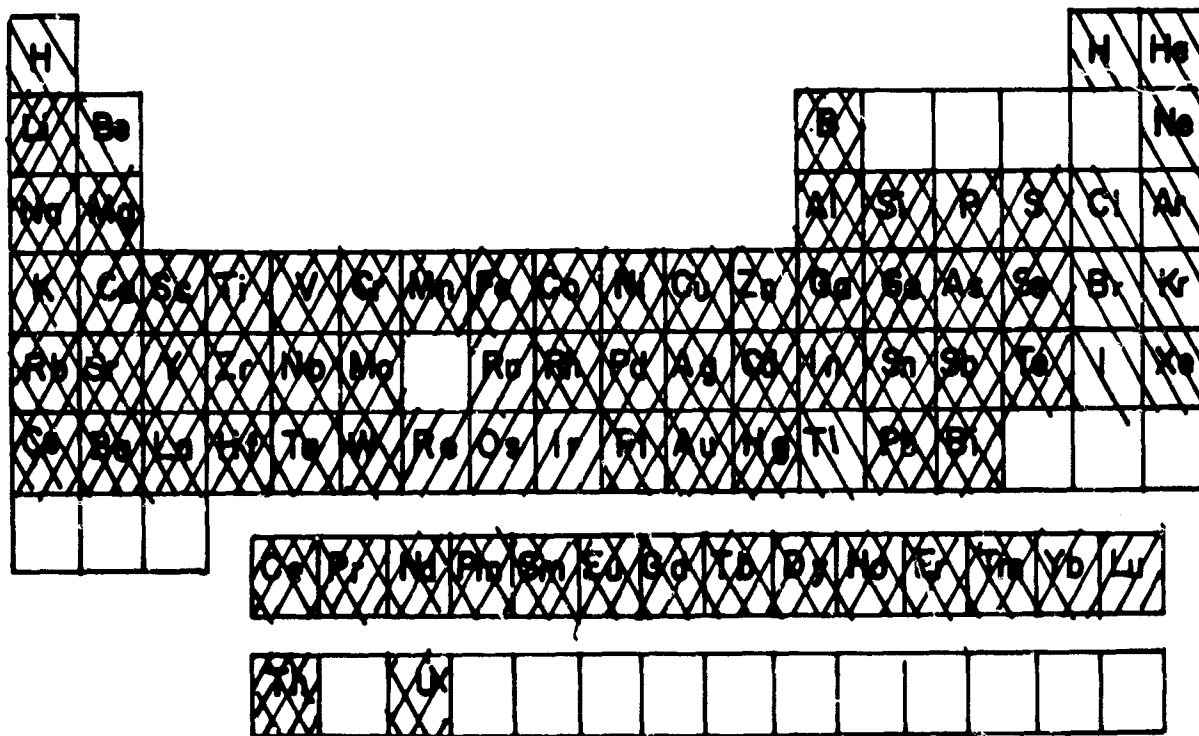
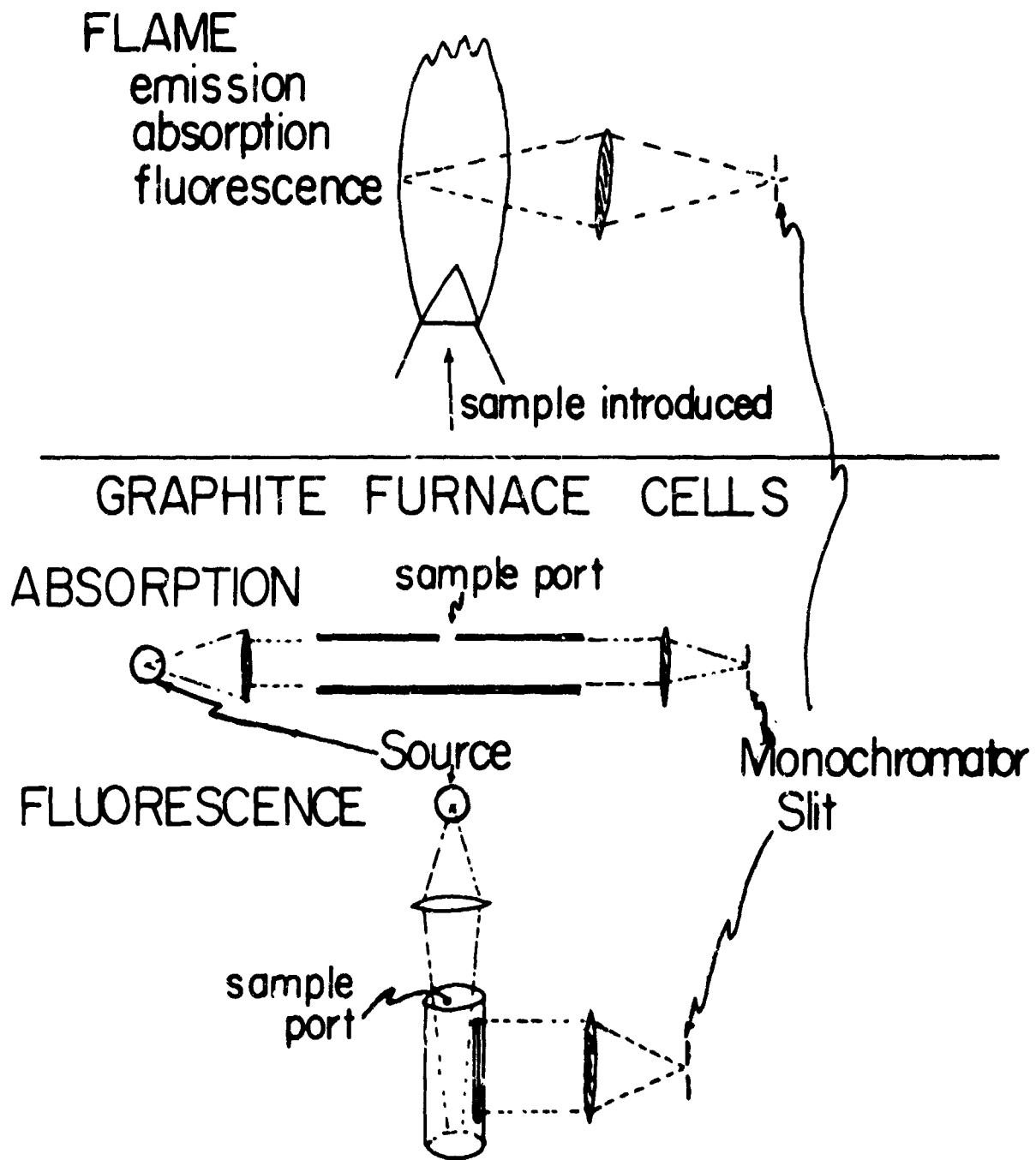


FIGURE 4



**FIGURE 5**

PLAN SHEAR INDICATOR FOR REAL-TIME DOPPLER  
RADAR IDENTIFICATION OF HAZARDOUS STORM WINDS

Graham M. Armstrong and Ralph J. Donaldson, Jr.

Meteorology Laboratory

Air Force Cambridge Research Laboratories

L. G. Hanscom Field, Bedford, Massachusetts

PLAN SHEAR INDICATOR FOR REAL-TIME DOPPLER RADAR  
IDENTIFICATION OF HAZARDOUS STORM WINDS

by

Graham M. Armstrong and Ralph J. Donaldson, Jr.  
Meteorology Laboratory  
Air Force Cambridge Research Laboratories  
L. G. Hanscom Field, Bedford, Massachusetts

ABSTRACT

The Plan Shear Indicator (PSI) is a new mode for display of ground-based meteorological Doppler radar information which may prove to be valuable in identification of hazardous winds and turbulence in storms. It provides real-time location and convenient highlighting of regions within precipitation echoes of abnormally large shear and spectral broadening of the Doppler velocity. The real-time capability of the PSI and its high data rate are achieved at the cost of mediocre resolution of ranges and velocities and the ability to measure only the shear and not the absolute value of wind components along the Doppler beam.

The PSI display for a scanning Doppler radar utilizes an ordinary PPI scope intensity-modulated by a coherent memory filter. The resultant pattern is a series of concentric arcs, each located on the scope at its appropriate range in addition to an incremental displacement which depends on the radial component of velocity measured at that range. Radial shear is indicated by gaps or bunching of the arcs, whereas tangential shear, as, for example, a vortex, is indicated by wrinkles in the arcs. Turbulence on a scale smaller than measurable wind shear would broaden the Doppler spectrum and would be revealed on the PSI by an increase in line widths of the arcs. The instrument has been used during an outbreak of severe thunderstorms in New England, with apparent success in identification of storms that produced damaging winds and hail.

## 1. INTRODUCTION

Wind measurement by Doppler radar is dependent on a medium that can trace the air motion reliably and, at the same time, scatter sufficient power back to the radar to provide a detectable signal. These requirements are satisfied well by the precipitation in a storm, for determination of the component of mean wind velocity along the radar beam, in a scale of resolution attainable by meteorological radars.

The employment of Doppler radar for measurement of winds in a tornado was first reported by Smith and Holmes (1961). Using a cw Doppler without ranging capability, they measured wind speeds as high as 206 statute miles/hour when the radar was directed toward a tornado that devastated El Dorado, Kansas on 10 June 1958. The use of pulse Doppler radar with range-velocity display was suggested by Lhermitte (1964) for detection of a vortex. Although no pulse Doppler data have been acquired in a high-speed vortex such as a tornado, Lhermitte derived the characteristic patterns revealed by vortices larger and smaller than the resolution of the radar beam and ranging circuitry. Neither of these schemes, however, provide the convenience of a map-like presentation of dangerous wind speeds in real time.

A compromise solution is offered by the Plan Shear Indicator, or PSI, developed by the authors (1968) for use with the AFCRL meteorological Doppler radar at Sudbury, Massachusetts. This technique reclaims mediocre range resolution, an inherent limitation, by utilizing the distance between adjacent range elements as a field for presentation of velocity. The velocity information is obtained in real time from a coherent memory filter that performs a frequency analysis at all ranges of the Doppler signal returned by precipitation or detectable cloud. The display of the coherent memory filter output on an ordinary PPI scope, as the Doppler radar scans in azimuth, provides a pattern in which regions of intense wind shear or turbulence may be located with ease and readily distinguished from a homogeneous wind field. Although the magnitude of the wind cannot be measured quantitatively in this manner, the PSI technique is a sensitive probe of the radial component of the gradient of the wind in space, or wind shear. The technique has a potential application as an aid to flight safety because wind shears within precipitation hazardous to aircraft may be recognized immediately and evaluated. Furthermore, a vortex circulation of sufficient scale to be resolved by the radar has a characteristic signature on the PSI display which may be of use in identifying and warning of severe thunderstorm events at the surface.

## 2. VELOCITY DETERMINATION BY THE COHERENT MEMORY FILTER

Spectral analysis of the received echo signal is a basic requirement for full utilization of the information provided by pulse Doppler radar. The most common technique for obtaining the required spectra uses a range gate at the selected range interval, followed by a boxcar circuit to stretch

the return signal, and then by a bank of parallel band pass filters to perform the frequency analysis. If it were desirable to view the Doppler spectrum at all ranges in the field of view of the radar, it would be necessary to duplicate this equipment at each resolvable range interval or, alternatively, to store the Doppler video for later analysis, thereby losing real-time capability.

In recent years, however, a novel technique has been developed for providing real-time Doppler spectral analysis over the entire range capability of the radar. This circuit is called a Coherent Memory Filter (CMF) or again a Velocity Indicating Coherent Integrator (VICI). It has the capability of producing Doppler spectra at all ranges almost simultaneously. A simple explanation of CMF operation is sufficient for understanding its use in measurement of velocities. However, a more comprehensive discussion, together with full mathematical treatment, is available in a review article by Groginsky (1965), which also lists references to the basic development work by Bickel and others (1959). Chimera (1960) first recognized the possibilities for application of the CMF to meteorological analysis. A concise description of the CMF and an illustration of its use in a snowstorm have been presented in an excellent review by Atlas (1963).

The signal which is scattered back from a fixed target exhibits a constant phase difference,  $\phi$ , with respect to the transmitter signal phase. This phase difference, given by

$$\phi = 4\pi r/\lambda \quad (1)$$

is merely the time required for radar energy of wavelength  $\lambda$  to reach the target at range  $r$ , and return, expressed as a multiple of the time required for one oscillation of the radar transmitter. In Doppler radar, provision is made for measuring the phase difference of the returned signal within the limits of 0 to  $2\pi$ . If the range of the target changes, the phase difference,  $\phi$ , also changes and becomes a function of time. A change in phase with respect to time is an angular speed  $2\pi f_d$ ; therefore, time differentiation of Eq. (1) yields

$$f_d = 2v_r/\lambda \quad (2)$$

where  $f_d$  is the Doppler frequency shift and  $v_r$  the radial velocity of the target.

The CMF, as shown in Figure 1, consists simply of a summing network,  $\Sigma$ , a delay line and associated amplifiers, a single sideband mixer, a frequency generator which produces a frequency whose period matches the radar pulse width  $\tau$ , and an envelope detector. Let us neglect the single sideband mixer for a moment and circulate a series of  $N$  pulses from a stationary target through a delay line whose delay time equals the pulse repetition interval,  $T$ . If we add them together in the summing network, they will produce an output with a peak  $N$  times as great as the amplitude of the individual pulse.

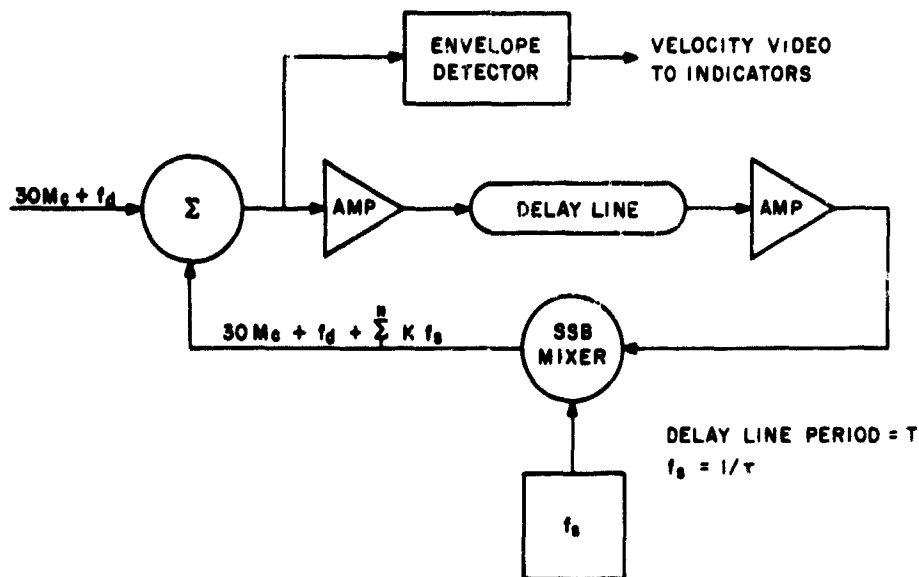


Figure 1. Simplified Block Diagram of the Coherent Memory Filter

It is obvious from Eq. (1) that successive pulses from moving targets delayed by  $T$  will not be in phase and will not add directly. If moving targets are to be detected, the phase of successive pulses must be shifted from 0 to  $2\pi$  during the time of each pulse width,  $\tau$ . This is for the purpose of achieving the correct phase relationship for adding coherently during some portion of the time a particular pulse is present in the summing network. A linear time-varying phase shift is equivalent to a frequency shift. Accordingly, the compensating phase shifter can be replaced by a scanning frequency,  $f_s$ , with a period equal to the pulse width,  $\tau$ , (that is,  $f_s = 1/\tau$ ) and a single sideband mixer whose output is the sum of the input frequency and the scanning frequency  $f_s$ . Since the CMF works in the IF region, a simple envelope detector is needed to produce the output video.

There are two inherent difficulties in the characteristics of the quartz delay line which must be overcome. First, the signal is attenuated about 60 dB from input to output and therefore must be amplified. However, harmful oscillations will be generated within the delay line unless the loop gain from the summing network through the delay line and back is kept at unity or below. This is accomplished by sending a pulse through the loop, monitoring its amplitude, and adjusting the gain of the delay line amplifiers accordingly.

The second problem is the variation of line delay with temperature. This limitation is overcome by circulating the radar trigger through the delay-line loop so that the radar pulse repetition interval,  $T$ , becomes a function of the delay time of the line, assuring that successive pulses will arrive at the summing network simultaneously.



Figure 2a. Typical "A" Scope Display of Radar Video

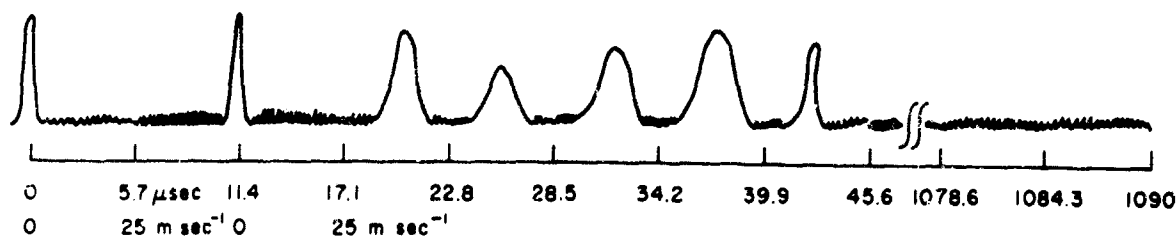


Figure 2b. Corresponding display of Coherent Memory Filter Output Video. Note the velocity interval of 0 - 25 m sec<sup>-1</sup> every 5.7 μsec. Fixed targets appear at zero velocity while moving targets appear somewhere in the velocity interval depending upon their radial velocity component

The output signal of the AFCRL CMF, illustrated in Figure 2(b), is a series of 192 range bins each with a period ( $\tau$ ) equal to 5.7 μsec. The Doppler spectrum of the target(s) within each range bin is displayed with zero velocity at the left of the bin; increasing radial velocity (toward the radar) is displayed as an increasing displacement toward the right. In the case of a pulse Doppler radar the phase change,  $\phi$ , is measured only at discrete time intervals  $T$ , equal to the pulse repetition period. Therefore, a phase change of  $2\pi$  during  $T$  would appear as a zero velocity target. Substituting  $v_r T$  for  $r$  in Eq. (1), one sees that a phase shift of  $2\pi$  occurs whenever  $v_r T$  equals  $\lambda/2$ . In our CMF,  $T = 1090 \mu\text{sec}$  and  $\lambda = 5.45 \text{ cm}$ . Solving for  $v_r$  when  $\phi = 2\pi$ , we get  $v_{\text{max}}$ , or maximum unambiguous velocity, equal to 25 m sec<sup>-1</sup>. Velocities in excess of 25 m sec<sup>-1</sup> are displayed as the difference between the actual velocity and an integral multiple of 25 m sec<sup>-1</sup>.

Since the CMF is performing a frequency analysis, its output closely resembles the Fourier transform of the input time function. In the case of a pulse Doppler radar, this input time function is a series of pulses. Thus the Fourier transform is the familiar  $\sin x/x$  spectrum with the first side lobe appearing 13.5 dB down from the main lobe, and its 3 dB-width is a function of the number of pulses circulated. In order to increase the dynamic range and velocity resolution of the CMF, it is desirable to decrease the amplitude of the side lobes and at the same time keep the width of the main lobe small. This can be done by amplitude-weighting the input

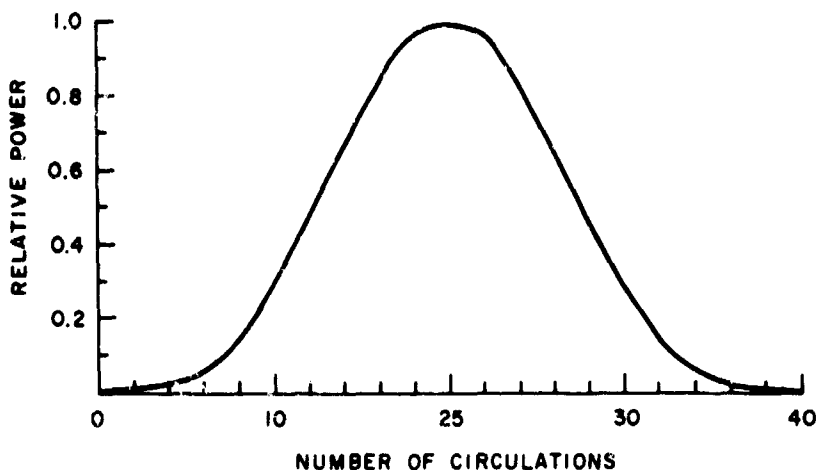


Figure 3. Plot of the Hamming Function. This is used to weight the relative power of successive circulations of the returned Doppler signal in the CMF delay line

pulse train as it circulates through the delay line loop; that is, the bandwidth of the delay line and associated amplifiers is shaped to approximate a time function called the Hamming function. Amplitude-weighting the pulses with this Hamming function reduces the side lobes to about -42 dB as compared to -13.5 dB with no weighting. Each time a pulse is circulated through the delay line, it is stepped up in frequency by an amount  $f_s$ . Thus it can be seen from Figure 3 that after 20 circulations the pulse reaches a peak amplitude and that circulations 10 to 30 provide most of the contribution to the output spectrum.

Another feature of the CMF is its capacity to improve the signal-to-noise ratio of the radar. In-phase addition from 40 pulses takes place in our CMF. The addition of noise energy associated with each return yields a total noise energy which fluctuates about some average value because noise has a random phase characteristic. On the other hand, in-phase addition yields a total signal energy that increases as successive signals are added and consequently an improved signal-to-noise ratio is obtained.

Let us say that the output of the CMF as illustrated in Figure 2(b) is connected to the Z-axis of a PPI scope with sufficient sweep speed to resolve the range bins. As the antenna is rotated in azimuth, a series of concentric arcs will appear wherever there are echoes. We call this display a Plan Shear Indicator or PSI because of its capability to detect and locate regions of strong wind shear from the characteristics of the arc pattern.

### 3. INTERPRETATION OF PLAN SHEAR INDICATOR PATTERNS

The indicated range  $r_n$  of an arc on the PSI display is the sum of the true distance of the range element in which the target is detected, plus an incremental displacement, no greater than the width of a range element, which corresponds to the radial velocity of the target:

$$r_n = (c \tau / 2) (n - v_n / v_{\max}), \quad (3)$$

where  $c$  is the speed of electromagnetic propagation,  $\tau$  the radar pulse duration and  $\tau/2$  the time interval required for the radar waves to traverse the width of a range element;  $n$  is an integer between 1 and  $T/\tau$  which denotes the number of range elements between radar and target;  $v_{\max} = \lambda/2T$  is the maximum velocity which can be detected unambiguously by the radar; and  $v_n$  is the indicated radial velocity. Velocities are considered positive for motions directed away from the radar. Hence a target motion toward the radar will increase  $r_n$ , as illustrated in Figure 4.

The true radial velocity of the target will not be indicated correctly if it is positive, or if it is negative (toward the radar) with a magnitude in excess of  $v_{\max}$ . During the pulse repetition period  $T$ , the Doppler radar can detect phase changes only within  $0$  to  $2\pi$ , corresponding to

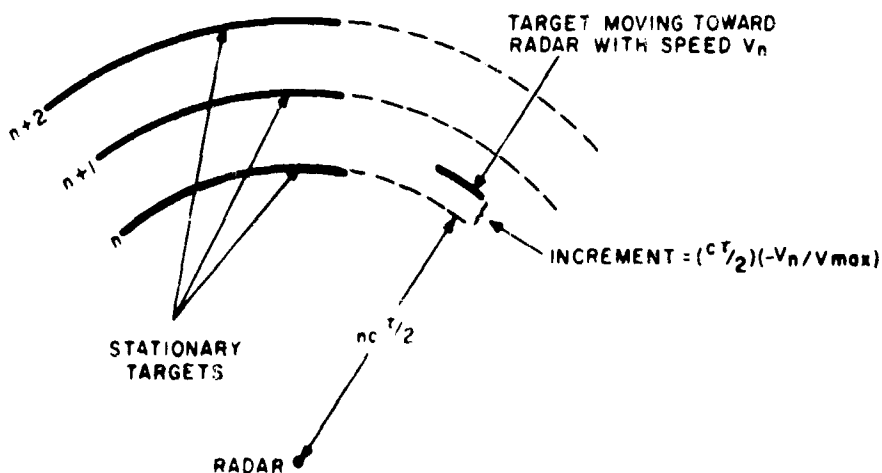


Figure 4. PSI Display for Stationary Targets (left) and a Moving Target (right). The moving target is located at the same distance from the radar as the nearest stationary target, but is displaced from it on the PSI display by an increment which depends on its velocity

$0 \leq -v_n \leq v_{\max}$ . Velocity ambiguity will occur if the true radial velocity exceeds this range, and the indicated radial velocity  $v_n$  will then express the remainder after the true velocity is reduced by an integral multiple of  $v_{\max}$  until  $0 \leq -v_n \leq v_{\max}$ . For example, if  $v_{\max} = 25 \text{ m sec}^{-1}$  and a target is moving toward the radar at a speed of  $60 \text{ m sec}^{-1}$ , its indicated velocity will be  $10 \text{ m sec}^{-1}$ . Another target retreating from the radar at a speed of  $20 \text{ m sec}^{-1}$  will be indicated the same as a target moving toward the radar at  $5 \text{ m sec}^{-1}$ .

Note that the two terms of  $r_n$  in Eq. (3) differ considerably in magnitude. The increment corresponding to velocity,  $(c \tau/2) (-v_n/v_{\max})$ , is generally very small compared with the target range  $n c \tau/2$ . Therefore, the PSI display cannot be used to measure velocities with acceptable accuracy. However, changes in velocity from one range element to the next, or along a single range element as the antenna scans, are easily detectable and may be evaluated without great difficulty. As the radar antenna rotates, the PSI presents a series of up to  $T/\tau$  concentric arcs. The number, as well as size of the arcs, depends on the area of target detected. If the radial velocity were constant, as in observation of fixed ground targets, the arcs would be circular and evenly spaced. If, however, there is a gradient of the radial velocities of the detected targets along the radial direction (that is, radial shear), the spacing between arcs would vary. Similarly, if a gradient of the radial velocities exists normal to the radar beam (that is, tangential shear), the radius of an arc will vary with azimuth as the antenna scans, and the PSI display will have wiggles.

Consider first the significance of arc spacing in the PSI pattern. At a fixed azimuth angle, the indicated distance  $\Delta r$  between two successive arcs  $n$  and  $n + 1$ , is given from Eq. (3):

$$\Delta r = r_{n+1} - r_n = (c \tau/2) (1 - [v_{n+1} - v_n]/v_{\max}) \quad (4)$$

Substituting  $\lambda/2T$  for  $v_{\max}$ , we can express the change in velocity  $\Delta v = v_{n+1} - v_n$  by

$$\Delta v = (c \tau/2 - \Delta r) (\lambda/c \tau T) \quad (5)$$

If the y-axis of Cartesian coordinates is assumed to be identical with the direction in which the radar antenna points, the true range  $\Delta y$  between adjacent arcs is  $c \tau/2$ , and the radial shear of the radial wind component is given by division of Eq. (5) by  $\Delta y$ :

$$\Delta v/\Delta y = (1 - 2 \Delta r/c\tau) (\lambda/c \tau T) \quad (6)$$

The maximum value of  $\Delta v/\Delta y$  which can be measured unambiguously is  $\lambda/c \tau T$ , which would be the case if  $\Delta v = v_{\max}$  and  $\Delta r = 0$ . With our particular radar and CME,  $\lambda = 5.45 \text{ cm}$ ,  $\tau = 5.7 \text{ } \mu\text{sec}$ , and  $T = 1090 \text{ } \mu\text{sec}$ ,

so  $\lambda/c \tau T = 2.9 \times 10^{-2} \text{ sec}^{-1}$ . If  $\Delta v$  is positive but less than  $v_{\text{max}}$ ,  $\Delta r$  will be smaller than the width of a range element. Positive  $\Delta v$  means that the air motion away from the radar increases with distance. Consequently, the bunching-up of arcs on the PSI display indicates a divergent radial component of the wind and, conversely, a larger than normal gap between arcs indicates a convergent radial component of air motion. If the magnitude of  $\Delta v$  exceeds  $v_{\text{max}}$ , one (or both) of the velocities is ambiguously recorded, and the resultant arc spacing cannot be interpreted without examination of the continuity of airflow in surrounding areas.

Abnormal spectral broadening is indicated by thickening of a PSI arc. Unfortunately, the width of the CMF output signal, which controls the thickness of the PSI arcs, is a function of received power as well as the width of the Doppler velocity spectrum. On the other hand, extremely wide arcs which fill up practically all of a range bin almost certainly reveal regions with a very large variance of the Doppler velocity spectrum, which suggests, or indicates turbulence of sufficient intensity to constitute a hazard to aircraft (Donaldson and Wexler, 1969).

Now let us interpret the term "wiggles" in a PSI arc. The slope of an arc at indicated range  $r_n$  with respect to the scanning radar beam is  $dr_n/r_n d\beta$ , where  $\beta$  is azimuth angle of the radar beam increasing with clockwise rotation. This slope may be evaluated in terms of tangential shear of the radial velocity by differentiation of Eq. (3) with respect to the velocity  $v_n$ , substituting  $\lambda/2T$  for  $v_{\text{max}}$ :

$$dr_n/dv_n = -c\tau T/\lambda. \quad (7)$$

Tangential shear of radial velocity is defined by  $dv/dx$  in Cartesian coordinates, adopting the convention that the radar points in the  $y$  direction. In polar coordinates appropriate to a scanning radar,  $dx = y d\beta$ . Now on the PSI display true range  $y_n (= n c \tau/2)$  does not equal indicated range  $r_n$ , unless  $v_n = 0$  or an integral multiple of  $v_{\text{max}}$ . However, the maximum fractional error in approximating  $y_n \approx r_n$  is  $1/n$ . (This occurs when  $-v_n = v_{\text{max}}$ .) The average error would be half as large. Since the velocity resolution of the CMF is no better than 2.5 percent, the approximation  $y_n \approx r_n$  is completely acceptable for any  $n > 20$ , or true range of 17 km or more. Even at a range of 10 km the error is less than 5 percent. Therefore, tangential shear may be evaluated directly from the slope of the arc with respect to a circle by using Eq. (7) and the approximation  $y_n \approx r_n$ .

$$dv_n/dx = dv_n/y_n d\beta \approx -(\lambda/c \tau T) dr_n/r_n d\beta \quad (8)$$

Note that tangential shear as defined in the foregoing is the first of the two terms,  $dv/dx - du/dy$ , which express vorticity in Cartesian coordinates. Accordingly, positive tangential shear, indicated on the PSI display by slope of an arc toward the radar, moving clockwise, contributes toward

positive or cyclonic vorticity. If an arc tilts  $45^\circ$  from a constant-velocity circular path, the magnitude of the shear will be  $\lambda/c \tau T$ , or  $2.9 \times 10^{-2} \text{ sec}^{-1}$  with our equipment.

The maximum value of tangential shear which can be measured unambiguously occurs when the entire breadth of the unambiguous velocity spectrum is filled with contributions from either side of the radar antenna beam. It is difficult to state the effective antenna aperture for detection of velocities, because this depends to a great extent on received power levels and sensitivity of the radar receiver. It is almost certainly greater than the traditional half-power beam width but unlikely to exceed twice this size. Our Doppler radar antenna has a half-power beam width of  $0.9^\circ$ , and  $v_{\text{max}}$  of our coherent memory filter is  $25 \text{ m sec}^{-1}$ . Therefore, the maximum tangential shear which can be measured with our equipment is in the neighborhood of  $0.8/r$  to  $1.6/r \text{ sec}^{-1}$ , where  $r$  is range in kilometers.

Another possible limitation on the angular resolution of the PSI is the antenna scanning rate. Figure 3 shows that the output powers of the CMF delay line weighting function exceed one-fourth of the maximum power during 20 pulse repetition periods, or  $20 \times 1090 = 21,800 \mu\text{sec}$ . If the antenna scans through one half-power beam width in this time ( $0.9^\circ/0.0218 \text{ sec}$  or 7 rpm) the CMF delay line will limit the angular resolution to the same extent as the antenna. Generally the antenna scans at a rate of 5 rpm, somewhat less than the rate at which the CMF delay line would have an appreciable effect on angular resolution. However, the CMF output peak amplitude is delayed by 20 recirculations in the delay line, or  $20T = 0.0218 \text{ sec}$ . Consequently, at a normal antenna scanning rate of 5 rpm, the PSI pattern will be rotated about  $2/3$  of a degree in the direction of antenna scan.

The most easily distinguished pattern feature on the PSI display is the contrast between areas of little or no wind shear, where the arcs are smooth and evenly spaced, and regions of intense shear in which the arcs exhibit a disturbed and sometimes confused appearance. The interpretation of a complex tangle of arcs, beyond the recognition that severe wind shear and turbulence is present, may be extremely difficult because (1) only the radial component of wind can be observed by Doppler radar, and only when suitable tracers are present; (2) careful inspection is required to circumvent the ambiguity of foldover velocities which exceed the maximum unambiguous range; and (3) sometimes regions of large shear are also regions of broad velocity spectra which produce arc segments so thick that the boundaries between them are ill-defined. Nevertheless, some simple types of air circulation are revealed by a characteristic PSI pattern. For example, a wind-shift line with relatively smooth air on either side would show up on the PSI display as a locus of wrinkled arcs cutting across an otherwise undisturbed pattern, as sketched in Figure 5. The PSI pattern for convergent flow or a sink, illustrated schematically in Figure 6, would have the largest gaps in the arcs where convergence is greatest. A cyclonic vortex would have the pattern type sketched in Figure 7, with the center of maximum vorticity indicated by the maximum clockwise slope of an arc toward the radar. We must caution, however, that the appearance of a pattern on a PSI display should not be taken as proof of the existence of the airflow model that corresponds to these

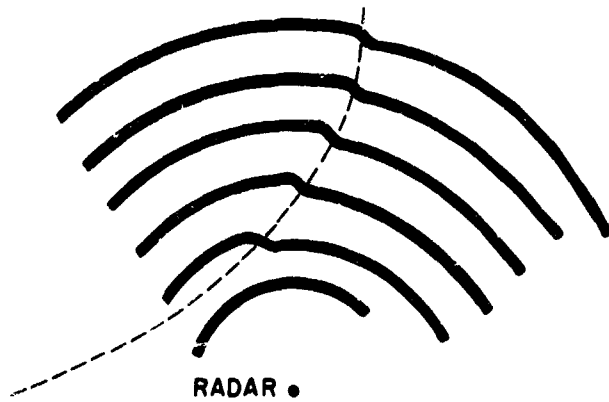


Figure 5. Schematic PSI Pattern of a Wind Shift Line (indicated by light dashed curve) Which Might Accompany a Frontal Passage. PSI arcs are indicated by thick lines

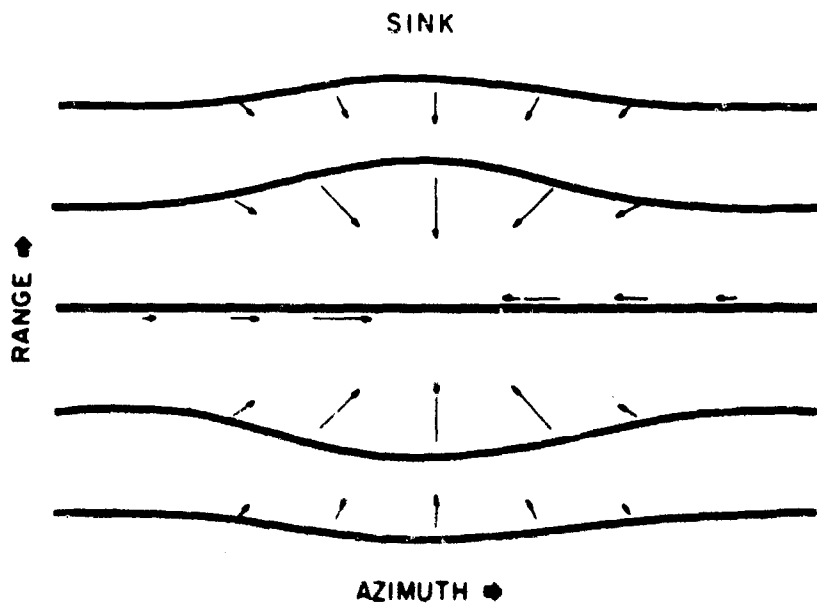


Figure 6. Schematic PSI Pattern for a Sink, or Convergent Flow. Maximum convergence is located at the center of the pattern where arc spacing is greatest. Arrows represent wind vectors; PSI arcs are indicated by thick lines

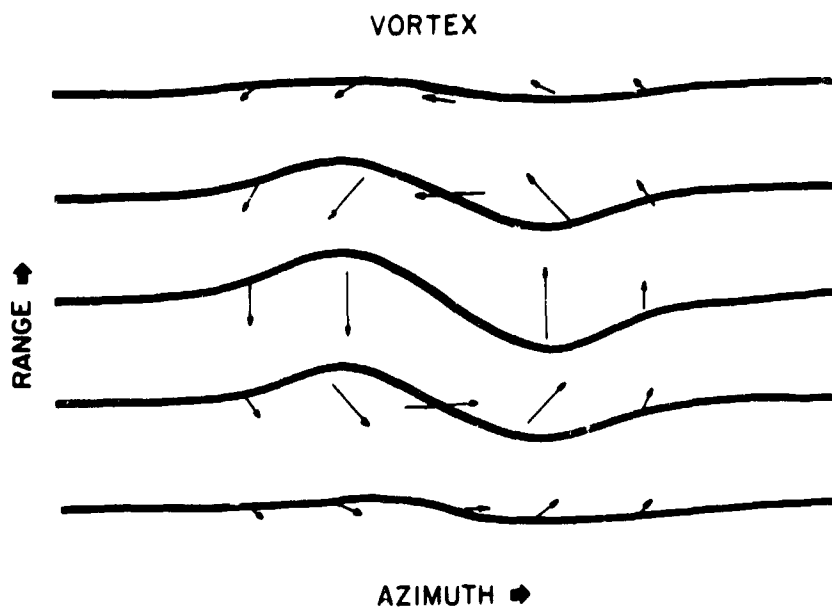


Figure 7. Schematic PSI Pattern for a Cyclonic Vortex. Maximum vorticity is denoted by maximum arc slope, in the center of the sketch. PSI arcs are indicated by thick lines. Arrows represent wind vectors

examples, because a single Doppler radar can sense only the radial component of the total wind vector.

#### 4. APPLICATION OF PLAN SHEAR INDICATOR TO SEVERE STORM IDENTIFICATION

Wind shear information has been acquired in a variety of convective storms, using the PSI display. Armstrong and Donaldson (1968) showed an example of an ordinary thunderstorm which occurred during the summer of 1967 near the AFCRL Doppler radar site at Sudbury, Massachusetts, in which no high winds or hailstones were reported. A few places in this storm showed minor wrinkles in the PSI arcs, indicating moderate shear. A line of small rain showers of moderate intensity followed by a wide band of very light steady rain, observed on 19 July 1968, exhibited smooth, evenly spaced arcs throughout the entire storm (see Figure 8). Apparently very little shear was present in this area of precipitation.

The most interesting set of storms observed to date with the PSI display occurred on 9 August 1968. Several of the widely scattered thunderstorms observed were severely damaging. Within range of the PSI display, one storm released a small tornado and one-inch hail; a second storm nearby was not confirmed as a tornado although it caused heavy wind



Figure 8. Photograph of PSI Display on 19 July 1968 in a Band of Small Showers. Antenna elevation angle is  $0^{\circ}$ . Circles near the center and a few nearby circular arcs are signals from fixed ground targets. This photograph and all of the succeeding ones (Figures 9-14) were taken from the AFCRL meteorological radar site at Sudbury, Mass., and show north at the top of the picture with 5-mile range markers in an eastern sector

damage with hail nearly one inch in diameter; a third storm releasing marble-size hail struck a harbor, inflicting extensive and heavy wind damage to small boats; and a fourth storm deposited hail up to two inches in diameter, although accompanied by only minor wind damage. We shall label these storms A, B, C, and D, respectively, for convenience of description. Figure 9 shows the low-level or  $0^{\circ}$  elevation PSI pattern in three of these storms and a little of the fourth before any wind damage or hail on the ground.

In all four severe storms, disturbances occurred in the PSI pattern aloft for periods of 15 minutes to an hour before damaging winds or hail reached the ground. The storm A tornado and storm B episode of heavy wind damage both occurred around 1405 to 1410 EST. Some 10 to 15 minutes earlier, a relatively undisturbed low-level PSI pattern was shown (Figure 9), but a minute later with the antenna elevated  $7^{\circ}$  there was a broad area of shear covering parts of storms A and B (Figure 10) at heights of about 5 and 3 km, respectively, in contrast to the more regular pattern of storm C. A few minutes later with antenna elevation  $2^{\circ}$ , a confused shear line just under 2 km in the incipient tornado of storm A was shown and sharp wiggles at the 1-km level in a couple of the arcs of storm B (Figure 11). However, storm C, which did not release severe surface gusts until more than an hour later, still displayed a smooth arc pattern.

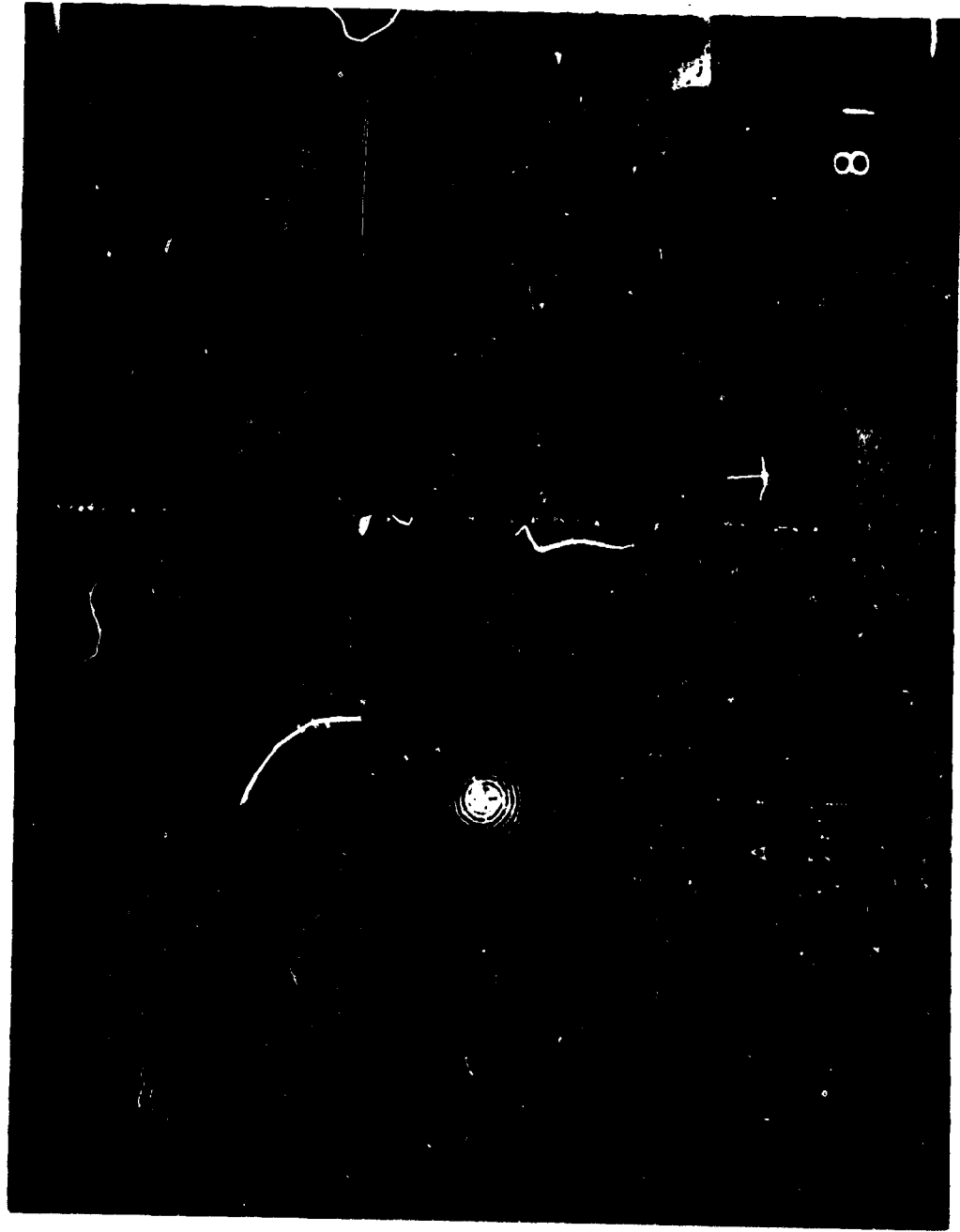


Figure 9. Photograph of PSI Display on 9 August 1968(0° Antenna Elevation, 1352 EST). Letters A, B, C, and D designate severe thunderstorms as described. All the remaining figures were photographed on the same date



Figure 10. PSI Pattern in Storms A, B, and C ( $7^{\circ}$  Elevation Angle, 1353 EST). Note irregularities in PSI arcs in storms A and B

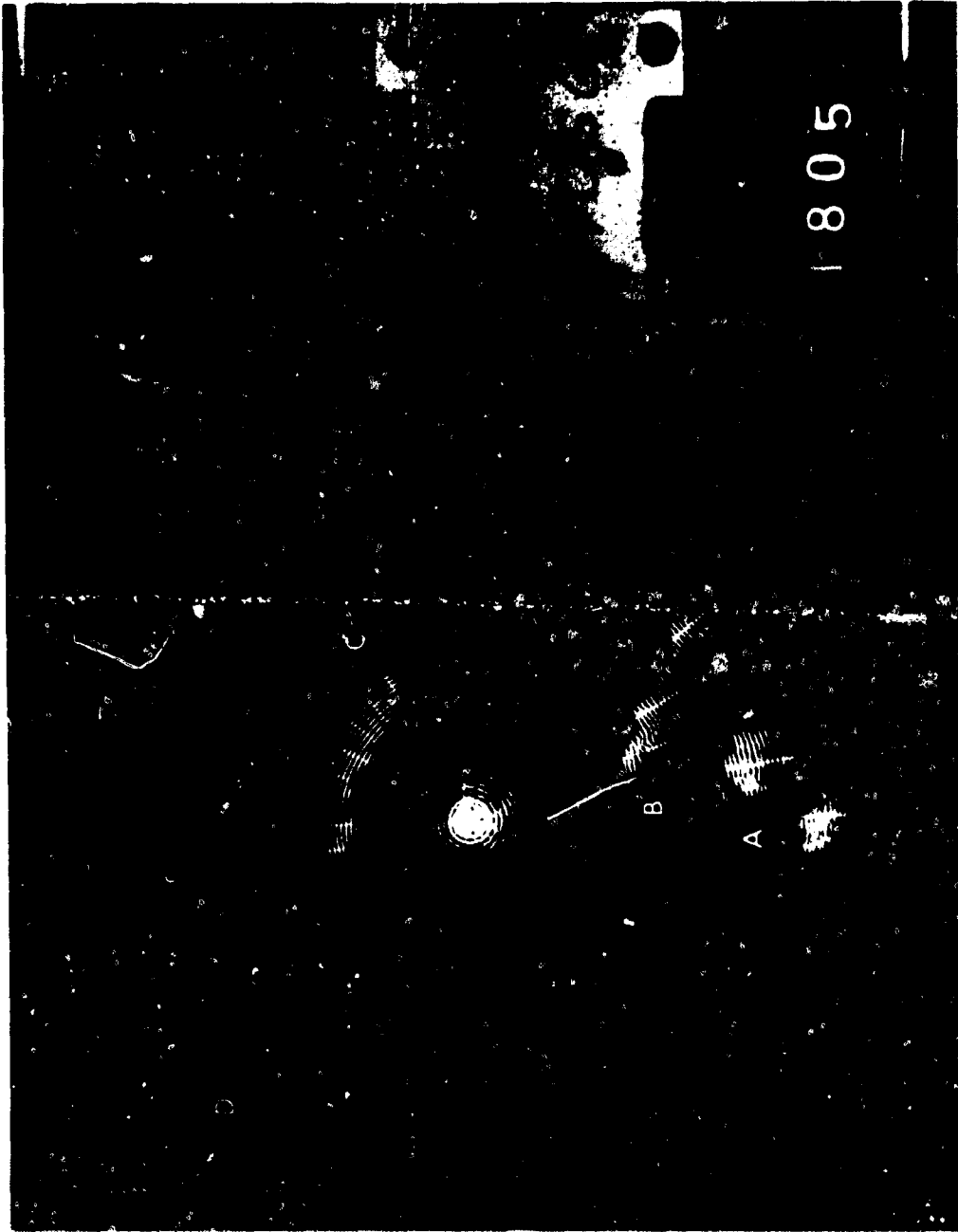


Figure 11. PSI Pattern in Storms A, B, C, and D ( $2^{\circ}$  Elevation Angle, 1357 EST)

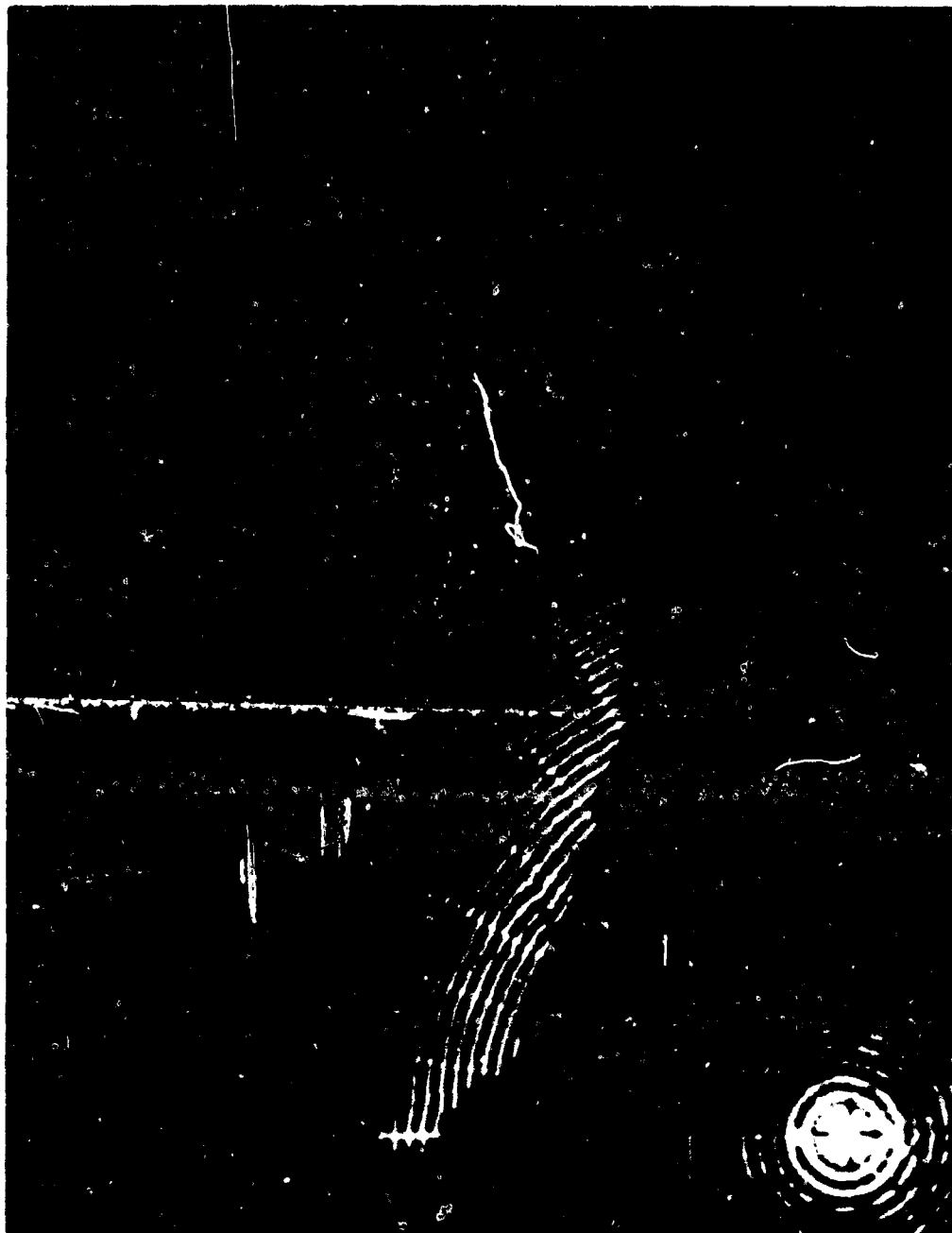


Figure 12. Detail of PSI Pattern in Storm C ( $4^{\circ}$  Elevation Angle, 1411 EST). Arrow points to characteristic cyclonic vortex pattern, similar to the sketch in Figure 7



Figure 13. Detail of PSI Pattern in Storm D (9° Elevation Angle, 1607 EST). Arrow points to echo hole around which the arcs curve in a manner suggestive of cyclonic vorticity

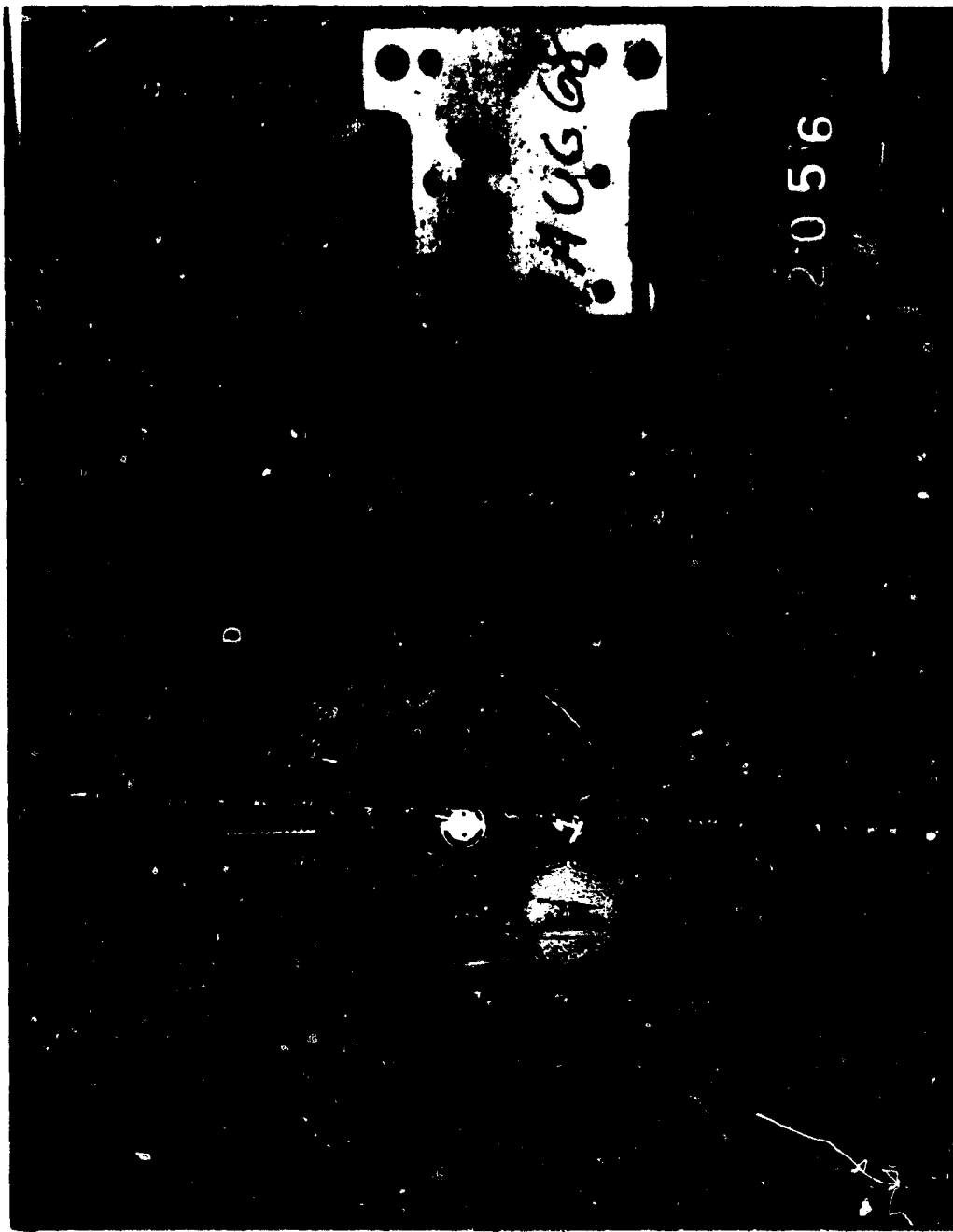


Figure 14. Contrast in PSI Pattern of Storm D, North of Radar, and Anvil of Another Storm South of Radar (22° elevation angle, 1551 EST)

A PSI pattern suggestive of a cyclonic vortex, as sketched in Figure 7, appeared aloft in storm C about an hour earlier, causing severe wind damage, and persisting for most of this period. Figure 12 shows detail of the PSI pattern of storm C, elevation angle  $4^{\circ}$ , when the vortex configuration first appeared in the 1 to 2-km height level. Frequently the indicated vortex encircled an echo-free hole. Storm D also displayed a vortex-type PSI pattern around an echo-free hole which at times extended well above 4 km, for about half an hour before 2-inch hailstones fell on the ground; see, for example, Figure 13, elevation  $9^{\circ}$ , showing a hole at 3.5 km. A careful tracing of the arc continuity across the hole, especially in its southern part, reveals an arc pattern which moves toward the radar with clockwise change of azimuth, suggesting cyclonic vorticity in the vicinity of the hole. Note also the very thick arcs near the hole, possibly indicating hazardous turbulence. At lower altitudes the arcs were more smooth and the hole opened up, revealing the hook echo sometimes observed with tornadoes (Stout and Huff, 1953). However, no tornado ever touched ground from this storm.

A striking contrast between the shear in two echoes is provided by Figure 14, taken at  $22^{\circ}$  elevation. The echo to the south, extending up to about 9 km in height, shows very little if any shear in its PSI pattern. On the other hand, the one north of the radar, which has a top at about 13 km, has a very disturbed PSI pattern over much of its area, indicative of strong shear. If a Doppler radar with PSI display were available to an aircraft controller at a terminal, aircraft could be warned against entering the northern echo which would very likely be uncomfortable, if not dangerous, to penetrate.

In summary, three applications of the PSI display are suggested by the observations of the severe storms of 9 August 1968. First, the appearance of strong wind shear aloft may provide warnings of 15 minutes or more of the occurrence of large hail and tornadoes or other damaging winds at the ground. Of course, many more cases must be studied to define the limits of reliability of this method for warning of severe thunderstorm hazards. The second application is real-time identification of storms, or portions of storms, in which strong wind shear and turbulence would adversely affect the safety of penetrating aircraft. Third, the PSI display offers an opportunity for study of airflow throughout the depth of thunderstorms, a study inspired by the appearance in two storms of patterns suggestive of vortices.

## 5. DIRECTION OF FUTURE IMPROVEMENTS OF THE PSI TECHNIQUE

The Plan Shear Indicator is currently in an early stage of development. This technique, illustrated by the examples selected for Figures 8 through 14, has been demonstrated as a valuable operational aid for ground-based Doppler radar. However, these examples also suggest possibilities for a number of improvements.

One helpful change would be a clarification of the display in regions where the arcs are so broad that they appear to merge, as shown, for

instance, in the area south of the echo hole in Figure 13. This could be accomplished by inserting a peak detector between the CMF and the indicator, so that only a narrow signal centered around the peak power of the velocity spectrum would be recorded. Evaluation of shear would be easier with uniformly narrow PSI arcs. The clarification would carry with it a built-in disadvantage, however, because the operator would lose the ability to recognize the broadening of arcs, a characteristic function of small-scale turbulence. Perhaps the best solution would be an option either to insert or to bypass the peak detector.

Quantitative measurement of tangential (or radial) shear would be another useful improvement. This might be accomplished by a scheme for blanking out any arc segments which indicate shear values below a preselected variable threshold. Any echoes which remained on the display would then reveal only those regions with shear in excess of the threshold.

An increase in maximum unambiguous velocity would be desirable, in order to eliminate or at least reduce velocity foldover in storms that feature unusually high wind speeds. This would provide more certain identification and much easier measurement of tornadoes and other damaging winds on a scale that can be resolved by the radar. Flexibility of the pulse repetition frequency (PRF) of the radar would produce the desired result, but this cannot be done conveniently with the present coherent memory filter. However, the PSI display may incorporate PRF flexibility in the near future, because of recent developments in spectral analysis by fast Fourier transformation with digital techniques.

Finally, adaptation of the PSI display to airborne radar may be considered. Here the questions of economy, weight, and space are basic. However, the operational advantage may be worth the cost in certain applications. For example, pilots of subsonic transports may desire increased assurance of passenger comfort during penetration of clouds outside the range of terminal-based radar control.

Airborne display of PSI data would be most useful in providing information on wind shear within a relatively narrow sector centered around the aircraft heading. The component of wind observed in this manner would be directed along the length of the aircraft. However, airflow continuity in an essentially incompressible atmosphere requires that a strong shear vector in one direction be compensated by comparable magnitudes of shear in the plane normal to this direction. Therefore, observation of intense wind shear along the aircraft heading is an indication of the more dangerous lateral shear components in the same location.

A complete azimuthal scan of the Doppler radar antenna from a rapidly moving aircraft would be confused by a multiplicity of velocity ambiguities, since aircraft speeds may be an order of magnitude higher than the maximum unambiguous velocity of the radar. This problem can be eliminated, however, by restricting the antenna beam motion to a sufficiently small scan angle on either side of the aircraft heading. If the aircraft speed is a factor  $s$  times  $v_{max}$ , then we can solve trigonometrically for the antenna scan angle  $\pm \beta$  within which the component of aircraft speed varies by no more than  $v_{max}$ :

$$\cos \beta = 1 - 1/s .$$

(9)

If an airplane speed is 500 kts, or about  $250 \text{ m sec}^{-1}$ , and the radar  $v_{\text{max}}$  is  $25 \text{ m sec}^{-1}$ ,  $s = 10$  and the solution of Eq. (9) shows that the antenna beam must scan within  $\pm 26^\circ$  of the aircraft heading. This restriction is not at all unreasonable for avoidance of dangerous PSI patterns.

It is noteworthy that airborne Doppler radar cannot measure wind speeds directly in precipitation or detectable clouds, because the maximum unambiguous velocity of the radar relative to the air is exceeded by an unknown multiple. However, by working within the limitations specified by Eq. (9), wind shear components may be measured from an aircraft with no more difficulty than from a comparable ground-based radar. After all, it is wind variability or shear, not the magnitude of the wind, which gives the bumpy ride.

#### ACKNOWLEDGMENTS

We are especially grateful for this opportunity to express our appreciation to Dr. Kenneth R. Hardy, Chief, Weather Radar Branch of the Meteorology Laboratory of AFCRL. Dr. Hardy's encouragement of the development of the Plan Shear Indicator and his many valuable suggestions offered during the course of our study were vital contributions to this work. We are also pleased to acknowledge assistance from other members of the Weather Radar Branch, particularly, Mr. Albert C. Chmela and Mr. Michael J. Kraus for their alert, competent job of data acquisition and Mr. Claude R. Landry for careful photographic processing. We also thank Dr. Morton L. Barad, Director, Meteorology Laboratory, for his helpful criticism of our manuscript.

#### REFERENCES

- Armstrong, G. M. and Donaldson, R. J., Jr. (1968) A convenient indicator of tangential shear in radial velocity, Proc. 13th Radar Meteorology Conf., Am. Meteorol. Soc., Boston, 50-53. In this paper "PVI" was erroneously used in place of the more appropriate "PSI."
- Atlas, D. (1963) Radar analysis of severe storms, Meteorol. Monographs 5:177-220.
- Bickel, H., Brookner, E., Weiss, M., and Vogel, R. (1959) Performance characteristics of the coherent memory filter, Proc. Fifth Annual Radar Symposium, Univ. Michigan. (Secret)
- Chimera, A. J. (1960) Meteorological radar echo study, Final Report (Appendix C), Contract No. AF 33(616)-6352, Cornell Aeronaut. Lab., Buffalo, New York.

Donaldson, R. J., Jr. and Wexler, R. (1969) Flight hazards in thunderstorms determined by Doppler velocity variance, J. Appl. Meteorol., Vol. 7, (to be published).

Groginsky, H. L. (1965) The coherent memory filter, Electronic Progress, IX, (No. 3):7-13. Copies available on request from the author, Raytheon Company, Wayland, Massachusetts, 01778.

Lhermitte, R. M. (1964) Doppler radars as severe storm sensors, Bull. Am. Meteorol. Soc. 45:587-596.

Smith, R. L., and Holmes, D. W. (1961) Use of Doppler radar in meteorological observations, Mon. Weather Rev. 89:1-7.

Stout, G. E., and Huff, F. A. (1953) Radar records Illinois tornado-genesis, Bull. Am. Meteorol. Soc. 34:281-284.

Figure 1. Simplified Block Diagram of the Coherent Memory Filter

Figure 2a. Typical "A" Scope Display of Radar Video

Figure 2b. Corresponding Display of Coherent Memory Filter Output Video. Note the velocity interval of  $0 - 25 \text{ m sec}^{-1}$  every  $5.7 \mu\text{sec}$ . Fixed targets appear at zero velocity while moving targets appear somewhere in the velocity interval depending upon their radial velocity component

Figure 3. Plot of the Hamming Function. This is used to weight the relative power of successive circulations of the returned Doppler signal in the CMF delay line

Figure 4. PSI Display for Stationary Targets (left) and a Moving Target (right). The moving target is located at the same distance from the radar as the nearest stationary target, but is displaced from it on the PSI display by an increment which depends on its velocity

Figure 5. Schematic PSI Pattern of a Wind Shift Line (indicated by light dashed curve) Which Might Accompany a Frontal Passage. PSI arcs are indicated by thick lines

Figure 6. Schematic PSI Pattern for a Sink, or Convergent Flow. Maximum convergence is located at the center of the pattern where arc spacing is greatest. Arrows represent wind vectors; PSI arcs are indicated by thick lines

Figure 7. Schematic PSI Pattern for a Cyclonic Vortex. Maximum vorticity is denoted by maximum arc slope, in the center of the sketch. PSI arcs are indicated by thick lines. Arrows represent wind vectors

Figure 8. Photograph of PSI Display on 19 July 1968 in a Band of Small Showers. Antenna elevation angle is  $0^\circ$ . Circles near the center and a few nearby circular arcs are signals from fixed ground targets. This photograph and all of the succeeding ones (Figs. 9 - 14) were taken from the AFCRL meteorological radar site at Sudbury, Mass., and show north at the top of the picture with 5-mile range markers in an eastern sector

Figure 9. Photograph of PSI Display on 9 August 1968 ( $0^\circ$  antenna elevation, 1352 EST). Letters A, B, C, and D designate severe thunderstorms as described. All the remaining figures were photographed on the same date

Figure 10. PSI Pattern in Storms A, B, and C ( $7^\circ$  elevation angle, 1353 EST). Note irregularities in PSI arcs in Storms A and B

Figure 11. PSI Pattern in Storms A, B, C, and D ( $2^\circ$  elevation angle, 1357 EST)

Figure 12. Detail of PSI Pattern in Storm C ( $4^\circ$  elevation angle, 1411 EST). Arrow points to characteristic cyclonic vortex pattern, similar to the sketch in Fig. 7

Figure 13. Detail of PSI Pattern in Storm D ( $9^{\circ}$  elevation angle, 1607 EST). Arrow points to echo hole around which the arcs curve in a manner suggestive of cyclonic vorticity

Figure 14. Contrast in PSI Pattern of Storm D, North of Radar, and Anvil of Another Storm South of Radar ( $22^{\circ}$  elevation angle, 1551 EST)

STRESS CORROSION CRACKING OF 6-4 TITANIUM ALLOY

Major William E. Craven

Metallurgy and Ceramics Research Laboratory

Aerospace Research Laboratories

Wright-Patterson AFB, Ohio

## STRESS CORROSION CRACKING OF 6-4 TITANIUM ALLOY

by

Major William E. Craven  
Metallurgy and Ceramics Research Laboratory  
Aerospace Research Laboratories  
Wright-Patterson AFB, Ohio 45433

### ABSTRACT

Stress corrosion cracking is the most insidious and undoubtedly the most important corrosion problem facing the Air Force today. This results from the rapid onset, the difficulty of its detection, and the cataclysmic effects of this form of corrosion. To provide insight into the mechanisms involved in the initiation of the cracking process, the regeneration of the surface layers on Titanium 6Al-4V was studied potentiometrically. A small portion of these layers were removed by scratching the surface with a diamond stylus. The potentials exhibited during the regrowth of the surface layers indicated that the passive film regrowth was extremely rapid while the adsorbed layer regenerated at a much slower rate, exhibiting an exponentially decaying return to quasi-equilibrium potentials. The exponential constants characterizing these potentials which were indicative of the regeneration rate of the adsorbed surface layer, were determined over a period of time ranging from first immersion in the corrosive medium until near the period of crack initiation. The regrowth pattern was that of greater sluggishness as time went on, indicating that the surface chemistry was changing as the conditions approached those needed to support crack initiation. Future experimentation was suggested to establish the exact correlation between the surface layer recovery coefficient and the time of crack initiation. Also suggested were modifications to the experimental procedures to enable the quantitative study of the passive film growth rate.

## STRESS CORROSION CRACKING OF 6-4 TITANIUM ALLOY

Major William E. Craven  
Metallurgy and Ceramics Research Laboratory  
Aerospace Research Laboratories  
Wright-Patterson AFB, Ohio 45433

### INTRODUCTION

Stress corrosion cracking is the most insidious and undoubtedly the most important corrosion problem facing the Air Force today. A cataclysmic disaster such as total engine failure or collapse of a wing during flight can result from a tiny crack propagating in a matter of a few hours through a structure whose surface is shiny and bright and displays no trace of corrosion products. Virtually every aircraft in the Air Force inventory has had some problem involving stress corrosion cracking. Twenty percent of one type aircraft were recently found to have stress corrosion cracks in the aft wing spar after less than fifty hours of flight time. This problem was alleviated prior to any accident attributable to this cause, but the potential for disaster is readily apparent.

Aluminum is not the only metal so affected. Titanium, the much-touted wonder metal, has lost much of its figurative luster as a result of its stress-corrosion susceptibility. However, because of its low density and fine mechanical properties, titanium is still used extensively in our aircraft today, and most of our supersonic aircraft of the future, including the SST, will be essentially all titanium. Thus an understanding of the casual relationships and failure mechanisms involved in this phenomenon is most germane to the Air Force Mission.

### DISCUSSION

Titanium, like aluminum, is a very reactive metal which would rapidly corrode if it were not for the passive protective film which forms on its surface. This film is not stable chemically in all environments. Fortunately, due to the pioneering work of Marcel Pourbaix using thermodynamic considerations, the aqueous environments which affect this metal have been well tabulated. Figure 1a. illustrates the regions of pH and impressed electrical potential where titanium will either be immune to simple aqueous attack or will form the stable protective passive film. Likewise auspicious is the fact that the passive region encompasses the region of neutral pH wherein most water such as rain or ordinary tap-water lies. Thus titanium in the pure state should be

quite resistant to corrosion in the environments it is most likely to encounter. However, to realize the full potential of this metal it must be alloyed with other metals, each of which also have their stable and reactive regions in the aqueous environment. Aluminum, up to the present time, has been the major alloying constituent for titanium, it being present at six percent along with four percent vanadium in the most useful aircraft alloy: 6-4 Titanium. Thus, for the aluminum alloys, one must examine the Pourbaix Diagram (4) for aluminum as well as for titanium. Figure 1b. shows the corrosive, immune, and passive regions for aluminum. Similarly, Figure 1c. shows these same areas for vanadium, which must be considered when the alloy also contains this third element. It is possible that where one metal is passive or immune, another in the alloy is subject to corrosion. This can result in the selective leaching of that element, resulting in the physical and chemical destruction of the alloy. Superimposing the Pourbaix Diagrams for titanium, aluminum, and vanadium as in Figure 1d., one can see that there are regions of common immunity and passivity for all three elements, but the passive region is much more restricted after the addition of vanadium. This may give a clue why the alloy is subject to stress corrosion cracking in certain environments. However, before any conclusions can be reached one must consider the kinetics of the corrosive reactions. These reaction kinetics are highly dependent upon the adsorbed molecules on the surface of the metal and also upon the nature of the passive film which in reality is the surface of the metal. It was the purpose of this work to examine this region by removing a portion of the surface layers through the use of a diamond stylus and trace the regrowth of the films potentiometrically. Prior to the actual experimentation, it was felt that the passive metallic film would be the major contributor to the observed potentials, but during the course of the experiment, it was found that the passive film rebuilt much more rapidly than the instrumentation could detect, and that the adsorbed surface layer did indeed alter the apparent potential of the corroding metal to a considerable degree.

It is generally accepted that for stress corrosion cracking to occur there must exist three simultaneous conditions: the susceptible alloy must be in a specific environment under a load of sufficient stress. Chloride environments are known to produce stress corrosion in both aluminum and titanium alloys. Not only is chloride present in the salt of all marine environments, it is most difficult to avoid in any exposed area. Thus the choice of chloride in a medium known to produce stress corrosion cracking in 6-4 titanium would not only provide the conditions necessary for the study of the initiation of the cracking process, but also might enable the results of the study to be applied directly to the realistic problems of stress corrosion encountered by the Air Force.

## EXPERIMENTAL PROCEDURE

A sheet of Titanium 6Al-4V from Reactive Metals, Inc. which had been annealed at 1450 °F for 3 hours, water quenched, reheated to 1100 °F for 5 hours and then air cooled (all under gettered Argon), was sheared into strips, 0.25 inch by 2.05 inches. Both surfaces were finished on 600 grit silicon carbide paper and the specimen mounted in the stressing jig shown in Figure 2. This buckling device as described by Weber and Davis (9) induces a tensile stress level in the outer surface which is a function of its coordinates, thus varying in magnitude along the length of the sample. The differential equation describing this system was first derived by Euler and resulted in an equation of the form:

$$\frac{\frac{d^2y}{dx^2}}{\left[1 + \left(\frac{dy}{dx}\right)^2\right]^{3/2}} + \frac{P}{EI}y = 0 \quad (1)$$

where E is the elastic modulus of the material and I is the moment of inertia of the cross sectional area, P being the restoring force.

From this equation can be derived another equation which describes the outer fiber stress at any y coordinate:

$$S = \frac{q^2 E t}{3D^2 u^2} (6y - t \cos \phi) \quad (2)$$

where t is the specimen thickness

u is a dimensionless parameter describing the ratio of the radius of curvature at y to the diameter of arc.

q is another dimensionless parameter related to u by means of a function involving elliptic integrals and tabulated in this reference.

$\phi$  is the slope angle at the coordinate y

The final length of the specimen was adjusted so as to produce a stress of 90 ksi in the outer fibers as calculated by equation (2).

The test jig also provided space to accommodate an electrical connector consisting of the same alloy, finished in a similar manner to the actual test specimen. This connector completed the circuit to the recording electrometer which recorded the potential of the specimen in relation to a standard calomel electrode immersed in saturated KCl solution which in turn was connected through a salt bridge to the corroding solution. This setup is illustrated in Figure 3.

For this series of tests the corroding medium was chosen to be 99% methanol saturated with analytical grade NaCl. At the temperature of the tests, 18°C, the concentration of salt is 8.2 grams/liter.

The procedure was to make all electrical connections and then immerse the entire test jig in the saturated methanol, recording all of the transient potentials developed while the stressed titanium specimen arrived at equilibrium with the test solution. With the alloy under discussion, the initial potential that could be recorded was close to -310 mV referenced to the standard hydrogen electrode (SHE). Within a minute the potential would rise to just above -100 mV (SHE), i. e., between -85 mV and -95 mV, at which time a temporary plateau was established. Over a period of several hours this plateau would be gradually reduced to about -50 mV (SHE). The procedure for the first few specimen runs was simply to continue the monitoring of the freely corroding potentials described above until the specimen failed due to stress corrosion cracking. Once this base-line data had been established, future specimens would be scratched in situ by a diamond stylus, the potentials developed during and after scratching recorded and subsequently analyzed to provide insight into the processes occurring during the actual cracking phase.

The diamond stylus used during this portion of the experiment was fashioned out of a 0.0007 inch diameter phonograph needle mounted in a lucite holder in the shape of a pencil. Cost and availability were not the only factors considered in arriving at the design. The hard round diamond tip would produce a rounded groove of specific dimensions in the surface of the specimen. The non-metallic nature of the tip would preclude charging of the specimen as a result of dissimilar metal contact, and it was not likely that stylus fragments would be left behind to contaminate either the specimen surface or the corroding medium. The rounded groove was considered essential since crevice corrosion was definitely to be avoided.

Subsequent to the actual corrosion and cracking phase of this experiment, photomicrographs and electron photomicrographs of surface replicas were to be made of both the exposed and fractured surfaces. Chemical analysis of either the spent solution or adherant corrosion products was not anticipated during this first study.

## RESULTS

Figure 4 illustrates the typical potential-time curve obtained in this study. The potential gradually increases until just prior to the onset of cracking at which time the trend drastically reverses and more negative potentials are developed up to the point that failure of the specimen occurs. Subsequent to failure the potential rapidly recovers

to a value near that achieved prior to cracking, and then the potential continues the gradual trend toward a more positive value.

The results of the potential recovery after scratching of the specimen surface are shown for a typical case in Figure 5. The exponential recovery curves labeled A through E are the result of scratches imposed upon a single sample at different times after initial immersion of the sample in the corroding medium. These curves can be accurately described by an exponential equation of the form:

$$E = A - Be^{-CT} \quad (3)$$

- where E is the potential of the specimen at time, T, in minutes.
- A is an arbitrary constant describing the asymptotic value of the curve.
- B is an arbitrary constant describing the ordinate intercept of the curve.
- C is the pertinent constant describing the slope of the curve, thus describing the rate of recovery of the potential.

Neither constants A nor B are pertinent to the present discussion, A being dependent upon the potential reference system used, and B being incapable of determination by the slowly responding experimental apparatus. The constant, C, however, is the point of the whole experiment. As time progressed nearer to the point of stress cracking of the specimen, the recovery times of the freely corroding potential became progressively longer. This effect is summarized below in Table I.

TABLE I

RECOVERY COEFFICIENT VERSUS TIME

<u>Curve</u>	<u>Recovery Coefficient, C</u>	<u>Time From Specimen Immersion</u>
A	0.698	6 Minutes
B	0.655	1 Hour
C	0.512	3 Hours
D	0.225	4 Hours
E	0.172	6 Hours

An extremely important result of this experiment came from a rather casual observation during the course of the scratching operation. First it was noticed that a single scratch would only produce a decrease in potential of about 20 mV, a second scratch another 20 mV and so on until with a large number of immediately successive scratches a limiting value was reached, approximately -310 mV (SHE). Not only was this the same potential usually found when the specimen was first immersed, it was also approximately the same value that the specimen exhibited at the moment of failure by stress corrosion cracking. Likewise intriguing, was the fact that under no circumstances could anywhere near the equilibrium potential of -1300 mV (SHE) which metallic titanium is capable of developing in water be found. Similarly, it was noticed that agitation of the corroding solution would produce a definite reduction in potential. Violent agitation was then attempted and a potential near -300 mV (SHE) could be obtained. This same potential could be achieved by rubbing the specimen with the back end of the lucite pencil which is definitely not hard enough to produce a scratch and expose bare metal. What suddenly became apparent was that this procedure yielded information concerning the adsorbed surface layer of solute molecules rather than the passive film of the metallic surface. The passive film must form so rapidly that potentials from the bare metal are never observed by the instrumentation of this procedure. Also apparent is the intimate effect of the surface layer upon the stress corrosion processes.

Photomicrographs in Figures 6a. and 6b. show the apparent stemming of the advancing crack front by the dispersed beta phase. Notice also the crack developing ahead of what appears to be the contiguous crack tip.

The electron microphotographs of the carbon shadowed replicas of the internal surface of the stress corrosion crack were included primarily for those more experienced in Fractography than the Author. The cleavage fan in the lower left corner of Figure 7a. demonstrates that this failure mechanism adds to the damage of corrosion. Figures 7b. and 7c., two different magnifications of the same area, are rather interesting in that they show leaves of corrosion product which have apparently grown along cleavage striations. Figure 7d. shows the growth of corrosion products along one side of an abrupt edge.

## DISCUSSION OF RESULTS

The main result of this experiment is the tabulation of the effects of the adsorbed surface layers upon the corrosion potential of Titanium 6Al-4V. The exponential growth rates determined are certainly not inconsistent with the Bockris Devanathan Model of Electrical Double Layers at electrolyte-metal surfaces and actually may provide some information concerning their structure. Definite correlations between

these growth rates and the onset of cracking have not been established, and as yet a definitive experiment has not been devised. However, Table I shows a definite trend which cannot be ignored. To speculate, it does not appear unreasonable that the initiation of the stress corrosion crack may occur once the Recovery Coefficient approaches zero and the adsorbed surface layer is unable to repair itself as rapidly as it is disturbed by the cracking process. Also to be considered is the causal relationship that this degraded surface layer may have upon the crack initiation process itself.

Another result of this experiment is the confirmation of the rapid regrowth of the passive film. The highly sensitive and fairly responsive electrometer used in this experiment gave absolutely no indication of a potential fluctuation. It would be most interesting to repeat these experiments using a high speed oscillograph to record any transient potentials that develop. Not only would this enable one to determine the constant, B, in the exponential growth equation for the adsorbed layer, but also it is quite likely to provide the same information in regards to the repassivation of the metal surface.

#### FUTURE PLANS

Future experimentation will involve potentiostatic dissolution techniques using other alloys of titanium and different corrosive media. A fast response oscilloscope will be used to augment the potentiometric studies. Analysis of the corrosion products precipitated in the crack surfaces will be accomplished through the use of an electron microprobe.

#### ACKNOWLEDGMENTS

The author would like to express his appreciation for the support received from all of the members of the Metallurgy Group of the Aerospace Research Laboratories. Special thanks to Dr. Dale O. Condit for his counsel and to Jack Smith and Darrell Frank for their highly specialized laboratory support throughout the course of this work.

## REFERENCES

1. Fontana, M. G., Corrosion: A Compilation, Columbus: The Press of Hollenback, (1957).
2. Fontana, M. G. and Greene, N. D., Corrosion Engineering, New York McGraw-Hill Book Company, (1967).
3. Logan, H. L., Stress Corrosion of Metals, New York: John Wiley and Sons, Inc., (1966).
4. Pourbaix, M., Atlas of Electrochemical Equilibria in Aqueous Solutions, Oxford: Pergamon Press, (1966).
5. Rapp, R. A. and Staehle, R. W., Fundamentals of Corrosion, New York: American Institute of Chemical Engineers, (1968).
6. Stress-Corrosion Cracking of Titanium, ASTM Special Publication No. 397, Philadelphia: American Society for Testing and Materials, (1966).
7. Stress Corrosion Testing, ASTM Special Publication No. 425, Philadelphia: American Society for Testing and Materials, (1967).
8. Tomashov, N. D., Theory of Corrosion and Protection of Metals, New York: The Macmillan Company, (1966).
9. Weber, K. E. and Davis, A. O., Stress Corrosion of Titanium Alloys Under Simulated Supersonic Flight Conditions, (NASA CR-981) Lockheed-California Company, Burbank, California for Langley Research Center, (1967).

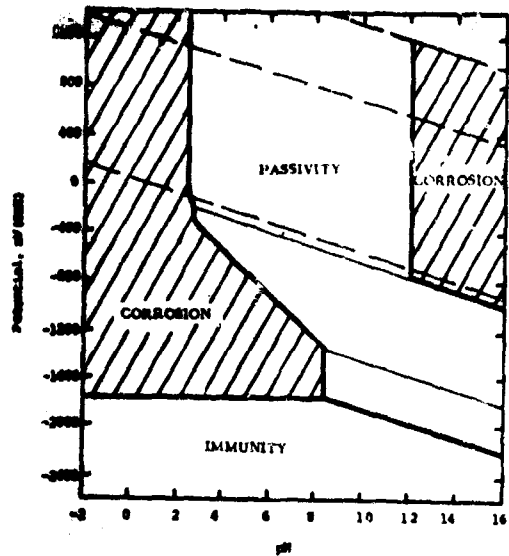


Figure 1a.  
Pourbaix Diagram For Titanium

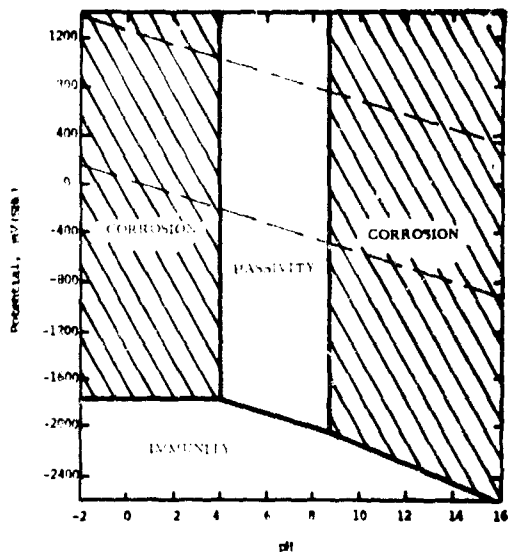


Figure 1b.  
Pourbaix Diagram For Aluminum

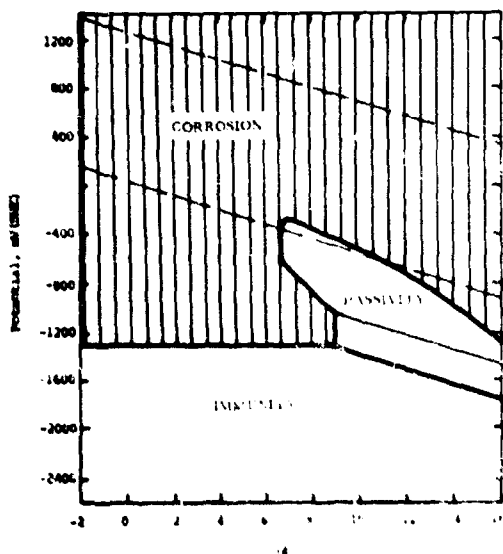


Figure 1c.  
Pourbaix Diagram For Vanadium

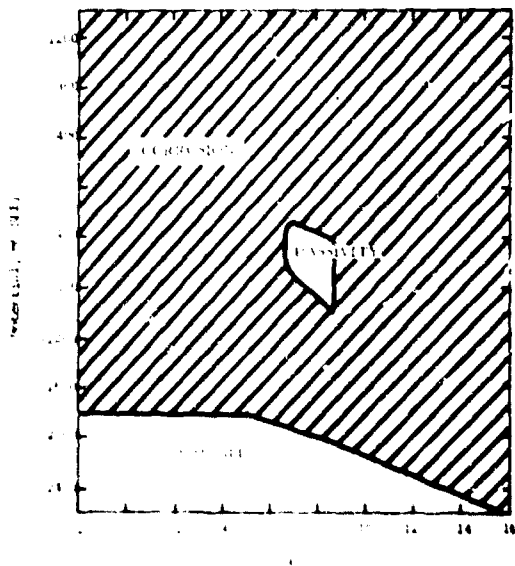


Figure 1d.  
Pourbaix Diagram For Ti-Al-V Alloys

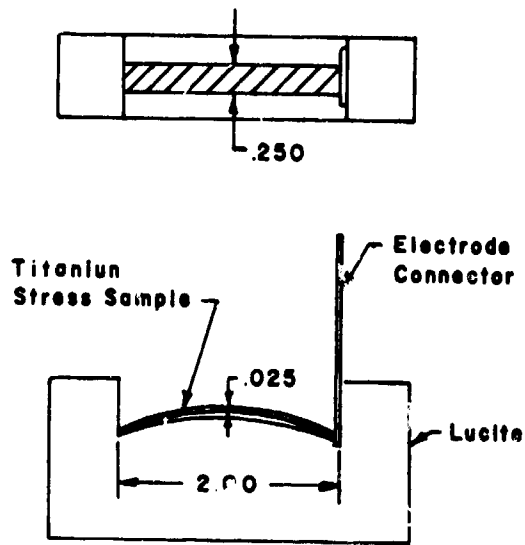


Figure 2.  
Stressing Jig for Corrosion Specimens.

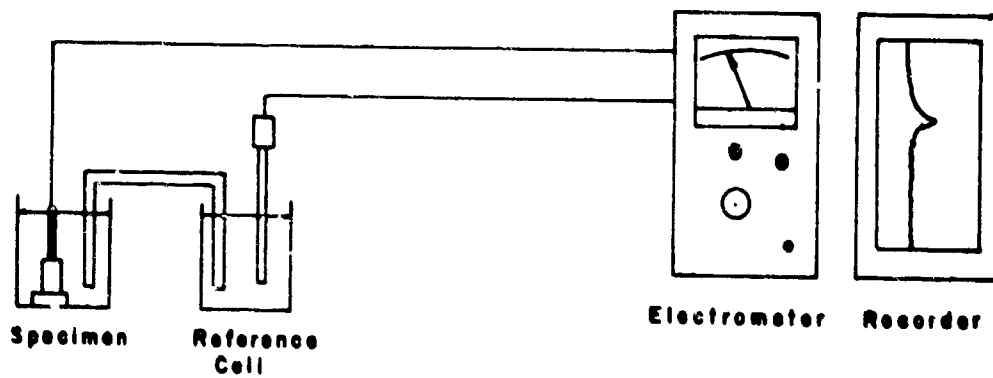


Figure 3.  
Potentiometric Setup

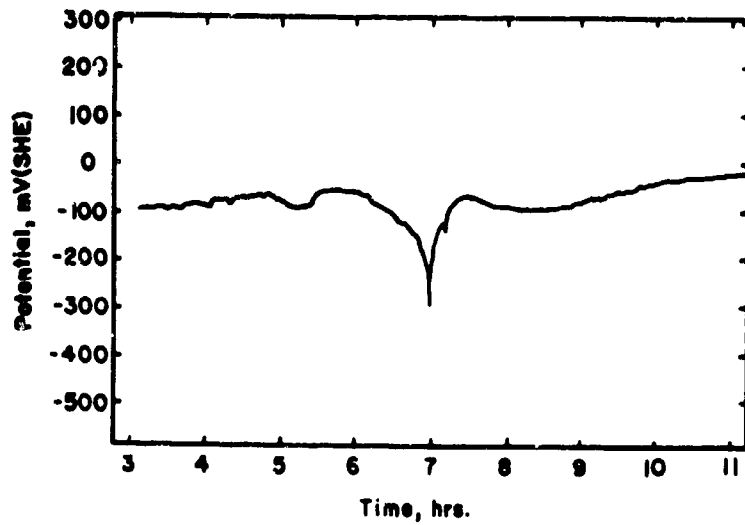


Figure 4.  
Change in Potential of Ti 6Al-4V  
During Stress Corrosion Failure

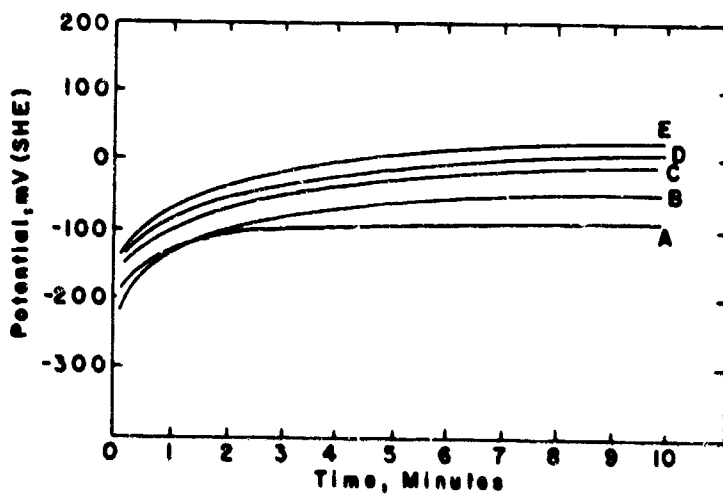


Figure 5.  
Potential Recovery Curves for Ti 6Al-4V  
After Surface Scratch.



Figure 6a.  
Stress Corrosion Crack in Ti 6Al-4V (X 233)

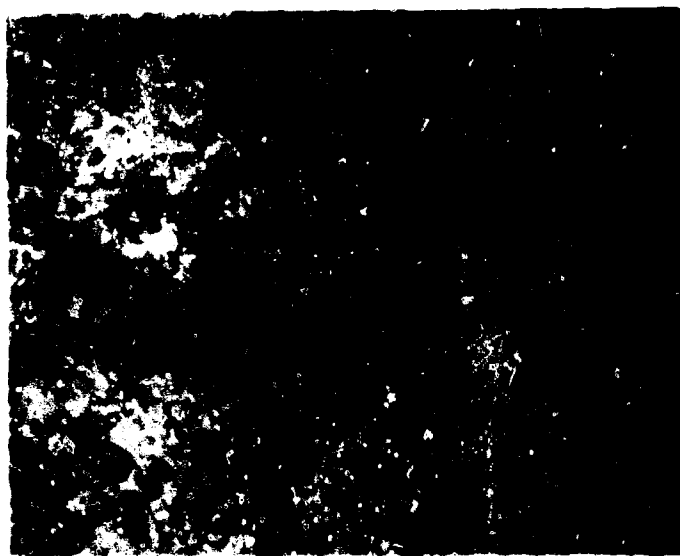


Figure 6b.  
Enlarged View of the Same Area As Above (X 833)

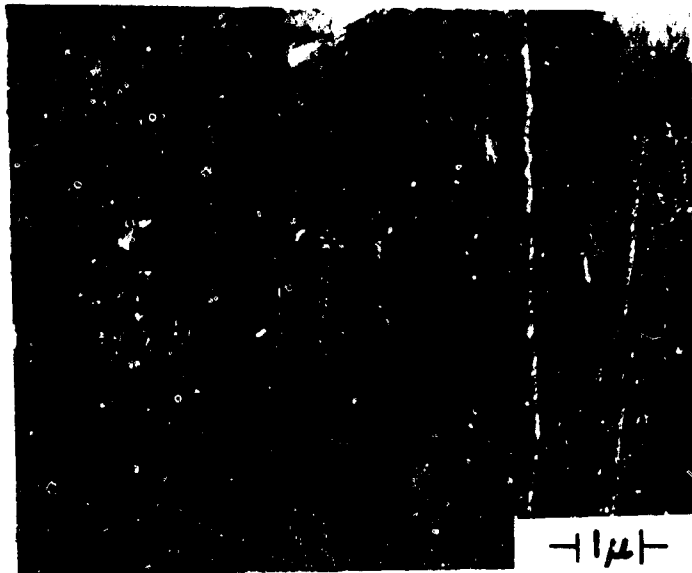


Figure 7a.  
Electron Fractograph of Ti 6Al-4V (X 8750)



Figure 7b.  
Electron Fractograph of Ti 6Al-4V (X 8750)

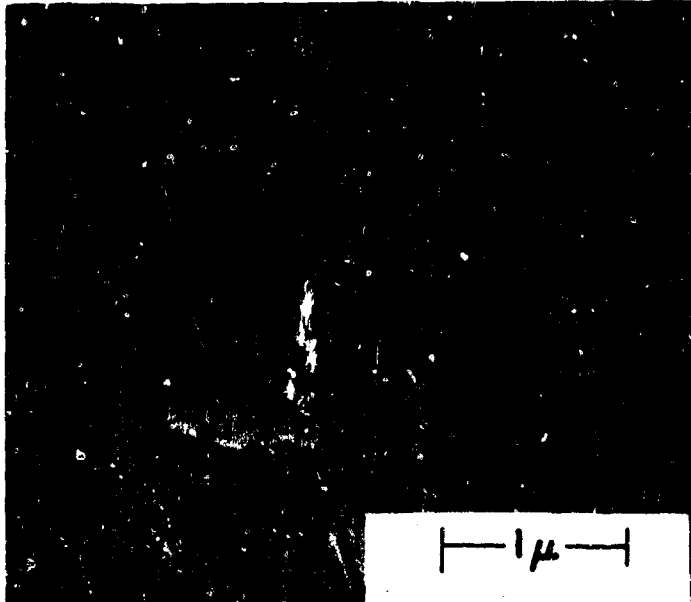


Figure 7c.  
Electron Fractograph of Ti 6Al-4V (X 25, 500)  
(Portion of Fig. 7b.)

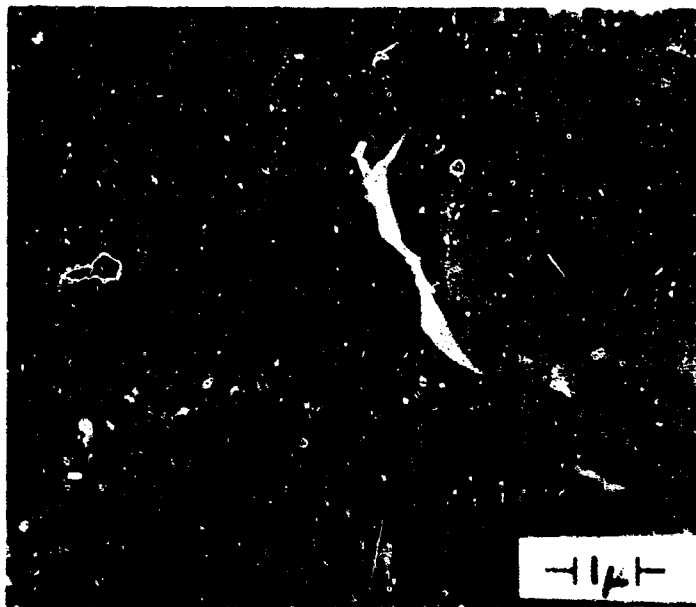


Figure 7d.  
Electron Fractograph of Ti 6Al-4V (X 9750)

**THE SPECTRUM-ANALYSIS RADAR**

**J. L. Poirier**

**Microwave Physics Laboratory**

**Air Force Cambridge Research Laboratories**

**L. G. Hanscom Field, Bedford, Massachusetts**

# THE SPECTRUM-ANALYSIS RADAR

by

J. L. Poirier  
Microwave Physics Laboratory  
Air Force Cambridge Research Laboratories  
L. G. Hanscom Field, Bedford, Massachusetts

## ABSTRACT

The spectrum-analysis radar is a random-signal radar that does not require the complex storage or delaying mechanisms normally associated with radars of this type. Instead, signals are processed through a spectrum analyzer.

In operation, this technique requires only that the target be illuminated by a noise-like signal and that a reference signal (a small part of the transmitted signal) be available. The power spectrum of the sum of the reference and reflected signals is a modulated spectrum. The modulation frequency depends only on the range to the target; its amplitude is proportional to the intensity of the target signal relative to the total received signal. Also, the modulations are coherent even though the illuminating signal is unmodulated noise.

This novel technique of radar-ranging is simple and straightforward. Its uses are manifold: in synthetic aperture applications, when coherent signal-processing is necessary; as a space-docking radar, when near-zero minimum range is necessary; or in interdiction or high-density radar areas, where low mutual interference is necessary.

## 1. INTRODUCTION

The search for techniques that would improve certain operational and physical characteristics of conventional radars has generated a greater interest in random-signal radars. Areas of principal concern are operation in the presence of clutter or other interfering signals, greater use of the target phase information by processing both the amplitude and phase of the return signal, elimination of range and velocity ambiguities, and a reduction in size and complexity.

Although the use of random (noise) signals can improve radar performance, extraction of the range and phase information from the reflected signal is not as direct as in conventional radars. Random-signal radars have traditionally required special processing techniques that are based on the radar-range ambiguity function. This is determined by comparing the received signal with a reference signal in a cross correlator, the reference signal being an arbitrarily delayed portion of the transmitted signal. The radar range is then taken as the delay that is necessary to make the reference signal match the received signal.

The cross correlator is a complex mechanism that in practice often takes the form of a special-purpose digital computer. Processors of this type have a tendency to destroy target phase information.

The spectrum-analysis radar described in this paper needs no cross correlator or delayed reference signal. It processes an unmodulated random illuminating signal, yielding the same range information as a cross correlator but preserving the target phase information.

## 2. OPERATING PRINCIPLES

Although the mathematical analysis that describes the operation of the spectrum-analysis radar is lengthy (a synopsis is indicated in Appendix A), the principles of operation are easy to explain. A random signal is generated by a noise source and transmitted (see Figure 1). A very small part of the transmitted signal is coupled off for the reference signal and applied to one side of the summing tee. The other input to the tee is the received signal. The power spectrum of the resulting sum signal is modulated, a fact that is not altogether obvious. This modulation forms the basis of the spectrum analysis radar.

The modulation comes about because as each component of the transmitted power spectrum propagates out to the target and back again, it is shifted in phase by an amount proportional to its frequency. Now, by definition, the time-averaged amplitude and phase characteristics of any frequency component of a noise signal remain constant. Since the reference signal originated in the transmitted signal it is also a noise signal, and therefore a standard against which to compare the received signal.

The simple addition of the reference and received signals simultaneously yields a measurement of the phase shift undergone by every frequency component as it propagates out to the target and back. As the two superposed spectra go through cycles of constructive and destructive interference, a modulation, or fringe, pattern is set up in the sum spectrum. It should be noted that the presence of these modulations necessarily means that the received and reference signals are completely uncorrelated. It is significant, however, that the frequency difference between nulls in the modulation pattern depends only on the range to the target; the modulation amplitude depends on the relative intensities of

the target and reference signals; and the absolute location of the nulls depends on the total phase shift induced in the transmitted signal by both the range and reflection of the target.

The block diagram of an experimental model that was assembled to demonstrate these principles is shown in Figure 2. The illuminating signal, obtained from a gaseous discharge noise tube and amplified by a traveling-wave-tube (TWT) amplifier, was band-limited (bandwidth of about 12 MHz) and had a center frequency of 2800 MHz. An attenuator in the reference arm maximized the modulation amplitude. Figure 3 shows the spectra obtained. By measuring the frequency difference between the nulls, the range to a target 324 ft away was determined to within 3 ft.

The phase coherence of the modulation nulls was easily demonstrated with the same setup. The upper spectrum in Figure 4 was obtained from a target about 150 ft away. The lower spectrum was obtained from the same target after it had been moved about 1/2 in. The shift in the null location is clearly evident. A change of one-half wavelength ( $\lambda/2$ ) in range moves the null to the adjacent null location. Even with incoherent noise signals, these modulations are completely coherent and can be processed like any other monochromatic signal.

### 3. DISCUSSION

A convenient method for determining the range to a target is to add a second spectrum analyzer to the system and then measure the modulation frequency. The modulation frequency is a linear function of range, and so the horizontal axis of the second spectrum analyzer can be calibrated directly in range like an A scope.

The A-scope display of the one target in Figure 4 is shown in Figure 5(a). If two targets are simultaneously illuminated, then the spectrum modulation will contain two frequency components, one for each of the targets. Such a situation is shown in Figure 5(b), where the targets of Figures 3 and 4 are simultaneously illuminated.

The total range displayed on the A scope would be much greater in practice than our experiments have indicated. The bottom trace in Figure 6, for example, shows how a target located at a range of 3000 ft would look in a range display covering about one mile. The upper trace is a low-dispersion display of the same target.

Under typical operating conditions, the power spectrum modulation frequencies range from about 100 to 10000 Hz. Since this coincides with the audiofrequency range, why not let the ear determine the modulation frequency? In certain applications, the second spectrum analyzer could be replaced by a simple loudspeaker or headphone system, and the human brain could then directly perform part of the signal-processing. The idea was tested experimentally. The presence of a target was disclosed

as a tone whose frequency was proportional to the range of the target. Multiple targets produce multiple tones. The modulation frequencies corresponding to the two targets used in our tests were 100 Hz and 200 Hz respectively. The difference in tones was clearly distinguishable as the antennas were turned from one target to the other.

The coherent nature of the spectral modulation can be directly applied to determine the angular location of a target. Two systems are used. The location of the null pattern of one is found to be displaced from that of the other, the amount of displacement being directly related to the separation between antennas and the angle of arrival of the signal. This is the counterpart of the well-known interferometer used with coherent signals except that the result is an interferogram between the power spectra instead of between the amplitudes of two signals.

An arrangement of two systems could be used for simultaneously determining both range and angular direction of a target. It would not be necessary to operate two systems simultaneously since one system time-shared between two adjacent locations would suffice so long as some kind of storage device could be used to remember the null pattern of one location for later comparison with that of the other. Once the number of space samples is extended from two to many, we are immediately led into application of the spectrum-analysis radar to the synthetic aperture.

#### 4. SUMMARY

The spectrum-analysis radar, a noise radar, determines the range of a target from the frequency of modulation of the power spectrum of the sum of the received and reference signals, and it determines the angle of a target from the location of the modulation nulls. The modulation is coherent, even though the illuminating signal is unmodulated noise. It is therefore possible to use coherent signal-processing techniques while retaining the advantages of using incoherent signals.

One of the advantages of the spectrum-analysis radar is that there is little interaction between it and similar radars, and so several can be used in the same vicinity without undue interference. Another is that since the signal it processes is unmodulated, the conventional spectral signature associated with coherent time-modulated signals is lacking; the radar may therefore be useful in covert applications. Also related to its use of unmodulated signals is its ability to function at near-zero range. This property might make it useful in altimeter or space-docking applications.

The coherent nature of the power-spectrum modulations can be used to determine the angle of arrival of a target signal, thereby fixing the exact location of the target in both range and angle. The modulations can also be processed in synthetic aperture applications.

An interesting characteristic of this radar is that in certain applications much of the signal-processing could be done by ear. The intervention of the human element could lead to significant reductions in size, cost, and weight of a most useful radar system.

## BIBLIOGRAPHY

- Cooper, G. R., and Gassner, R. L. (1966), Analysis of a Wideband Random Signal Radar System, Purdue Rpt No. TR-EE66-9, NSF Contract No. GK-189.
- Craig, S. E., Fishbein, W., and Rittenbach, O. E. (1962), Continuous-wave radar with high resolution and unambiguous velocity determination, IRE Tr. Mil. Electron. 6:153-161.
- Fishbein, W., and Rittenbach, O. E. (1961), Correlation radar using pseudo-random modulations, IRE Interntl Conv. Record (Pt V), pp. 259-277.
- MacPhie, R. W. (1964), A new type of cross-correlation radar system, Paper 11 in Proc. Symp. Signal Processing in Radar and Sonar Directional Systems, Univ. of Birmingham (IERE, Bedford Square, London), pp. 11-1-11-12.
- McGillem, C. D., Cooper, G. R., and Waltman, W. B. (1967), An experimental random signal radar, Proc. Ntl. Electron. Conf., Vol. 23 (Ntl Electron. Conf., Inc., Chicago, Ill.).
- Poirier, J. L. (1967), Random Scattering of Quasi-Monochromatic Radiation in a Long Transmission Line, Rpt. No. AFCRL-67-0353, Air Force Cambridge Research Laboratories, Bedford, Mass. (DDC Rpt No. AD-655789).
- Poirier, J. L. (1968), Quasi-monochromatic scattering and some possible radar applications, Radio Science 3:821-886.
- Rotman, W. (1968), Effects of Signal Bandwidth Upon the Reflections From Randomly Spaced Discontinuities in a Transmission Line, (AFCRL Rpt to be published).

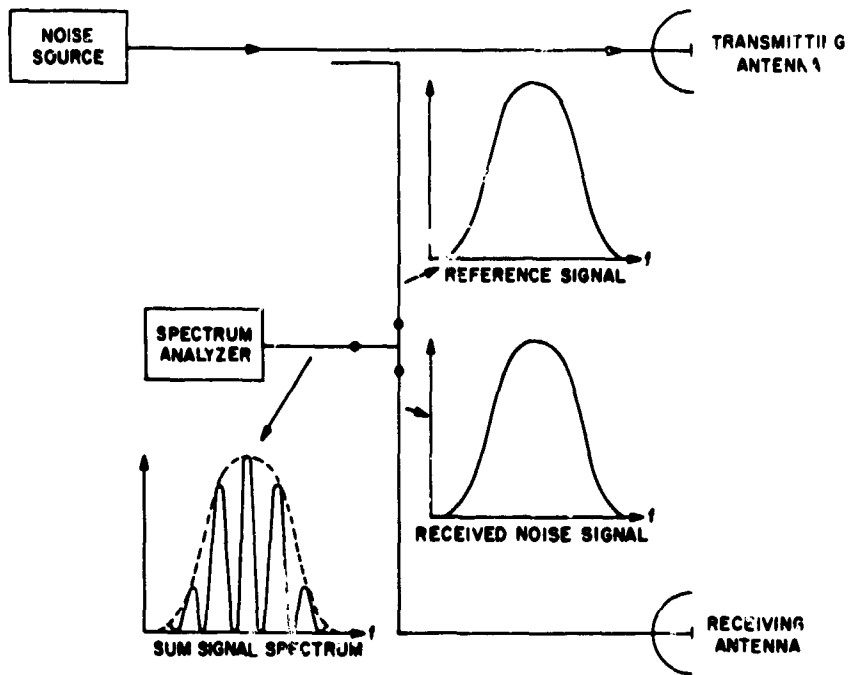


Figure 1. Block Diagram of a Spectrum-Analysis Radar

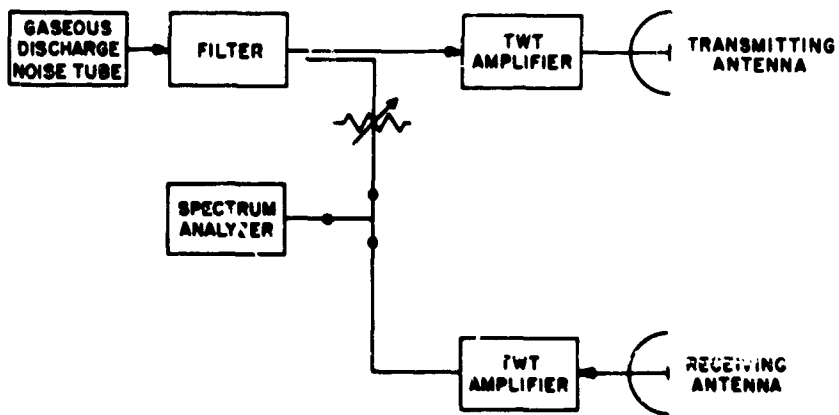
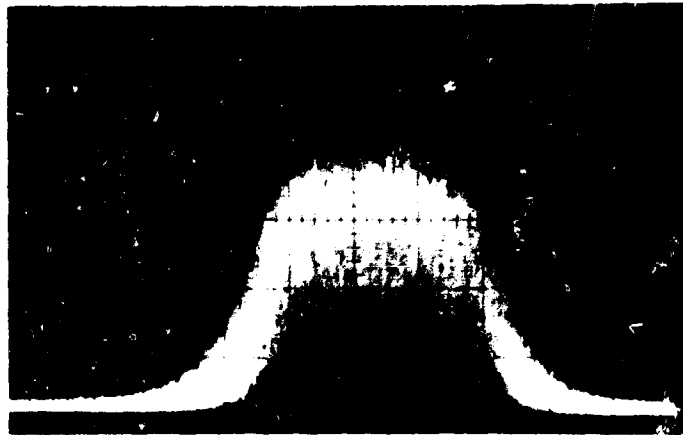
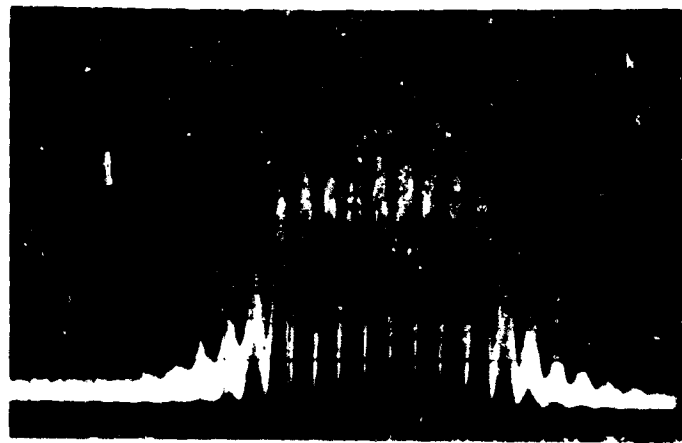


Figure 2. Block Diagram of Experimental Spectrum-Analysis Radar



Frequency →

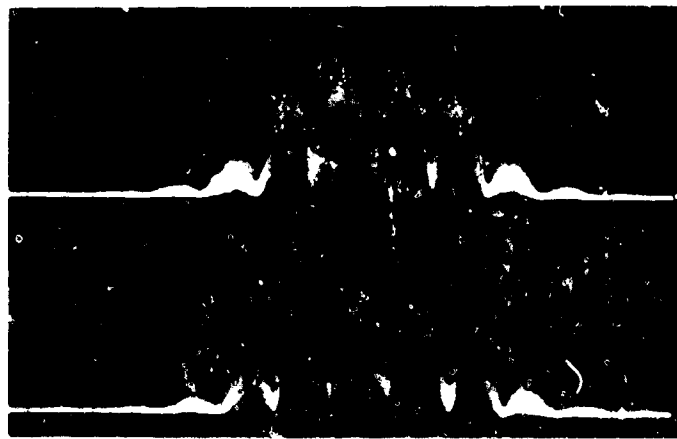
(a)



Frequency →

(b)

Figure 3. Experimental Radar Power Spectra:  
(a) Transmitted Signal; (b) Sum Signal



Frequency →

**Figure 4. Demonstration of the Phase Coherence of Power Spectrum Modulations (the range to the target in the upper and lower traces differs by 1/2 in.)**



Range →

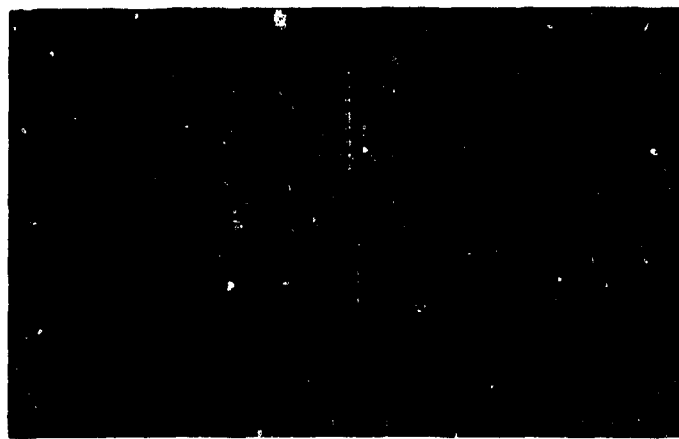
(a)



Range →

(b)

Figure 5. A-Scope Presentation: (a) One Target; (b) Two Targets (dispersion = 25 ft/cm)



Range →

Top trace: low dispersion, 50 ft/cm  
Bottom trace: high dispersion, 500 ft/cm

Figure 6. High- and Low-Dispersion Displays of Same Target

## APPENDIX A

Some of the principal expressions that quantitatively describe the spectrum-analysis radar are stated here without proof. For a model, consider a noise signal whose normalized power spectrum  $\phi^+(f)$  illuminates  $N$  targets, each with a voltage reflection coefficient  $\Gamma_j$ , a phase  $\theta_j$ , and a range  $L_j$ . It is assumed that  $\Gamma_j$  includes range attenuation effects and that  $t_j$  is the total propagation time. The reference signal is the  $j = 1$  term, and  $k$  is a dummy summation index. The modulated power spectrum  $\phi^-(f)$  can then be represented by

$$\phi^-(f) = \phi^+(f) \frac{I^+}{I^-} \sum_{k=1}^N \sum_{j=1}^N \Gamma_k \Gamma_j \cos \left[ 2\pi f \{t_j - t_k\} + \theta_j - \theta_k \right], \quad (1)$$

where  $I^+$  and  $I^-$  are the time-averaged transmitted and received signal intensities. For the case of a single target  $\Gamma_0$ , Eq. (1) can be simplified to

$$\phi^-(f) = \phi^+(f) \left\{ 1 + \frac{2\Gamma_0 \Gamma_r}{\Gamma_0^2 + \Gamma_r^2} \cos \left[ \frac{4\pi f}{c} L_0 + \theta_0 \right] \right\}. \quad (2)$$

From Eq. (2), the range  $L_0$  can be determined by measuring the frequency difference between nulls  $\Delta f_m$ . Thus,

$$L_0 = \frac{c}{2\Delta f_m}. \quad (3)$$

Measuring the absolute location  $f_n$  of a null establishes the phase of the target  $\theta_0$ , which is written:

$$\theta_0 = \left\{ 2n+1 - \frac{2f_n}{\Delta f_m} \right\} \pi, \quad n = 0, \pm 1, \dots \quad (4)$$

The fractional modulation amplitude  $M$  can be used to gauge the size  $\Gamma_0$  of the target by using the relation

$$\Gamma_0 = \left\{ \frac{1 \pm \sqrt{1-M^2}}{M} \right\} \Gamma_r. \quad (5)$$

If it is assumed that  $\phi^+(f)$  is gaussian, with a variance  $\sigma$ , then it can be shown that the range resolution

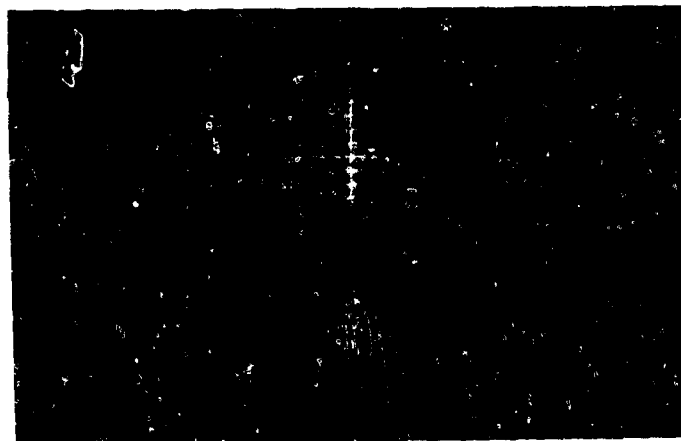
$$\Delta R = \frac{c}{2\pi\sigma} \quad (6)$$

The A scope displays shown in Figure A1 demonstrate the effect of the illuminating signal bandwidth on range resolution. The upper and lower traces show the return from the same target, the only difference being that the bandwidth used for the lower trace is twice that of the upper trace.

The effective modulating frequency  $f'_m$  at the output of the first of the two spectrum analyzers is a function of its sweep speed  $S_s$ , and given by

$$f'_m = \frac{2RS_s}{c} \quad (7)$$

For typical spectrum analyzer sweep speeds,  $f'_m$  is in the audio region.



Range →

Figure A1. Displays Showing Effect of  
Signal Bandwidth on Resolution (bandwidths:  
top = 10 MHz; bottom = 20 MHz)

Figure 1. Block Diagram of a Spectrum-Analysis Radar

Figure 2. Block Diagram of Experimental Spectrum-Analysis Radar

Figure 3. Experimental Radar Power Spectra: (a) Transmitted Signal;  
(b) Sum Signal

Figure 4. Demonstration of the Phase Coherence of Power Spectrum  
Modulations (the range to the target in the upper and lower traces  
differs by 1/2 in.)

Figure 5. A-Scope Presentation: (a) One Target; (b) Two Targets  
(dispersion = 25 ft/cm)

Figure 6. High- and Low-Dispersion Displays of Same Target

Figure A1. Displays Showing Effect of Signal Bandwidth on Resolution  
(bandwidths: top = 10 MHz; bottom = 20 MHz)

NONDESTRUCTIVE EVALUATION OF METAL FATIGUE

J. R. Barton, W. Lyle Donaldson, F. N. Kusenberger

Division of Electronics and Electrical Engineering  
and Applied Economics

Southwest Research Institute, San Antonio, Texas

NONDESTRUCTIVE EVALUATION OF METAL FATIGUE

J. R. Barton, W. Lyle Donaldson, F. N. Kusenberger  
Division of Electronics and Electrical Engineering  
and Applied Economics  
Southwest Research Institute, San Antonio, Texas

## ACKNOWLEDGEMENTS

Most of the research reported here has been supported by the Air Force Office of Scientific Research, Engineering Sciences Directorate, Mechanics Division. The authors wish to acknowledge the continued interest of Dr. Jacob Pomerantz, Technical Monitor at OSR, and also the help of other colleagues at Southwest Research Institute which include B. E. Leonard, R. D. Williams, H. C. Burghard, and P. H. Francis.

## NONDESTRUCTIVE EVALUATION OF METAL FATIGUE

J. R. Barton, W. Lyle Donaldson, F. N. Kusenberger  
Division of Electronics and Electrical Engineering  
and Applied Economics  
Southwest Research Institute, San Antonio, Texas

### ABSTRACT

Nondestructive methods and instrumentation have been developed for evaluation of fatigue damage in metals used in aircraft and space vehicles. A description of the fundamentals of the ultrasonic, magnetic perturbation, and electric current injection techniques is presented. These techniques have been adapted for the inspection of aircraft service parts during overhaul. In addition to the development and the application instrumentation techniques to current engineering problems, such techniques are being applied to the more fundamental study of fatigue in metals, including the determination of the effect of pressure and atmospheric environment on fatigue phenomena. Results suggesting the possibility of flaw removal to obtain superior fatigue performance are presented and discussed.

Brief descriptions of inspection hardware developed, on the basis of this and other research, for several critical components are also included.

### I. INTRODUCTION

It is a well established fact that catastrophic failures of structures and equipments subjected to alternating stresses are often traced to fatigue failure of a primary structural element or machine component. Consequently, the fatigue characteristics of a component or a structure usually exert a dominant influence on the design approaches for aerospace and aeronautical vehicles and equipments where "trade-offs" between weight reduction and acceptable reliability are necessary. To achieve the high reliability required, stringent quality control and inspection procedures are employed during fabrication and assembly and, during service, periodic inspections are specified at which time it is often necessary to completely disassemble complex systems such as aircraft gas turbine engines to permit meticulous and critical nondestructive inspection of individual components. Although such procedures have aided in maintaining reliability of equipments, it is generally conceded by user organizations that such procedures are often inadequate, unrealistic, and too expensive both in terms of man-hours and materials. Also, considerable controversy often exists in determining inspection intervals and methods. Further more, the practice of "retiring" or discarding certain critical components on the basis of hours service rather than on measured deterioration is continually being questioned and rightly so.

In fact, a number of studies have been conducted leading to the ideas of overhaul and inspection on the basis of condition only. In other words, continue using the equipment, somewhat regardless of service time, so long as there are no definite indications of deterioration in the equipment or structure. Documented examples of savings in the multimillion dollar category have accrued from such practices. However, the persistent questions, HOW MUCH LIFE REMAINS?, and HOW MUCH HAS THE PROBABILITY OF FAILURE INCREASED? become increasingly important as service time increases. At present these questions cannot be answered except on a statistical basis, and it is still impossible to predict with satisfactory accuracy the life of an individual item. The inability of the presently employed nondestructive inspection methods to adequately characterize materials and, in particular, individual components is one of the major limitations in our ability to predict safe operating life.

Progress is being made toward developing realistic predictive techniques based on fracture mechanics concepts and critical flaw sizes, but one factor, cited in a recent (May, 1968) comprehensive report<sup>(1)</sup>, which severely compromises these approaches is the inadequacy of the presently used nondestructive inspection methods for locating and defining small flaws. This report indicates that all presently used nondestructive inspection methods, those methods routinely used during fabrication and overhaul, have very poor sensitivity for detecting fatigue cracks smaller than 0.2 inches. This is nearly 1/4-inch long, and on cursory appraisal, it would appear that such cracks should readily be detectable, but the peculiar nature of fatigue cracks, does in fact often prohibit easy detection of cracks even as long as this. Figure 1 shows an example illustrating this fact. This is a magnified view<sup>(2)</sup> (100X) of a small region on a T53 gas turbine engine compressor blade which contains a long fatigue crack. Certainly the crack is not obvious, and, in fact, it is impossible to visually locate the crack, even though it extends almost completely across the region shown and is, in fact, almost 0.05 inches long. This crack is readily apparent after being enhanced by application of a bending load which separates the crack interfaces as shown in Figure 2. Upon release of the load, the crack is, of course, closed and presents the appearance shown in Figure 1. From this it is apparent that fatigue cracks may indeed be difficult to detect.

It is probable that the use of conventional nondestructive inspection methods and fracture mechanics design concepts can be usefully employed on some structures where relatively short cracks--less than 0.10 inches--are not critical, but it is certain that high strength components such as bearings, gears, turbine blades, landing gears, etc., may be impending catastrophic failures long before cracks reach this size. In view of the rather severe limitations of most presently used nondestructive inspection approaches, it should be apparent that development of better instrumentation methods for the detection of fatigue cracks and other flaws is desirable and perhaps even mandatory.



FIGURE 1. PHOTOGRAPH (100X) OF T53 ENGINE COMPRESSOR BLADE WITH FATIGUE DAMAGE



**FIGURE 2. PHOTOGRAPH (100X) OF T53 ENGINE COMPRESSOR BLADE WITH FATIGUE DAMAGE, LOAD APPLIED**

Southwest Research Institute has concentrated much research on developing better instrumentation methods for the detection and study of fatigue damage, and some of this research as well as present and future applications will be reviewed in the following.

## II. EXPERIMENTAL APPROACH

Most nondestructive methods become increasingly unreliable as the flaw dimensions become smaller, less than approximately 0.05 inches, and this is the area in which the work at Southwest Research Institute has been concentrated. This work has used "engineering size" specimens fabricated from materials that are currently in wide-spread use in the aerospace industries. Specimens are carefully machined to remove all stress concentration sources, except those inherent in the material, and fatigue cracks are developed in the specimens by stress cycling in uniaxial tension. Specimens are carefully examined optically and with developmental nondestructive inspection methods before initiation of cycling, and at frequent intervals during the stress cycling history. As a consequence, a large volume of data is accumulated from each specimen. These procedures are time consuming and it is only possible to examine a limited number of specimens in contrast to the several hundred specimens usually employed for fatigue programs. The advantage is, of course, that the detailed history of individual specimens can be studied and thereby greater insight is gained into those aspects of fatigue cracks and fatigue phenomena which are important in their nondestructive detection.

Figure 3 shows several of the AISI 4340 rod type tensile specimens used in the research. Other specimens have been fabricated from: an 18 percent nickel maraging steel, a titanium alloy (Ti-6Al-4V), and an aluminum alloy 7075-T6.

## III. INSTRUMENTATION AND FACILITIES

At the present time, four different nondestructive inspection procedures are used in the research. These are magnetic perturbation, electric current injection, ultrasonic surface wave, and high magnification optical examination.

The magnetic perturbation method essentially consists of establishing a suitable magnetic flux in the specimen and then scanning the surface of the specimen with a sensitive magnetic probe to detect flux perturbations caused by flaws in the material. This is illustrated schematically in Figure 4 which shows the effect of a small inclusion on the magnetic flux distribution. Hall effect probes are used to convert the magnetic flux to an electrical voltage. The magnetic perturbation method is applicable only to ferromagnetic materials.

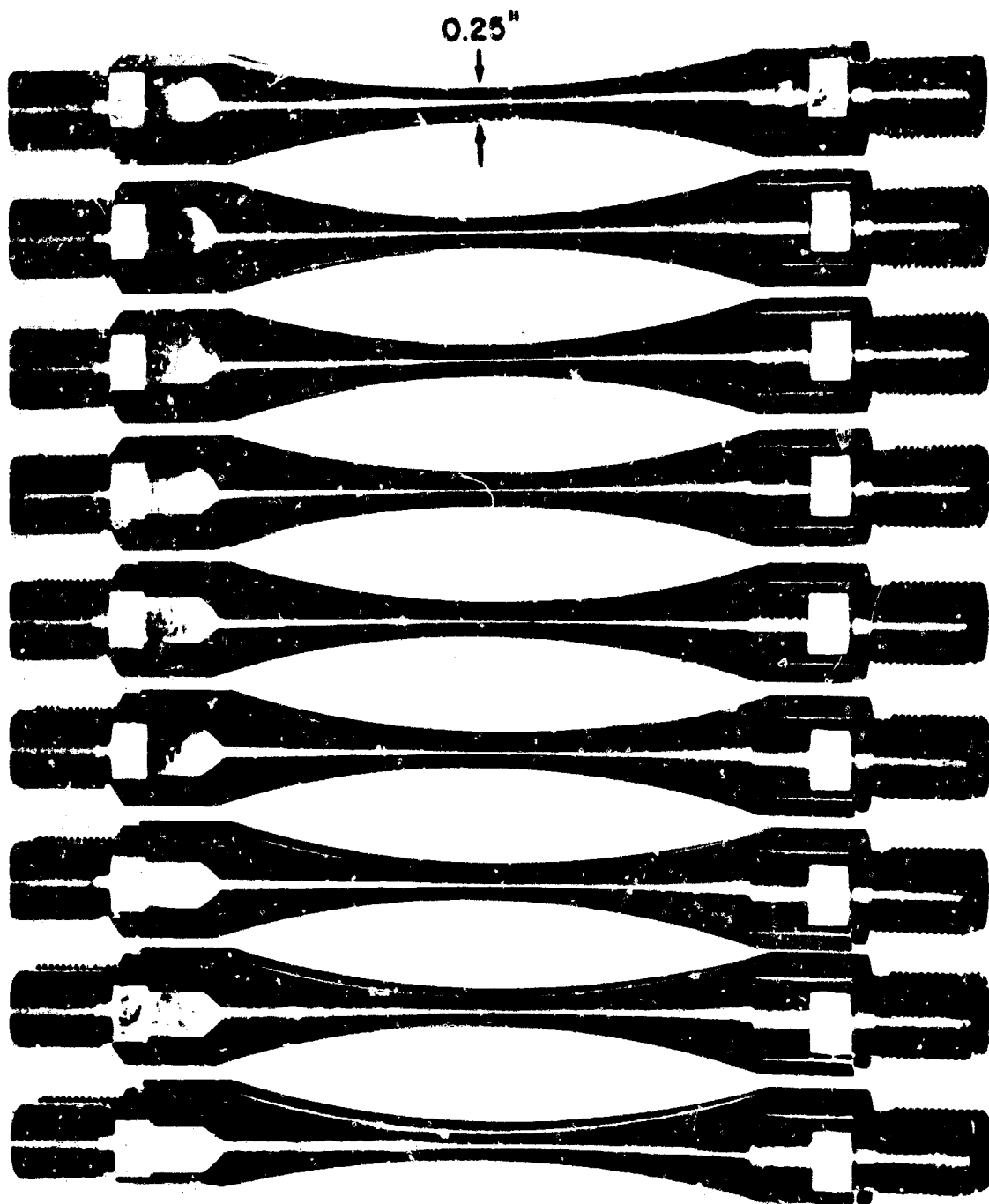
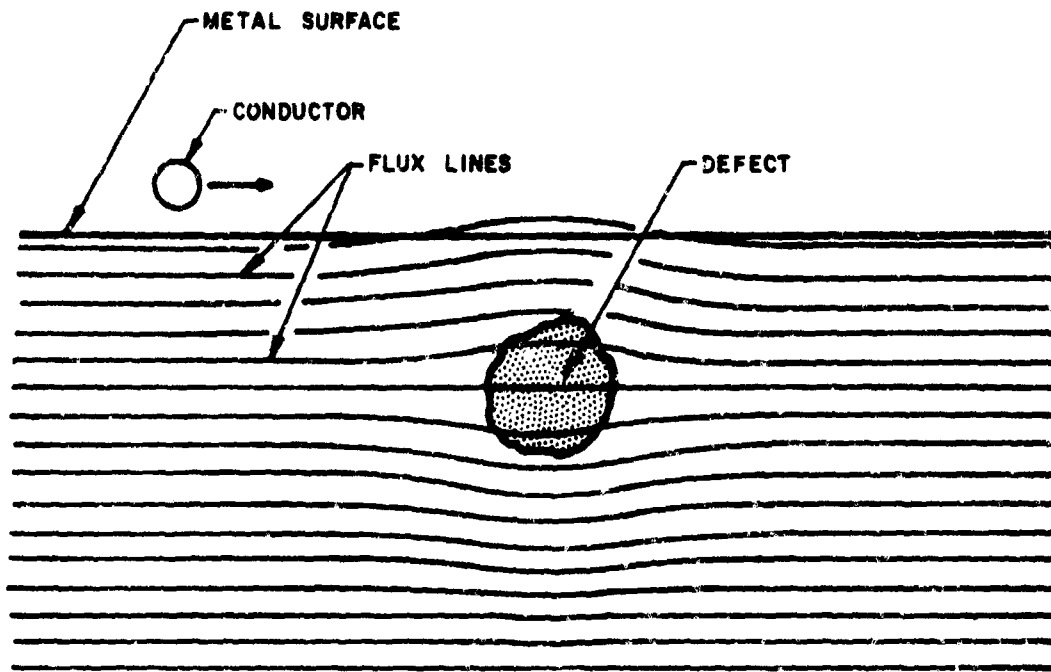
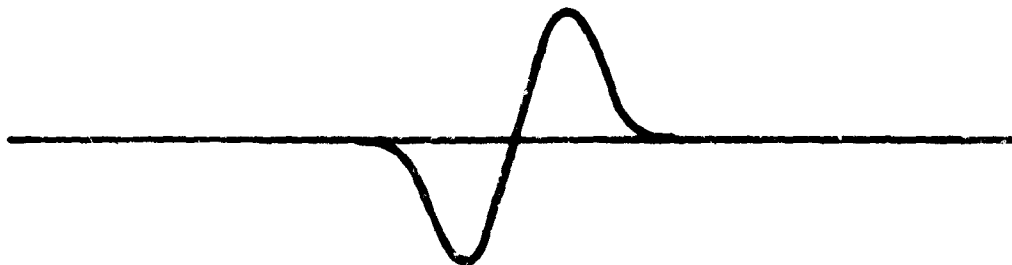


FIGURE 3. SEVERAL OF THE AISI 4340 ROD-TYPE TENSILE SPECIMENS



(A) FLUX PERTURBATION



(B) SIGNAL SHAPE AS A FUNCTION OF CONDUCTOR LOCATION

FIGURE 4.

SCHEMATIC REPRESENTATION SHOWING THE INFLUENCE OF AN INCLUSION ON MAGNETIC FLUX DISTRIBUTION

A method analagous to magnetic perturbation which is useful on non-ferromagnetic but electrically conducting materials such as titanium, aluminum, the super/alloy steels, refractory metals, etc., is the electric current injection method. This consists essentially of establishing, by means of electrical contacts, a current flow through the region of the material of interest, and then scanning the surface of the material with a magnetic field sensitive probe to detect and measure magnetic perturbations associated with the electric current perturbations caused by flaws. Figure 5 is a schematic illustration of this method.

Another method which has proven to be very useful is the ultrasonic surface wave pulse-echo method. This is shown schematically in Figure 6. Among other advantages this approach permits continuous monitoring of specimens while they are being fatigue cycled. A disadvantage is that it is necessary to intimately couple the acoustic energy at a very precise angle into the material being examined. Accordingly, transducers are bonded to each of six flat surfaces machined for this purpose on the specimens.

An overall view of the experimental apparatus is shown in Figure 7. The vacuum chamber and vacuum control system permits investigations to be conducted at reduced atmospheric pressures and/or with a controlled atmosphere of a selected gas since the system can be constantly pumped. A close-up of the specimen showing the probe, microscope, and other items is presented in Figure 8. The microscope is of great advantage in following the development of fatigue cracks as a function of stress cycles for crack initiation and propagation studies.

#### IV. EXPERIMENTAL RESULTS

Examples of selected experimental results obtained during the work conducted in the last several years will be presented in this section. From time to time improvements have been made in the instrumentation and apparatus and these have permitted more detailed and comprehensive investigations. The results to be presented will cover examples of data obtained on several different specimen materials and also using several different non-destructive inspection methods. For conciseness, only brief descriptions of the results will be made; most results have been comprehensively discussed in several reports (2-7) which have been included as references.

Figure 9 shows several magnetic inspection records taken at different intervals of stress cycling and also under two different conditions of magnetic field. In these inspection records the vertical axis is the signal amplitude, and the horizontal axis is the axial distance along the specimen surface. First, a comparison of the two records in the second column shows that they are practically identical and no changes have occurred after 50,000 cycles. The signal indicated by the arrow is caused by a small surface pit or surface inclusion. By contrast, a comparison of the three records in the first column shows that a marked change has occurred after 50,000 stress cycles.

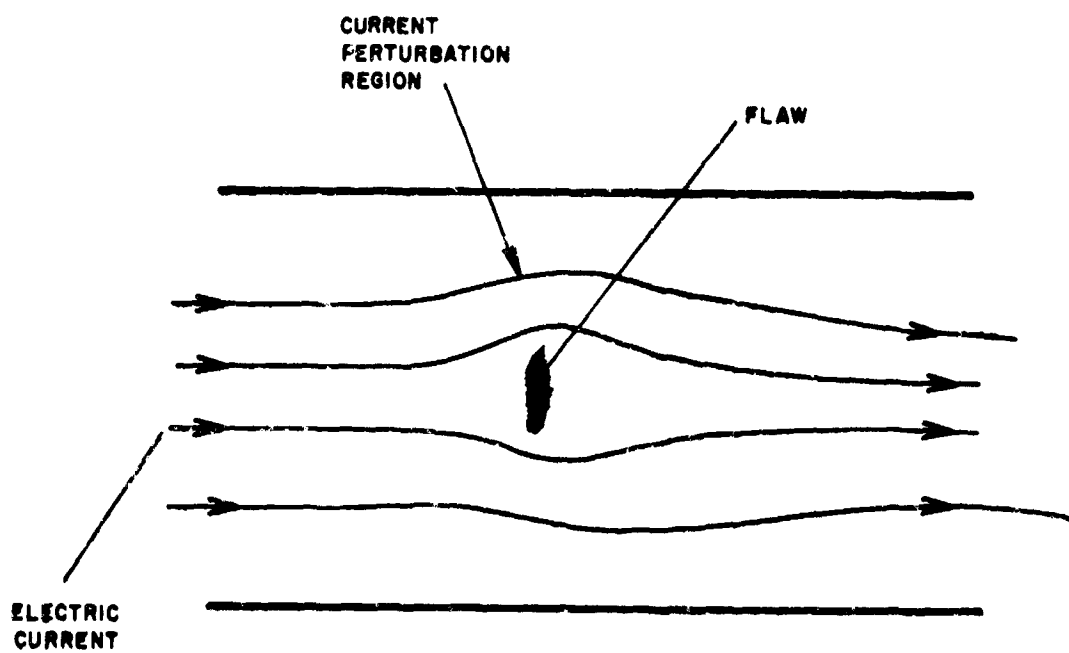


FIGURE 5.

SCHEMATIC REPRESENTATION SHOWING THE INFLUENCE OF A FLAW ON ELECTRIC CURRENT DISTRIBUTION

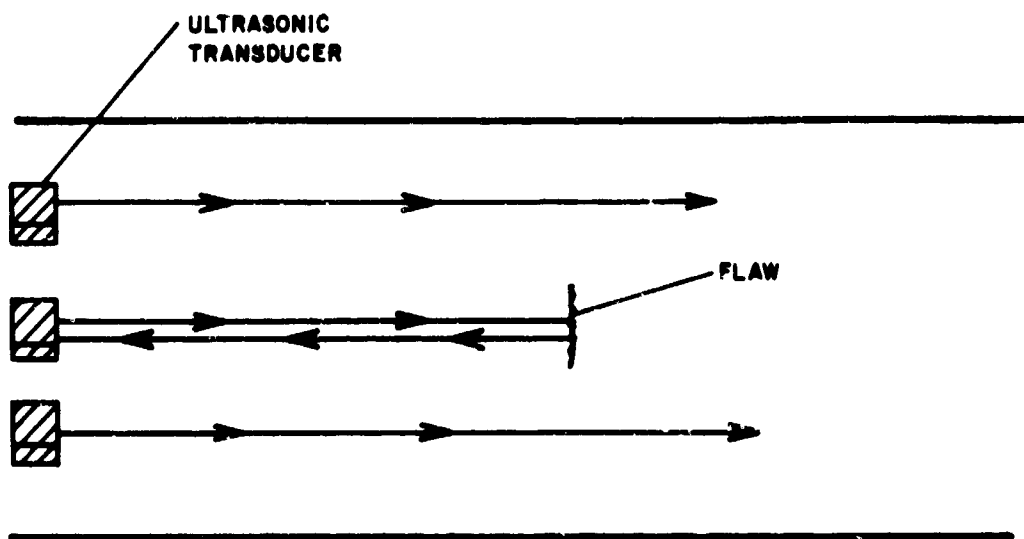
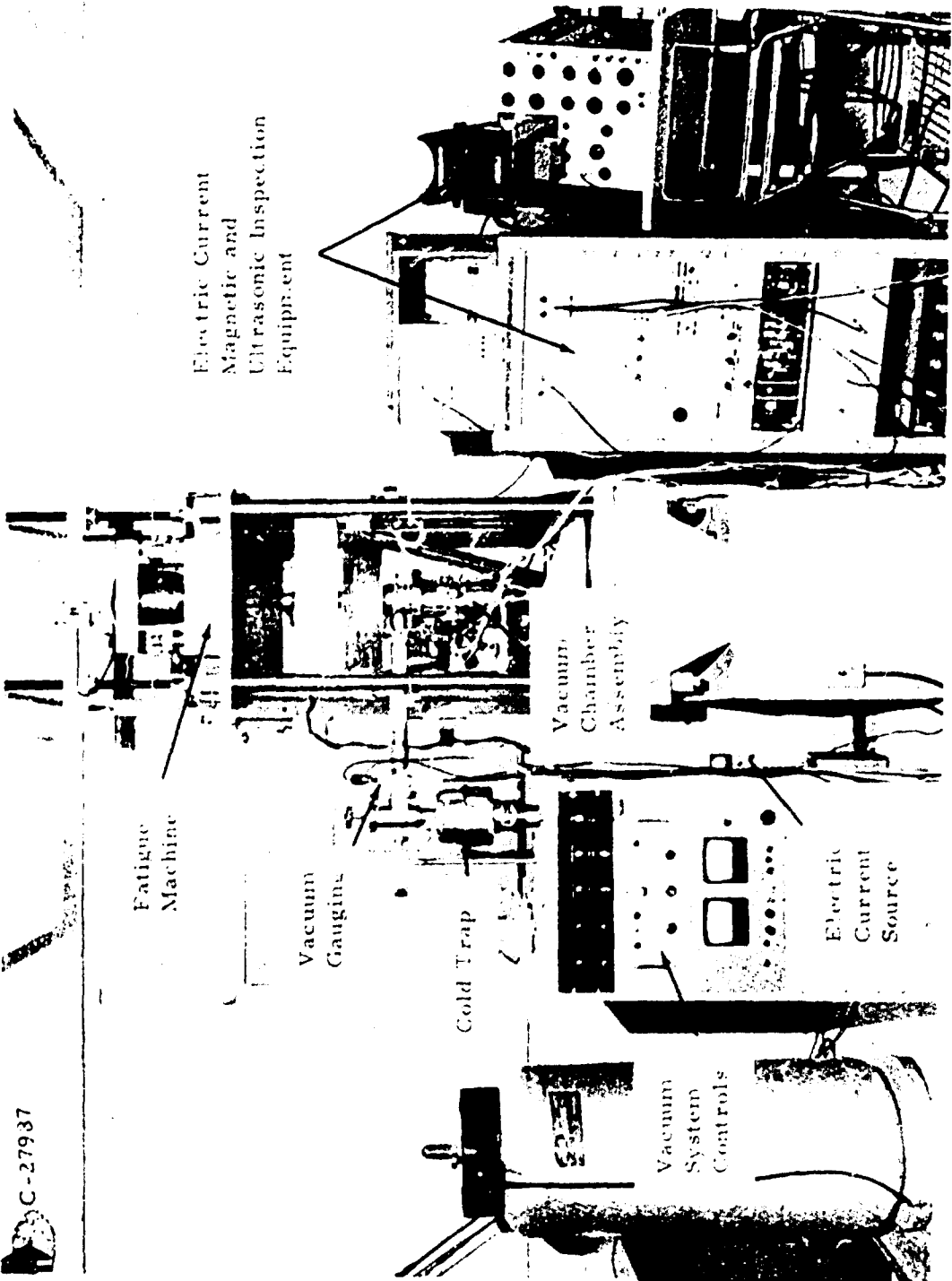


FIGURE 6.

SCHEMATIC REPRESENTATION OF THE ULTRASONIC SURFACE WAVE  
PULSE-ECHO METHOD



C-27937

FIGURE 7. OVERALL VIEW OF NONDESTRUCTIVE FATIGUE EVALUATION FACILITY

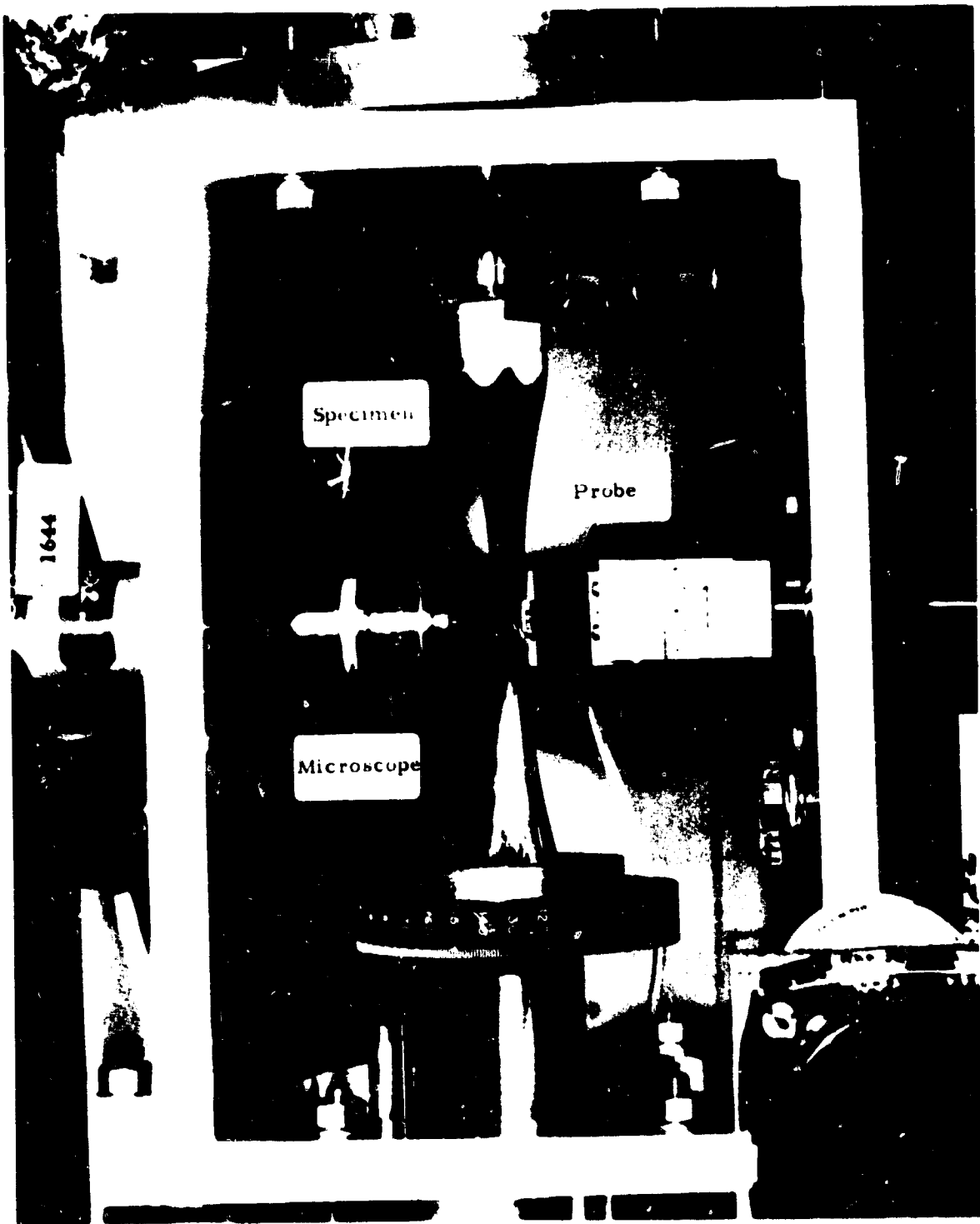
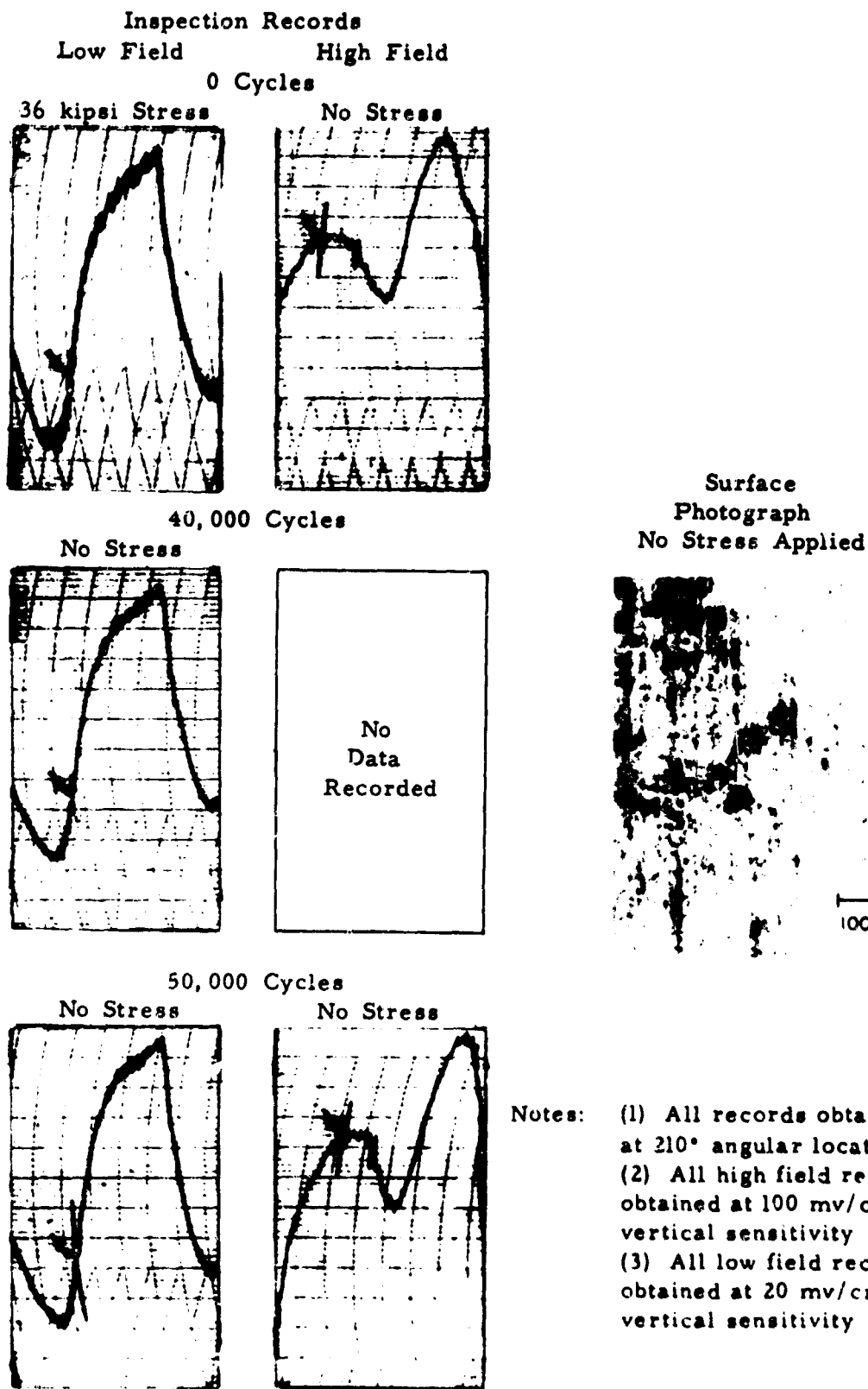


FIGURE 8.

PHOTOGRAPH OF SPECIMEN MOUNTED IN FATIGUE TESTER SHOWING  
MICROSCOPE AND PROBE ASSEMBLY



Notes: (1) All records obtained at 210° angular location.  
 (2) All high field records obtained at 100 mv/cm vertical sensitivity  
 (3) All low field records obtained at 20 mv/cm vertical sensitivity

FIGURE 9. MAGNETIC INSPECTION RECORDS SHOWING DEVELOPMENT OF FATIGUE DAMAGE SIGNAL ON SPECIMEN NO. 14

This prominent signal is readily apparent in the lower left record, and the arrow indicates the portion of the record corresponding with this location on each record. The inspection records in the left column were obtained at a relatively low magnetic field which has been experimentally determined to offer the best fatigue damage detection while those records in the second column were obtained under high magnetic field which is sensitive to geometric discontinuities and inclusions. A photomicrograph of the surface region corresponding with the signal from the fatigue damage is also shown with the minute fatigue crack indicated by the arrow.

Examples of inspection records obtained on another specimen are shown in Figure 10. Again the fatigue damage is detected best at low magnetic field, and in fact, after 64,500 cycles, there is no evidence whatsoever of fatigue damage on the basis of the high magnetic field inspection records in the right column. It has been found that application of a stress during the inspection enhances the fatigue damage signal, and approximately one half the peak tensile stress used during cycling was applied at the time the records in the first and second columns were obtained. Note the progressive increase of the signal amplitude in the first column of records. After developing the tiny fatigue crack, additional programmed cycling, simulating a predicted aircraft loading environment, was applied to the specimen. Inspection records obtained before and after this programmed cycling are shown in Figure 11 along with a surface photomicrograph showing the minute fatigue crack extending approximately 0.004 inches from either side of the inclusion. In this illustration the fatigue crack is oriented in the horizontal direction. The many fine straight lines approximately vertically oriented are from a polishing operation.

A third example showing fatigue damage development is presented in Figure 12. The outstanding fatigue damage signal obtained after  $2.76 \times 10^6$  stress cycles is shown in the lower left magnetic inspection record. The enhancement, an approximate four-fold increase, of this signal caused by the application of applied stress is shown in the lower center two records. The signal indicated by the arrow in the two records in the right column is caused by a tiny surface inclusion from which the fatigue crack developed. This is clearly shown in the surface photomicrographs of Figure 13. This specimen was continuously monitored during stress cycling by using pulse echo ultrasonic surface wave methods. Six 10 MHz transducers were permanently bonded to the flats on one end of the specimen prior to stress cycling. These transducers were used to launch surface or Rayleigh waves which travel along the specimen surface and are reflected back to the transducer whenever a reflecting discontinuity is encountered. Much insight has been gained into the behavior of fatigue cracks by this approach. Figure 14 shows photographs of the ultrasonic signals displayed on an oscilloscope. For these records the transducer is initially pulsed at the left, and reflected pulses are then received thereafter. Accordingly, a measurement of the time interval between a reflected pulse and the initial pulse permits a determination of the reflecting source location on the specimen surface. In the

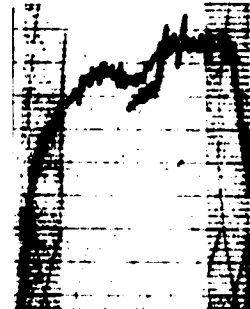
0.6A Residual Field  
65 kipsi Static Stress  
20 mv/cm Sensitivity



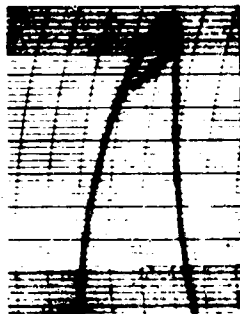
3.0A Residual Field  
65 kipsi Static Stress  
50 mv/cm Sensitivity



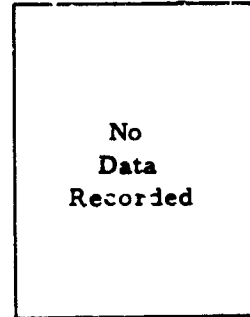
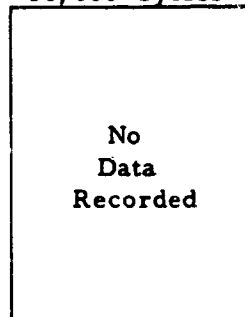
3.0A High Field  
0 kipsi Static Stress  
100 mv/cm Sensitivity



0 Cycles

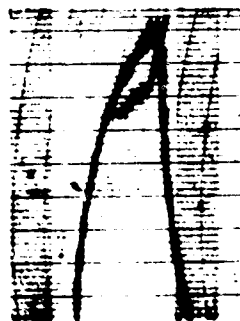


50,000 Cycles

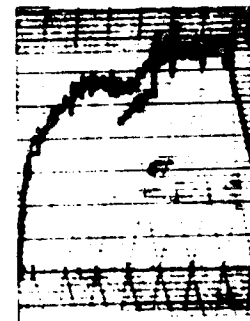


No  
Data  
Recorded

No  
Data  
Recorded



61,000 Cycles



64,500 Cycles

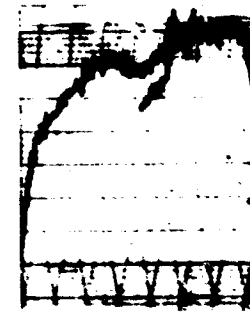


FIGURE 10. MAGNETIC INSPECTION RECORDS SHOWING DEVELOPMENT OF FATIGUE DAMAGE SIGNAL ON SPECIMEN NO. 15

Inspection Records  
0.6A Residual Field

65 kipsi Static Stress  
20 mv/cm Sensitivity

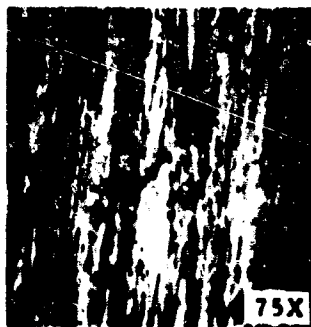
Before  
Programmed  
Load



After  
Programmed  
Load



Surface  
Photograph  
No Stress Applied



After Programmed Load

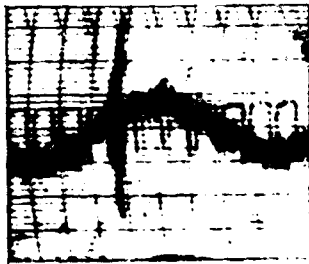
FIGURE 11. MAGNETIC SIGNALS INDICATING FATIGUE DAMAGE BEFORE AND AFTER COMPLETION OF A PROGRAMMED LOAD ON SPECIMEN NO. 15

0.35A Residual Field  
0 Kipsi Static Stress  
10 mv/cm Sensitivity



No  
Data  
Recorded

No  
Data  
Recorded



0.35A Residual Field  
127 Kipsi Static Stress  
10 mv/cm Sensitivity

$2.62 \times 10^6$  Stress Cycles



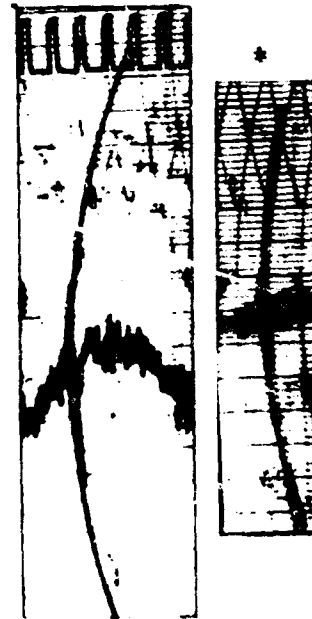
$2.72 \times 10^6$  Stress Cycles



$2.74 \times 10^6$  Stress Cycles



$2.76 \times 10^6$  Stress Cycles



3.0A High Field  
0 Kipsi Static Stress  
50 mv/cm Sensitivity



No  
Data  
Recorded

No  
Data  
Recorded

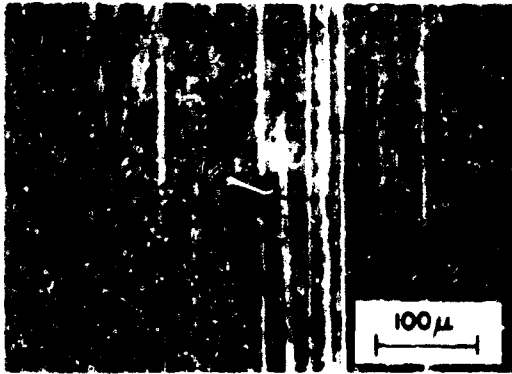


\* - 20 mv/cm sensitivity  
N - transient noise

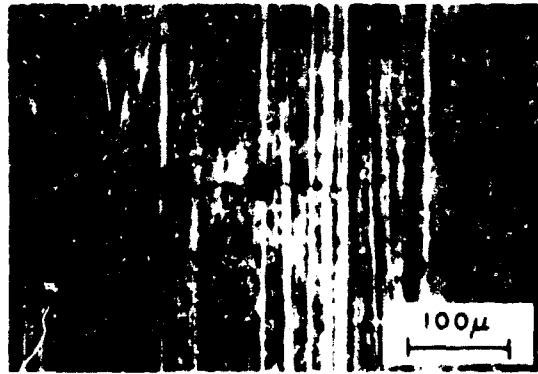
FIGURE 12. FATIGUE DAMAGE SIGNALS SHOWING "LOAD ENHANCEMENT" ON SPECIMEN NO. 18

## Surface Microphotographs

No Stress Applied

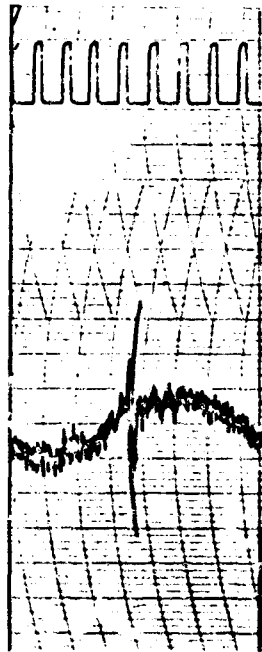


64 Kipsi Stress Applied

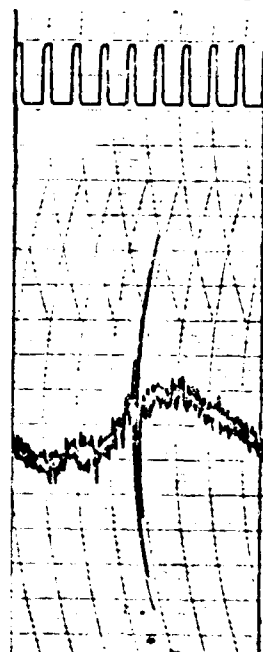


## Inspection Records at 210° Angular Location

No Stress Applied



64 Kipsi Stress Applied



Notes: Inspection records obtained at residual field from 0.35 amperes applied magnetizing current

Inspection records obtained at  $2.76 \times 10^6$  stress cycles with 10 mv/cm vertical sensitivity.

FIGURE 13.

SURFACE PHOTOGRAPHS AND MAGNETIC RECORDS SHOWING FATIGUE DAMAGE UNDER TWO STATIC LOADS ON SPECIMEN NO. 18

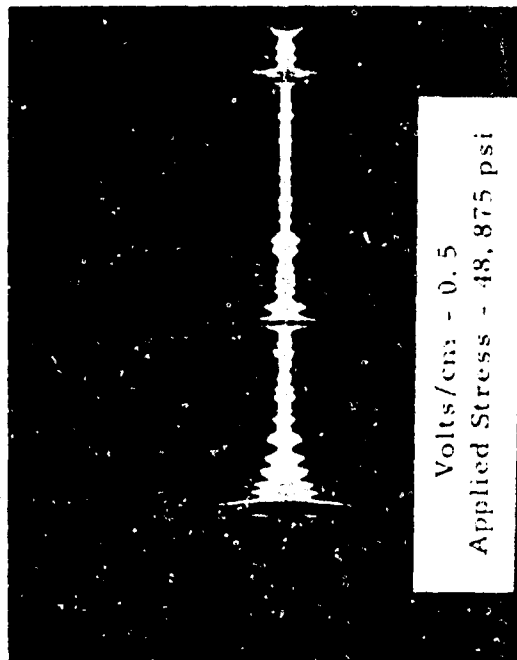
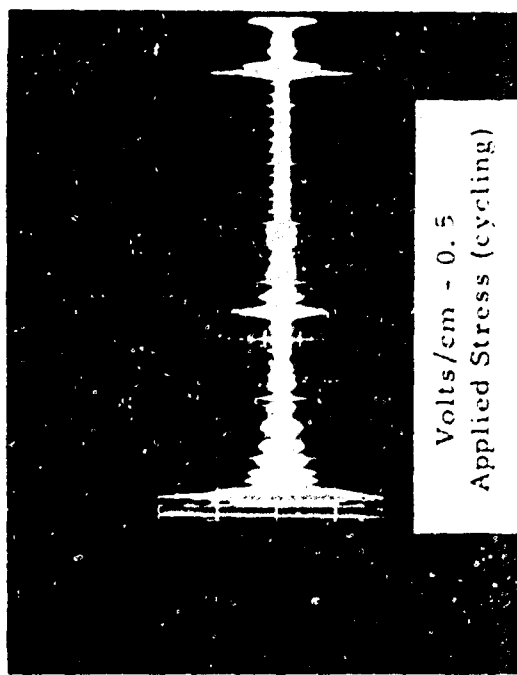
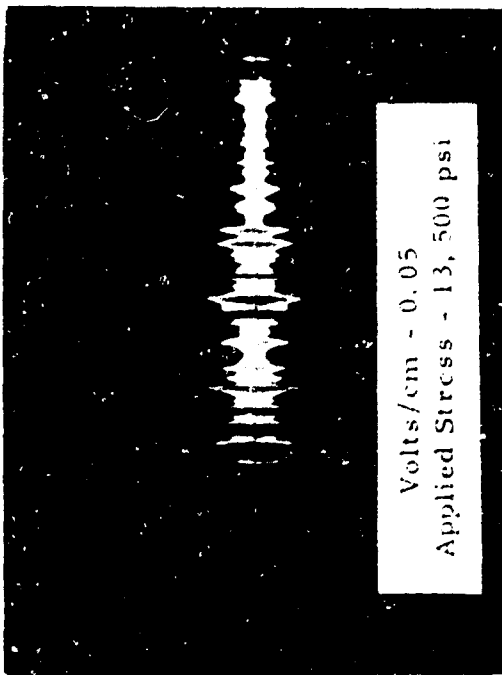


FIGURE 14. PHOTOGRAPHS OF RAYLEIGH WAVE REFLECTION SIGNALS FROM FATIGUE CRACK IN SPECIMEN NO. 18 AS A FUNCTION OF APPLIED STRESS

upper left record it is apparent that none of the reflections are very outstanding, and in fact, the reflection indicated by the arrow, although coinciding with the fatigue crack location, is certainly no assurance of a fatigue crack. By comparison the record immediately below shows a very prominent signal, and it was necessary to change the vertical sensitivity to maintain this outstanding signal on scale. Note that a stress was applied to the specimen during the time this record was obtained. The record in the upper right column, obtained under identical conditions with the record at the left, with the exception that a 13,500 psi stress was applied, shows a prominent signal from the fatigue crack. The lower right photograph shows a record obtained while the specimen was being cycled, and in this instance, the signal is observed to increase and decrease in synchronism with the applied load. This, of course, causes a signal to be readily evident, and can provide a warning that a fatigue crack has developed. It is quite interesting that fatigue cracks approaching 0.05 inches long do not act as a reflecting surface even at frequencies as high as 30 MHz because of the intimate contact between the crack interface surfaces when no load is applied. Accordingly it is possible for ultrasonic inspections to "miss" sizeable fatigue cracks. This statement should not be taken as a generalization since the conditions in the fatigue damage region may vary depending upon the material, the heat treatment, the loading history, etc.

A graphical presentation of magnetic signals vs stress cycles on two different specimens is presented in Figure 15. The data from specimen No. 17 were obtained several years ago while those from specimen No. 21; namely, those three points plotted at the lower left, were obtained recently with considerably improved instrumentation. It is apparent that a significant improvement has been made and, in fact, it is now possible to detect magnetic signal changes associated with cracks which are of the order of 0.001 to 0.002 inches long. Corresponding ultrasonic and magnetic inspection records are shown for points 1 and 3, and a surface photomicrograph showing the appearance of the fatigue crack and the inclusion from which the crack emanated are shown for point 2. The functional relationship is well defined and provides a reasonable basis for indicating that specimen failure will occur within approximately 30,000 to perhaps 60,000 cycles depending on the crack length when it is first detected.

A few examples of data obtained using the electric current injection instrumentation will now be presented. Figure 16 shows inspection records obtained on an aluminum specimen at three different intervals during cycling. The prominent signal indicated by the arrow in the two lower records corresponded with the fatigue crack location. This signal occurred near the limit of the probe scan, and the characteristic signal shape is symmetrical about the point just to the left of the arrow. It was necessary to reduce the recording sensitivity and also to reduce the current in order to maintain this signal on scale. Also note that this specimen was cycled and the data obtained with the chamber maintained at a vacuum of approximately  $2 \times 10^{-6}$  torr. When ambient laboratory atmosphere was readmitted to the chamber the

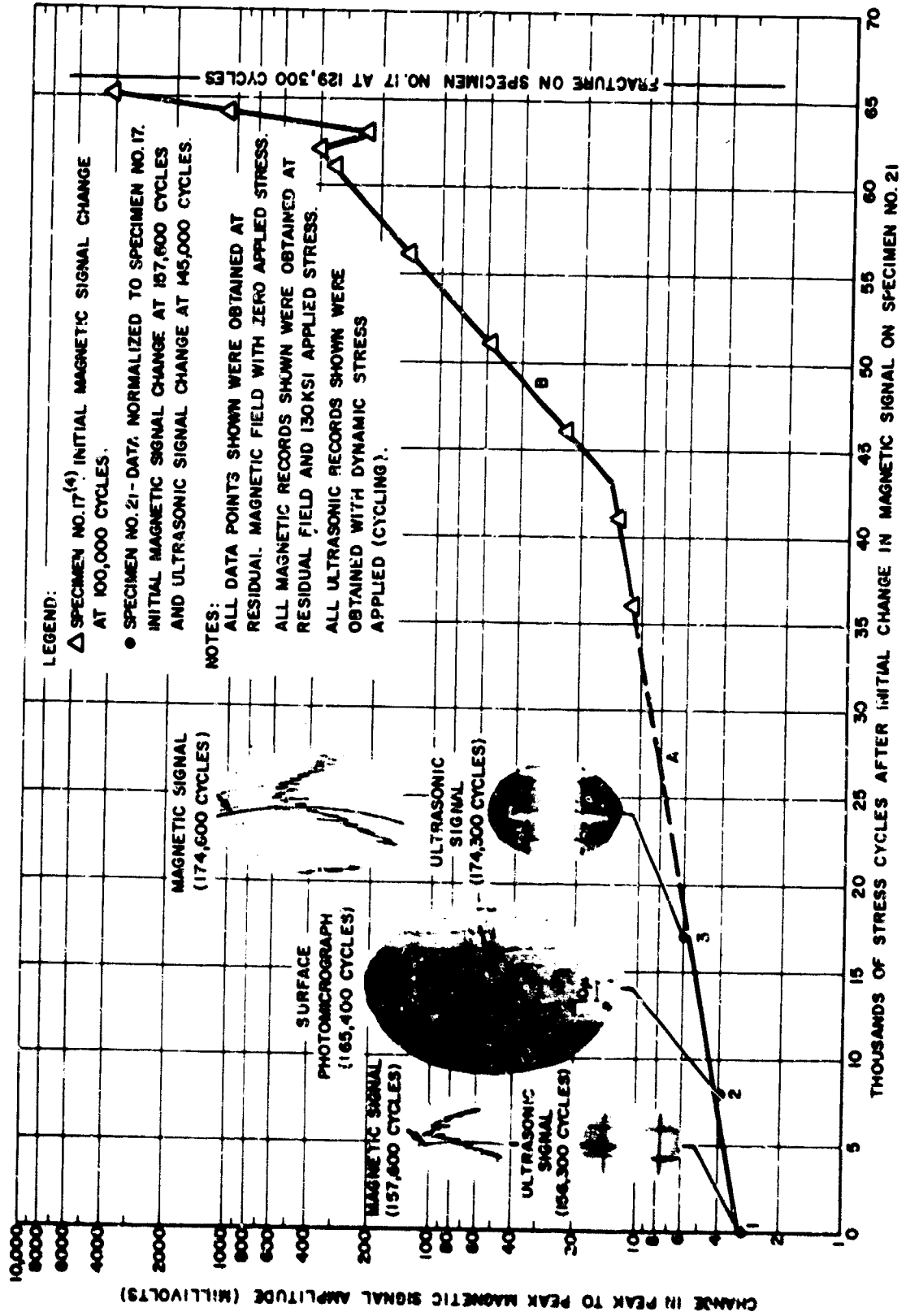
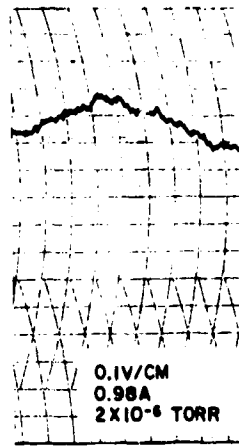
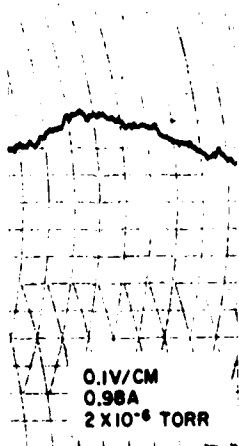


FIGURE 15. GRAPH OF MAGNETIC SIGNAL AMPLITUDE AS A FUNCTION OF ADDITIONAL STRESS CYCLES WITH TYPICAL SIGNALS

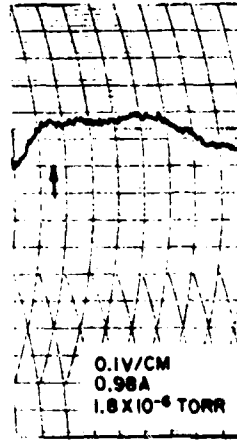
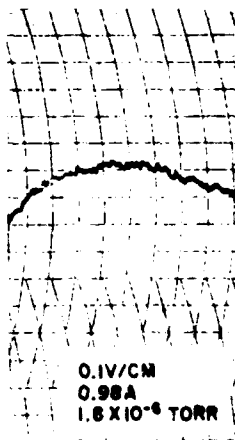
0 KSI STATIC STRESS

48 KSI STATIC STRESS

0 STRESS CYCLES



300,200 STRESS CYCLES



335,800 STRESS CYCLES



\* 24 KSI STATIC STRESS

FIGURE 16.

ELECTRIC CURRENT INJECTION RECORDS SHOWING FATIGUE CRACK DEVELOPMENT IN AN ALUMINUM SPECIMEN NO. 31 IN VACUUM

electric current signal changed dramatically. These records are shown in the left column of Figure 17, and the change amounts to an approximate six-fold increase. A surface photomicrograph of the crack is also shown.

Electric current injection records obtained on a titanium specimen along with surface photomicrographs of the developed fatigue crack are shown in Figure 18.

Recently experiments have been conducted which dramatically confirm that fatigue damage is limited to a very local region in agreement with the work of Grosskreutz<sup>(8, 9)</sup>. In these experiments the local region containing the fatigue crack and the fatigue damage source is removed by local mechanical abrasive polishing until no evidence of the crack remains. Figure 19 shows surface photomicrographs of the crack region at successive stages in the crack removal operation on specimen No. 18 along with the corresponding magnetic and ultrasonic inspection records. Note that only a very nominal magnetic signal is obtained after the second polish. Subsequent to these records, the crack was completely removed as determined by very careful microscopic examination, and at this time the magnetic signal was also completely gone. This required removal of approximately 0.006 inches of material in the local region. It is important to note that only the material in the immediate or local vicinity of this crack was mechanically polished, and the remainder of the specimen circumference was unaltered. Stress cycling of this specimen was then continued for approximately 130,000 cycles without any evidence of ultrasonic or magnetic signal changes. A somewhat similar sequence of magnetic inspection records from another specimen is presented in Figure 20. Note the prominent magnetic perturbation signal caused by the fatigue crack emanating from the tiny inclusion. This crack is oriented vertically in this illustration, however, in common with all the cracks, it developed normal to the tension axis of the specimen. Records obtained after crack removal are shown in the third and fourth rows, records obtained after adding an additional 80,000 cycles are also presented. A comparison of the third and fourth row of records shows these to be essentially identical, and it may be concluded, that no further fatigue crack has developed in this region. These results are deemed very significant and they will be discussed in a later section in more detail.

## V. PRESENT APPLICATIONS

Much of the information which has already been developed has also been very useful in developing specialized hardware for critical inspection applications. Some of these will be reviewed now.

Figure 21 shows a semi-automatic equipment using the magnetic perturbation method for fatigue damage detection during overhaul inspection of a large ring gear from the SH3A helicopter transmission. This equipment automatically scans the area of interest and has automatic alarm features when a fatigue damage region is encountered. Presently, the equipment is being

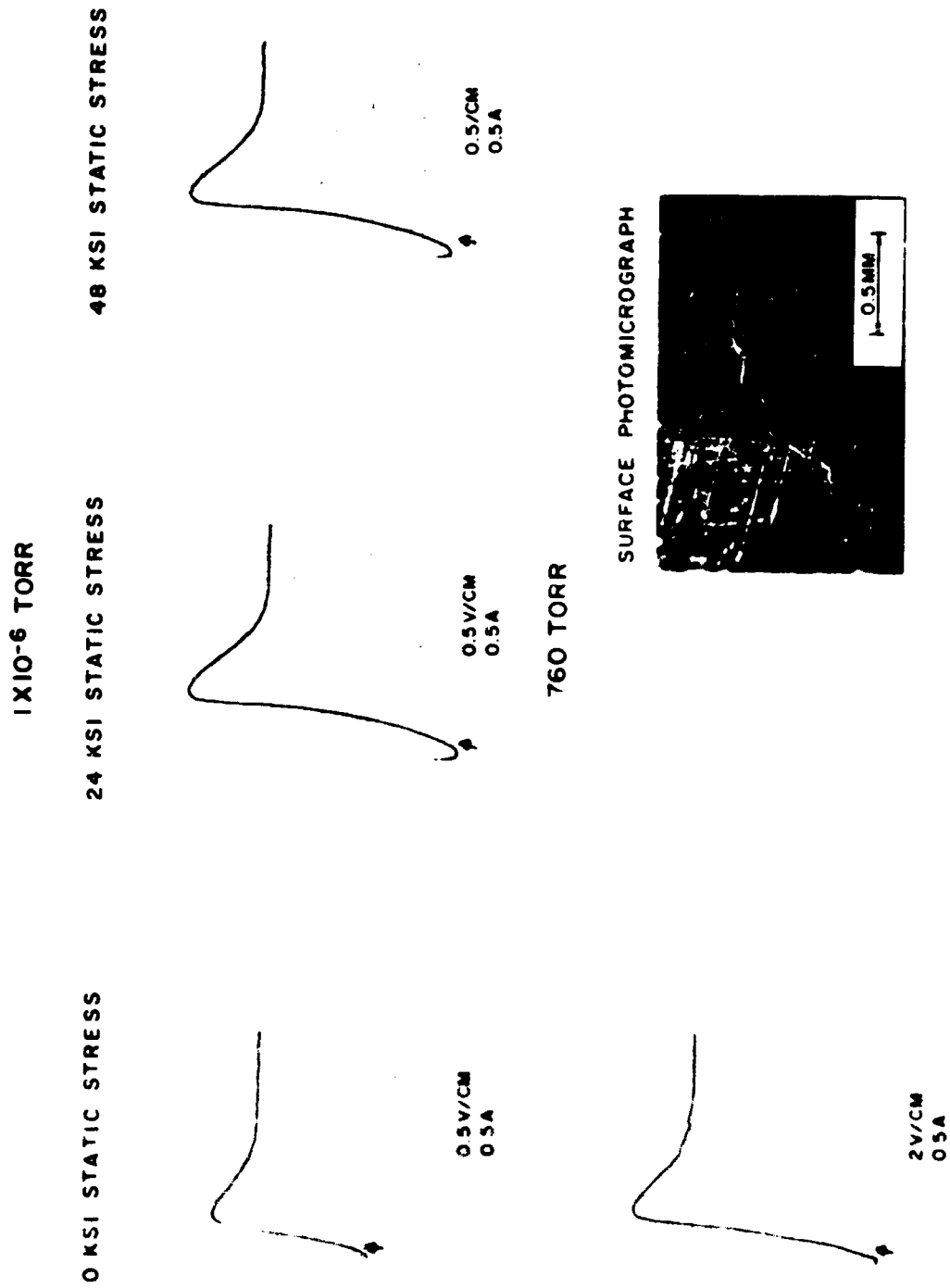


FIGURE 17. ELECTRIC CURRENT SIGNAL FROM FATIGUE CRACK IN ALUMINUM SPECIMEN NO. 31 AS A FUNCTION OF STATIC STRESS AND CHAMBER PRESSURE (SURFACE PHOTOMICROGRAPH INCLUDED)

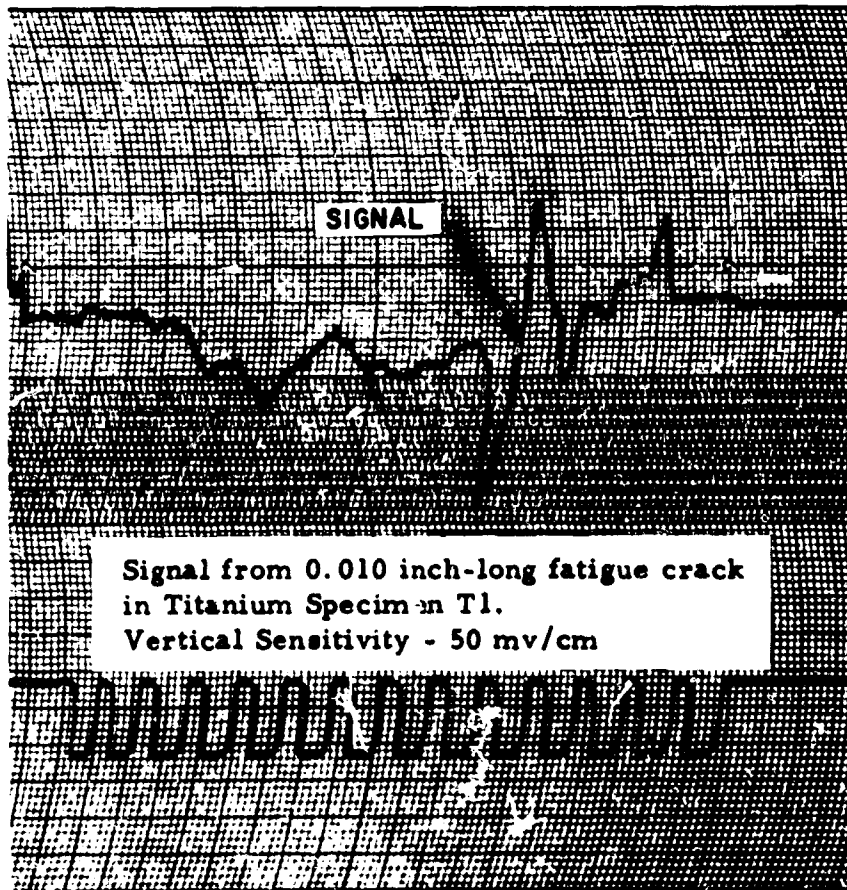


FIGURE 18.  
ELECTRIC CURRENT INJECTION FATIGUE DAMAGE SIGNAL ON A  
TITANIUM SPECIMEN

**SURFACE PHOTOMICROGRAPHS**  
BEFORE POLISHING



**AFTER FIRST POLISH**

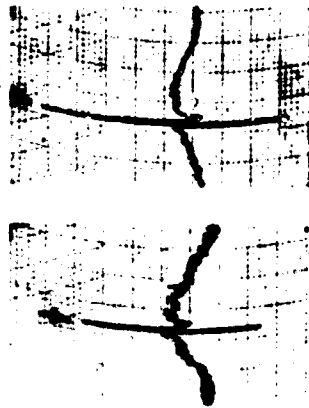


**AFTER SECOND POLISH**

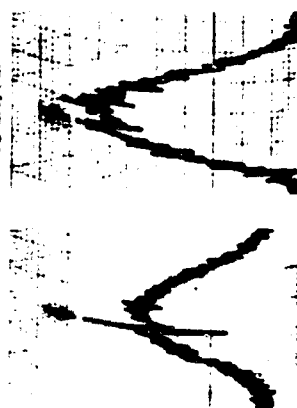


**MAGNETIC RECORDS**

NO STRESS 20 MV/CM  
127 KSI STRESS 50 MV/CM



AFTER FIRST POLISH 10 MV/CM



AFTER SECOND POLISH 10 MV/CM



**ULTRASONIC RECORDS**

NO STRESS 0.02 V/CM  
127 KSI STRESS 0.05 V/CM



AFTER FIRST POLISH 0.02 V/CM



AFTER SECOND POLISH 0.02 V/CM



NOTES: ALL RECORDS MADE AFTER  $2.76 \times 10^6$  STRESS CYCLES  
THE MAGNETIC AND ULTRASONIC RECORDS ARE FOR CRACK SIZE AND POLISH CONDITIONS INDICATED BY PHOTOMICROGRAPH  
IN CORRESPONDING ROW

**FIGURE 19. SURFACE PHOTOMICROGRAPHS WITH CORRESPONDING MAGNETIC AND ULTRASONIC RECORDS DURING CRACK REMOVAL SEQUENCE ON SPECIMEN NO. 18**

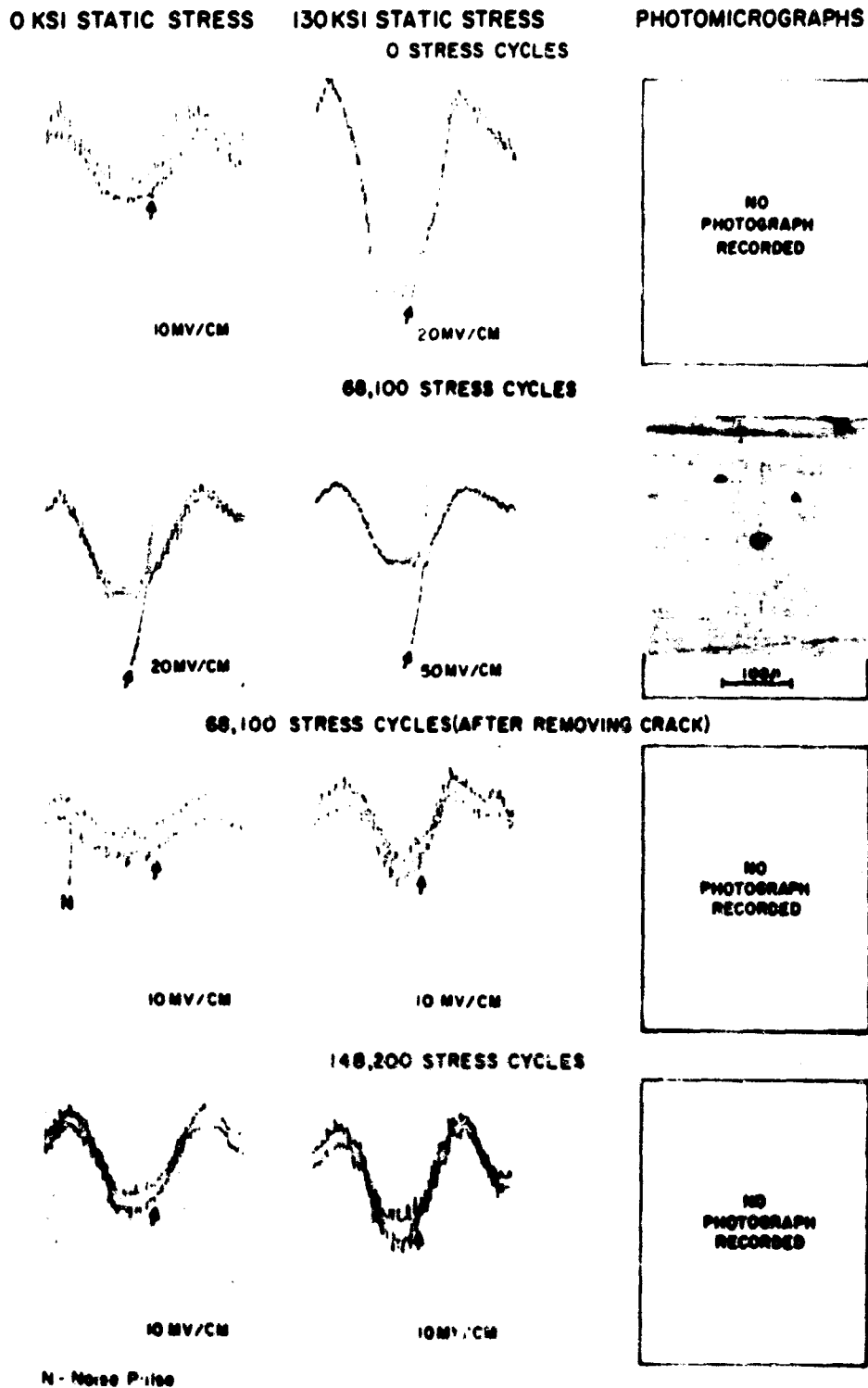


FIGURE 20. MAGNETIC INSPECTION RECORDS BEFORE AND AFTER FATIGUE CRACK REMOVAL AND SUBSEQUENT CYCLING ON SPECIMEN NO. 20  
H-29

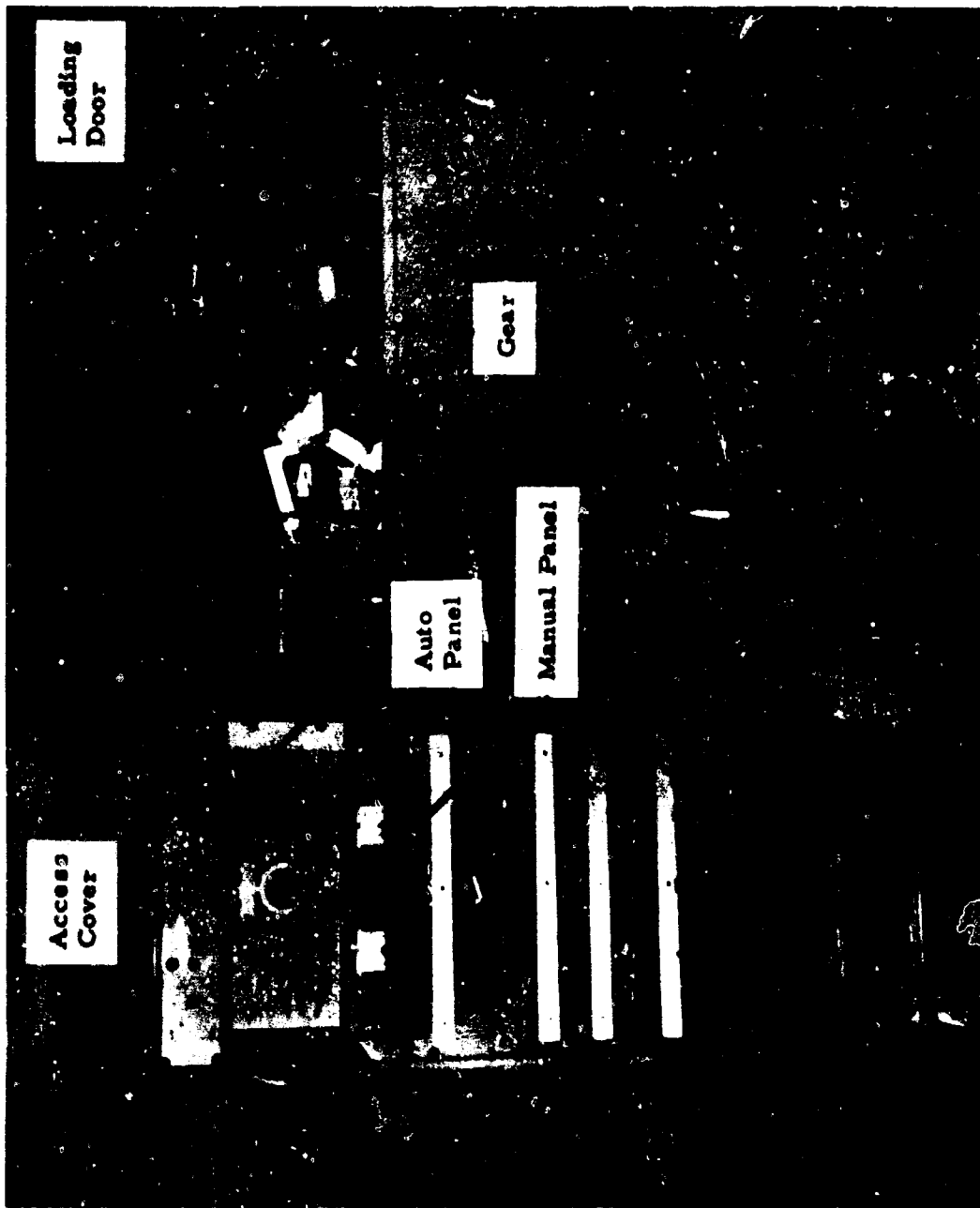


FIGURE 21.  
OVERALL VIEW OF SEMI-AUTOMATIC MAGNETIC PERTURBATION INSPECTION EQUIPMENT  
FOR FATIGUE DETECTION IN RING GEAR FROM SH3A HELICOPTER TRANSMISSION

evaluated at the Naval Air Rework Facility at North Island, California. This gear inspection equipment uses a special design of Hall probe, and the fabrication techniques previously developed on the AFOSR program were essential.

Recently, a specialized equipment was developed for inspecting the steel structural spar of the CH46 helicopter rotor blade. It was necessary that the inspection be accomplished entirely from inside the spar in the fully assembled blade. Figure 22 shows an overall view of the semi-automatic equipment, and Figure 23 shows the 40-channel probe which is inserted into the inside of the spar for inspection. Automatic alarms are actuated when a specified size of flaw is encountered. One equipment is in use at the Boeing Company, and a second equipment is used at the Naval Air Rework Facility at North Island, California.

Although no actual equipment has as yet been designed and fabricated to permit routine inspection of compressor blades using the ultrasonic surface wave approaches enhanced by an applied bending load, a rudimentary laboratory apparatus which confirms the validity of the approach has been built. This apparatus is shown in Figure 24 which includes a detachable transducer and a fulcrum for applying a bending load during examination. A number of compressor blades which have been in service have been routinely examined using this approach. Typical inspection results obtained on a service blade which was stress cycled to develop a tiny fatigue crack are shown in Figure 25. Note the outstanding signal obtained in the left record which is a reflection from the platform edge. With a bending load applied, note the signal adjacent to the platform signal which is caused by the tiny fatigue crack. This crack is only approximately 0.012 inches long.

Other applications have included use of the ultrasonic surface wave and also the electric current injection in the detection of tenon cracks in an aluminum compressor disk of the T58 gas turbine engine. Also, recently the feasibility of inspecting turbine blades for leading and trailing edge thermal fatigue cracks using the electric current injection method has been demonstrated.

## VI. FUTURE RESEARCH AND POTENTIAL APPLICATIONS

It has been found that the fatigue cracks on these rod type tensile specimens have invariably initiated at surface or near-surface inclusions in the absence of other geometric stress concentrators such as gauges and nicks. Other work has shown a similar situation to occur in anti-friction bearings and several other types of components. While it is not possible at this time to generalize, these results as well as other research<sup>(10-12)</sup> suggest that such sources, inclusions, are the real sites for fatigue damage development in many types of steels. Furthermore, it is reasonable to suggest that removal of these sites might, in fact, result in specimens which would exhibit superior fatigue performance.

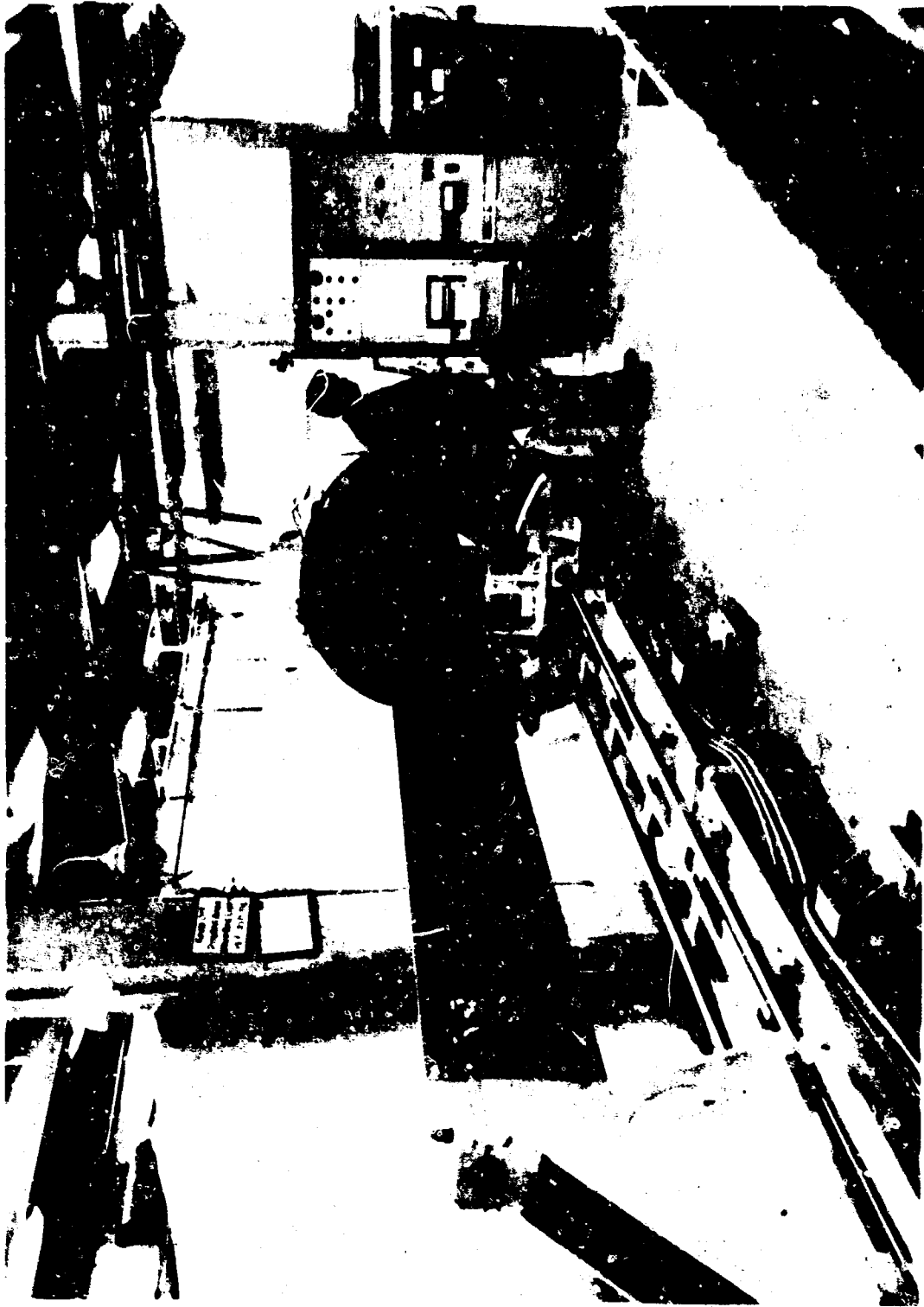


FIGURE 22 MAGNETIC PERTURBATION INSPECTION SYSTEM  
(A02GS005-1) FOR CH-46 ROTOR BLADES

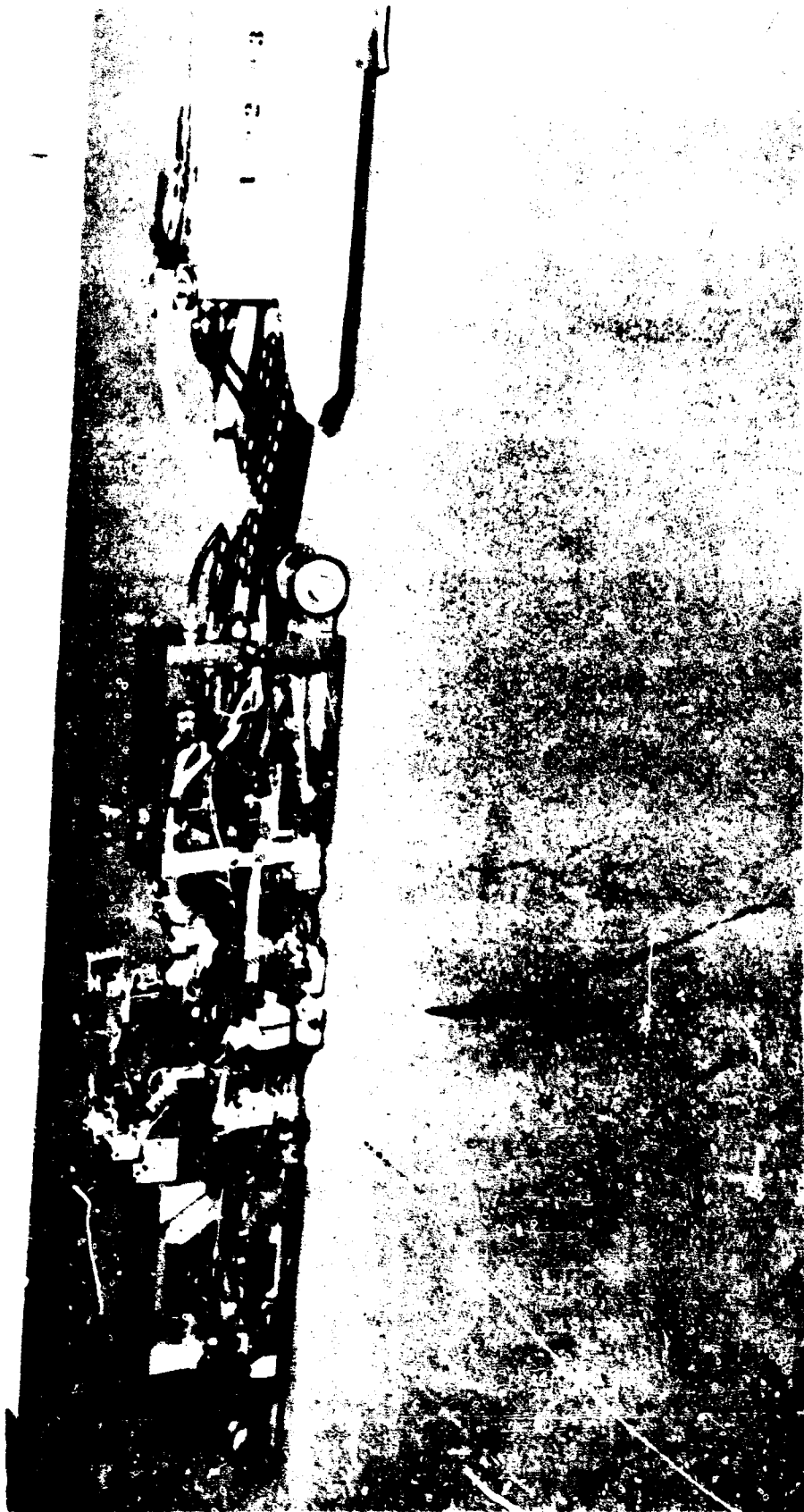
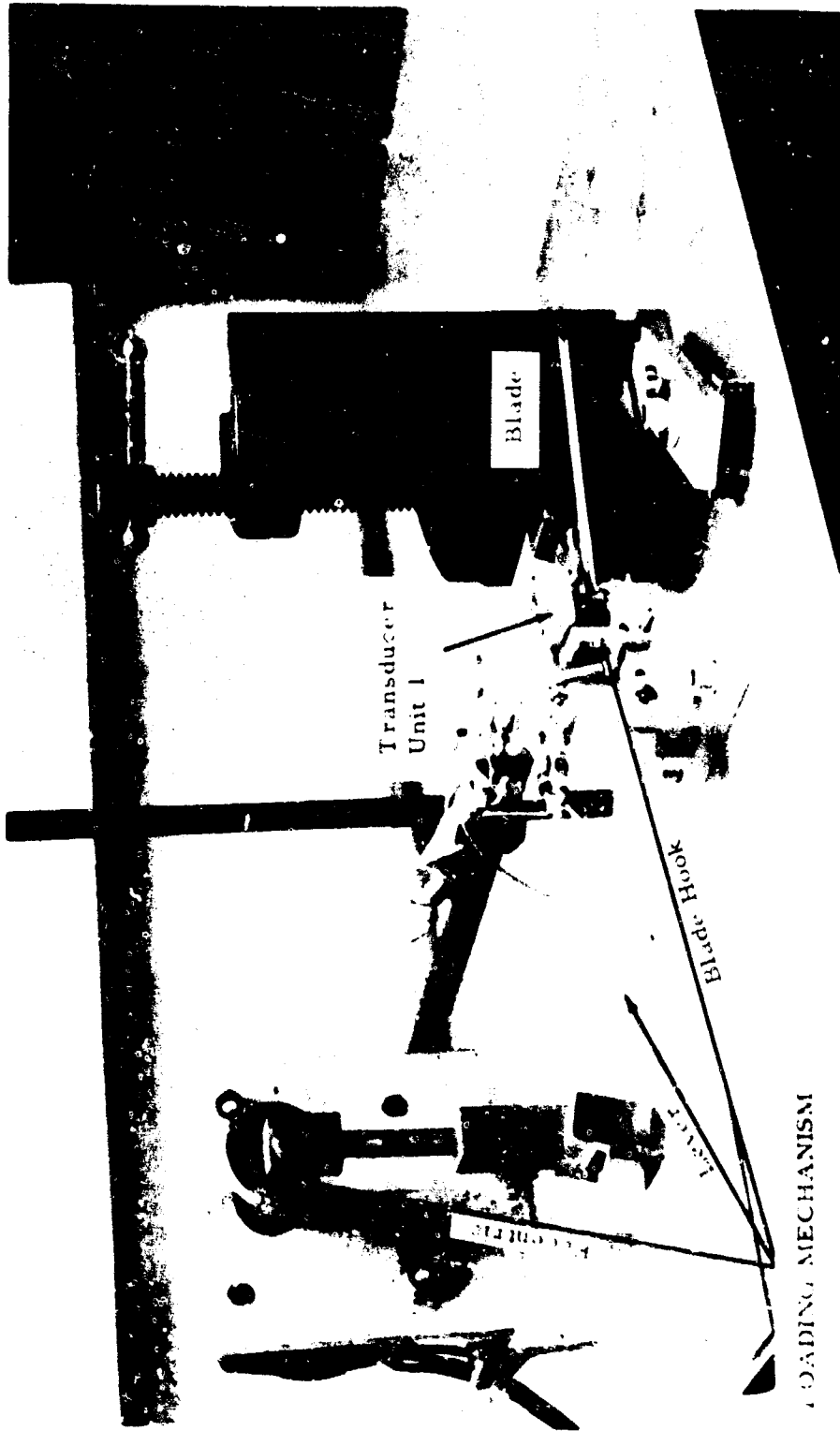


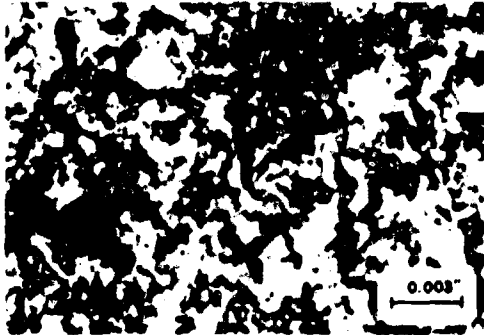
FIGURE 23. FORTY CHANNEL PROBE FOR D-SPAR INSPECTION



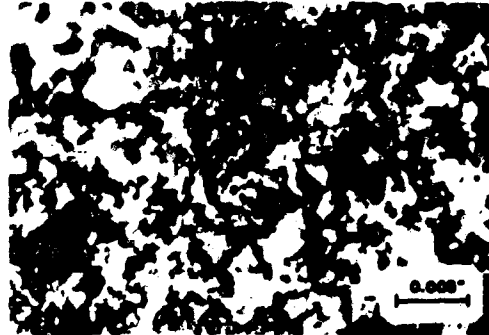
LOADING MECHANISM

FIGURE 24. LABORATORY APPARATUS FOR STRESS ENHANCED ULTRASONIC SURFACE WAVE INSPECTION OF T53 ENGINE COMPRESSOR BLADES

PHOTOMICROGRAPHS OF SURFACE FATIGUE CRACK IN BLADE NO. 4



NO STRESS APPLIED



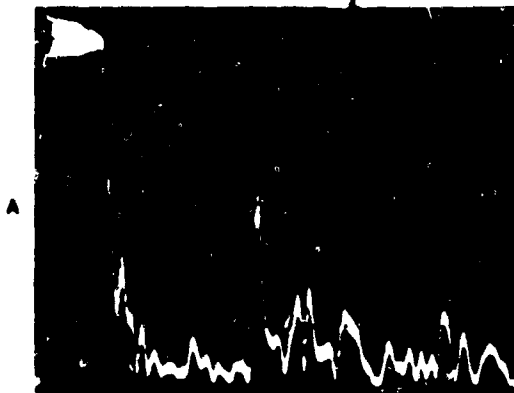
BENDING STRESS APPLIED

ULTRASONIC RESPONSE

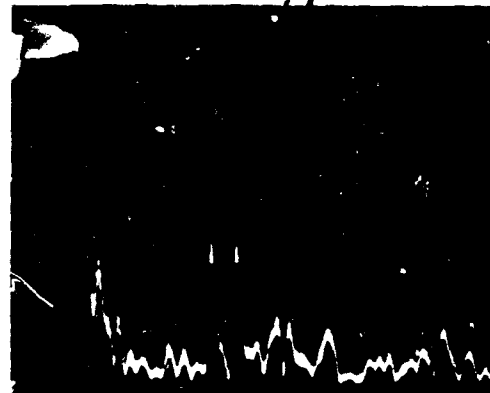
PLATFORM EDGE



0.012 INCH LONG FATIGUE CRACK



NO STRESS APPLIED



BENDING STRESS APPLIED

NOTE: VERTICAL SENSITIVITY - 15MV/CM  
HORIZONTAL SWEEP - 5μ SEC/CM

FIGURE 25. ULTRASONIC RECORDS FROM FATIGUE DAMAGED COMPRESSOR BLADE WITH SURFACE PHOTOMICROGRAPHS OF FATIGUED REGION

As a preliminary step in this direction, a statistical comparison of the fatigue performance of the specimens used on this program with handbook data has been made. These results are presented on the S-N curve of Figure 26. Although only a relatively few specimens are involved, it is apparent that no marked discrepancy exists between the "lives" obtained on these rod-type tensile specimens and other published fatigue data<sup>(13, 14)</sup>. Only those specimens which have actually failed or which have developed a fatigue crack were included in the data of Figure 26. Data from all specimens including suspended items are shown in the S-N plot of Figure 27. Several significant aspects of these data will be discussed. The specimens, triangular symbols, in which the fatigue crack initiated at a source significantly subsurface, that is greater than approximately 0.010 inches, all fall well above the standard handbook S-N curve; in fact, specimens No. 11 and No. 13 are remarkably well above the curve. It should be noted that the ordinate for each point is determined by the calculated section stress existing at the point of crack development or failure initiation, and the abscissa include the projected cycles to failure for unfailed specimens with fatigue cracks. Also, the suspended items are well above the curve, and several of these have been cycled to approximately 3 million cycles at which time cycling was terminated. The open circle points in which the fatigue crack initiated at or near the surface, with few exceptions, fall approximately on the curve for the handbook data. The points for specimen No. 6 and No. 19 are quite conspicuously well below the curve. Specimen No. 6 was one of the first specimens used in the program a number of years ago and was cycled to failure only to obtain approximate life cycles to failure. No nondestructive inspection records were obtained and the specimen was not monitored in any fashion. However, in the case of specimen 19, which was only recently cycled and, of course, was monitored, a logical basis - this will be discussed later - has been established for the occurrence of the crack at this low stress, which is well below the endurance limit for the material.

Results of the crack removal experiments can be shown in a significant fashion on this curve. Specimen 20, located at approximately 130,000 psi and  $10^5$  cycles developed a crack at 68,100 cycles which was mechanically removed and cycling continued. The specimen failed at 176,000 cycles. Examination of the fracture surface disclosed that the fatigue crack had initiated at a minute inclusion approximately 0.0005 inches diameter and located approximately 0.001 inches beneath the surface. Specimen No. 18, slightly below 130,000 psi and near the right end of the curve, developed a crack at a small surface inclusion, see Figures 12 and 13, after 2,760,000 cycles. This crack was removed and subsequently an additional 130,000 cycles were added. This is approximately four times the anticipated number of cycles which could have been added before the specimen fractured if the original crack had been left in the specimen. Cycling was suspended after 130,000 cycles and no significant changes had apparently occurred.

The most recent specimen involved in the crack removal studies has been specimen No. 19. During cycling of this specimen an ultrasonic

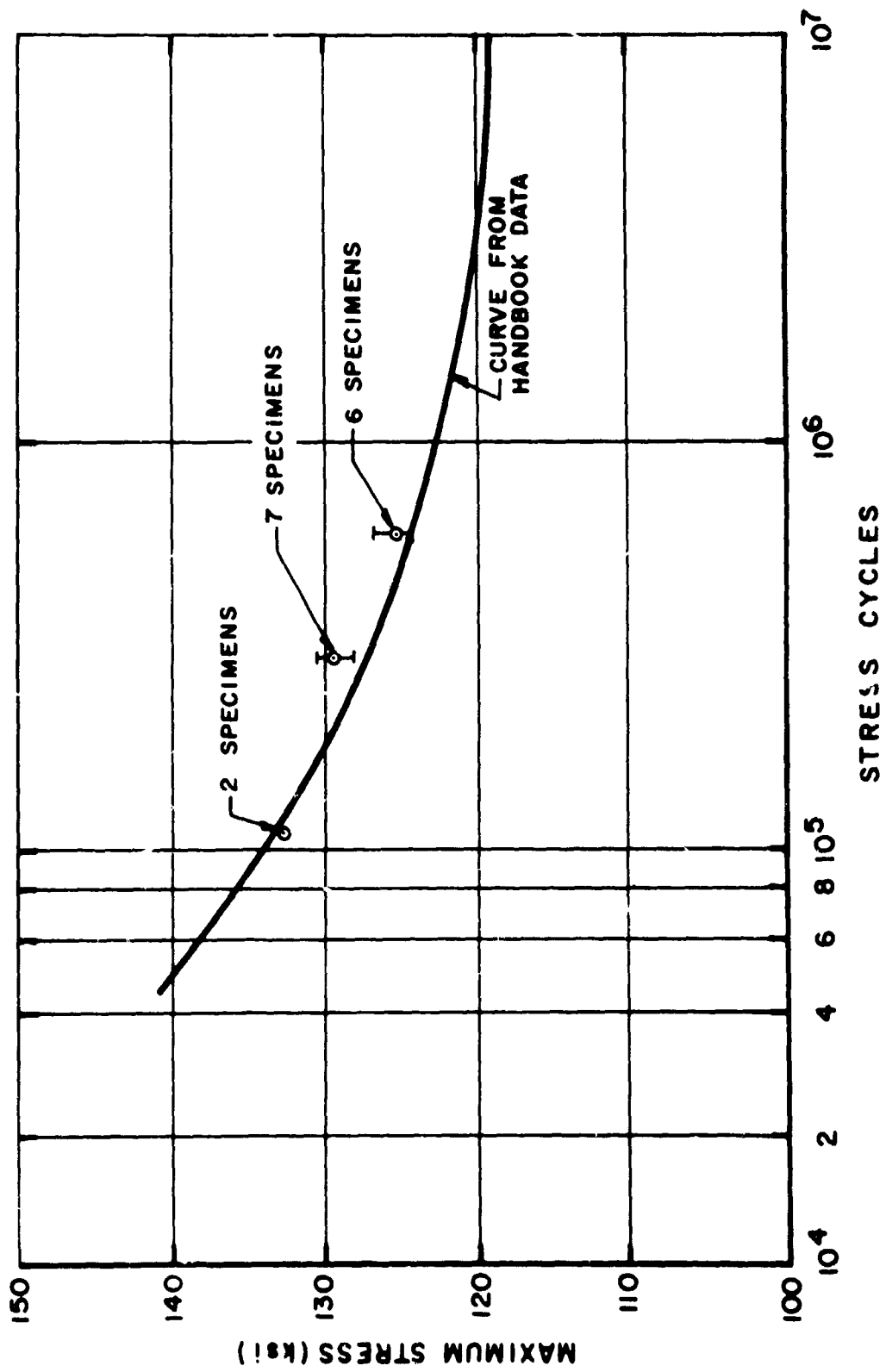


FIGURE 26. STATISTICAL COMPARISON OF SPECIMEN LIVES WITH S-N CURVE FOR AISI 4340 SMOOTH UNNOTCHED TENSILE SPECIMENS

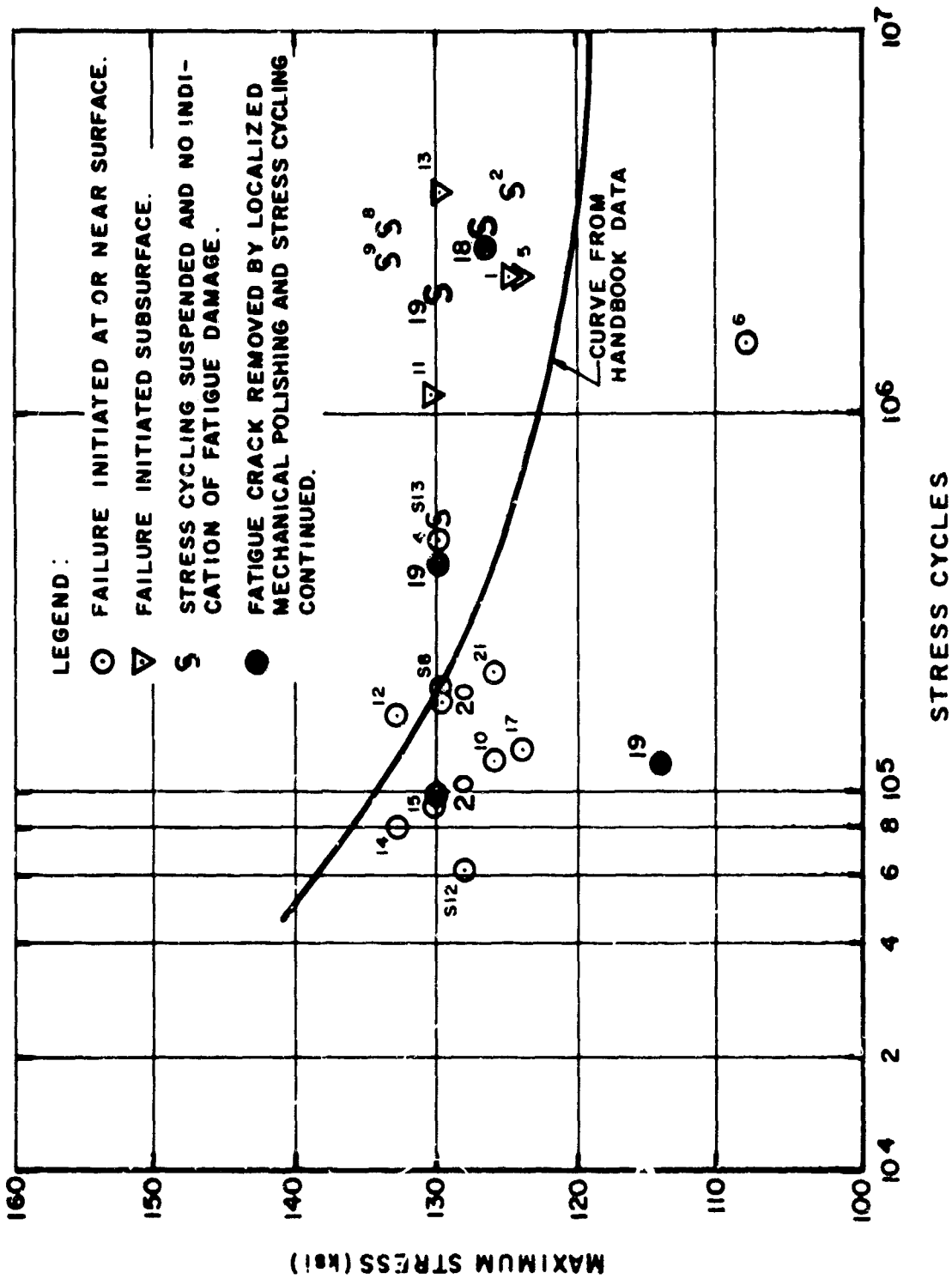


FIGURE 27. INDIVIDUAL COMPARISON OF SPECIMEN LIVES WITH S-N CURVE FOR AISI 4340 SMOOTH UNNOTCHED TENSILE SPECIMENS

signal indication was observed at 86,600 cycles at which time cycling was interrupted for microscopic examination. Subsequent studies indicated that two tiny cracks had initiated from two adjacent subsurface inclusions. Photomicrographs showing the cracks and the inclusions are presented in Figure 28, illustrations A. Undoubtedly the proximity of these two inclusions and the consequent stress concentration accounts for the cracks developing at this low section stress. After these cracks were completely removed, cycling was continued until 377,000 cycles at which time another crack developed from a surface inclusion or surface pit. This crack region is also shown in Figure 28, illustration B. After removal of this crack cycling was again continued until two million cycles were accumulated at which time cycling was suspended, and no changes had apparently occurred.

It is reasonable to assume that removal of the nucleating sources for fatigue cracks, namely, surface and near-surface inclusions and pits, will result in significantly increased specimen lives, since it has been possible to achieve extended life on specimens by removal of "developed fatigue cracks and the nucleating source". A direct demonstration of such an approach will be made in the near future. Provided the defect removal concept is substantiated, it is reasonable to anticipate that practical methods can be developed by which the life of components and structures may be significantly extended through selective removal of potential fatigue nuclei. Furthermore, on the basis of results already obtained, it should be possible to salvage many "fatigued" parts by selective removal of fatigue cracks during overhaul inspection when detection equipment with adequate sensitivity and precision is available. It should be cautioned that each case will have to be treated individually, since no general predictive basis has been developed for a wide range of materials and conditions. Furthermore, it appears that specialized rather than general purpose equipment will be required. However, it should not be difficult to establish economic justification since in many instances components that would be inspected and "saved" are extremely costly.



(A) BEFORE INITIAL POLISH

86,400 CYCLES - SPECIMEN 19



(B)

377,000 CYCLES - SPECIMEN 19



(A) AFTER INITIAL POLISH

86,600 CYCLES - SPECIMEN 19



68,100 CYCLES - SPECIMEN 20

FIGURE 28. PHOTOMICROGRAPHS OF SURFACE FATIGUE CRACKS IN SPECIMENS NO. 19 AND 20

## REFERENCES

1. Pattman, P. F., Peirson, H. F., Owens, J. S., and Marchese, G. B., "The Applicability of a Fracture Mechanics-Nondestructive Testing Design Criterion", AFML Technical Report 68-32, May, 1968.
2. Leonard, B. E., Kusenberger, F. N., Barton, J. R., "Feasibility Investigation for Stress Enhanced Ultrasonic Surface Wave Inspection of Compressor Blades", Final Report, August, 1967, under contract DAAJ01-67-C-0721(G).
3. Kusenberger, F. N., Barton, J. R., and Donaldson, W. Lyle, "Nondestructive Evaluation of Metal Fatigue", AFOSR Final Scientific Report 65-0668, 13 March 1964.
4. Kusenberger, F. N., Leonard, B. E., Barton, J. R., and Donaldson, W. Lyle, "Nondestructive Evaluation of Metal Fatigue," AFOSR Scientific Report 65-0981, March, 1965.
5. Kusenberger, F. N., Leonard, B. E., Pasley, R. L., Barton, J. R. and Donaldson, W. Lyle, "Nondestructive Evaluation of Metal Fatigue", Scientific Report 1965-1966, March, 1966.
6. Kusenberger, F. N., Barton, J. R., and Donaldson, W. Lyle, "Nondestructive Evaluation of Metal Fatigue", AFOSR Final Scientific Report 67-1288, April, 1967.
7. Kusenberger, F. N., Leonard, B. E., Francis, P. H., Barton, J. R., and Donaldson, W. Lyle, "Nondestructive Evaluation of Metal Fatigue", Scientific Report 1967-1968, April, 1968.
8. Grosskreutz, J. C., Rollins, F. R., "Research on the Mechanisms of Fatigue," WADC Technical Report 59-192, September, 1959.
9. Grosskreutz, J. C., "Research on the Mechanisms of Fatigue, WADD Technical Report 60-313, April, 1960.
10. Gilman, J. J., "Physical Nature of Plastic Flow and Fracture", Plasticity - Proceedings of the Symposium on Naval Structural Mechanics, Pergamon Press, 1960.
11. Atkinson, M., "Influence of Nonmetallic Inclusions on Fatigue Properties", Journal of the Iron and Steel Institute, Vol. 195, p. 64 1960 .
12. Cummings, H. N., Stulen, F. B., and Schulte, W. C., "Tentative Fatigue Strength Reduction Factors for Silicate-Type Inclusions in High Strength Steels", Proceedings of the ASTM, Vol. 58, p. 505 1958

13. Grover, H. J., "Fatigue of Aircraft Structures", Appendix C, NAVAIR 01-1A-13, Department of the Navy, 1960.
14. ASM Metals Handbook, Vol. 1, Eighth Edition, Reinhold Publishing Corp., 1961.

APPLICATION OF THE STATISTICS OF  
IONOSPHERIC SCINTILLATION TO VHF AND UHF SYSTEMS

Richard S. Allen

Ionospheric Physics Laboratory

Air Force Cambridge Research Laboratories

L. G. Hanscom Field, Bedford, Massachusetts

APPLICATION OF THE STATISTICS  
OF IONOSPHERIC SCINTILLATION TO VHF  
AND UHF SYSTEMS

by

Richard S. Allen  
Ionospheric Physics Laboratory  
Air Force Cambridge Research Laboratories  
L. G. Hanscom Field, Bedford, Massachusetts

ABSTRACT

Irregularities in the ionosphere cause multipath, diffraction, and time jitter of radio waves relayed by satellites. These effects can seriously hamper communication, navigation, and surveillance systems. Proposed new systems require information on such properties as depth and rate of fading, power spectra, and time delay, whereas most previously accumulated data provided information only on depth and rate of fading. In addition, the proposed new systems create a need for predicting the effects at remote locations, new radio frequencies, and extremes of geophysical conditions.

Using the facilities at AFCRL and at observatories of a cooperative world-wide group, new measurements are being made with military and civilian satellite systems in order to apply the statistics of irregularities to the new requirements. Results provide first-order estimates of the statistical effects of the irregularities in the ionosphere with the observing radio frequency, sub-ionospheric latitude, geomagnetic conditions, seasonal and diurnal time, and with solar cycle. Techniques are being developed for predicting trends and mean characteristics, both of which are required for operational systems. The conversion of the radio star and satellite observations into engineering data is assisting systems designers of communications satellite systems in their choice of modulation schemes, in their estimates of system capabilities, and in improving system reliability.

## 1. INTRODUCTION

Irregularities in the ionosphere cause deep amplitude fading, phase changes, and time jitter of radio signals relayed through communication satellites. The strength and occurrence of these irregularities are related to the sporadic geophysical storms that disrupt the North Atlantic (aurora!) and South East Asia (equatorial) radio links. During periods of geophysical disturbance, as in Figure 1, the irregularities are greatly enhanced. VHF and UHF communication via satellite can then fade rapidly to 10 to 20 dB below normal signal level for periods of several minutes or several hours. Operational users are concerned about the degradation of present communication and detection systems. Strategic and tactical users are particularly concerned with the degree to which this degradation is related to those geophysical events that also degrade other point to point systems. Designers of proposed navigation and constant surveillance systems using VHF signals relayed through two satellites are concerned that storms of irregularities could cause time or phase jitter than would force using agencies to turn back to less precise methods of air traffic control.

Present research on ionospheric irregularities at AFCRL is aimed at providing pertinent statistical information to designers and operational agencies. Operational users can then forecast the probabilities of future irregularity behavior from current geophysical data. In addition, AFCRL's studies can help provide the long term statistical data upon which system decisions can be made.

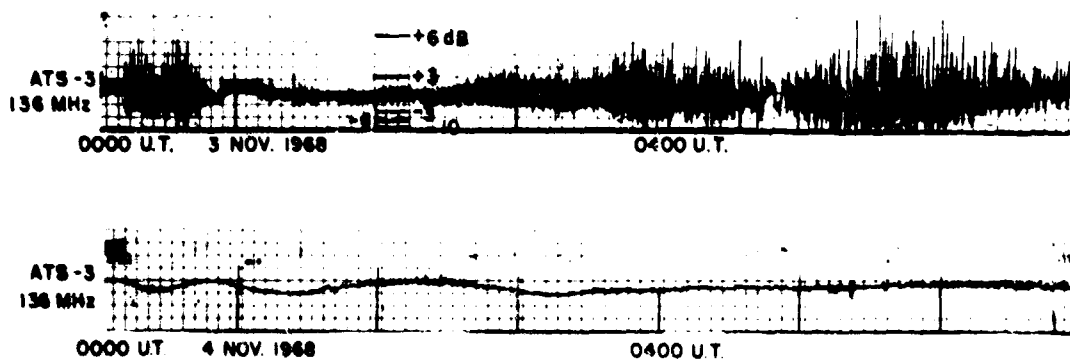


Figure 1. Intense Scintillation of ATS-3 Beacon. Deep fades to -10 or -20 dB can occur at VHF and UHF during periods of ionospheric disturbance, as on November 1968. Behavior is normal the following night, 4 November. Matched loads are reference level each hour

## 2. BACKGROUND

The amplitude and phase deviations found on a radio wave (Figure 1) that has traversed a region of ionospheric irregularities are known as scintillations. They were first observed during the late forties and early fifties when it was established that the fluctuations in intensity of radio stars were caused by irregularities in the ionosphere. Several theoretical treatments evolved to explain the observations. A two-dimensional, "thin-screen" analysis such as that of Mercier (1962) is useful when the irregularities are weak and appear to occur in thin layers, but during extremes of geophysical disturbances the thickness of the irregularity region must be considered, as in the three-dimensional treatment of Orhaug (1965).

In the model, the effective strength of the irregularities was restricted so that the radio wave underwent weak diffraction or weak scattering. In effect this means that at the exit of the irregularity region the radio wave intensity averaged over many fluctuations is the same as the normal undisturbed level. Yet the converse is more nearly true for the enhanced irregularity regions which degrade VHF and UHF satellite relays. Appreciable energy may be diverted from the relay path. In that case the assumptions of existing theory are violated, and the behavior for strong irregularities cannot be predicted from theoretical characteristics derived from studies of weak irregularities. Since it is extreme disturbances, when the irregularity region is enhanced beyond the limits permitted by the simplifying assumptions of these theoretical studies, that degrades the satellite radio link, other means must be found to predict their effect on the system.

## 3. OBSERVATIONAL PROCEDURE

A great deal of data on the effects of ionospheric irregularities exists from scintillation studies made since 1949 with radio star sources and beacon satellites. Most of this data is in the form of indices for the depth or rate of fluctuation of the intensity of radio waves. Specific organizations need data that is not explicitly contained in the reports of these studies.

Systems now in use and those being developed require statistical summaries and reliable techniques for predicting the effects of ionospheric irregularities at remote locations, on new radio frequencies, and during extremes of geophysical conditions.

It is not practical to rescale existing data to meet these new requirements, nor is it practical to re-instrument all of the observatories so that they can measure the critical radio frequencies for the latitude-longitude network needed to collect new data. Rather, enough new measurements can be performed to statistically relate the new requirements, such as depth and duration of deep fading, to the existing indices. Since existing theory cannot be used to extend median observations to those expected for extreme conditions, a world-wide morphology of irregularity effects must be established, using the various quantitative scintillation indices presently available.

### 3.1 Source of Data

The radio stars Cassiopeia A and Cygnus A were the principal sources of data in the early scintillation studies at Hamilton, Mass. The 84-ft-diam, polar-mounted antenna was instrumented to simultaneously record 63, 113, 228, 400, and 1200 MHz; the 150-ft-diam antenna simultaneously recorded 30, 63, 113, and 228 MHz.

At the latitude of Hamilton, Mass., the circumpolar source, Cassiopeia A, rotates about the polar star and its elevation angle varies from about 11 to about 77 deg; Cygnus A rises in the northeast, passes almost exactly overhead, and sets in the northwest. Results of studies of both sources are thus confined to the northern sub-auroral region (Allen et al, 1964; Aarons and Allen, 1966).

Observations of the 54 MHz beacon of satellite Transit 4A were made at Hamilton from July 1961 to February 1965. Observations on the 20, 40, and 41 MHz beacons of satellite BE-B have been made since November 1964. Both the satellites were placed in near circular orbits at about 1000 km height and at high orbital inclination. Results are available for all locations encompassed by the radio horizon (Aarons et al, 1964).

For contrast, note that the radio star sources have finite angular size, are at immense distance from the irregularities, and radiate unpolarized, incoherent noise-like signals. The satellites are point sources, are close to the ionosphere, and radiate linearly polarized, coherent signals.

Additional data was obtained from a world-wide network of observatories. The Joint Satellite Studies Group is a 23-member group of stations, voluntarily cooperating to provide comparative data on the ionosphere. Sources included the ionospheric satellites (Transit 4A, 54 MHz; BE-B and BE-C, 20, 40, 41 MHz), the communication satellites (Early Bird and Canary Bird, 136 MHz), and the air-to-ground relay satellites (ATS-1 and ATS-3, 136 MHz). This data represents a wide longitude and latitude sample and, therefore, provides a basis for studying morphological details of the irregularity region (JSSG, 1965; 1968).

### 3.2 Empirical Indices

Attempts to establish standard methods for scaling records have been only partially successful. If each observatory measured the root-mean-square value of the fluctuation of the received signal there could be consistent comparison of results with other observatories and with theory. Since few can afford the cost of that measurement, empirical indices have been established in several ways.

The arbitrary but consistent indices used by the Radio Astronomy Branch of AFCRL for reducing radio star and satellite observations can be described briefly as follows:

Rate is determined by counting peaks. A peak is counted only if it is at least one third the amplitude of the previous peak.

Scintillation Index (SI) is also a relative measurement. A sample interval containing at least 10 peaks, counted by the above rule, of at least

5 min duration is chosen from radio star records. A similar sample at the top of a Faraday peak is chosen for the satellite case. Representative peaks are established by the third peak down from greatest and the third up from the lowest. The power scintillation index is then the percentage ratio of the varying component to the expected steady component:

$$SI(\%) = \frac{P(\text{third peak up}) - P(\text{third peak down})}{2P(\text{average})} = \frac{\Delta P}{P}, \%$$

Analysis by planimeter and by point computations has indicated that this arbitrary index is from 1.5 to 2.5 times the rms value of the power variation. For radio star observations, the ratio is nearly the same at several frequencies but varies from day to day. From a statistical viewpoint, it may be assumed to have a fixed relation to the rms value.

All members of the JSSG use the same definition; however, some use the amplitude of the signal rather than the power.

In addition, many of the observatories that have published previously, and some that are doing current work, have assigned subjective indices. Simplest are 0, 1, 2 for zero, some, and fully fluctuating records. If samples of actual records are set up to define the class intervals for such indices and are carefully used during reduction, the final results can be reanalyzed to provide consistent comparative data.

#### 4. COMPARATIVE STATISTICS

The fluctuations observed on radio waves from distant satellites are indicators of irregularities that were formed in the upper ionosphere in response to outside forces. To describe the variation of these fluctuations in terms applicable to communication problems, it is convenient to use a morphological approach expressed in terms of three classes of variables that can be isolated in the statistical data. These are stimulus variables that represent changes in the forces that produce the irregularities, trait variables that characterize the ability of the ionosphere to respond to stimulation, and experimental variables that affect the amount of fluctuation observed for given irregularities.

##### 4.1 Stimulus Variables

The outside stimulators can be any pertinent energy source, such as an influx of charged particles induced by changes of the solar wind, turbulence arising from vertical motions produced by electric field changes, or other external forces that are presently unknown. Although the prime sources of all disturbing energies appear to be within the sun, the physical details of their interaction with the terrestrial atmosphere have not been determined.

At the present time it is necessary to use terrestrial responses to represent changes in solar energy. The variation of the earth's magnetic field, known to be associated with variations in the solar wind, has been useful in this study. Other responses, such as riometer absorption or airglow intensity, may prove useful. The effects of several solar sources of energy are implicitly included in some of the trait variables discussed in Section 4.3.

#### 4.1.1 Variation With Magnetic K Index (Solar Wind)

Magnetic K index is used here to relate the variation in response of irregularities to variation in the solar energy carried by the solar wind.

Individual observatories characterize the degree of disturbance of the local magnetic field during 3-hr periods by indices varying from 0 to 9. Normalized data from a world-wide network is then combined in a planetary index,  $K_p$ . Distribution functions for  $K_p$  conditional on calendar years are shown in Figure 2. The highest values represent periods when the magnetic field displayed major changes identified with period of intense solar disturbance. Note that the significant change with solar cycle is a change in the proportion of these high indices.

Just how the depth of scintillation varies with the state of magnetic activity depends on the geographic latitude and longitude of the irregularity region.

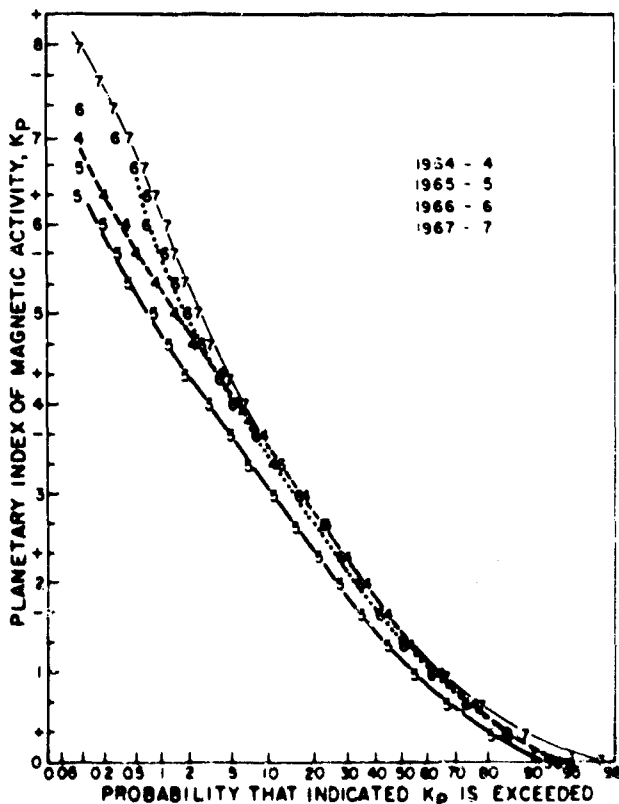


Figure 2. Variation of Magnetic Index, 1964-1967. The planetary index of magnetic activity is not normally distributed. Note the disproportionate increase of high K values for years of increased solar activity over 1964-1965, the period of solar minimum

At high geomagnetic latitudes the depth of scintillation increases with magnetic K index. Figure 3 contains distributions for sets of observations conditional on local magnetic K index. They represent the ionosphere region  $51^{\circ}$  N. Lat. to about  $55^{\circ}$  N. Lat., as seen from Hamilton, Mass., using the radio star Cassiopeia A. Effects of the increased thickness of the irregularity region arising from the slant viewing angle have not been removed; their effect is constant within the sample. For any statistic in the data, such as median or decile, there is a nearly linear increase with the index of the state of magnetic activity.

The change of this dependence with latitude is summarized (Figure 4) by data from a study of the 54 MHz beacon of satellite Transit 4A, taken at Hamilton, Mass., during regularly scheduled periods each month from January 1962 to February 1965. Conditional samples were based on sub-ionospheric (400 km) ranges of  $\pm 10^{\circ}$  Long. and  $5^{\circ}$  Lat. Mean values were produced for all data in sub-sets determined by integral values of the local magnetic K index  $K_{FR}$  from Fredericksburg, Va. Again, the effects of elevation angle have not been removed; this is unimportant since the effect is constant within each latitude sample.

The results for data pooled in this fashion can be summarized as follows:

At high latitudes there is an increase in depth of scintillation for increase of magnetic K index. The functional behavior of mean values can be related to the functional behavior of other statistics, such as the medians of Figure 3.

There is a progressive change in the functional relationship with decreasing latitude until, at mid-latitudes, the depth of scintillation does not increase with K index until the K index exceeds 4 or 5. Studies of a limited number of magnetic storms indicate that the depth of scintillation at mid latitudes increases sharply with very high K index.

As the irregularity region approaches equatorial latitudes, the functional relationship inverts and the depth of scintillation decreases with increasing K index (Latitude interval  $30^{\circ}$  to  $35^{\circ}$  in Figure 4). Special studies in the equatorial region over Africa (Koster and Wright, 1960) have shown that there is negligible change with K index during the minimum of the solar cycle, but a strong inverse relationship during solar maximum.

#### 4.2 Experimental Variables

For identical conditions in the irregularity region, the fluctuations found by different observers will depend on several experimental variables. These are, principally, the frequency and bandwidth of the radio wave signal and the geometric angle at which the irregularity region is viewed. In some cases the distance of the source from the irregularities and the separation of antennas used for space diversity on the ground can also be treated as experimental variables.

If these variables are independent of the trait and stimulus variables, then some form of an analytic function can be uniquely determined to

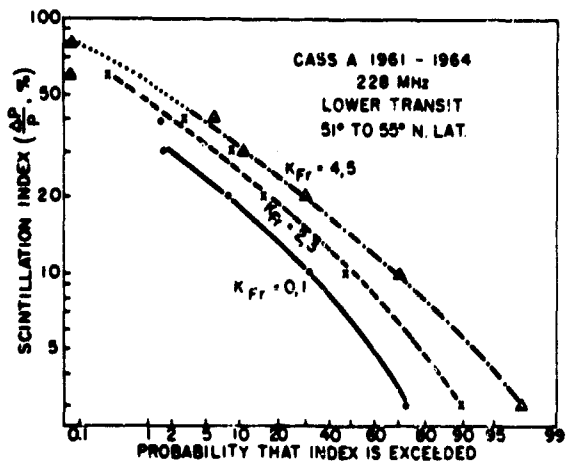
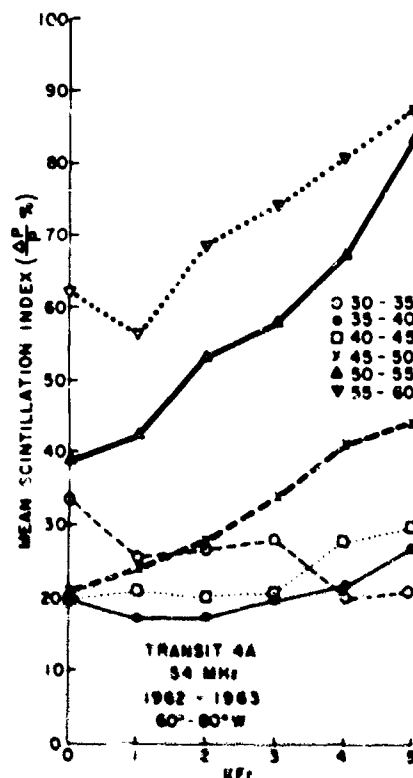


Figure 3. Variation of Scintillation Index With Local Magnetic K Index. The probability that a given depth of scintillation is exceeded increases nearly linearly with local K index for observations at the southern edge of the auroral region

Figure 4. Latitude Change of the Magnetic K Dependence. At high latitudes above Hamilton, Mass., the mean depth of scintillation increases nearly linearly with local magnetic K index. Overhead, in the region  $40^\circ$  to  $45^\circ$  geographic, there is no change until K is greater than about 5. Southward,  $30^\circ$  to  $35^\circ$ , the mean depth of scintillation decreases with increasing K index



represent their variation, as is done for radio frequency in Section 4.2.1. Otherwise a set of functions must be determined, conditional on the other variables that influence their behavior.

#### 4.2.1 Variation With Radio Frequency

The theoretical prediction of the frequency variation of scintillation depends on several parameters of the irregularity region. Although these are generally unknown, limits can be derived. If the irregularity region can be represented by a thin screen, then close to the irregularity region the depth of scintillation is nearly inversely related to the square of the frequency; far from the region it is inversely related to the first power of the radio frequency (Briggs and Parkin, 1963). As the thickness of the layer becomes more significant, the exponent decreases toward zero.

- Emperical studies of this variation were made by AFCRL at Hamilton, Massachusetts (Aarons et al, 1967). Simultaneous observations were taken at 30, 63, 113, and 228 MHz, using the 150-ft radio astronomy antenna, and at 63, 113, and 228, using the 84-ft antenna, for the overhead and northern regions covered by the daily motion of the radio star Cassiopeia A. Figure 5 shows cumulative distributions for observations made through the auroral region. When the irregularities are weak, the depth of scintillation and, hence, the scintillation indices are low. The

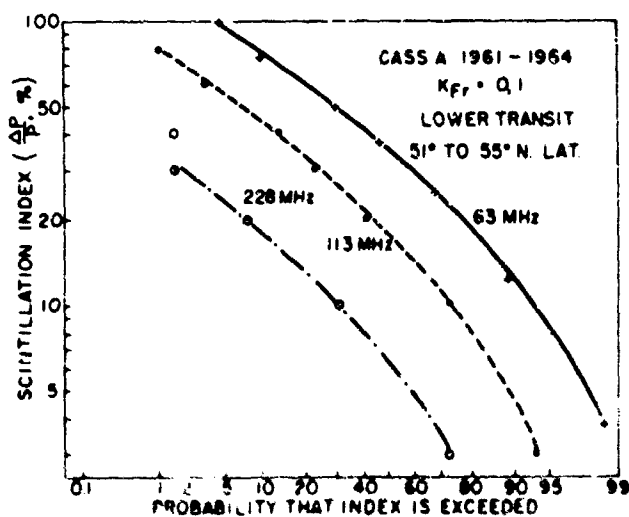


Figure 5. Variation of the Depth of Scintillation With Radio Frequency. At low depths of scintillation there is a nearly inverse square-law-dependence on radio frequencies for low depth of scintillation. As the intensity of the irregularity region increases, the exponent of dependence decreases

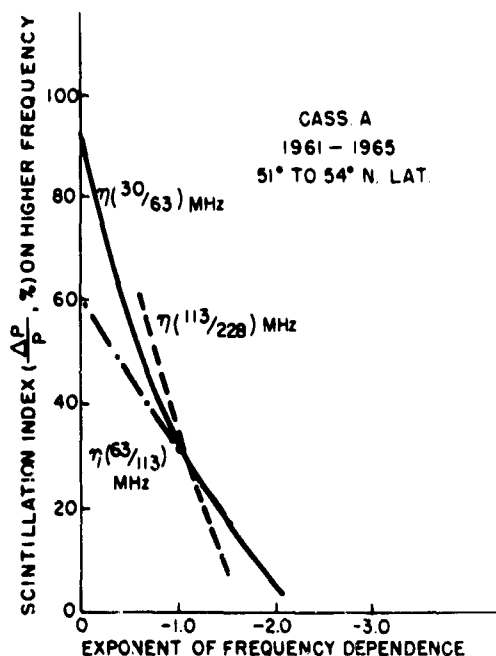


Figure 6. Variation of Frequency Dependence With Scintillation Index. Observations of Cassiopeia A at 30, 63, 113, and 228 MHz indicate that the mean frequency dependence can be specified in terms of the depth of scintillation on one of the frequencies

depth of fluctuation then depends inversely on the square of the radio frequency.

As the irregularities are enhanced, the indices increase and the exponent of frequency dependence decreases.

Results for the auroral ( $51^{\circ}$  to  $55^{\circ}$ N. Lat) and for the overhead regions ( $43^{\circ}$  to  $45^{\circ}$ N. Lat) are summarized in Figure 6. The frequency variation seems to depend only on the effective strength of the irregularities. No appreciable change was noted between the latitude samples. No systematic difference was found for samples conditional on the state of the local magnetic field, an indicator of disturbance in the ionosphere.

It is not known if these results will also apply to low latitudes and the equatorial region.

#### 4.2.2 Geometric Variation

If the distribution of irregularities in the ionosphere were similar to a reasonably thin screen, the depth of fluctuation would be expected to vary with elevation angle to the source in the same manner as the apparent thickness of the screen varied. It is now known that this is not valid at all latitudes.

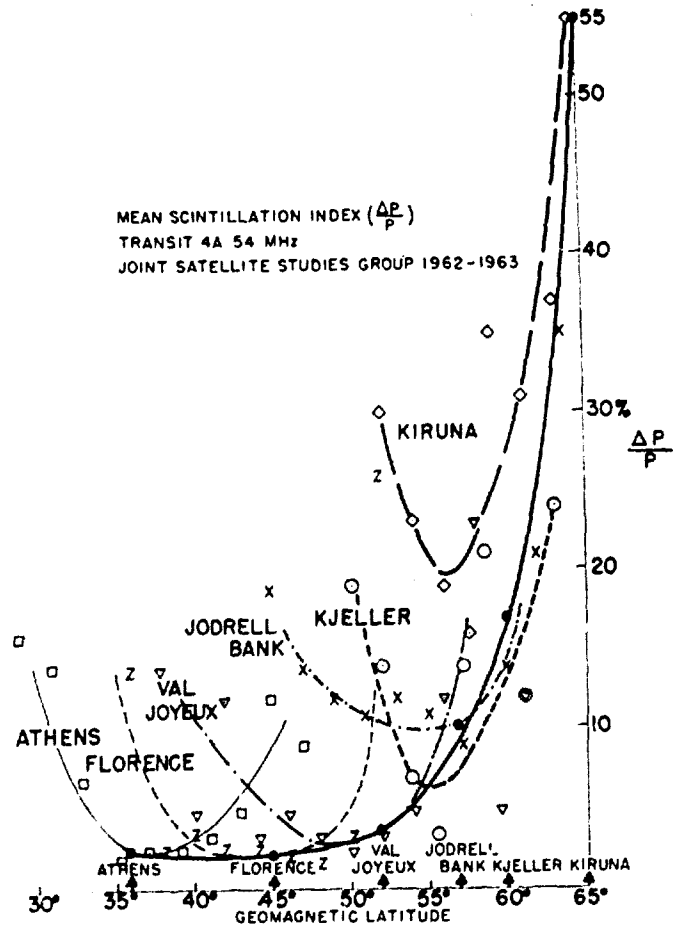


Figure 7. Geometric Variation of the Depth of Scintillation. Derived from simultaneous measurements by members of the Joint Satellite Studies Group. Mean overhead values are linked by a smooth curve representing the latitude variation. Off-vertical observations show the effect of elevation angle

When a statistical latitude variation can be derived from mutually consistent observations, as in the JSSG study to be discussed in Section 4.3.1, the nonoverhead observations at a particular site can be examined for geometric effects. Data from the JSSG study shown in Figure 7 were restricted to common periods of observations for which the magnetic K index was less than 3 and, therefore, represent the main geometric features during quiet geomagnetic conditions. At mid-latitudes where the average depth of scintillation was low, the non-overhead indices increase toward the horizon more or less as the secant of the zenith angle times the expected sub-ionospheric depths of scintillation. At sub-auroral latitudes where the overhead depth of scintillation increased somewhat, observations southward still increase with the slant thickness of the irregularity region but northward the increase is less than expected. This is probably

the result of several factors: a thickening of the irregularity region, a reduction of slant range to the irregularity, and perhaps also a decrease in the size of the irregularities.

#### 4.3 Trait Variables

Trait variables ( $T_i$ ) characterize the ability of the ionosphere to respond to a given stimulus. For example, a difference in response on two different occasions may be due to a difference in the recombination rates of ions and electrons and, hence, a difference in the life time for initially identical irregularities. Physical parameters, such as recombination rates change because of undetected changes in the energy sources that affect the ionosphere. The changes in the irregularity behavior caused by integrated changes in physical parameters can be characterized by trait variables, such as the cyclic changes over the day, solar month, year, and sunspot period. Each of these most likely combine the effects of several parameters, such as electron temperature, neutral gas density, ionospheric wind systems, and so on. Less easy to identify in the data are changes in these trait variables caused by a sudden change in a single parameter, such as a sudden change in composition ratio or in temperature.

Use of trait variables to determine the degree to which the ionosphere responds to physical changes indicates the need for a more reliable way to determine physical parameters and a better theory of irregularity formation and behavior.

Since trait variables are averages over time or space, they represent the integrated effects of a number of undetected, unknown, or sporadic stimuli. An understanding of the physical process at work within the irregularity regions is lost in such a characterization.

For just that reason trait variables are desirable for a study such as this one. By submerging the response of individual events, they establish overall systematic trends in the response of the whole irregularity region without depending on a complete physical understanding of individual processes.

##### 4.3.1 Latitudinal Variation

Early reports of the scintillation of radio stars (Little, 1951) and beacon satellites (Kent, 1959) noted that the depth of scintillation increased toward the polar region faster than would be expected from purely geometric effects. In a recent study (JSSG, 1968), observations from several stations were combined to establish the quantitative aspects of this variation.

Figure 8 summarizes the results from two sets of data. The first set is from simultaneous observations of the 54 MHz beacon of satellite Transit 4A. The resultant smooth variation with geomagnetic latitude is conditional on nearly identical geometric factors over each JSSG station and on periods of magnetic activity with K index less than 3. The individual observations were spaced from June 1962 to March 1963 by cooperative observational periods selected without meaningful bias.

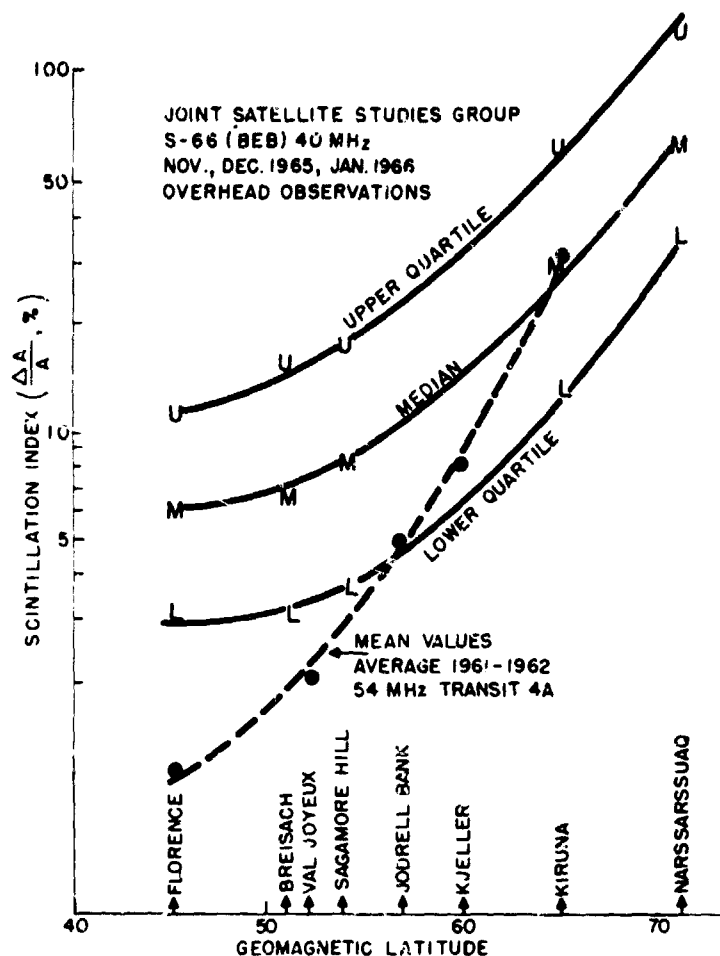


FIG. 4 LATITUDE VARIATION OF THE DEPTH OF SCINTILLATION FOR SEVERAL EUROPEAN OBSERVATORIES.

Figure 8. Latitude Variation of the Depth of Scintillation. Derived from simultaneous overhead observations of the Joint Satellite Studies Group. The 1965-1966 results may indicate a change of the latitude variation with solar cycle

The second set of data is the result of simultaneous observations of the 40 MHz beacon of satellite BE-B (S-66). In this case statistics were produced for all overhead observations during the period 1 November 1965 to 21 January 1966. The resultant latitude variation is flatter than that in the first set of data, but further study is needed to decide whether the difference is in the prime distribution of irregularities changing with solar cycle or is caused by some other factor.

Records of scintillation of the radio beacons on BE-B and the synchronous Satellite ATS-3 taken at the AFCRL station at Thule, Greenland, indicates that the latitude function does not dip over the polar region, as do certain auroral phenomenon, but, as yet, there is insufficient data for a quantitative statement.

A second peak of the latitude variation over the equatorial region has been suggested by unpublished JSSG observations of BEB scintillations. It is expected that the quantitative features will be determined from current studies made by the JSSG using the 136 MHz beacons of ATS-3 and Canary Bird.

As a final note, the latitudinal variation is a reactive variable, depending on the state of magnetic activity, the time of day, and probably the longitude of observation as well as other variables. Observations from Hamilton, Mass., in Figure 4 show this for incremental changes in the local index of magnetic activity; the other qualifications follow from evidence in other sections.

#### 4.3.2 Diurnal - Seasonal Variation

From the early observations of radio star sources it was apparent that there was a nighttime peak in the occurrence and mean intensity of the irregularity regions causing scintillation. A controversy on the existence of a secondary peak during the daytime and the nature of the seasonal variation has only begin to be resolved by recent observations of the beacons of stationary satellites.

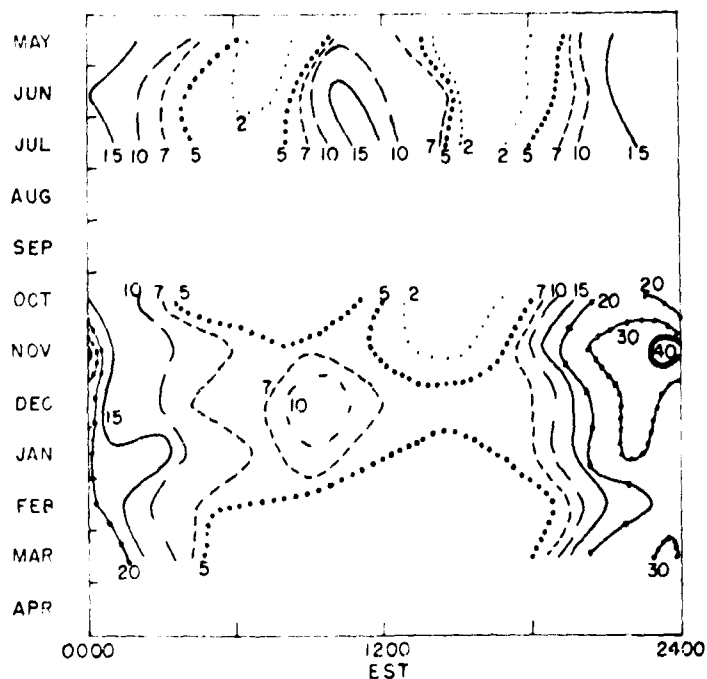
Unfortunately, for observations made with either radio stars or low-altitude satellites, the effects of seasonal change cannot be uniquely separated from the effects of diurnal change. For a fixed geographic position of the irregularity region, the times of day when either type of source can be viewed is fixed by season; therefore, in any set of observations, certain pairs of seasonal-diurnal values are always missing. If complimentary sets of data are normalized and combined, such as data from several radio stars or satellites, some aspects of the resultant diurnal seasonal variation may be caused by unintentional bias in the normalization process.

Since synchronous satellites remain at fixed positions, analysis of their data does not have this limitation, and seasonal and diurnal effects can be studied separately. Reduced data for observations of the 136 MHz beacon of commercial communication satellite Canary Bird are shown in Figure 9. There is a persistent nighttime peak throughout the year.

The secondary daytime maximum of the scintillations of the Canary Bird beacon during the months of May, June, July, and August 1967 was a principal feature of observations made with the commercial satellite Early Bird during the same period of 1965. The daytime maximum is not significant in similar observations for 1968 made with Canary Bird and with the 137 MHz beacon of the ATS-3 communication satellite.

Comparable daytime scintillations of the Canary Bird 136 MHz beacon were observed at a mid-latitude station in Florence, Italy, but they were not found in observations taken at Kiruna, Sweden, near the auroral zone nor in observations taken at Accra, Ghana, at the magnetic equator.

Like the latitude variation, the diurnal-seasonal variation is also a reactive variable. There is a dependence on the latitude of



DIURNAL SEASON CONTOURS OF CANARY BIRD 136 MHz  
SCINTILLATION, HAMILTON, MASS., 1967, 1968.

Figure 9. Diurnal-Seasonal Variation of Scintillation. Continuous observation of the 137 MHz beacon of a synchronous satellite show that the diurnal and seasonal variations are interrelated. Note the secondary maximums during the day hours

observation, the state of magnetic activity, and the phase of the sun spot cycle. Details of the dependence of the diurnal-seasonal variation on these other variables are still being determined.

#### 4.3.3 Variation With Phase of the Solar Cycle

Briggs (1964) has shown that the depth of scintillation of 38 MHz signals of Cassiopeia A received at Cambridge, England, varied systematically with the solar cycle from 1950 to 1961. Since his data was classified by semi-logarithmic indices ranging from 0 to 5 and averaged over each period, it is difficult to extend his results to other frequencies, times, or latitudes.

In order to compare the mean values of his semi-logarithmic class intervals with statistics derived from linear indices, as in the present study, a conversion is necessary. From the sample records that defined the Cambridge class intervals, linear indices can be established using the arbitrary rules defined above. The Cambridge index is then a translated logarithm of the AFCRL index. Since the studies of the Hamilton observations have shown that the logarithm of the depth of scintillation is nearly

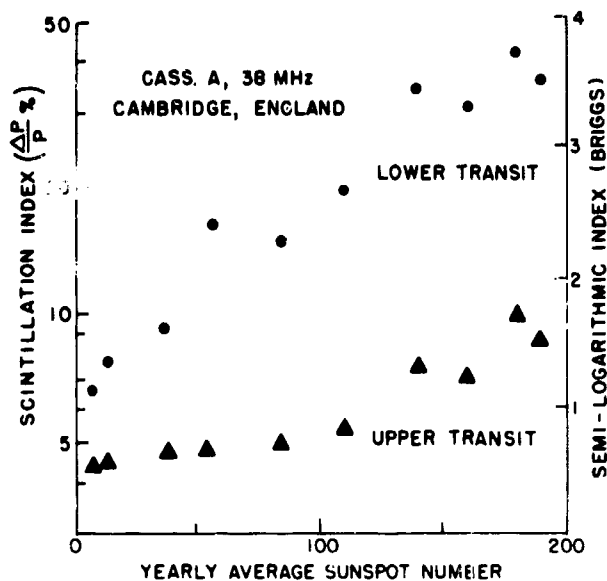


Figure 10. Variation of Scintillation With Solar Cycle. There is a linear dependence of the logarithm of scintillation index with the yearly mean sunspot number. The proportionate increase is the same in the auroral zone as near overhead at Cambridge, England (after Briggs, 1964)

normally distributed (Figures 3, 5, and 8), the mean value of the data reduced by Briggs is nearly the median value of the distribution function of the depth of scintillation for each observation period. Therefore, Briggs' data can be transformed as in Figure 10. The logarithm of the depth of scintillation depends nearly linearly on the yearly average of the sun spot number.

This variation with sun spot number (or with the phase of the sun spot cycle) can be extended to other frequencies by using the empirical frequency dependence discussed in Section 4.2.1.

The differences between the behavior for the overhead and lower transit observations indicates that this variation is dependent on the latitude of the irregularity regions and requires further study.

## 5. APPLICATION TO SYSTEM PROBLEMS

A current example will demonstrate how the morphological data can be applied to a system requirement. Consider an aircraft over the North Atlantic depending on FM voice communication and a pulsed navigation system, where VHF signals are relayed between the aircraft and a synchronous satellite. What prediction can be made for fading greater than 3, 6, and 10 dB below normal signal level?

In a special study at AFCRL, the 228 MHz beacon of experimental communication satellite LES-5 was used to establish a link between the empirical scintillation indices and the duration of fading. For observations between 1 August and 31 December 1967, each 15-min sample was scaled for a scintillation index of from 0 to 100, as defined in Section 3.2. In addition, the duration of fading 3, 6, 10, and 20 dB below normal level was measured for each sample showing intense scintillation.

Table 1 compares the duration of deep fading with scintillation index. The 228 MHz beacon faded 3 dB below its expected intensity only about 0.15 percent of the 1100 hr of observation.

Table 1. Minutes of Fading Below Set Levels

Fading Level	Range of Scintillation Index			Total
	40-56	57-79	80-100	
≥ 3 dB	5.0	21.1	66.2	92.3
≥ 6 dB	0.9	5.5	29.3	35.7
≥ 10 dB	-	0.8	9.5	10.3
≥ 20 dB	-	0.1	2.0	2.1
Observation Time	480	195	240	915

Although the data in Table 1 represents results for a particular set of conditions, it can be used for comparative analysis. For instance, when the scintillation index of a sample period is greater than about 57, the signal will be below the 3 dB level about 20 percent of the time, or below the 10 dB level about 2.5 percent of the time.

The morphological results of Section 4 can be used with Table 1 to predict fading for an example such as an aircraft flying over the North Atlantic somewhere between the southern tip of Greenland and Iceland. This flight path is at the edge of the region of maximum auroral disturbance, say at 60°N. geomagnetic latitude. The raypath to a synchronous satellite, however, is low to the south. The geometric analysis of the JSSG data, Figure 7, suggests that the median depth of the slant southern path is about four to five times the median depth observed overhead at the penetration point, near 50° N. geomagnetic latitude. Since the best data at hand for a VHF comparison are the Canary Bird or ATS-3 observations made at Hamilton, Mass., it is preferable to use the smooth latitude variation to estimate the depth at the penetration point. From Figure 8 it can be seen that the depth of scintillation would be twice that measured

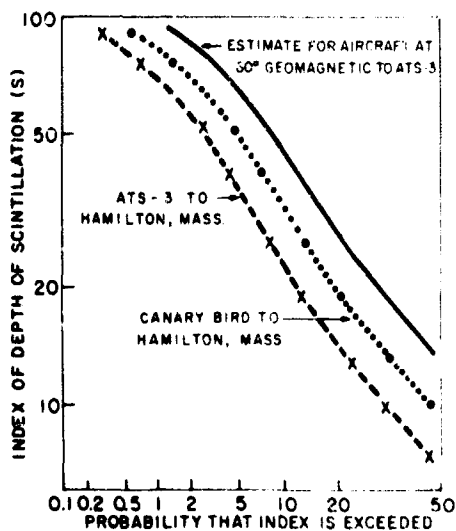


Figure 11. Estimated Scintillation for an Air to Satellite Relay. For a mid Atlantic Synchronous satellite and an aircraft over southern Greenland, the cumulative distribution of depth of scintillation at 136 MHz is estimated from scaled data taken with Canary Bird at Hamilton, Mass.

on ATS-3 signals at the Hamilton observatory, which represent the behavior between  $50^{\circ}$  and  $52^{\circ}$  N. geomagnetic.

The estimated cumulative distribution representing this case is shown in Figure 11. For about 7 percent of the time the scintillation index for 137 MHz signals would be greater than 57, so that an aircraft at  $60^{\circ}$  N. geomagnetic transmitting at 137 MHz to a synchronous satellite would experience fading greater than 3 dB only about 1.4 percent of the total time. Since the diurnal study of signals at this latitude, Figure 9, shows that the occurrence of strong scintillation in the daytime is rare, this estimate can be doubled to represent the night hours.

Other details can be estimated by using the variations established in Section 4. About 90 to 95 percent of the time the K index of magnetic activity is less than 5 (Figure 2), and the effects of geomagnetic variability will not be noticed at this latitude. Therefore, while moderate geophysical activity at the edge of the auroral zone may seriously degrade local HF and VHF communication, it should not degrade the VHF satellite link. The occurrence of deep scintillations does increase for K indices greater than 5, but the statistics are not established yet.

The estimated cumulative distributions of Figure 11 can be translated for changes in the radio frequency by using the empirical dependence on radio frequency of Section 4.2.1; changes in solar activity can be translated by using the dependence on mean annual sunspot number of Section 4.3.3.

## 6. CONCLUSION

Irregularities in the ionosphere cause changes in signal characteristics that are of concern to system designers and users. The effects of such

irregularities have been studied since about 1950 using radio stars and since 1957 using low-altitude satellites. The reduction techniques used for these observations have submerged characteristics of the irregularities of interest to specific communication, detection, or navigation systems.

Often a relationship can be found that statistically relates the desired new characteristic and the older index used to characterize the scintillation caused by these irregularities. In that case, a morphological study of existing indices will provide a framework for prediction.

Using existing studies of AFRL and the Joint Satellite Studies Group, a cooperative network of foreign stations, a morphology of the irregularity region has been developed. An index based on the depth of scintillation was used to establish the variation of the strength of irregularities with magnetic K index, the radio frequency of observation, the latitude of the station, and cyclic variables such as time of day, season, and phase of the sun spot cycle.

Not every feature can be determined from available data, but the present results can be used to estimate the behavior of proposed VHF systems, as for instance fading on an air-to-satellite radio link.

## REFERENCES

- Aarons, J., and Allen, R. S. (1966) Scintillation of a radio star at a sub-auroral latitude, Radio Science 1 (No. 10): 1180-1186.
- Aarons, J., Allen, R. S., and Elkins, T. J. (1967) Frequency dependence of radio star scintillation, Jour. Geophys. Res. 72 (No. 11): 2891-2902.
- Aarons, J., Mullen, J. P. and Basu, Sunanda (1964) The statistics of satellite scintillations at a sub-auroral latitude, Jour. Geophys. Res. 69 (No. 9): 1785-1794.
- Allen, R. S., Aarons, J., and Whitney, H. E. (1964) Measurements of radio star and satellite scintillations at a sub-auroral latitude, IEE Trans. Ant. Prop. AP-12 (No. 7): 812-822.
- Briggs, B. H. (1964) Observations of radio star scintillations and spread-F echoes over a solar cycle, Jour. Atmos. Terr. Phys. 26: 1-23.
- Briggs, B. H., and Parkin, I. A. (1963) On the variation of radio star and satellite scintillations with zenith angle, Jour. Atmos. Terr. Phys. 25: 339-350.
- Joint Satellite Studies Group (1965) A synoptic study of scintillations of ionospheric origin in satellite signals, Planet. Space Sci. 13: 51-62.
- Joint Satellite Studies Group (1968) On the latitude variation of scintillations of ionospheric origin in satellite signals, Planet. Space Sci. 16: 775-781.

- Kent, G. S. (1959) High frequency fading observed on the 40 Mc/s wave radiated from artificial satellite 1957 a, Jour. Atmos. Terr. Phys 16: 10-20. <sup>MM</sup>
- Little, C. G. (1951) Diffraction theory of the scintillations of stars on optical and radio wavelengths, Monthly Notices Roy. Astron. Soc. 111: 289-302. <sup>MM</sup>
- Koster, J. R., and Wright, R. W. (1960) Scintillation, spread F and transequatorial scatter, Jour. Geophys. Res. 65: 2303-2306. <sup>MM</sup>
- Mercier (1962) Diffraction by a screen causing large random phase fluctuations, Proc. Cambridge Phil. Soc. 58 382-400. <sup>MM</sup>
- Orhaug, T. A. (1965) Scintillation of discrete radio sources, Chalmers Tek. Hogskol. Handl. 229. <sup>MM</sup>

Figure 1. Intense Scintillation of ATS-3 Beacon. Deep fades to -10 or -20 dB can occur at VHF and UHF during periods of ionospheric disturbance, as on 3 November 1968. Behavior is normal the following night 4 November. Matched loads are reference level each hour

Figure 2. Variation of Magnetic Index, 1964 - 1967. The planetary index of magnetic activity is not normally distributed. Note the disproportionate increase of high K values for years of increased solar activity over 1964-1965, the period of solar minimum

Figure 3. Variation of Scintillation Index With Local Magnetic K Index. The probability that a given depth of scintillation is exceeded increases nearly linearly with local K index for observations at the southern edge of the auroral region

Figure 4. Latitude Change of the Magnetic K Dependence. At high latitudes above Hamilton, Mass., the mean depth of scintillation increases nearly linearly with local magnetic K index. Overhead, in the region 40° to 45° geographic, there is no change until K is greater than about 5. Southward, 30° to 35°, the mean depth of scintillation decreases with increasing K index

Figure 5. Variation of the Depth of Scintillation With Radio Frequency. At low depths of scintillation there is a nearly inverse square-law-dependence on radio frequencies for low depth of scintillation. As the intensity of the irregularity region increases, the exponent of dependence decreases

Figure 6. Variation of Frequency Dependence With Scintillation Index. Observation of Cassiopeia A at 30, 63, 113, and 228 MHz indicate that the mean frequency dependence can be specified in terms of the depth of scintillation on one of the frequencies

Figure 7. Geometric Variation of the Depth of Scintillation. Derived from simultaneous measurements by members of the Joint Satellite Studies Group. Mean overhead values are linked by a smooth curve representing the latitude variation. Off-vertical observations show the effect of elevation angle

Figure 8. Latitude Variation of the Depth of Scintillation. Derived from simultaneous overhead observations of the Joint Satellite Studies Group. The 1965-1966 results may indicate a change of the latitude variation with solar cycle

Figure 9. Diurnal-Season Variation of Scintillation. Continuous observation of the 137 MHz beacon of a synchronous satellite show that the diurnal and seasonal variations are interrelated. Note the secondary maximums during the day hours

Figure 10. Variation of Scintillation With Solar Cycle. There is a linear dependence of the logarithm of scintillation index with the yearly mean sunspot number. The proportionate increase is the same in the auroral zone as near overhead at Cambridge England (After Briggs, 1964)

Figure 11. Estimated Scintillation for an Air to Satellite Relay. For a mid Atlantic Synchronous satellite and an aircraft over southern Greenland, the cumulative distribution of depth of scintillation at 136 Mhz is estimated from scaled data taken with Canary Bird at Hamilton, Mass.

ELECTROCHEMICAL BEHAVIOR OF A MOLTEN  
ALUMINUM-CHLORIDE/ SODIUM-CHLORIDE ELECTROLYTE

Major L. A. King and Major D. W. Seegmiller  
The Frank J. Seiler Research Laboratory (OAR)  
United States Air Force Academy, Colorado

ELECTROCHEMICAL BEHAVIOR OF A MOLTEN  
ALUMINUM-CHLORIDE/ SODIUM-CHLORIDE ELECTROLYTE

## ELECTROCHEMICAL BEHAVIOR OF A MOLTEN ALUMINUM

### CHLORIDE SODIUM CHLORIDE ELECTROLYTE

Maj L. A. King and Maj D. W. Seegmiller  
The Frank J. Seiler Research Laboratory (OAR)  
United States Air Force Academy, Colorado 80840

#### ABSTRACT

The electrochemical oxidation of aluminum holds promise for the design of sources of electrical power having high theoretical energy density. Aluminum anodes operate successfully in fused mixtures of aluminum chloride and sodium chloride, and the system is current and power limited only by the properties of the electrolyte. This paper discusses the electrochemical behavior under open-circuit conditions of aluminum chloride, sodium chloride melts. Some speculations are offered on the structure of these melts.

#### INTRODUCTION

We are studying aluminum metal electrodes operating in aluminum chloride based molten salt electrolytes as part of a general research program aimed toward providing new high energy density electrochemical power supplies. Aluminum anodes in such molten ionic media are able to provide extremely high electric current densities with very low losses due to electrode polarization or related limiting processes. The electrical transport properties of the electrolyte itself are limiting, and we are presently examining the structure and some of the physical properties of the fused electrolyte.

#### PRESENT STATUS

Electrochemical power sources comprised of low equivalent weight metallic anodes and reactive, low equivalent weight oxidizing agents at the cathode should operate at high energy or power densities. A particularly attractive anode candidate is aluminum. The metal is readily available, easily purified, inexpensive, and capable of being fabricated into any reasonable shape. Some examples of high energy density power sources, along with equivalent data for some conventional batteries and fuel cells are shown in Table 1.

Many workers have tried to utilize aluminum anodes, but none has been able to circumvent either the inevitable aluminum passivation in acidic aqueous electrolytes or aluminum corrosion in basic aqueous media. Zaromb [1] has operated successfully an aluminum-air cell with alkaline KOH electrolyte at an estimated 200 watt-hours per pound. However, he found it necessary to drain the electrolyte into a reservoir to prevent destruction of the aluminum anodes when no power was being drawn.

We are aware of no work with non-aqueous electrolytes specifically directed toward the use of aluminum in electrochemical power sources, except

our own and a newly awarded NASA contract.\* Previously in our laboratory a number of organic compounds and molten salt mixtures were examined as candidate electrolytes. King, Brown and Frayer [2] studied the electrochemical behaviour of aluminum anodes in six such electrolytes, and selected the mixture 40 mole percent sodium chloride, 60 mole percent aluminum chloride as their most promising model electrolyte. The objective of their effort, following the selection of an electrolyte, was to determine the current and power limiting properties of the anode-electrolyte system. They reported that aluminum exhibited its thermodynamically calculable potential versus a chlorine electrode in a NaCl-AlCl<sub>3</sub> melt. We now have extended these measurements to several temperatures and melt compositions and still conclude that the agreement between theory and experiment is good.\*\*

TABLE 1. Energy Densities of Batteries and Fuel Cells

Cell	Theoretical Energy Density <sup>a</sup> (Watt-hour/Pound)
<u>Commercial Batteries</u>	
Lead-Acid	112
Nickel-Cadmium	107
Zinc-Air	500
<u>Advanced Systems</u>	
Na/ceramic/S, Na <sub>2</sub> S <sub>3</sub>	600
Al + $\frac{3}{2}$ Cl <sub>2</sub> → AlCl <sub>3</sub>	600
Li + $\frac{1}{2}$ Cl <sub>2</sub> → LiCl	1050
2Al + $\frac{3}{2}$ O <sub>2</sub> → Al <sub>2</sub> O <sub>3</sub>	1610

<sup>a</sup>Calculated from thermodynamic data.

King, Brown, and Frayer [2] also found that aluminum did not passivate in their NaCl-AlCl<sub>3</sub> melt until anodic current densities as high as 800 ma cm<sup>-2</sup> were reached. They reported that an extremely small fraction of the overall polarization in an operating cell was attributable to charge transfer or

\*NAS 12-688, with Tyco Laboratories, Waltham, Mass.

\*\*The potential exhibited by aluminum in aqueous media is generally significantly lower than the theoretical value.

diffusion polarization associated with the aluminum anode, electrolyte interface. These workers observed that aluminum dissolved anodically with approximately 100 percent current efficiency, and did not self-discharge upon standing at open circuit conditions.

In summary, the aluminum anode, NaCl-AlCl<sub>3</sub> electrolyte system is neither current nor power limited by the processes which are usually detrimental to aluminum anode, aqueous electrolyte combinations. Instead, the electrical conductivity of the electrolyte is the limiting process.

## EXPERIMENTAL WORK

### Electrolytes

Only after several attempts were we able to prepare sufficiently pure molten salt mixtures. The purification of AlCl<sub>3</sub> was particularly troublesome, and was accomplished by repetitive sublimation of "Baker Analyzed" reagent grade AlCl<sub>3</sub> in dry argon along the length of a 60 cm long, 5.4 cm o.d. Pyrex tube and finally into a receptacle which was capped with a standard taper plug. "Baker Analyzed" reagent grade NaCl was dried by fusion in air. The two chlorides were stored, handled and mixed in a glove box filled with dry air and equipped with a recirculation train which passed the box atmosphere over a molecular sieve for moisture removal. Electrolyte compositions were fixed by weight. All weights were known to at least three significant figures. Water-clear, colorless molten mixtures were obtained.

### Cells

The Pyrex concentration cells used were similar to that shown in Figure 1, with standard taper tops used in some cases in place of the Teflon sleeve seals. The asbestos fiber served as electrical contact between the two melt compositions. We found that the pressure equalizing capillary eliminated any detectable mass transport of melt through the asbestos fiber. The electrodes were made from "Baker Analyzed" reagent grade 0.032 inch diameter aluminum wire. The melt in each arm of the cell was stirred with a Teflon-covered magnetic stirring bar. Cells were immersed in a well-stirred constant temperature silicone oil bath. Melt composition ratios were changed by adding known weights of either AlCl<sub>3</sub> or NaCl to one of the arms of the cell. A new, steady cell voltage was reached once the added salt was dissolved and well mixed.

The aluminum chloride formation cell was also a two-compartment configuration in which the melt composition was identical in both compartments. Dissolved chlorine was prevented from diffusing into the anode compartment by plugging the opening between the two compartments with Pyrex wool and granular aluminum.

### Apparatus

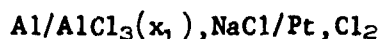
The oil bath was heated by an external hot plate and an immersed Nichrome wire coil. Temperatures remained constant with no more than

one Centigrade degree drift per hour. Bath temperature was measured with a mercury thermometer which had been calibrated against a Chromel-Alumel thermocouple. Vertical temperature gradients in the bath were measured by moving a bare Chromel-Alumel thermocouple about the bath volume. The total temperature variation over a 10 cm height in which the cells were suspended never exceeded 0.5°C. Cell voltages were measured with a Leeds and Northrup K-3 potentiometer and a Leeds and Northrup Electronic DC Null Detector.

## RESULTS

We indicated above that the electrical transport properties of the electrolyte itself constitute the current and power limiting factors associated with the anode electrolyte system. The electric conductivity of NaCl-AlCl<sub>3</sub> melts has been measured several times [3], but considerable disagreement exists in the results. The conductivities of representative NaCl-AlCl<sub>3</sub> compositions at various temperatures were measured in our laboratory [4], and fell between 0.2 and 0.5 ohm<sup>-1</sup> cm<sup>-1</sup>. These values are in agreement with published values, but our experience led us to suspect a marked dependence on melt purity and composition, both of which are exceedingly difficult to specify unambiguously.

We decided first to determine the activity coefficient of aluminum in various NaCl-AlCl<sub>3</sub> melts. The most direct route to this information is by means of a formation cell:



Here the net cell reaction is the formation of AlCl<sub>3</sub> at mole fraction  $x_1$ . As  $x_1$  approaches 1.0, the observed cell voltage should approach the standard EMF of formation of AlCl<sub>3</sub>. The deviation from the standard voltage at any particular  $x_1$  yields the activity and activity coefficient of the Al<sup>3+</sup> ion by

$$\mathcal{E}_1 = \mathcal{E}^\circ + \frac{RT}{nF} \ln a_1$$

and

$$a_1 = \gamma_1 x_1$$

where  $\mathcal{E}_1$  and  $\mathcal{E}^\circ$  are the observed and standard voltages, respectively;  $a_1$  and  $\gamma_1$  the activity and activity coefficients, respectively; and the remaining symbols have their usual significance.

Formation cells were first applied to molten halide mixtures by Hildebrand and Rühle [5]. Unfortunately there are some practical problems associated with using formation cells. In the present case, difficulties arise in measuring  $\mathcal{E}^\circ$  for AlCl<sub>3</sub>, a near insulator. There also is a problem due to changes in the melt composition caused by bubbling chlorine gas through the volatile electrolyte.

The bulk of our work is with concentration cells of the type



where  $\mathcal{E} = \frac{RT}{nF} \ln (a_1/a_2)$

and  $a_1 = \gamma_1 x_1; a_2 = \gamma_2 x_2$

Murgulescu and Sternberg [6] discussed the applications of concentration cells to molten salts; these cells avoid the difficulties inherent in  $\text{AlCl}_3$  formation cells. Since concentration cells give activity ratios, a series of such ratios together with one absolute value measured with a formation cell will provide the needed activity and activity coefficient data.

The principal difficulty with this type of concentration cell is due to the possible existence of a junction potential across the asbestos fiber. The magnitude of the junction potential depends on the relative differences in mobility of the current carrying species on the two sides of the fiber. For melts of similar composition in which the current carrying species are present in high concentrations on both sides, the junction potential should be negligibly small. Murgulescu and Sternberg tested five binary melt systems, each over virtually its entire composition span, and found junction potentials never exceeded their limit of experimental error (approximately 0.001V). We will eventually test our electrolyte system for a junction potential, but this determination requires vapor pressure data which we are presently gathering.

Eighteen successful runs were made with concentration cells, most of them with composition ratios varied as described in the Experimental Work section. All voltages were reproducible (within approximately 0.005V), but were found to be surprisingly large. This may be seen by examining some typical data, as are shown in the first three columns of Table 2. The fourth column gives the aluminum ion activity ratios required to calculate the observed voltages from the Nernst equation. The fifth column gives the aluminum ion activity ratios calculated by assuming that the activity ratio is equal to the apparent mole fraction ratio; that is, the stoichiometric mole fraction ratio. The great differences between the activity ratios given in these two columns emphasizes the need to invoke marked structural changes involving aluminum chloride in these melts as sodium chloride is added.

The remarkable increase in  $(N'/N)_{\text{calc}}$  as the apparent mole fraction ratio increased deserves close attention. Aluminum dissolves with 100% current efficiency ( $n = 3$ ) from aluminum anodes in  $\text{AlCl}_3$ ,  $\text{NaCl}$  melts. Aluminum metal also may be electroplated from such melts. Whatever the voltage determining aluminum species is, its activity should be dependent upon the concentration of some chloro-aluminum principal melt constituent. It is reasonable to expect this dependency to be similar in both arms of a concentration cell, and therefore to mathematically cancel in the Nernst equation for the cell. Hence, we should be able to explain observed cell voltages on the basis of ratios of activities of principal melt constituents, providing activity coefficients remain near unity.

Table 2. Concentration Cell Data<sup>a</sup>

M <sup>b</sup>	M <sup>b</sup>	P, V	(N'/N) <sup>c</sup> <sub>calc.</sub>	(N'/N) <sup>d</sup> <sub>I</sub>	(N'/N) <sup>e</sup> <sub>II</sub>	(N'/N) <sup>f</sup> <sub>III</sub>	(N'/N) <sup>g</sup> <sub>IV</sub>	(N'/N) <sup>h</sup> <sub>V</sub>
.5880	.7073	.0074	1.766	1.028	1.044	1.138	1.103	1.95
.6320	.7073	.0616	113.8	1.119	1.197	1.582	1.570	-
.5859	.7073	.1080	4031	1.207	1.361	1.998	2.413	-
.5587	.7073	.1301	22000	1.266	1.481	2.263	3.532	-
.5383	.7073	.1560	161000	1.314	1.586	2.475	5.413	-
.5171	.7073	.2025	5760000	1.368	1.712	2.705	12.12	-
.5089	.7073	.2299	47300000	1.390	1.766	2.798	23.29	-

<sup>a</sup>Run No. 191281. Other runs gave similar results.

<sup>b</sup>M and M' are apparent mole fractions of AlCl<sub>3</sub> in the two arms of the cell. M = (moles AlCl<sub>3</sub>)/(moles AlCl<sub>3</sub> + moles NaCl). See also text.

<sup>c</sup>(N'/N)<sub>calc</sub> = activity ratio of Al(III) calculated from  $\ln c = \frac{RT}{5.7} \ln (N'/N)_{\text{calc}}$ , T = 453 °K

<sup>d</sup>Calculated from Assumption I (see text); (N'/N)<sub>I</sub> = (M'/M)

<sup>e</sup>Calculated from Assumption II (see text).

<sup>f</sup>Calculated from Assumption III (see text).

<sup>g</sup>Calculated from Assumption IV (see text).

<sup>h</sup>Calculated from Assumption V (see text).

Murgulescu and Sternberg [6] reported activity coefficients for eight binary halide melts, over wide concentration ranges. In the most extreme cases they reported (AgCl, KCl and AgBr, LiBr),  $\gamma$  varied from 0.45 to 2.65. For their four reported univalent-divalent halide systems,  $\gamma$  varied from 0.90 to 1.07. A number of univalent-divalent, univalent-trivalent, and univalent-tetravalent halide systems also were discussed by Lumsden [7]. Again, approximately ideal mixing ( $\gamma \approx 1$ ) was reported for these systems. Accordingly, we tentatively have assumed unit activity coefficients in the  $\text{AlCl}_3$ ,  $\text{NaCl}$  system.

### Data Analysis

Five different assumptions were made regarding melt structure. Each of these is presented below, together with an expression for the aluminum activity ratios which result. Ratios calculated by each assumption are also presented in Table 2 for comparison with the ratio calculated from the Nernst equation.

Let  $r$  moles of  $\text{AlCl}_3$  be mixed with one mole of  $\text{NaCl}$ . Then

$$M = \frac{r}{r+1} \quad \text{and} \quad r = \frac{M}{1-M}$$

where  $M$  is the apparent mole fraction of  $\text{AlCl}_3$  in the electrolyte.  $M = (\text{moles AlCl}_3)/(\text{moles AlCl}_3 + \text{moles NaCl})$ .

Assumption I: Neither  $\text{AlCl}_3$  nor  $\text{NaCl}$  is significantly ionized.

$$N_{\text{AlCl}_3} = \frac{r}{r+1} = M$$

$$(N'/N)_I = M'/M \quad (I)$$

Assumption II: All of the  $\text{NaCl}$  added to  $\text{AlCl}_3$  forms  $\text{Na}^+$  and  $\text{AlCl}_4^-$ .  
(Valid for  $M \gg 0.25$ )

$$N_{\text{AlCl}_3} = \frac{r-1}{r+1}$$

$$(N'/N)_{II} = \frac{4M'-1}{4M-1} \quad (II)$$

Assumption III: All  $\text{NaCl}$  present dissociates to  $\text{Na}^+ + \text{Cl}^-$ . All aluminum is present as  $\text{Al}_2\text{Cl}_6$ , which slightly dissociates.



$$N_{\text{Al}_2\text{Cl}_6} = \frac{M}{4-3M}, \quad N_{\text{Cl}^-} = \frac{2(1-M)}{4-3M}$$

$$(N'/N)_{\text{III}} = \left[ \frac{\left(\frac{M'}{4-3M}\right) \left(\frac{1-M}{4-3M}\right)^6}{\left(\frac{M}{4-3M'}\right) \left(\frac{1-M'}{4-3M'}\right)^6} \right]^{\frac{1}{2}} \quad (\text{III})$$

Assumption IV: All of the NaCl added to  $\text{AlCl}_3$  forms  $\text{Na}^+$  and  $\text{AlCl}_4^-$ .  
(Valid for  $M \geq 0.5$ )

$$N_{\text{AlCl}_3} = \frac{r-1}{r+1}$$

$$(N'/N)_{\text{IV}} = \left(\frac{2M'-1}{2M-1}\right) \quad (\text{IV})$$

Assumption V: All of the NaCl added to  $\text{AlCl}_3$  ( $\text{Al}_2\text{Cl}_6$ ) forms  $\text{Na}^+$  and  $\text{Al}_2\text{Cl}_7^-$ . (Valid for  $M \geq 0.667$ ).

$$N_{\text{AlCl}_3} = \frac{r-2}{2}$$

$$(N'/N)_{\text{V}} = \left(\frac{3M'-2}{3M-2}\right) \left(\frac{M}{M'}\right) \quad (\text{V})$$

All activity ratios calculated from these assumptions (except V) and several others prove grossly inadequate to explain the cell voltage. We believe some species such as  $\text{Al}_2\text{Cl}_7^-$  (Assumption V) must be formed, and that it partially dissociates into simpler species to an extent required to yield the aluminum activity ratios calculated from observed cell voltages. The mathematics required to extract the pertinent dissociation constants is probably too formidable for the precision of our experimental data. Rather, this treatment will await the assignment of absolute activities from formation cells.

#### FUTURE WORK

Our immediate objective is to explain the very high cell voltages in our concentration cells. This presumably is a result of the equilibria in the melt in which  $\text{Al}^{3+}$  participates. Among the new experimental data needed will be vapor pressure and density of the melts, transport numbers, and spectroscopic information.

More distant objectives include extension of our data gathering to other melts. We are especially interested in the ternary sodium, potassium, aluminum chloride systems. Extremely low melting points are accessible, down to  $70^\circ\text{C}$  [8].

## APPLICATIONS

We believe the use of aluminum anodes in  $\text{AlCl}_3$ -based molten salt electrolytes will permit the development of electrochemical power supplies having volume and weight energy densities in excess of anything presently in use.

The type of electrolyte we have chosen may be amenable to back-pack applications. A wide melt composition range is available at temperatures above about  $160^\circ\text{C}$  [9] and a ternary  $\text{AlCl}_3$ ,  $\text{NaCl}$ ,  $\text{KCl}$  system melts at  $70^\circ\text{C}$  [8]. Such low temperatures should be easy to maintain with a minimum of thermal insulation. Even if units small enough to hand-carry are not practical, the light weight of aluminum and the halides should make a portable system feasible. For example, a quiet, portable central power supply could be carried in the field by ground forces for recharging smaller secondary back-pack cells.

With a variety of melting points available from  $70^\circ\text{C}$  to about  $180^\circ\text{C}$ , the possibility exists for producing a series of high energy batteries which become activated at specific elevated temperatures. Applications would include inexpensive thermal batteries of indefinite shelf life, and warning or alarm devices which are thermally activated at pre-selected temperatures.

Finally, high-energy systems operating in the tenths of volts range may be developed from simply exploiting the relatively high voltages obtained from concentration cells. Electrode fabrication in this case would be extremely easy; very inexpensive batteries should be possible.

## ACKNOWLEDGEMENTS

We wish to thank the Director of Faculty Research and the Department of Chemistry, United States Air Force Academy, for making time available for us in which to conduct this research program. We wish to thank the Frank J. Seiler Research Laboratory (OAR) for their generous financial support and for the use of their facilities.

#### REFERENCES

1. "Aluminum Fuel Cell for Electric Vehicles", Solomon Zaromb, in Power Systems for Electric Vehicles, Public Health Service Publication No. 999-AP-37, (1967).
2. "High Energy Density Electrochemical Cells", Maj L. A. King, Maj. A. D. Brown, Jr., and 1st Lt F. H. Frayer, in Proceedings of the OAR Research Applications Conference 21 Mar 1968, OAR 68-001, Vol I, (1968).
3. V. A. Plotnikov and P. T. Kalita. Zhur. Rusg. Fiz. Khim. Obschestva, 52, 2195 (1930); Y. Yamaguti and S. Sisido, J. Chem. Soc. Japan, 59, 1311 (1938); A. I. Kryagova, Zh. Obshch. Khim., 9, 2061 (1939).
4. Unpublished results, 1st Lt F. H. Frayer and Maj L. A. King, FJSRL (OAR).
5. J. H. Hildebrand and G. C. Ruhle, J. Amer. Chem. Soc., 49, 722 (1927).
6. I. G. Murgulescu and S. Sternberg., Disc. Faraday Soc., 32, 107 (1961).
7. Thermodynamics of Molten Salt Mixtures, J. Lumsden, Academic Press, London (1966)
8. D. A. Hames and J. A. Plambeck, Can. J. Chem., 46, 1727 (1968).
9. Phase Diagrams for Chemists, F. P. Hall and Herbert Insley, The American Ceramic Society (1947).

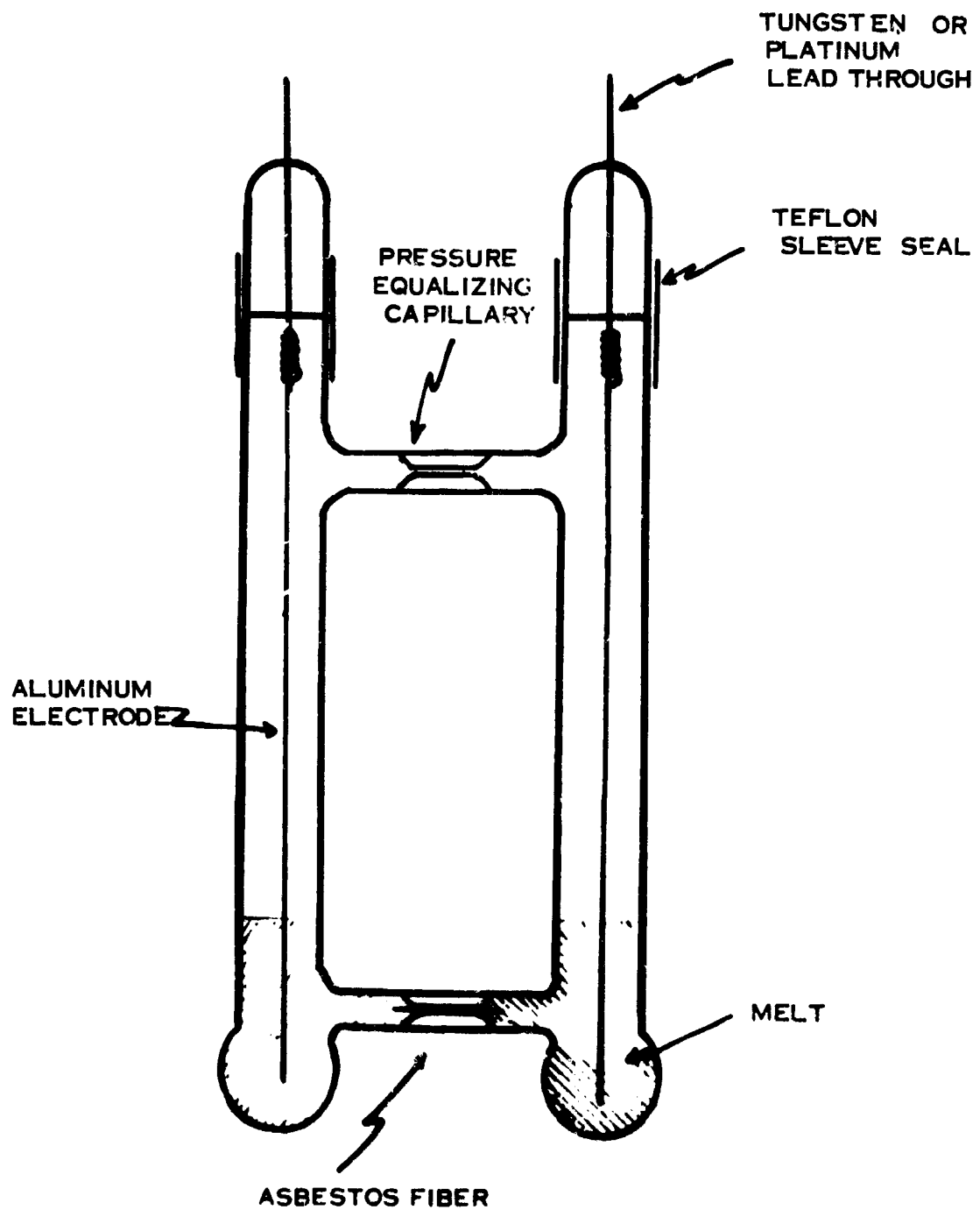


Figure 1. A Concentration Cell

THE MAGNETIC WIND-TUNNEL-MODEL  
SUSPENSION AND BALANCE SYSTEM

Eugene E. Covert

Aerophysics Laboratory

Department of Aeronautics and Astronautics

Massachusetts Institute of Technology

Cambridge, Massachusetts

and

Fred L. Daum

Fluid Dynamics Facilities Research Laboratory

Aerospace Research Laboratories

Office of Aerospace Research

Wright-Patterson AFB, Ohio

THE MAGNETIC WIND-TUNNEL-MODEL  
SUSPENSION AND BALANCE SYSTEM

EUGENE E. COVERE

Aerophysics Laboratory  
Department of Aeronautics and Astronautics  
Massachusetts Institute of Technology  
Cambridge, Massachusetts

FRED L. DAUM

Fluid Dynamics Facilities Research Laboratory  
Aerospace Research Laboratories  
Office of Aerospace Research  
Wright-Patterson Air Force Base, Ohio

# THE MAGNETIC WIND-TUNNEL-MODEL SUSPENSION AND BALANCE SYSTEM

by

EUGENE E. COVERT (MIT) and FRED L. DAUM (ARL)

## ABSTRACT

The magnetic wind-tunnel-model suspension and balance system is a unique aerodynamic testing tool which affords a method for obtaining test data which is absolutely free of model support interference effects. The suspension system is comprised of multiple pairs of electromagnets which surround the test section and provide the magnetic forces required for balancing the aerodynamic and gravitational loads acting on the model. Control of the magnets is accomplished through feedback control loops which receive signals from a set of model position sensors which may employ either optical or electromagnetic principles. The magnetic forces generated are proportional to the coil currents required; a measure of these currents provides an indication of the model forces. By inserting artificial position sensor signals into the control feedback loops, the magnetic fields may be controlled so as to force the model into various motions and oscillatory modes such as pitching, plunging, or rolling. Thus, the magnetic balance system is adaptable to dynamic, as well as static, testing situations. No longer merely a laboratory curiosity, the magnetic suspension and balance system has been born as a useful aerodynamic wind tunnel test instrument.

## INTRODUCTION

The use of small-scale models in the development of complicated systems is very common. During the design of a new airplane or missile it is not uncommon to test small-scale models in wind tunnels for many hundreds of hours. The scaling laws that relate the aerodynamic characteristics of these models to the aerodynamic characteristics of the prototype are well known. However, before these scaling laws can be used to extrapolate the wind tunnel data, the aerodynamic engineer must correct the data for the adverse effects of aerodynamic interference between the model and its suspension system on the measured aerodynamic characteristics. While the correction procedure is straightforward in low-speed flow, it becomes difficult in transonic testing. In testing at supersonic and hypersonic speeds, the model is usually sting supported; however, in this case there is an increasing body of evidence

suggesting that the flow near the base is seriously altered by the presence of the sting. Consequently the drag and the stability, for example, may not be measured as accurately as desired.

Two alternatives have been used to determine model aerodynamic characteristics without the presence of support interference. One of these is a free-flight technique where the model is literally flown in the wind tunnel test section for a few milliseconds. The aerodynamic characteristics are deduced from the observed motion of the model. Another approach, to be discussed here, is similar in appearance to the free-flight technique but rather than being in free flight the model is firmly fixed in the test section by magnetic fields and magnetic field gradients. Since the aerodynamic forces and moments acting on the model are balanced by magnetic forces and moments which are measurable, the instrumentation for the latter technique is commonly referred to as a magnetic suspension and balance system.

The basic operation of a magnetic suspension system can be explained by elementary considerations. First, recall that a magnetized bar, or magnet, acts approximately as if its magnetism were concentrated in a pole at either end. One pole is a source of magnetic flux lines while the other is a receiver, or sink, of these lines. Experiments have shown that like poles repel and unlike poles attract each other. Thus, if a magnet is placed at a random attitude in a uniform external magnetic field, a moment will act on the magnet tending to align the axis connecting the two magnetic poles with the direction of the external magnetic field. (The common north-seeking compass illustrates this idea.) A magnet placed in a uniform magnetic field feels no net force because each pole experiences the same force. If the external magnetic field is not uniform in strength, that is, if there are gradients in the field, then a different force acts on each pole. Thus, a net force may exist. This force will tend to move the magnet bar toward the region of higher field intensity even if the magnet is aligned with the external magnetic field lines. Therefore, it is possible to develop forces acting normal to the line connecting the magnetic poles. In this way, that is by controlling the magnetic field intensity and gradients, forces and moments can be made to act on the magnet. Second, a little reflection leads one to realize that the interaction force between the magnetic field and the magnet is unstable. For example, it is impossible to suspend a nail in space below a permanent magnet; if too near, the nail will jump to the magnet and if too distant, the nail will fall. However, it is possible to sense the position of the magnet and by means of a suitable automatic control system, adjust the external field to just balance the magnet against the applied forces and torques. This control also can provide a means for measuring the external forces and moments.

The principles underlying a magnetic balance and suspension system are not difficult. Conceptually, the ideas are straightforward; the problem lies in putting the ideas into practice. The

first practical magnet system was developed at the University of Virginia by Holmes and Beams [1] as a replacement for bearings in an ultra-centrifuge. During World War II, Beams suggested applying this technique for wind tunnel model suspension but his suggestion was not immediately followed up. The first actual successful magnetic suspension system for wind tunnel use was developed by ONERA (France) by Laurenceau and Tournier [2] and they reported interference-free drag measurements in 1956. In early 1957 MIT was granted permission to make an exact duplicate of the ONERA system. However, results of detailed studies suggested that a number of improvements would be necessary if the magnetic suspension were to become a practical instrument. At MIT, Covert, Chrisinger, Tilton, Stephens, et al, began concentrating on these studies and starting in 1960 this work was supported by ARL. Since that time the development has led to a practical, accurate system that has been used to measure static and dynamic aerodynamic characteristics as well as detailed characteristics of wakes [3-5]. Further, the considerable experience which has been gained with these early systems has been applied to the study of new configurations such as that now proposed for an ARL hypersonic wind tunnel. Before discussing this proposed third generation magnetic suspension and balance system a number of the basic ideas involved will be presented to put the design in its proper perspective.

#### FUNDAMENTAL MAGNETIC FORCE AND MOMENT RELATIONS

The torque acting on a volume V of magnetized material immersed in a magnetic field of strength B is

$$\vec{T} = \int_V (d\vec{M} \times \vec{B}) \quad (1)$$

The magnetic force acting on the same volume (i.e., tending to translate the body) is

$$\vec{F} = \int_V (d\vec{M} \cdot \nabla) \vec{B} \quad (2)$$

To design a six-degree-of-freedom system, it is necessary to develop the necessary uniform magnetic fields with respect to the three coordinate axes as well as the required field gradients. A difficulty arises immediately due to undesired coupling between the components. For example, consider the equations:

$$\text{Roll Torque} = \int_V (B_z dM_y - B_y dM_z) \quad (3)$$

$$\text{Pitch Torque} = \int_V (B_x dM_z - B_z dM_x) \quad (4)$$

$$\text{Yaw Torque} = \int_V (B_y dM_x - B_x dM_y) \quad (5)$$

In looking at the above torque equations, two thoughts become clear. First, a cross-coupling appears between the

components and, second, common terms appear. For example, the longitudinal component of magnetization  $M_x$  appears in both the pitch-torque and yaw-torque equations. However, if  $M_x$  is made very large compared with  $M_y$  and  $M_z$ , then the pitch-torque is essentially determined by  $M_x$  and  $B_z$  and the yaw-torque is essentially determined by  $M_x$  and  $B_y$ . Thus, the coupling between these two torques may be greatly reduced. By adopting the point of view that  $M_x$  will be the dominant magnetization, it follows that if  $M_x$  were constant, the problem becomes simplified. Therefore, Parker's idea [6] of using a separate set of coils to apply a model magnetizing field appears particularly attractive. (This idea permits the use of a simpler power supply for magnetization and it is economically attractive as well.) A further consequence of keeping  $M_y$  and  $M_z$  small is that the roll-torque that can be developed becomes very small. An alternate approach has been used.

Of the various possible approaches for generating roll-torque [7], the most promising appears to be that which in principle operates as does an induction motor. For example, consider the two pairs of opposed coils shown in Figure 1. A closed loop of wire is suspended between the coils and can rotate around its long axis as shown. Two-phase a.c. electrical power is used with one phase going to each set of coils. The cyclic current, which lags the voltage by  $90^\circ$  in each pair of coils, is also shown as a function of time. As the current rises and falls in each set of coils, a magnetic field builds up and then collapses at the same frequency as the a.c. The changing magnetic flux lines associated with this alternating magnetic field induces a current flow in the closed wire loop with the direction of flow depending on the direction of the magnetic field. The direction of the magnetic field, at each  $90^\circ$  of one electrical cycle, is shown in Part B of the figure and it is seen that for this case the magnetic field rotates at a steady rate. The closed loop is carrying a current and, being located in a magnetic field, has a force acting on it which will cause the loop to rotate at the same rate as the applied field. That is, the plane of the loop will try to remain aligned with the resultant magnetic field. The roll position control system must account for the slip which will occur by varying the power applied to the coils.

In the magnetic model suspension system, the model will have a closed loop of wire built into the model and the coils used to produce two magnetic fields  $H_y$  and  $H_z$ , for controlling yaw and pitch respectively, will be used for generating roll-torque. The pitch and yaw system will employ direct current while an alternating current of about 400 Hz will be used for roll control purposes. With this approach it is possible to obtain high model spin rates, up to 400 rps. Also, the magnetic torque produced by this effect may be calculated using the following expression:

$$T = - \frac{H^2 \omega}{4} \sin 2\theta \left[ \frac{kv}{Dc} \right] \left[ \frac{(\omega L/R)^2}{1 + (\omega L/R)^2} \right] \quad (6)$$

where

$D_c$  = c-axis demagnetizing factor

$\omega$  = excitation frequency

$L$  = inductance of loop in body

$R$  = resistance of loop in body

$v$  = volume

The high frequency of the a.c. produces a negligible ripple on the d.c. This equation implies that a torque exists whenever there is an angle  $\theta$  between the field and the plane of the coil. In this case there is a restoring rolling moment which is a function of the roll angle measured from the equilibrium position. Hence, through the use of position sensing and a control system the magnetic field lines can be made to produce a roll-torque that just balances the applied torque, thereby holding the model fixed in the roll direction, when so desired.

#### THE DEMAGNETIZATION FACTOR

When a ferromagnetic (or paramagnetic) body is immersed in a uniform magnetic field, a magnetic field is induced in the interior of the body. This internal field, or magnetization, acts to oppose the applied field so that the actual magnetic field induced in the body is less than expected from the simple product of the permeability  $\mu$  and the field strength  $H$ . Since the internal field is proportional to the magnetization, the simplest formula for the magnetization is

$$M = \mu H - D'H \quad (7)$$

where  $D'$  represents a tendency of the induced field to counterbalance the effects of the applied field  $H$ . Since for  $\mu = 1$ ,  $M = H$  and it is then better to write Eq (7) as follows:

$$H = \mu H - (\mu-1)DM \quad (8)$$

$D$  is called the demagnetization factor. In general,  $D$  depends on the shape of the volume to be magnetized and the permeability  $\mu$ . If the model is of arbitrary shape, then  $D$  is different in different directions. To avoid the problem of cross-coupling it is best to use an ellipsoid of revolution as a magnetized core for the body. In this case  $D$  is independent of  $\mu$ . The values of  $D$  in the direction of the major axis are denoted by  $D_x$  and the transverse components by  $D_y$  and  $D_z$ , which are equal. If one component is known, the other may be computed, since

$$D_x + D_y + D_z = 1 \quad (9)$$

The fact that ellipsoids are magnetized uniformly and  $D$  is independent of  $\mu$  results in further simplification;

$$M = \frac{\mu H_x}{1 + (\mu-1)D_x} \quad (10)$$

and, when  $\mu \gg 1$ , then

$$M_x \approx \frac{H_x}{D_x} \left[ 1 - \frac{1}{\mu} \frac{1 - D_x}{D_x} + \dots \right] \quad (11)$$

$$\approx \frac{H_x}{D_x} \quad (12)$$

Hence the magnetization is essentially independent of  $\mu$  to a first order and is consequently essentially independent of temperature as long as  $\frac{1 - D_x}{D_x}$  is negligibly small. In practice,

$D_x$  is measured by mounting the body in a field and measuring  $E \times B$  through the angular motion of the body. Not only are there advantages in using an ellipsoidal core due to control of the demagnetization factor, but also it is easier to use a minimum volume of magnetic material, thereby making the coil currents to be measured as large as possible, thus enhancing the accuracy of the force measuring system [8]. Also, the magnetization level in the interior will be known quite accurately; recalling that  $\mu$  must be large and that  $\mu$  becomes increasingly smaller as the material approaches saturation, it becomes clear that from the standpoint of model core design it is desirable to know the value of the interior field quite accurately. The demagnetization effect for a simple body shape is illustrated in Figure 2. The design of magnetic wind tunnel models is discussed in Reference 8.

#### THE MODEL POSITION SENSOR AND SYSTEM CONTROL

The final detailed matter to be discussed is that of model position sensing and system stabilization. Originally, the model position was determined optically and this technique has been made to operate satisfactorily. Indeed, during routine operation, the model position is known to within, at the most,  $\pm 0.0015$  inches. The primary problem associated with the optical sensing system is its strong dependence upon geometric detail. Thus, a better system was sought. Subsequently, Stephens of MIT applied the principle of the differential transformer to this problem. His solution was quite successful and has been adopted by other study groups in the USA and other countries. Basically, the model is magnetized slightly by a 20 kilo Hz uniform field generated by a Helmholtz pair. (A Helmholtz pair consists of two coils of the same diameter which are separated by a distance equal to a coil radius.) The high frequency alternating magnetic field of the magnetized

model is sensed by a set of 12 coils so arranged that the outputs from these coils may be appropriately added or subtracted to provide translation position indication in the x, y, z directions, pitch angle  $\alpha$  and yaw angle  $\psi$ . It is noted that ONERA (France) has also been successful in detecting roll angle of models without axial symmetry, using this approach.

The signals from the electromagnetic position sensor are fed to an automatic control or compensation system. This system is needed to provide system stability and to control the current in the suspension and balance coils. In addition to the usual components of the output signal due to position error rate, rate of position error, and higher derivatives of position error, a signal is also generated which is proportional to the integral of the position error. One consequence of the use of the integral of position error signal is that the model may be held in a desired position for any applied load. Thus, the current in the coil is proportional to the applied force (i.e., in effect the integral of position error gives infinite stiffness); hence, it is possible to determine the applied forces and moments conveniently. Further, the use of this type of compensation system simplifies the introduction of input control signal to give a desired model motion for dynamic stability testing. Introduction of a bias or forcing signal at the input to the integrator acts like a false error signal. The compensation system obediently calls for additional current in the force and moment coils, thereby inducing the desired motion in the model. Arbitrary model motions can be generated up to limits set by the power supply.

The results to date determined by use of the electromagnetic position sensor and the associated control system show it to be very sensitive ( $\pm 0.0002$  inches and  $\pm 0.05^\circ$ ). In routine operation the position error of the installed system is  $\pm 0.0008$  inches in translation and  $\pm 0.1^\circ$  in angle. In addition to its lack of dependence on model geometry, the sensing coil assembly is exceedingly compact and does not close off all optical paths desirable for Schlieren photography.

#### THE THIRD GENERATION MIT/ARL MAGNETIC SUSPENSION AND BALANCE SYSTEM

It is instructive to explain the evolution of the newest magnetic suspension and balance systems by considering more elementary systems first. (A good review of the total effort underway in this study area may be found in Reference 9.) In its simplest form, consider the magnetic suspension system for a vertical tunnel, with the wind blowing downward in the gravity direction. This system consists of a single coil located above the test section, as shown in Figure 3. This coil produces a diverging field and so will attract the model toward itself. As an instrument,

this system will have a quadratic calibration since the model magnetization and the drag gradient field are each proportional to the coil current. This calibration can be linearized by use of separate magnetizing and gradient coils. However, this system is not practicable because it lacks lateral control and no controlled moments can be applied to the model.

The first successful system, that at ONERA, (and the initial MIT system) consisted of the use of five coils, five optical position sensors, and five control systems and power supplies, one each for drag, forward pitch, forward yaw, aft pitch and aft yaw (Figure 4). The stability and flexibility of this system can be improved by a simple change in logic. Rather than dealing with position signals from forward lift and aft lift, for example, the two position signals may be in the following way:

lift, or plunge = forward lift + aft lift

moment, or pitch = forward lift - aft lift.

This step provides relatively simple adjustment of the control loop for the range of slender models (magnetically stiff in pitch and magnetically soft in plunge) to quasi-spherical models (magnetically soft in pitch and magnetically stiff in plunge). This step is also applied to yaw and side slip. Two important consequences follow. First, there is the natural flexibility in adjusting the control system for a variety of shapes. Second, and perhaps most important, it leads naturally to the orthogonal approach [6] to magnetic field synthesis. From the test section out, an orthogonal system consists of (like layers of an onion);

- a. Test section wall.
- b. Electromagnetic position sensing structure.
- c. Moment coils (called saddle coils because of their shape) (see Figure 5).

At each end of this assembly are located

- a. Magnetizing and drag gradient coils.
- b. Lift and side force coils.

The new complex magnet system is best illustrated by the exploded view shown in Figure 6. Only one-half of the system is shown since the other half is identical. Within the Helmholtz coil assembly shown, which is one-half of a Helmholtz pair, are two sets of coils; one provides the main field  $H_x$  for magnetizing the model and the other provides the gradient field  $\partial H_x / \partial x$  for balancing the drag force. Both magnetizing coils are excited by a steady current in the same sense, or direction, in each coil. The two drag coils are excited in opposite directions and produce a pure field gradient about the center of symmetry which makes no

contribution to the magnetizing field. The lift and side force coil assemblies are iron-cored magnets located at both ends of the system and these form quadrupole arrangements to furnish the required  $\partial H_x/\partial y$  and  $\partial H_x/\partial z$  gradient fields which do not influence the magnetizing field. The inner and outer saddle coils are located inside of the main Helmholtz coil assembly and generate the fields  $H_y$  and  $H_z$  needed for controlling the pitching and yawing moments. These same saddle coils are also used for controlling the rolling moment as described earlier. The saddle coils are at  $45^\circ$  angles in order to allow a clear horizontal space through the magnet system for viewing with a Schlieren optical system. A sketch in Figure 7 shows this 6-component system in a simplified form as it would appear when adapted to a hypersonic wind tunnel.

A function block diagram for this third generation balance is shown in Figure 8 to indicate the various design items which must be taken into account. The compensator system shown gives the system the desired stability and frequency response. The temperature and pressure scanning devices and indicators are part of a coil-system protection arrangement. The model driver computer is the device which generates signals to be fed into the model control unit when it is required to magnetically force the model through various modes of oscillatory motions. The model injector will mechanically insert the model into the flow after the tunnel is started and will remove the model after the test run is completed. There are three possible reasons for using this device. They are:

- a. Avoid model distortions due to relatively long runs in a heated test medium.
- b. Avoid model loss if the suspension system cannot accommodate the starting and stopping loads.
- c. The tunnel may not start with the model in place.

The first reason, hopefully, will be the most common need for the model injector.

#### CONTROL OF THIRD GENERATION SYSTEM

The signals derived from the position sensing system must be modified by means of a linear dynamic compensating network. The compensation network parameters are adjustable to provide stable closed loop performance, with zero steady-state position error of the suspended model, and a well-damped, rapid transient response. The compensation network output signals control the main power amplifiers, which in turn control the magnet coil currents.

For the translational components, drag, lift, and side force,

a separate magnet system controls each component. Consequently, the axial position signal controls the magnetic drag force, the lateral position signal controls the magnetic side force, and the vertical position signal controls the magnetic lift force.

For the control of pitch and yaw components, two pairs of magnet coils are used. Each pair contributes to the control of pitching moment. Thus, the signal controlling pitching moment will be used to control two power amplifiers and similarly the signal controlling yawing moment will be used to control the same two power amplifiers. A "cross-over" network is needed, therefore, to perform this control-sharing function.

### COOLING SYSTEM REQUIREMENTS

The magnet coils, and the conductors which form the interconnections between coils, must be provided with a means of removing the heat which is dissipated in them due to ohmic losses. The cooling system must be reliable and of moderately high power-density capability. The most suitable choice of cooling mediums appears to be water and, in order to maintain optimum heat transfer characteristics, the cooling water should be demineralized, deionized, and deaerated. The cooling water actually circulated through the magnet coils is contained in a closed loop and heat is removed from this water with a heat exchanger. The heat is removed from the heat exchanger by unpurified water, which is circulated through a cooling tower.

The inner "cooling loop" (purified water loop) is provided with a high-pressure circulating pump to force the purified water through the magnet coils. A reservoir is used to accommodate changes in volume of the coolant due to expansion, and a portion of the cooling fluid flow is circulated through a small demineralizer and deaerator to maintain the required purity. Pressure, temperature, and flow indicators are provided in order to protect the magnet system from over-heating, should the cooling system fail.

### THE POWER SUPPLY

The power supplies needed for driving the electromagnets need special attention. For the wind tunnel application being considered by AHS, the power requirements are comparable to the wind tunnel power requirements. Care must be taken to ensure that the polarity, in a d.c. circuit carrying hundreds of amperes, can be reversed safely at frequencies of several hundred Hz. The total estimated power for a magnetic suspension system which would accommodate a 12-inch hypersonic nozzle operating at Mach 10 with

a dynamic pressure of 4 psi is about 3.6 megawatts. It is the unsteady performance requirements, however, which push the power requirement to the high level. For example, the power required varies as the square of the amplitude of the motion and as the fifth power of the frequency. Thus, in order to attain desirable reduced frequencies of about 150 Hz, the amplitude must be limited to 0.1 inch because of the severe power requirements.

The control magnet coils are energized by five large d.c. power amplifiers which control drag, lift, side force, pitch, and yaw. In addition, two a.c. power amplifiers are used to control rolling moments. The d.c. amplifiers are required to operate in all four quadrants of voltage and current. Thus, bipolar voltages and currents are available and power may be applied to the magnet load or withdrawn in the form of reactive power. The two a.c. power amplifiers are connected to the saddle coil pairs through coupling networks which serve to match the impedance of the amplifiers to the coil load, and also isolate the a.c. from the two d.c. power supplies which are also connected to the saddle coils. The magnetizing bias windings of the Helmholtz coils are energized by a regulated d.c. power supply. The current level can be controlled over a wide range, but remain steady during a test. Current ripple is maintained at a low level by the use of multiple-phase a.c. rectification, and due to the inductive nature of the load.

The d.c. power amplifiers must have a continuously variable voltage and current output where the output current is linearly proportional to an input voltage control signal. Each of the amplifiers must be capable of reversing output voltage and current when the control signal polarity reverses. A fast response when operating into an inductive-resistive load is required. To meet the response requirements, these units must be able to absorb reflected energy by inverter action from the load during changes in output level.

To meet the requirements of the system, these amplifiers must have a small signal response of output voltage versus input signal, flat to within three db from d.c. to 200 Hz, with 0 db per decade attenuation above 200 Hz. The voltage rise time from 0 to full output should be of the order of 5-10 milliseconds.

A smooth transition through zero current and voltage is desirable, as some of the amplifiers will operate near zero at times. A low level circulating current from the forward rectifiers to the reverse rectifiers may be used to obtain a smooth reversal of power. Chokes in series with each bridge may provide an impedance for control of the circulating currents.

#### CALIBRATION

At the present time two alternate procedures are available

for calibrating the magnetic suspension and balance system. The first procedure is essentially an adaption of the standard wind tunnel calibration techniques. In the classical wind tunnel calibration case, three forces and three torques are applied at the resolving center of the balance. The resolving center is a fixed point, determined by the balance geometry. For calibrating a magnetic suspension and balance system the model is suspended magnetically and a variety of forces and torques are applied mechanically to the model [4]. The currents required to resist the applied loads are recorded and measured. The interactions are determined, in effect, by recalibrating each component with varying levels of force and torque on the remaining components. Frequently the determination of the interactions is incomplete because of the large number of possible conditions. The magnetic suspension and balance system possesses an additional degree of freedom which complicates calibration. This degree of freedom comes about because this system has a resolving volume rather than just a resolving point. While this affords considerable increase in the flexibility of the system and type of testing possible, it suggests that new approaches to the calibration procedure are needed. As a first step in this direction, a small 6-component air-bearing balance has been constructed. After the wind tunnel tests are complete, the model is located in the same position it occupied during the tests, the same electrical currents are applied, and the forces acting on the model are then measured by the air-bearing balance. This simplifies the general calibration procedure and affords excellent accuracy. (At MIT, experience with this particular balance calibration system has indicated that an accuracy of 0.2% can be achieved without difficulty.) Ultimately it is hoped to further simplify the calibration procedure by using measured fields and field gradients together with experimentally determined demagnetization factors and then compute the forces and torques without further calibration. The development of this simplified procedure will follow once experience is gained with the new air-bearing force and moment measuring balance.

In either case, the data handling for the magnetic suspension and balance system is no more complicated than any existing wind tunnel balance system whose output is in the form of an electrical signal. The data handling system must record current level from the force-torque coils and the voltage level from the electromagnetic position sensor and the transducers installed in the air-bearing calibration equipment.

#### A TYPICAL MAGNETIC BALANCE DESIGN

In order to acquire a feel for the "numbers" related to a typical third generation ARL magnetic suspension and balance system, a design prepared for ARL by MIT will be briefly discussed. The design was aimed at satisfying the following conditions:

Test section diameter	15-inch
Operating Mach number	10
Operating stream dynamic pressure	4 psi
Minimum test model size	1-inch sphere
Maximum pitching frequency	150 Hz
Maximum plunging frequency	150 Hz
Number of degrees of freedom	6

The magnet system for this balance is similar to that shown in Figure 6. The limiting magnetic fields and gradients are presented in Table I. Referring to this table, it is noted that the roll control power which would be applied to the saddle coil is not shown; however, both the inner and outer saddle coils would require about 50 kilowatts of a.c. power. This would bring the total maximum power requirement for the balance to 4.84 megawatts.

The balance would require approximately 13 tons of hollow copper conductor for the coils and about 5 tons of iron would be used for the magnet cores. The over-all dimension of the magnet coil system would be approximately 7x7x7 feet. Cooling water would be required at the rate of 400 gal/min at 500 psig pressure. About 50% of the total cost of the suspension system would be needed for the power supply system with the magnet coil system representing about 30% of the total cost. No serious studies have been made of the size limitation for such magnetic suspension and balance systems. Preliminary design studies have suggested that such a system feasibly can be built for a 30-inch wind tunnel. Since the power required increases at least linearly with size, economic considerations suggest that an upper size limit exists. There is also an upper limit on the dynamic pressure for which the magnetic balance systems can be used. This dynamic pressure level is reached when the sum of the fields acting in the model cause the model to be saturated. No case has been found to date for which this limit is reached. However, it would become important for large systems operating at Mach number near unity.

#### APPLICATION

Because the magnetic suspension and balance system may be applied over a test volume, it is ideally suited for determination of dynamic stability parameters, in addition to measurement of static aerodynamic parameters and properties of wakes behind the bodies of arbitrary shape. The motion of the model can be controlled in six degrees of freedom. This allows several dynamic stability parameters to be separated, which have previously had to

be treated as a lumped constant. Further, the ability to control the motion affords a unique opportunity to reproduce transverse and rotational flight motions for the study of roll "lock-in" and for investigating previously unsuspected aerodynamic cross-couplings. This may prove invaluable in studies of missile inter-stage separation and store separation studies. Also, this may be particularly useful for aerodynamic investigations of spin-stabilized systems and research on magnus effects. With its high accuracy and sensitivity, the balance will be useful at low test-medium densities; it has already produced useful drag data [9] in the high Knudsen number regime (high altitude satellites). Through telemetry systems, which have been tried and proven in connection with operating in conjunction with a magnetic balance, body surface pressure and temperature measurements can be made. Through the application of tele-control devices aerodynamic control systems may be evaluated. Those study subjects where the presence of a support sting or strut creates deleterious effects are of special interest.

The magnetic suspension and balance system is certainly not expected to replace the conventional wind tunnel balances. However, there are particular study areas, as indicated above, for which the magnetic system is ideally suited, and for some studies there simply are no other satisfactory test methods available.

Shown in Figure 9 is a test model which was used to obtain roll data with the early MIT balance [10]; the roll-damping moment coefficient data shown in Figure 10 is not only in excellent agreement with data obtained previously by others, but the overall scatter is considerably reduced. Examples of lift, drag, and pitching moments for this same model are presented in Figure 11 and show a scatter of well under 1%. Additional early test results may be found in Reference 11.

Many of the promising features of the magnetic suspension and balance system have materialized as working experience with the system has been gained. Clearly, this new and unique wind tunnel aerodynamic testing tool, which is still very much in its infancy, offers considerable promise in the future.

## REFERENCES

1. Holmes, F. T., "Axial Magnetic Suspensions," *The Review of Scientific Instruments*, 8 (1937) (also *Phys. Rev.*, 51, p. 689, 1937).
2. Tournier, M. and Laurenceau, P., "Suspension Magnetique d'une Maquette en Soufflerie," (Magnetic Suspension of a Model in a Wind Tunnel), *La Recherche Aeronautique*, No. 59, p. 21, Office National d'Etudes et de Recherches Aeronautiques, Paris, France, p. 21 (July - August 1957).
3. Chrisinger, J. E., Tilton, E. L., Parkin, W. J., Coffin, J. B., and Covert, E. E., "Magnetic Suspension and Balance System for Wind Tunnel Application," *Journal of the Royal Aeronautical Society*, 67, 635, pp. 717-724 (November 1963).
4. Copeland, A., Covert, E. E., Petersen, R., and Stephens, T., "Contribution to the Knowledge of Magnetic Balance and Suspension Systems," Report No. 67-0283, USAF Aerospace Research Laboratories, Wright-Patterson AFB, Ohio (December 1967).
5. Covert, E. E., et al., "Recent Advances in the Development of a Magnetic Suspension and Balance System for Wind Tunnels," Report No. 65-114, Aerospace Research Laboratories, Wright-Patterson AFB, Ohio (June 1965).
6. Parker, H. K. and Kuhlthau, A. R., "A Magnetic Wind Tunnel Balance," Report No. AST3420-105-04U, University of Virginia, Charlottesville, Virginia (February 1964).
7. Stephens, T., "Methods of Controlling the Roll Degree of Freedom in a Wind Tunnel: I - Production of Rolling Moments," Report No. ARL 65-242, Aerospace Research Laboratories, Wright-Patterson AFB, Ohio (December 1965).
8. Copeland, A. B. and Tilton, E. L., "The Design of Magnetic Models for Use in a Magnetic Suspension and Balance System for Wind Tunnels," Report No. 65-113, Aerospace Research Laboratories, Wright-Patterson AFB, Ohio (June 1965).
9. Laum, F. L., "Summary of ARL Symposium on Magnetic Wind Tunnel Model Suspension and Balance Systems," Report No. 66-0139, USAF Aerospace Research Laboratories, Wright-Patterson AFB, Ohio (July 1966).
10. Copeland, A. B., Covert, E. E., and Petersen, R. A., "Wind-Tunnel Measurement at  $M=4.28$  of Some Static and Dynamic Characteristics of Finned Missiles Suspended Magnetically," *Journal of Spacecraft and Rockets*, 2, 7, pp. 833-842 (July 1966).

11. Copeland, A. B., Covert, E. E., and Tilton, E. L., "Measured Aerodynamic Characteristics of a Cone-Cylinder-Cone Model with Base Separation at  $M=4.8$ ," *Journal of Spacecraft and Rockets*, 2, 6, pp. 998-1000 (November - December 1965).

## FIGURE CAPTIONS

1. Illustration of Development of a Rotating Magnetic Field Using Two-Phase Induction Motor Principle.
2. Influence of Body Shape on Magnetizing Force Required to Produce a Given Induction Showing Demagnetization Effect.
3. Simple Drage Balance on a Vertical Wind Tunnel.
4. Initial ONERA Magnetic Balance System.
5. Saddle Coils.
6. Exploded View - Third Generation Six-Component System.
7. Illustration of Six-Component Balance and Suspension System on a Wind Tunnel.
8. Function Block Diagram.
9. Basic Finner Test Model.
10. Roll-Damping Moment Coefficient Derivatives Obtained with Early MIT Magnetic Balance.
11. Aerodynamic Data Obtained with Early MIT Magnetic Balance.
  - (a) Lift and Drag Data.
  - (b) Pitching Moment Data

TABLE I

Function	Coil	Max Field or Gradient	I (Amps)	R (Ohms)	IR (Volts)	I <sup>2</sup> R (KW)
Magnetizing		B <sub>x</sub> = 8 kilogauss	1665	0.394	656	1000
Drag	Helmholtz	$\frac{\partial B_x}{\partial x} = 300$ gauss/inch	1500	0.323	485	728
		B <sub>y</sub> or B <sub>z</sub> = 3.5 kilogauss corresponding to	1210	0.155	187	228
Pitch & Yaw	Inner Saddle	B <sub>y</sub> or B <sub>z</sub> = 4.95 kilogauss	1405	0.238	334	470
	Outer Saddle		1420	0.550	782	1110
Lift	iron Core	$\frac{\partial B_z}{\partial x} = 100$ gauss/inch	1420	0.550	782	1110
Lateral		$\frac{\partial B_y}{\partial x} = 100$ gauss/inch	1420	0.550	782	1110

NOTES:

Amps: Max amps for specified max. field or gradient

Ohms: At 140°F, for complete series connection

Volts and kilowatts: DC component only, based on corresponding amps and ohms

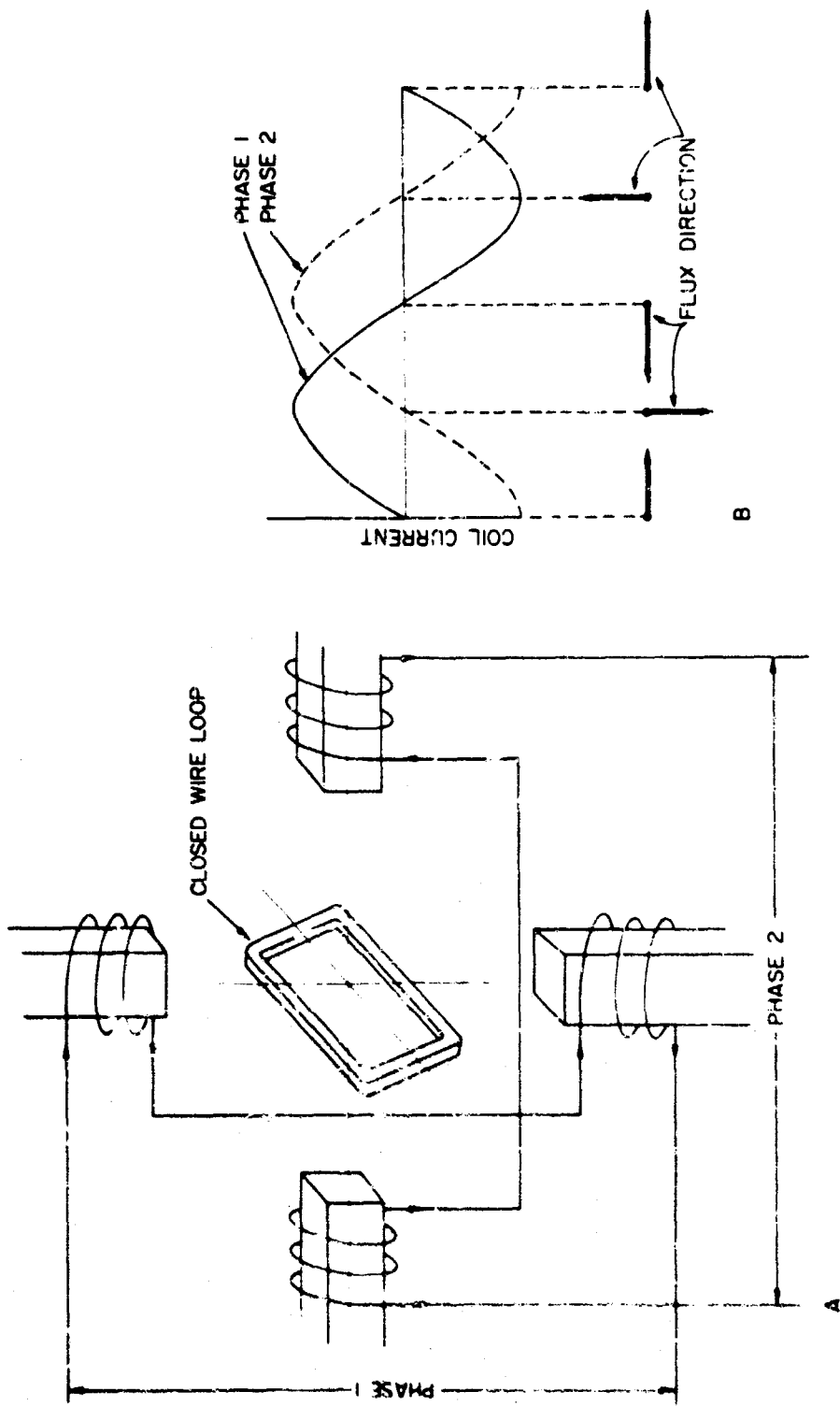


FIGURE 1

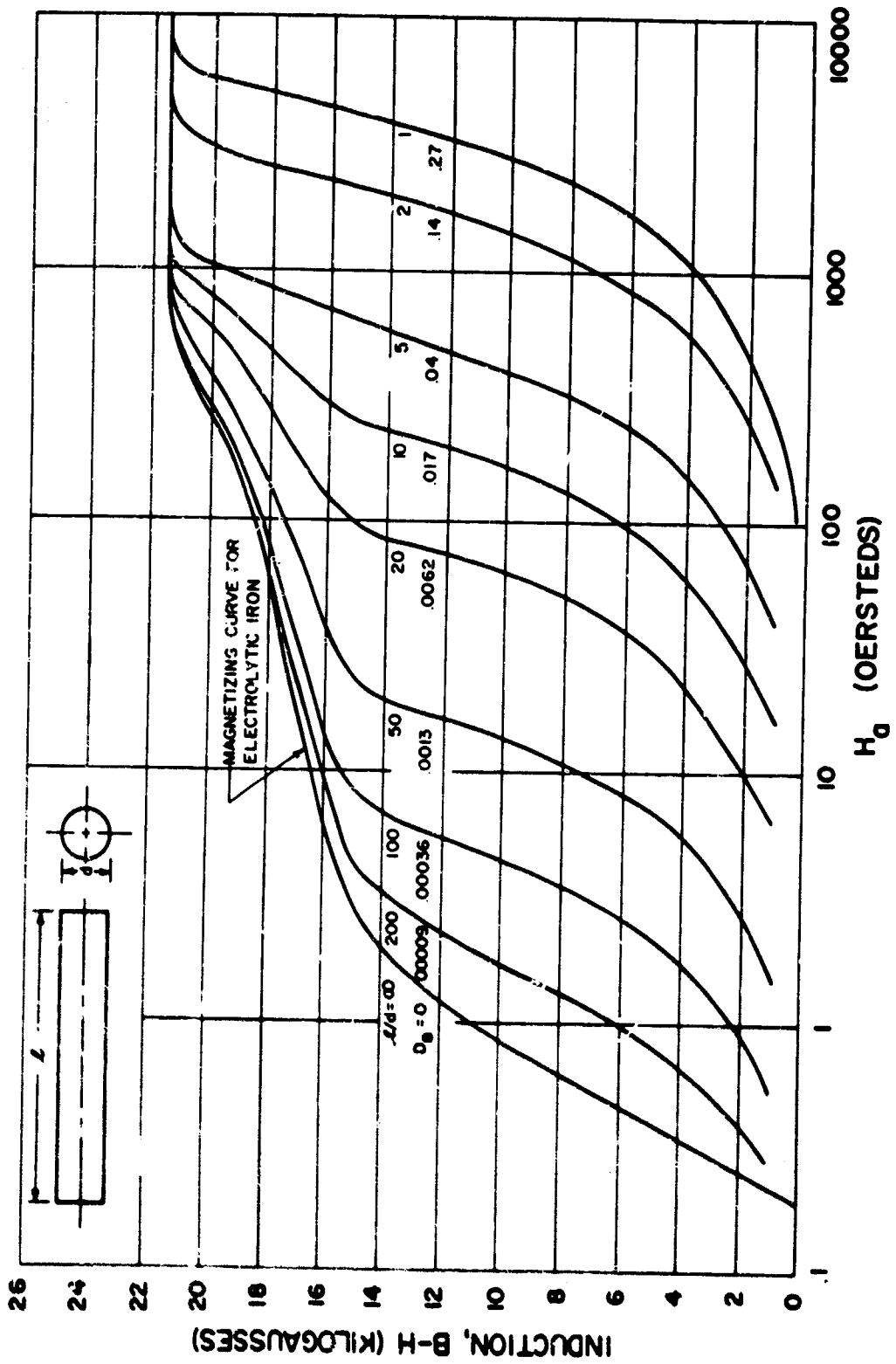


Figure 2

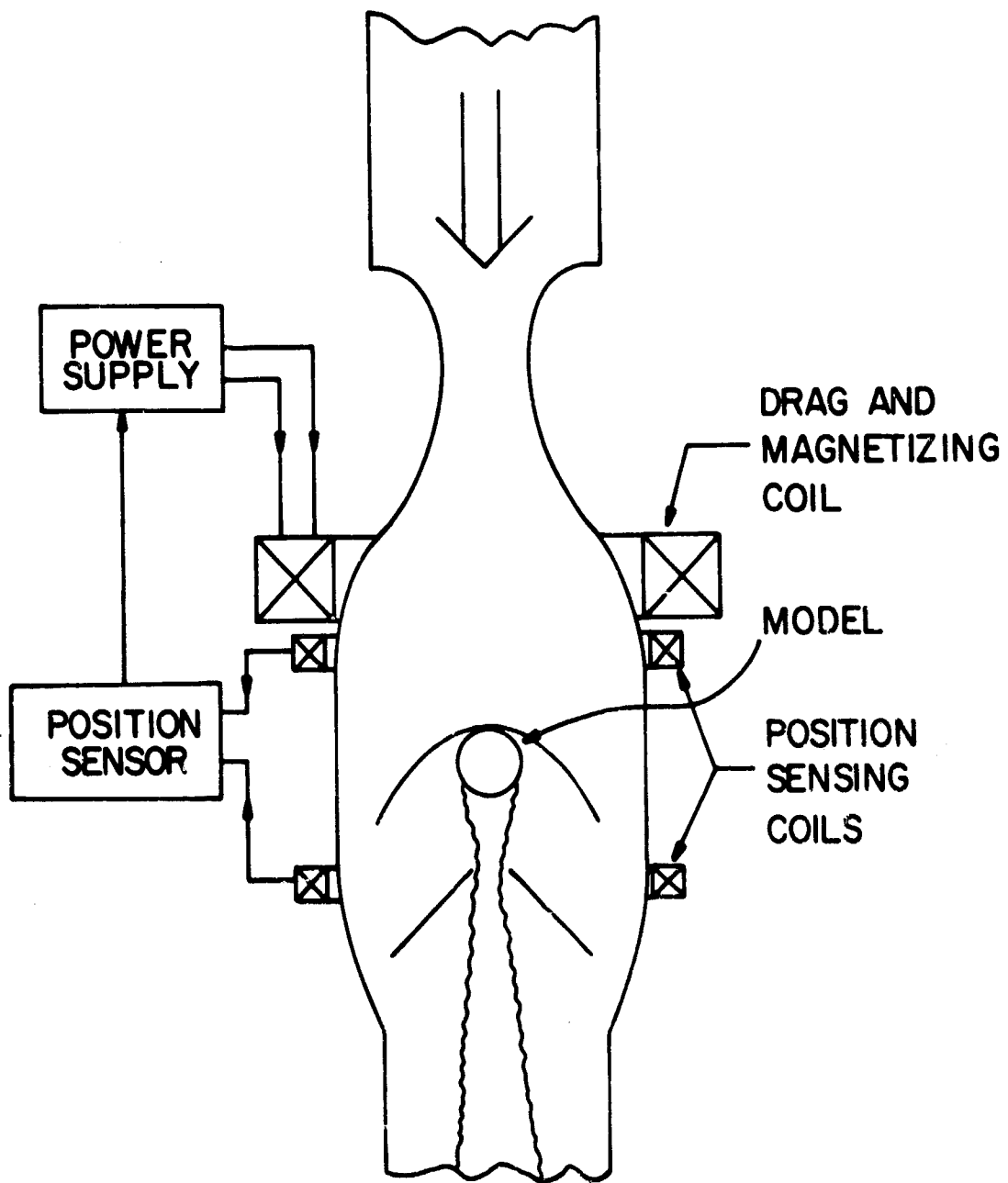
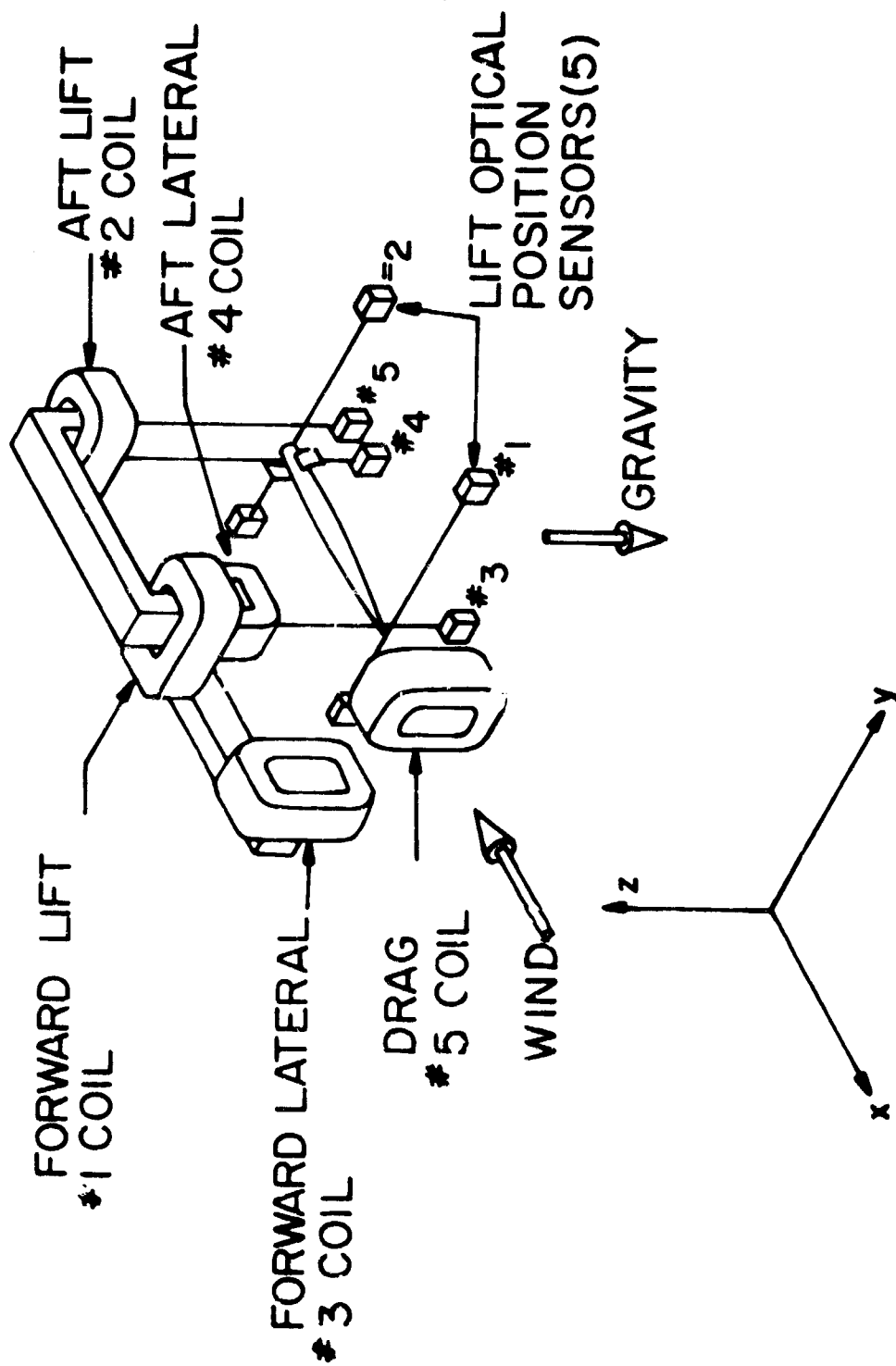


Figure 3

K-22



K-23

Figure 4

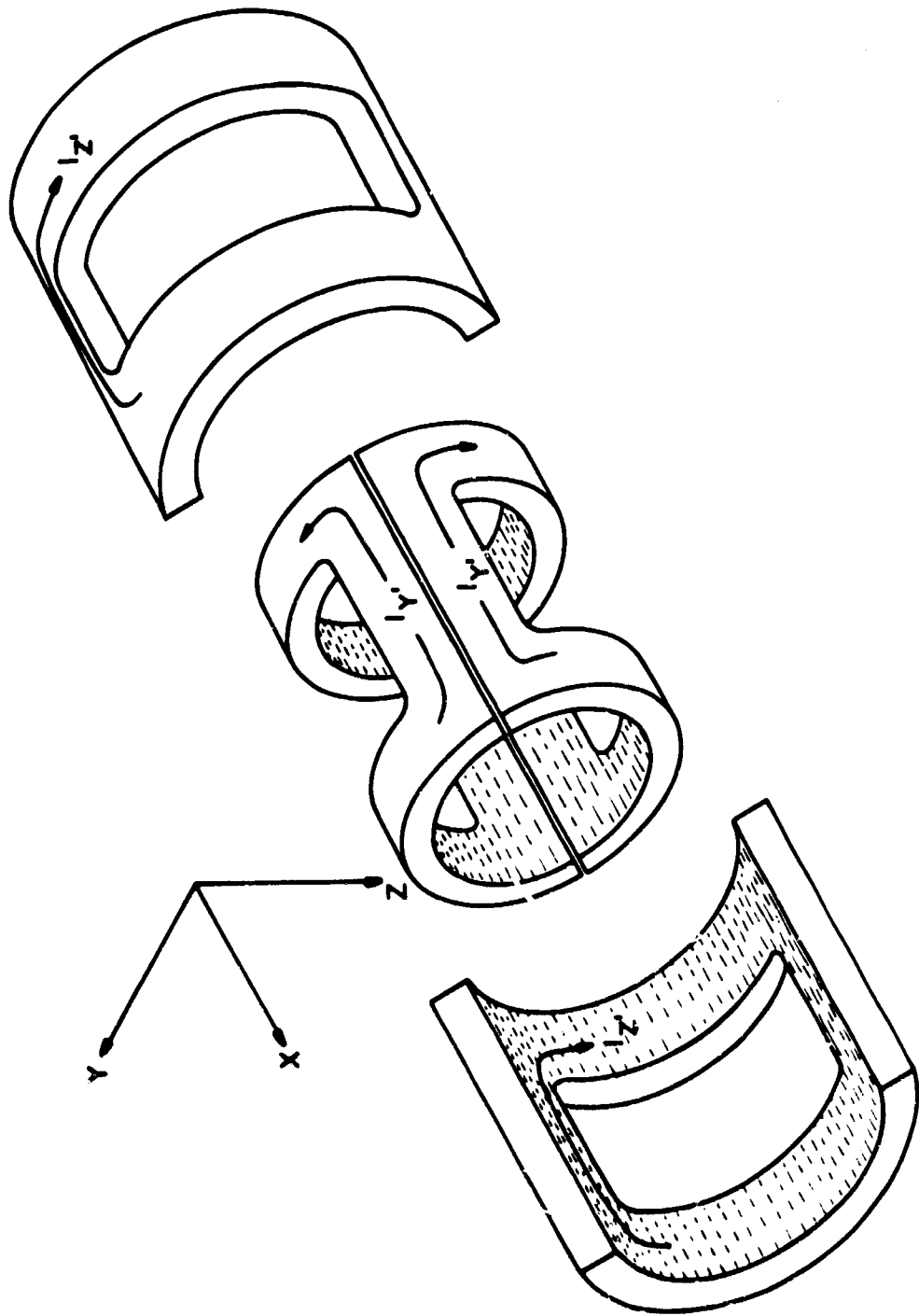


Figure 5

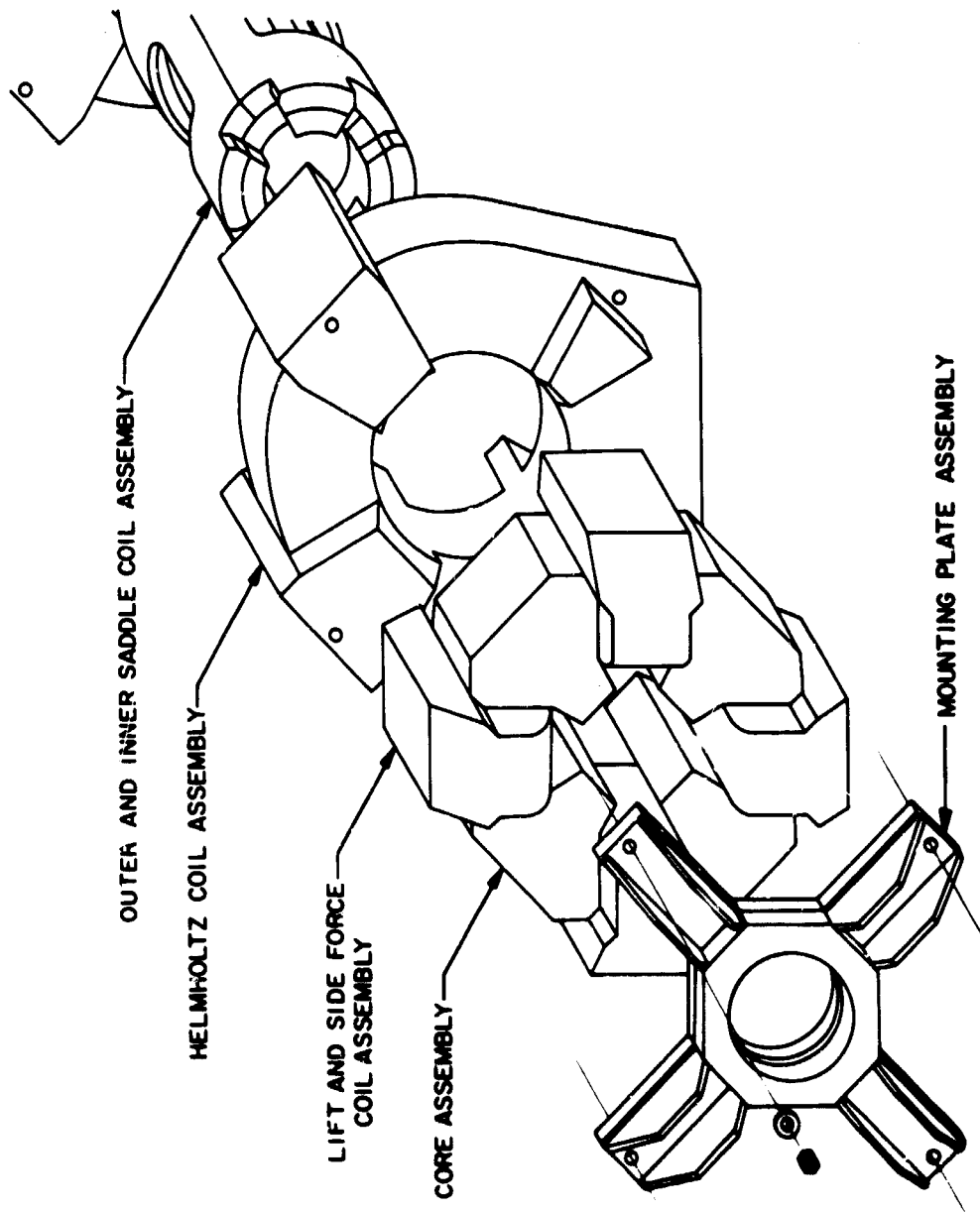
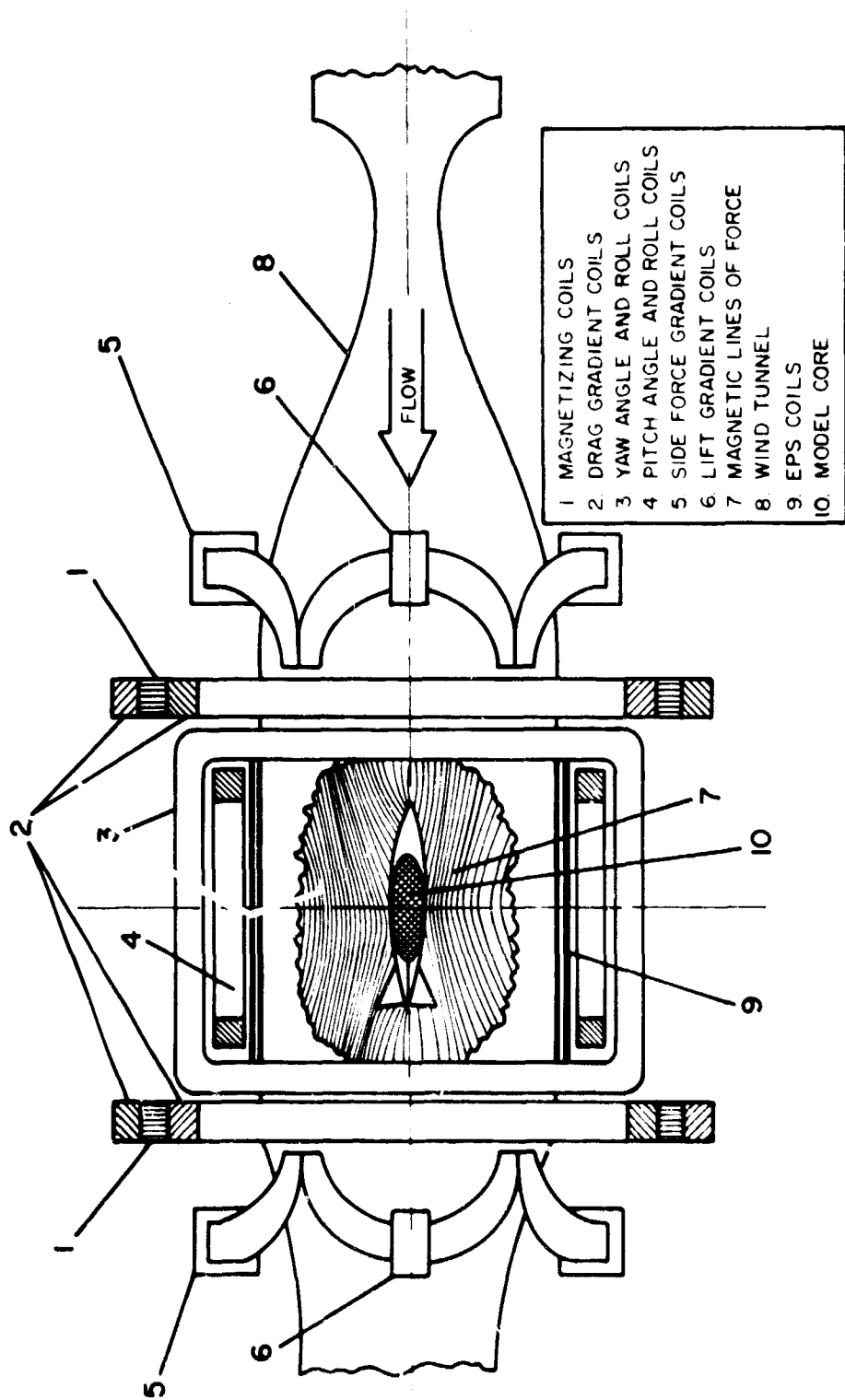


Figure 6



MAGNETIC WIND-TUNNEL-MODEL SUSPENSION AND BALANCE SYSTEM

Figure 7

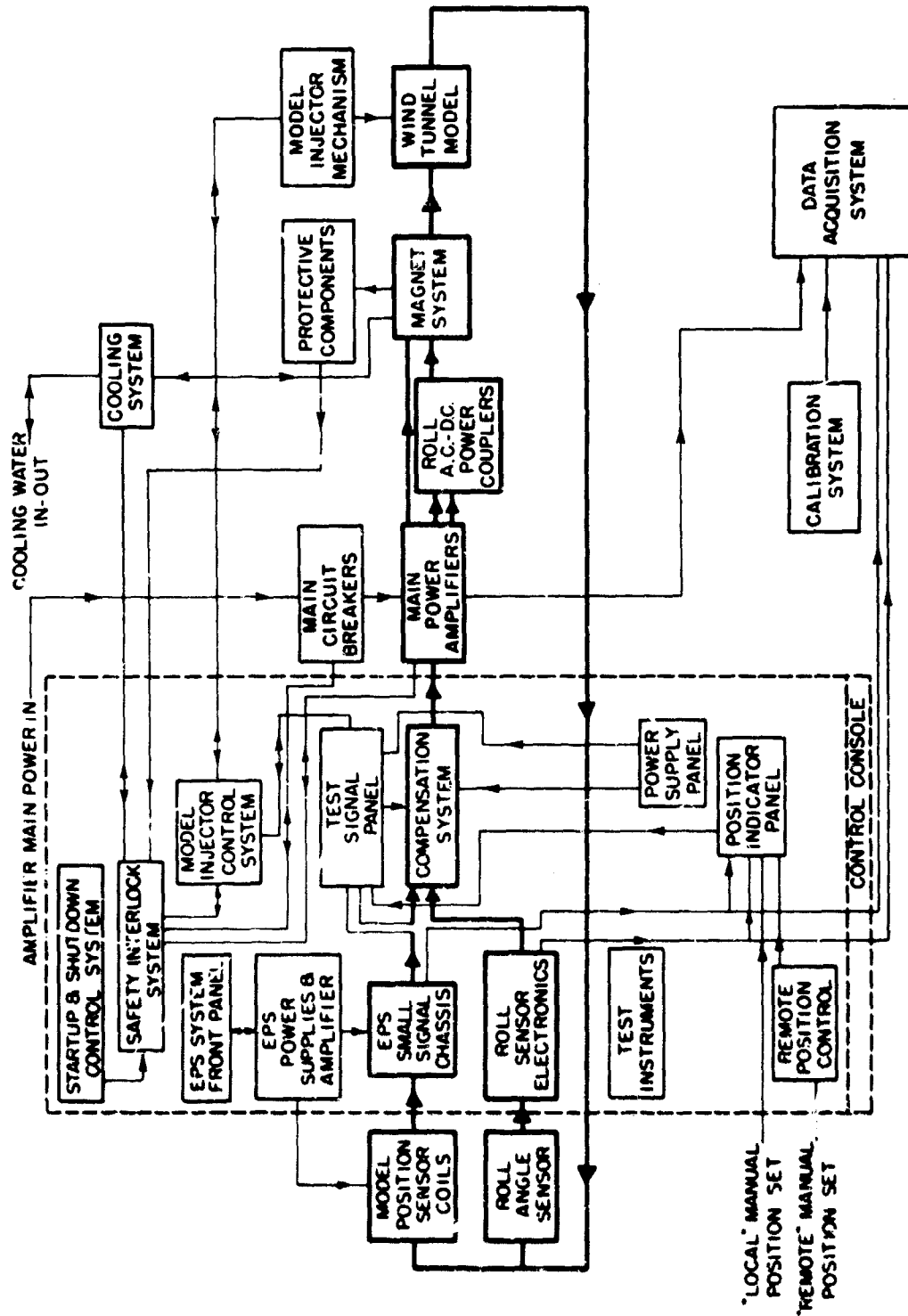
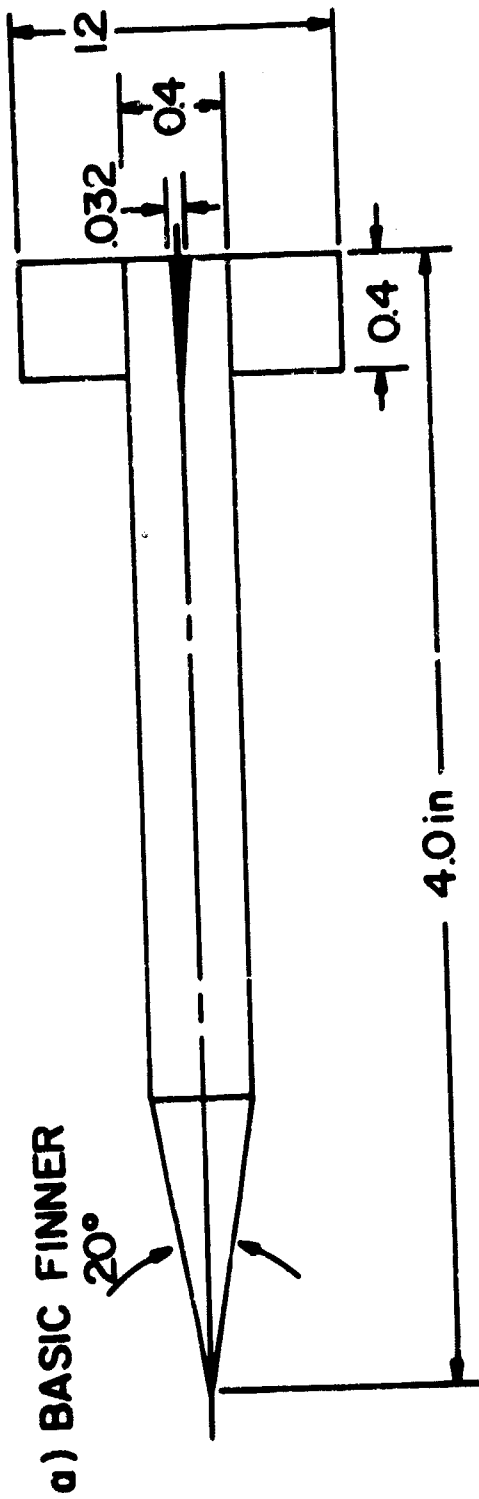
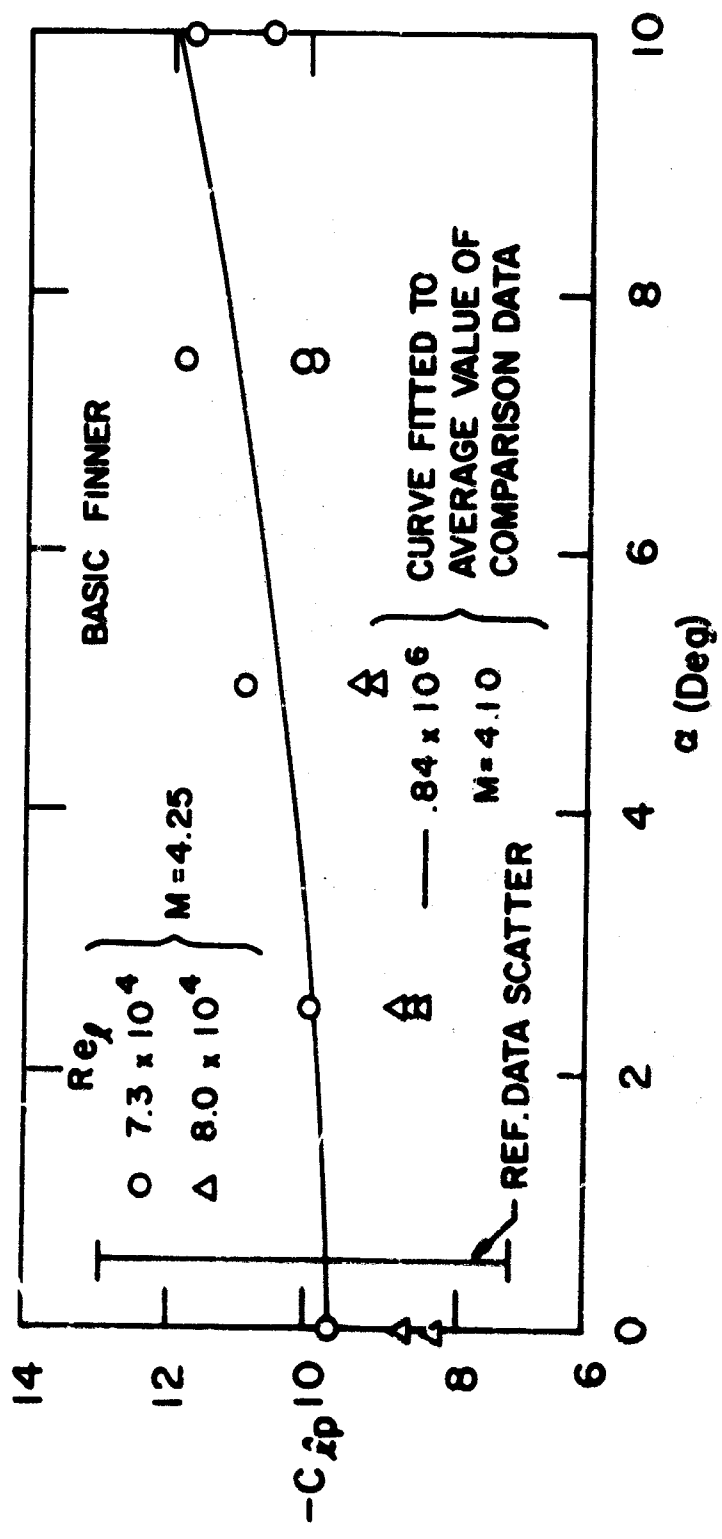


Figure 8



K-28

Figure 9



K-29

Figure 10

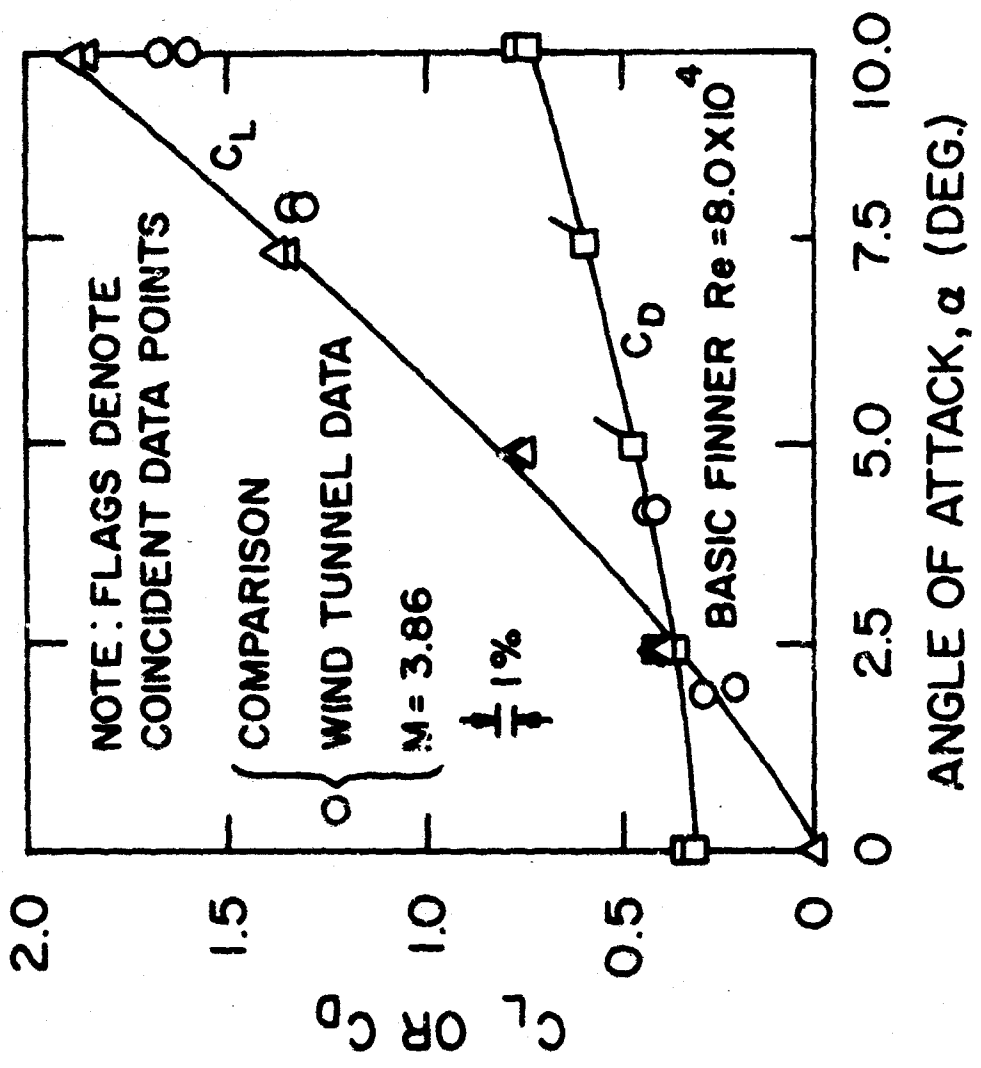


Figure 11 (a)

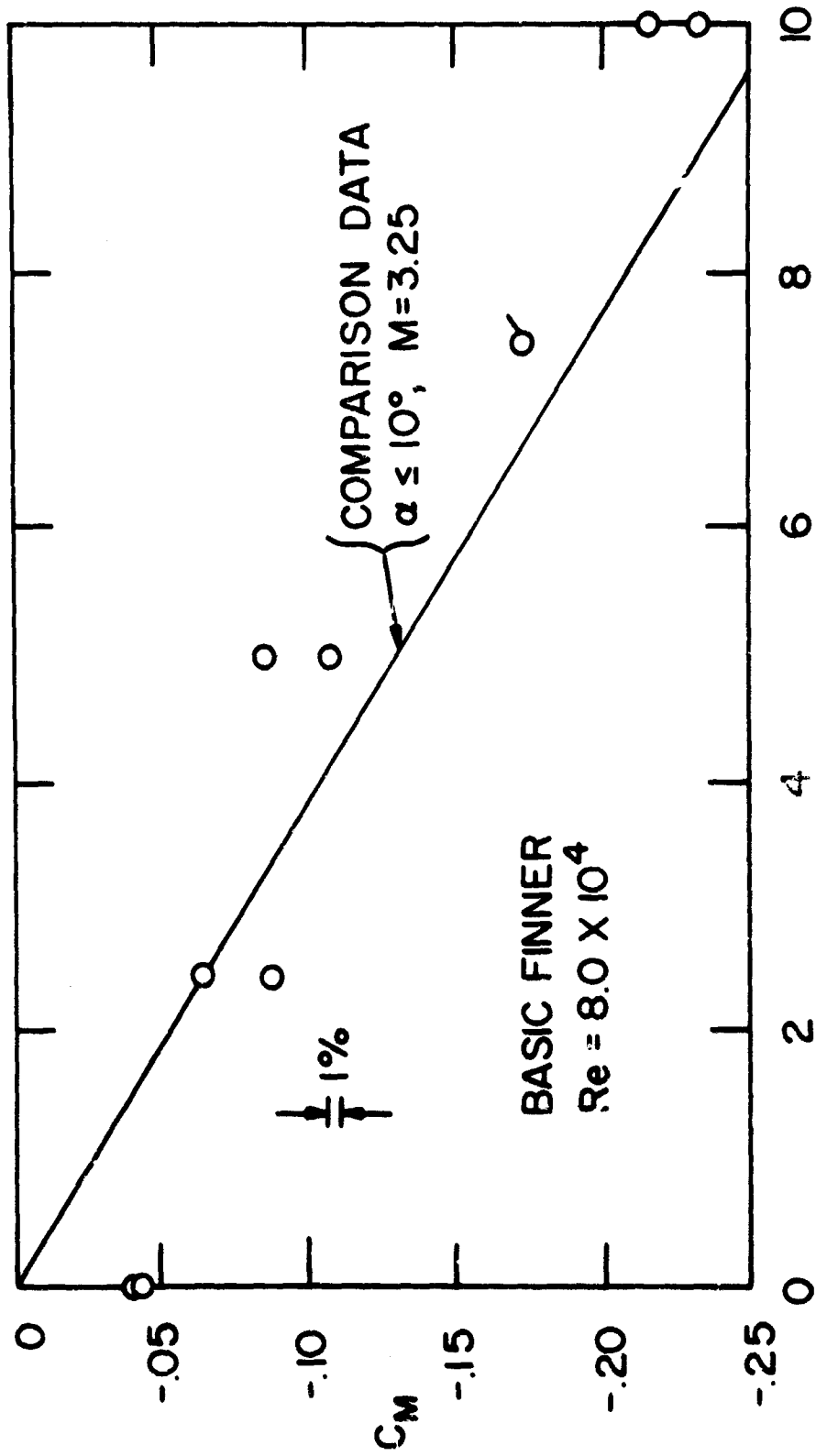


Figure 1. (b)

**RESEARCH IN ELECTROFLUID-DYNAMIC POWER GENERATION**

**Capt John A. Decaire and Mr. Maurice O. Lawson**

**Energetics Research Laboratory**

**Aerospace Research Laboratories**

**Wright-Patterson AFB, Ohio**

RESEARCH IN ELECTROFLUIDDYNAMIC  
POWER GENERATION

Capt John A. Decaire    Mr. Maurice O. Lawson

Energetics Research Laboratory  
Aerospace Research Laboratories  
Wright Patterson AFB, Ohio

ABSTRACT

Electrofluid dynamic (EFD) power generation, wherein fluid dynamic energy is directly converted into electrical energy, is being investigated at the Aerospace Research Laboratories. The basic process consists of electric charges of one polarity being carried to a high potential by a flowing gas. Fundamental characteristics are moderate gas temperatures, high gas densities, high electric potentials, and low electric current densities. ARL research is directed toward a unique two loop, two fluid generator cycle which promises attractive performance for space and remote area applications. EFD generators will also be suited to a variety of specialized applications.

## INTRODUCTION

The Aerospace Research Laboratories' initial interest in electrofluid dynamic (EFD) power generation processes began in the late 1950s in connection with electric propulsion concepts. At that time, increasing awareness of the space frontier and the associated power system requirements of high power-to-weight ratio, high reliability, and long life-time had led to a great interest in direct energy conversion processes, that is, those processes which generate electrical energy without the necessity of moving mechanical components. Subsequently, large scale research efforts were mounted worldwide into the areas of photovoltaic thermoelectric, thermionic, and magnetofluid dynamic converters. The earlier research results in electrofluid dynamic converters had proved largely discouraging and these processes thus received only scant attention. Feasibility studies however, indicated that EFD processes might be an important complement to other direct energy conversion processes pending the results of further research in several fundamental areas. Moreover, these research topics were well-suited to exploration with relatively modest facilities. As a result, an EFD research program was initiated about 1961-1962.

In the following text, the major aspects of the ARL-EFD research effort are given. Basic characteristics of EFD power generation processes and the fundamental nature of a special two-loop cycle are reviewed. The major results of theoretical and experimental studies are presented and potential application areas are discussed briefly.

## THE BASIC EFD GENERATOR PROCESS

In the basic EFD process, a flowing dielectric (electrically insulating) fluid\* transports electrically charged particles of one polarity through an electrostatic field. Figure 1 schematically illustrates the operation of a one-stage EFD power generator. It consists of three basic sections: charge production, energy conversion, and charge collection. Just upstream of the channel entrance electrode, electric charges of one sign (positive or negative) are seeded into the gas stream, e. g., by a corona discharge as shown. These charges are viscously coupled to the neutral gas molecules (momentum and energy transfer through collision) and are therefore carried downstream through the energy conversion section

---

\* In principle, the fluid may be either a liquid or a gas. However, practical considerations usually dictate the use of gaseous working media. The process is therefore also commonly referred to as the electrogas dynamic (EGD) process.

against the action of the electrostatic field due to the potential of the collector electrode. Downstream, the charges are neutralized, perhaps as shown, when they migrate to a surrounding metal surface. Because of the external load, charges accumulate on the collector until a steady neutralizing current is established through the load resistance.

The EFD generator then is simply a "fluid dynamic Van de Graaff" in that the flowing fluid performs the function of the mechanically-driven belt in a conventional Van de Graaff generator (indeed, Van de Graaff considered the possibility of fluid charge carriers in his patent [4]\*. Essential differences are that the coupling of the charges to the moving element is viscous rather than rigid and that much higher electrostatic field intensities are utilized. The basic electrical performance characteristics are similar, specifically very high voltage, low current D. C. power; however, the power densities of EFD generators can be far higher than those of conventional Van de Graaff generators.

A realistic physical model of the EFD process is simple and straightforward because the working gas is at a relatively high density level and can therefore be characterized by macroscopic parameters--temperature, pressure, molecular weight, breakdown field intensity, and charge mobility. Fundamental relationships between the major aerodynamic and electrical parameters are illustrated in Figure 2 where, for definiteness, a cylindrical conversion channel geometry is represented. Basic equations relating these parameters are listed in the lower part of the figure. Also listed are the fundamental limiting conditions associated with electrical breakdown, slip due to the non-rigid nature of the viscous coupling interaction, and charge deposition on insulator channel walls.

From the basic equations and limiting conditions, the general requirements on gas properties and flow conditions in the channel are as follows: [6, 9, 11, 14, 18, 19, 21]

. The breakdown field intensity ( $E_b$ ) of the gas should be high. Typical values of  $E_b$  at atmospheric density are listed in Table I for some common gases. For many gases  $E_b$  is linearly proportional to the density level over a wide range above atmospheric density.

. High gas densities are favorable over the range for which  $E_b$  is proportional to the density. For otherwise constant conditions, the power output increases with the square of the pressure level.

. The slip velocity of the charges relative to the gas flow should be

---

\*The numbers in brackets refer to references in the Bibliography at the end of this paper.

small. This condition indicates a low charge mobility which normally requires charged particles which are large compared to molecular ions (see Figure 3)[12,23].

. The flow Mach number ( $M$ ) in the channel should be low in order to have a high ratio of electrical forces to friction forces and thus a high stage efficiency. The choice of Mach numbers however, must reflect a compromise between efficiency and power density since the maximum power density (for a given stagnation pressure) is obtained at  $M \approx 0.7$  [9].

. A low molecular weight gas is favorable since flow speeds are then higher for the same Mach number.

The basic channel geometry is also a major performance determinant. Three main classes of channel configurations are shown in Figure 4. The relative performances among these channels vary with the charge generation capability, the electric field structure in the channel, and the necessity to keep the charged particles from contacting the insulator walls of the channel thereby placing a limit on the length-to-hydraulic radius ratio of the channel [8].

#### BASIC PERFORMANCE CHARACTERISTICS

Based upon the above considerations, the major performance characteristics for EFD power generation processes are itemized in Table II [10, 18, 19, 21, 22].

A high output voltage, on the order of 100,000 volts and higher, is perhaps the most notable characteristic of this energy conversion process. Highest power densities are achieved with field intensities in the conversion section approaching the dielectric strength of the gas. At high gas densities, the potential gradients are typically about 100,000 volts per centimeter.

The characteristic of low electric current density results from relatively low transport speeds of the charges which correspond approximately to the gas velocities (in comparison to electron speeds in vacuum), as well as to space charge effects. The self-generated field of the charge is limited in principle to the dielectric strength of the gas, and further, may be more strongly limited by the current production means itself.

The very high number of neutral molecules per elementary charge, order of magnitude  $10^8$ , is primarily an effect of space charge. Moreover, if the available energy per neutral molecule is approximately 1/100 of an electron volt, then to transport one elementary electric charge against a potential of, e. g.,  $10^5$  volts, the combined fluid dynamic energy

of a great number of neutral molecules of the working gas is required, on the order of  $10^7$ .

The characteristic value of power density is on the order of one kilowatt per square centimeter--the value depending principally on the desired efficiency, the gas or working medium properties, and the geometry of the channel.

A favorable power-to-weight ratio of the process is indicated because of the extremely high power output per unit volume of the conversion section. This high power per unit volume of the conversion section comes about because of the relatively short conversion section lengths (order of 10 centimeters) and the power density of 1 kilowatt per  $\text{cm}^2$ . In addition, no heavy magnetic or cryogenic equipment is required.

The EFD process is primarily suited for relatively low values of power levels. Typically, the power output can be increased by making the channel larger [19]. Unfortunately, this is also accompanied by an increase in the output potential. In most cases, a practical upper limit on output potential dictates individual channel sizes corresponding to power outputs in the kilowatt class. By paralleling channels however, a wide range of power can be covered--from kilowatts to megawatts.

Temperature levels are relatively moderate since the gas temperatures in the conversion duct must be below thermal instability values so that the gas is a good electrical insulator. Thus, closed cycle applications are feasible including the application of nuclear or isotope heat sources.

The basic EFD process is an inherently weak conversion process (a low total pressure ratio capability) which transforms only a small portion of the total thermal energy (enthalpy) of the gas [8, 18, 21]. Incorporation of an EFD generator into an overall energy conversion cycle from heat into electricity then, represents a major problem, since there is a lower limit on the thermal efficiency required for each application.

#### THERMODYNAMIC CONSIDERATIONS

The overall energy conversion cycle from heat into electrical power can be regarded as a two-step process: (1) heat is transformed into fluid dynamic energy and (2) fluid dynamic energy is transformed into electrical energy by the EFD process. Efficient energy transformation in the first step requires a high expansion pressure ratio process (e. g., a high Mach number expansion) which, as mentioned above, is incompatible with the low pressure ratio of an EFD conversion channel.

One possible approach to resolve this fundamental incompatibility is a multi-stage EFD generator, wherein individual EFD channels are placed in series in order to accomplish an overall high pressure ratio [18, 13]. However, in view of the extremely small pressure ratio per stage, a very large number (hundreds) of stages are required to achieve an attractive thermal efficiency. This is a major objection for space and remote area application where simplicity and compactness are highly desirable features. Moreover, multi-staging in series will be difficult to accomplish with working gases containing charged particles. Key problem areas are the production of the proper charge-to-size ratio particles in sufficient number densities at low subsonic speeds and the collection and neutralization of these particles. These processes must be highly efficient electrically as well as being accomplished with electrode and ducting configurations corresponding to extremely low aerodynamic drag losses. Other problem areas are the control of surface currents and breakdown in the initial stages where the gas is at its highest temperatures, the scheduling of the stage size to account for the change in flow properties through the generator, and the operational stability of very large numbers of interdependent channels.

In view of the above considerations, the EFD research at the Aerospace Research Laboratories is concentrated on a special power generation cycle which employs two flow loops with two working media, one for the thermodynamic process to transform heat into fluid dynamic energy, the other for the EFD process to transform fluid dynamic energy into electrical energy [18]. In such a special cycle the conflicting requirements of the thermodynamic and EFD processes are essentially uncoupled and favorable conditions can be provided for each individual process. The net result is that an attractive thermal efficiency can be achieved in a single stage EFD generator. Figure 5 shows a possible schematic of this two-loop power generation cycle. The primary flow loop for the thermodynamic process uses a steam (e. g., a metal vapor) of high molecular weight which is expanded to a high Mach number in the ejector nozzle. The high speed flow discharging from the nozzle induces a recirculating subsonic flow in the secondary loop which is filled with a low molecular weight gas of high dielectric strength (e. g., hydrogen) at a suitable temperature and pressure level. The temperature level of the recirculating EFD gas is kept sufficiently low to effect condensation of the thermodynamic steam. To complete the thermodynamic loop, the condensed steam is separated from the EFD medium and returned to the boiler (e. g., by a jet jump). The heat exchanger brings the EFD gas back to the appropriate temperature level while the waste heat is rejected.

In this two-loop cycle, the recirculating EFD gas has no available enthalpy of its own to be converted into electrical energy but rather acts only as an energy storage device (a gas flywheel), the kinetic energy of

which is sustained by the continuous driving action of the thermodynamic steam from the ejector nozzle. This primary flow must supply just enough energy to make up for the kinetic energy removed by the EFD process and fluid dynamic losses in the channel (including electrodes), diffuser, and recirculating duct. The energy transfer by the flow mixing process can be accomplished efficiently because the speed difference between the working media can be kept reasonably small. For example, the speed of the thermodynamic steam should be less than twice the speed of the EFD gas [18]. This requirement does not conflict with the requirement of a high expansion pressure ratio for the thermodynamic medium, provided its molecular weight is sufficiently high in comparison to that of the EFD working gas. Preferably as shown in Figure 5, the thermodynamic steam may not only be used for energization of the EFD gas but also for forming low mobility charged droplets by condensation around ions.

The design of ARL's experimental test generators has been based upon simulation of the closed cycle, two-loop system by using only one working fluid as shown schematically in Figure 6 [20]. A high pressure gas is expanded supersonically through the ejector nozzle and sets up a recirculating flow in a closed duct system. A mass flow rate equal to the inlet mass flow is bled out of the system to maintain steady flow conditions. The relative pressure levels between the inlet primary flow and the recirculating or secondary flow is controlled by means of an adjustable throttling valve located in the bleed line. To date, the experimental tests have used air as the working medium since it is routinely available at high pressures ( $\leq 200$  atmospheres) from the ARL bottle farm. Fortunately, air has a rather high value of breakdown field intensity which moreover is typically closely proportional to the density level over a wide range ( $\rho/\rho_n \approx 20$ ). Thus, although a major decrease in performance is incurred as compared to the use of two fluids, the air-air simulation serves satisfactorily to verify the major performance trends for the EFD process. In addition to low drag loss geometries, primary experimental emphasis has been given to the electrical aspects of the generator; that is, unipolar charge generation and electric field structures since these are fundamental considerations which are in essence, the foundation upon which the success of EFD power generation rests.

### ELECTRIC FIELD STRUCTURES

Basically, attractive performance is indicated for the two-loop recirculating EFD generator if sufficiently large number densities of low mobility charged particles are produced (the transverse Coulomb\* field associated with the particles should approach the dielectric strength of the

\*Applying the principle of superposition, the electric field in the EFD conversion section is composed of two components: (1) the Coulomb field

gas), if the average axial electric field intensity (applied field\*) is made to approach the gas dielectric strength, and if the charged particle cloud (not channel) of a large length-to-hydraulic radius ratio (the initial hydraulic radius should be small to keep the length small and thus the output voltage from becoming prohibitively high).

Typically, however, the axial electric field associated with a uniform unipolar charge distribution of large length-to-hydraulic radius ratio is greatly intensified in the end regions of the charge cloud with only mild field strengths over the major portion of the length [4, 16]. In the EFD channel, these over field strengths are particularly strong near the entrance where the charge density is typically highest. Moreover, the Coulomb and LaPlace fields are additive\*. Breakdown field intensities may be approached with relatively low values of charge density and average axial field intensity, corresponding then to a severe degradation of the generator performance.

The situation can be greatly improved however, by providing electrode shielding surfaces which effectively smooth out the potential gradient along the channel length. One possibility is to use field grading electrodes similar to those used in Van de Graaff generators. However, in EFD generators, the required potential distribution for the scheduling electrodes will be difficult to maintain. A much simpler approach is to utilize a single fixed-potential electrode surface which extends along the charge cloud in the manner shown schematically in Figure 7. In the region of charge production, the shielding electrode surface should be immediately adjacent to the charges. The electrode surface should slope away from the outer boundary of the charge cloud such that an increasing distance occurs as the collector is approached. The lateral spacing along the conversion section depends on the charge density, the LaPlace field, the desired potential gradient, and the basic channel geometry [2]. With this electrode shaping, a relatively uniform potential gradient can be obtained over the complete length of the channel.

The qualitative aspects of these electrode shielding requirements were recognized early in ARL's research effort. An entrance shielding electrode has always been incorporated in the design of experimental channels (see Figure 8). Quantitative information however, has only recently been determined. A notable contribution has been the development of a numerical computer program to calculate the LaPlace and Coulomb fields due to complex electrode shapes and charge distributions which have cylindrical or two-dimensional symmetry [3]. This program is being used to

---

\*(cont'd) which is due to the charged particles. This includes the effects of induced "image" charges on the electrodes. (2) the LaPlace field which is due to potentials applied to the electrodes by external circuitry (loads, power supplies, etc.)

determine the field strengths corresponding to electrode shapes in the experimental EFD generators.

### UNIPOLAR CHARGE GENERATION

A major research objective has been to demonstrate the capability to generate sufficient numbers of unipolar charges in the dense, high speed flows. The charging method most extensively studied is the corona discharge process which was illustrated in Figure 1 (see also Figures 8 and 9). Although this process is extremely complex, the gross characteristics can be understood as follows: a high potential applied to the attractor electrode results in a very intense electric field in the immediate vicinity of the sharp pointed tip of the grounded corona electrode. Ionization of the gas occurs locally in this high field region with subsequent charge separation as the ions move toward the electrode of opposite polarity. The ions moving toward the attractor electrode are swept downstream by the viscous coupling interaction. Typically, the expansion nozzle for the primary flow serves a dual purpose as the attractor electrode. Because of the supersonic expansion, the low mobility charged particles (droplets) can then conveniently be produced by free condensation upon the ions of the corona process [12]. A small mass fraction of a vapor (e. g., water, alcohol) added to the primary air becomes highly supersaturated in the high Mach number expansion. Preferably, the ions of the corona then act as condensation nuclei for this vapor component, resulting in small, primarily singly-charged droplets\*.

Experimental testing has primarily been conducted on the cylindrical channel EFD generator shown in Figure 8. A more detailed view of the electrode and conversion section assembly is shown in Figure 9. Primary construction materials are stainless steel and a resin-impregnated fiberglass. This test generator is clearly designed as a basic research tool rather than a generator with specified performance characteristics. All major components of the conversion section are easily interchangeable over a wide variety of shapes and sizes. Typical sizes are a 1/4 inch diameter nozzle designed for nominal Mach 2 operation, and a 1-1/4 inch diameter conversion duct 1 inch long. For convenience, long ducts are used as a simple and inexpensive outlet for the high voltage of the EFD process and also to provide a large charge collecting surface. The aluminum shields prevent corona losses from the sharp edges of bolts, flanges, etc.

---

\*Homogeneous condensation (where the vapor provides its own condensation nuclei) may occur in which case the ions attach to preformed droplets. Higher mobility, multiply-charged droplets are then probable.

The corona current-attractor voltage characteristics have been investigated for both ions and charged droplets by the free condensation methods (using water vapor) over total pressures of the primary air up to 80 atmospheres [7, 14]. Typical total temperatures have been relatively low (0-150°F), limited primarily by the heat resistance of the solid insulator materials. Figure 10 shows representative test results as a function of the total pressure level. For ions, the maximum current is linearly proportional to the pressure as expected. Above 40 atmospheres however, a special corona electrode geometry was required. This took the form of a sharp-edged disk rather than a single sharp point. The expansion waves produced by the air flow over the disk edge generates a favorable low density in the corona region. Even with the special electrode, the maximum currents for the charged droplet case deviate from the expected linear relationship above about 40 atmospheres [17]. This is due to the non-linearity of the maximum attractor voltage (sparkover voltage) for the corona electrodes.

The effect of geometric scaling on the corona current production has also been investigated. Generator configurations photographically scaled for inlet nozzle critical diameters of 1/8, 3/16, 1/4, and 5/16 inches were tested. Figure 11 shows current and attractor voltages relative to the largest configuration. As the solid curves show, the smaller configurations yield higher currents than would be predicted from a linear scaling relationship [17]. These test results are thought to be largely due to an experimental inability to scale the sharpness of the corona electrode and to the well known increase in gas dielectric strength with very small electrode spacings. In any case, the previously indicated interest in small flow geometries is strengthened.

Initial experimental tests have also been conducted with electrohydrodynamic spraying as the charge generation process. The electrode geometry is essentially the same as that for the corona process, except that the corona electrode is replaced by a capillary tube. As an electrically conductive liquid is expelled through the tube in the presence of the high electric field, the liquid is inductively charged and disintegrates into small droplets in the dense flowing gas. Current levels obtained with this process have been comparable, but somewhat less than the currents obtained with the corona process. Unfortunately, the charged droplets apparently have a broad, highly non-uniform range of charge-to-mass ratios [5].

#### HIGH VOLTAGE CONSIDERATIONS

The output potential of the test generator shown in Figure 8 is practically limited to about 400,000 volts at which sparkover occurs from the large sphere along the external surfaces of the long ducts. Thus, with

the current levels indicated above, the highest power levels attained with this generator have been about 1/2 kilowatt. In order to be able to experimentally work within a somewhat higher voltage limitation, an encapsulated EFD test generator was designed and built. The overall construction of this generator is shown in Figure 12. A grounded steel tank surrounds the basic generator assembly which is supported by four long ( $\approx 2$  feet) nylon "legs". Within the voltage limitations of this support structure, the primary electrical insulation medium is now the secondary flow inside the tank which typically is at 10 atmospheres pressure.

Initial "shakedown" tests demonstrated a voltage capability of the collector support structure in excess of one million volts. Initial experimental tests however, with conversion duct lengths up to 6 inches (otherwise retaining the same generator components as in the original generator) yielded an increase in voltage from slightly greater than 400,000 volts at one inch, to only about 600,000 volts at 6 inches. The basic limit is spark-over on the insulator walls of the channel.

One hypothesis advanced for this low voltage performance was charge deposition on the walls. The recirculating air is extremely dry because of the large increase in specific volume accompanying the expansion from the primary to secondary condition. Charged droplets which diffuse into the secondary flow tend to evaporate and travel rapidly to the channel walls. Even a very small current deposition will lead to very large wall charge accumulations since the reverse drift velocity of the charge on the wall is very small compared to the main flow velocity. The test generator was modified to allow control of the humidity of the secondary air. Introductory tests with special conversion ducts have shown that there was indeed a substantial current to the duct walls and that it is significantly reduced by increasing the moisture content of the secondary flow. High voltage tests are presently continuing with secondary air humidification.

#### WORKING MEDIA

In addition to the research outlined and already mentioned above, ARL has conducted static high pressure investigations into the breakdown voltage characteristics of the low molecular weight gases, hydrogen and helium, and of mixtures of these gases with trace amount of highly electro-negative (breakdown inhibiting) gases (sulfur hexafluoride and freon 12) [14, 15].

#### TWO-DIMENSIONAL CHANNELS

With the improved understanding of the fundamental requirements of EFD processes developed from the theoretical and experimental research,

the past year has seen a shift in emphasis to two-dimensional channels in the special form of a radial outflow geometry [1]. The configuration of the test generator is schematically shown in Figure 13. The principle of encapsulation has been carried over in the design; the primary nozzle is a 4 inch diameter disk nozzle which discharges radially outward. This particular geometry was selected for its high mass flow capability, even for small hydraulic radii, and because it can be relatively cheaply and easily manufactured with extremely close machine tolerances which is of paramount importance since the main interest is in very small hydraulic radii nozzles; that is, slot heights of only several thousandths of an inch. Initial experimental tests with this nozzle have indicated that corona charge production may have to be accomplished with the corona electrode external to the primary nozzle. Present research is emphasizing corona charge production immediately downstream of the nozzle and the influence of corona electrode geometry and secondary flow relative humidity on charge production.

#### POTENTIAL APPLICATION AREAS

In view of the early stage of experimental investigations in EFD power generation, a discussion of specific application is quite premature. However, as shown in Table III, the potential of EFD processes with regard to both small and large powers, both closed and open cycles, and various energy sources point toward many attractive applications, particularly in space and other remote infrequently serviced areas. Several possibilities which might be envisioned are listed in Table III. High voltage application such as electric propulsion, fluid dynamic Van de Graaffs, and high power, burst type systems (where efficiency is not an important consideration) are, of course, naturally suited to EFD generators. Other application areas, such as air and space vehicle power, will require the development of compact inexpensive power conditioning equipment.

#### ACKNOWLEDGEMENTS

The authors gratefully acknowledge the guidance and help of Dr. Hans J. P. von Ohain - ARL's Chief Scientist and also Research Leader for Energy Conversion. Appreciation is also expressed to Messrs. Siegfried Hasinger, Krishan Joshi, Capts J. R. Wifall and D. T. Smith, Jr. for many hours of critical discussion on electrofluid dynamic research and to Mrs. Marcia Homan for the typing of the manuscript.

## BIBLIOGRAPHY

The following is only a partial list of EFD references. An extensive bibliography can be found in Reference 14.

1. M. O. Lawson, "Electrofluid Dynamic Energy Conversion", OAR Research Review, Vol VII, Nr 6, pp 32-33, (June 1968).
2. J. E. Minardi, "Computer Study of Electrofluid Dynamic Colloid Generator", 1968 Intersociety Energy Conversion Engineering Conference, Boulder, Colorado (13-16 August 1968).
3. J. E. Minardi, "Computer Program For The Calculation of Electric Fields in an Electrofluid Dynamic Generator", ARL Report 68-0156, Aerospace Research Laboratories, WPAFB, Ohio (August 1968).
4. J. E. Minardi, "Theoretical and Analytical Research Study of Axisymmetric Electrofluid Dynamic Energy Conversion Processes", Eleventh Quarterly Progress Report, Contract AF 33(615)-3203, Aerospace Research Laboratories, WPAFB, Ohio (April 1968).
5. K. K. Joshi, "Electrical Charging of Liquid Sprays in High Pressure Gas Flows for Electrofluid Dynamic Processes", IEEE International Electron Devices Meeting, Washington, D.C. (18-20 October 1967).
6. J. Decaire and M. Lawson, "Outlook for Electrofluid Dynamic Power Generation", ASME Paper 67-PWR-11, Invited Paper ASME-IEEE Joint Power Generation Conference, Detroit, Michigan (24-28 Sept 67).
7. J. Decaire and J. Wifall, "Charge Generation by Corona Discharge in Electrofluid Dynamic Energy Conversion Processes", Advances in Energy Conversion Engineering-ASME pp 465-471 (1967) (Papers presented at the 1967 Intersociety Energy Conversion Engineering Conference, Miami Beach, Florida, 14-17 August 1967).
8. H. E. Brandmaier, "The Major Problem in Electrofluid Dynamic Power Generation", Advances in Energy Conversion Engineering-ASME pp 457-464 (1967) (Papers presented at 1967 Intersociety Energy Conversion Engineering Conference, Miami Beach, Florida, 14-17 August 1967).
9. J. Decaire and M. Lawson, "Investigation on Power Generation Using Electrofluid Dynamic Processes", Advances in Energy Conversion Engineering-ASME pp 473-483 (1967) (Papers presented at the 1967 Intersociety Conversion Engineering Conference, Miami Beach, Florida, 14-17 August 1967).

10. P. L. Cowan, T. Gunzler, R. Kulka, and M. C. Gourdine, "Electrogasdynamic Power Generation", Advances in Energy Conversion Engineering-ASME pp 435-455 (1967) (Papers presented at the 1967 Intersociety Energy Conversion Engineering Conference, Miami Beach, Florida, 14-17 August 1967).
11. J. Decaire and M. Lawson, "Electrofluid Dynamic Power Generation: Trends and Expectations", Invited Paper Eighth Symposium on Engineering Aspects of Magnetohydrodynamics, Stanford University, Stanford, California, (28-30 March 1967).
12. J. Decaire, "The Effects of Partial Condensation Around Ions in Electrofluid Dynamic Energy Conversion Processes", ARL Report 66-0187, Aerospace Research Laboratories, WPAFB, Ohio (September 1966).
13. E. L. Daman and M. C. Gourdine, "Electrogasdynamic Power Generation", International Symposium on Magnetohydrodynamic Power Generation, Paper SM-74/197, Salzburg, Austria (July 1966).
14. Invitational Working Electrofluid Dynamic Energy Conversion Conference, Aerospace Research Laboratories, WPAFB, Ohio (24-26 May 1966). AGARDograph 122, "Selected Topics in Electrofluid Dynamic Energy Conversion (1968).
15. M. Hawes, "Electrofluid Dynamic Working Media for Direct Energy Conversion Processes", OAR Research Review, Vol V, Nr 1, pp 5-9, (March 1966).
16. A. Maciulaitis, "A Theoretical Investigation of Electrofluid Dynamic Propulsion in the Earth's Atmosphere", Grumman Research Department Report RE-204, Grumman Aircraft Engineering Corporation, Bethpage, New York (March 1965).
17. M. O. Lawson, "Ion Generation by Corona Discharge for Electrofluid Dynamic Energy Conversion", Sixth AGARD Combustion and Propulsion Colloquium, Cannes, France (16-20 March 1964). ARL Report 64-76, Aerospace Research Laboratories, WPAFB, Ohio (October 1964). AGARDograph 81 "Energy Sources and Energy Conversion" pp 539-630 (1967) AD 455870.
18. H. von Ohain and F. Wattendorf, "Potentialities of Direct Electrofluid Dynamic Energy Conversion Processes for Power Generation", Sixth AGARD Combustion and Propulsion Colloquium, Cannes, France, (16-20 March 1964). ARL Report 64-73, Aerospace Research Laboratories, WPAFB, Ohio (October 1964). AGARDograph 81, "Energy Sources and Energy Conversion", pp 539-630 (1967).

19. M. O. Lawson, "Performance Characteristics of Electrofluid Dynamic Energy Conversion Processes Employing Viscous Coupling", Sixth AGARD Combustion and Propulsion Colloquium, Cannes, France (16-20 March 1964). ARL Report 64-74, Aerospace Research Laboratories, WPAFB, Ohio (October 1964). AGARDograph 81, "Energy Sources and Energy Conversion" 11 539-630 (1967).
20. M. Hawes, "Experimental Techniques in Electrofluid Dynamic Energy Conversion Research", Sixth AGARD Combustion and Propulsion Colloquium, Cannes, France (16-20 March 1964). ARL Report 64-77, Aerospace Research Laboratories, WPAFB, Ohio (October 1964). AGARDograph 81 "Energy Sources and Energy Conversion" pp 539-630 (1967) AD 455788.
21. M. Lawson, H. von Ohain, and F. Wattendorf, "Performance Potentialities of Direct Energy Conversion Processes Between Electrostatic and Fluid Dynamic Energy", ARL Report 178, Aerospace Research Laboratories, WPAFB, Ohio (December 1961) AD 273015.
22. J. M. Smith, "Theoretical Study of the Electrohydrodynamic Generator" GE Space Sciences Laboratory Report R61SD192 (November 1961) AD 271768.
23. A. M. Marks, "Heat-Electrical Power Conversion Through the Medium of a Charged Aerosol", U. S. Patent Nr 2, 638, 555 (12 May 1953).
24. R. J. Van de Graaff, "Electrostatic Generator", U. S. Patent Number 1, 991, 236 (12 February 1935).

**TABLE I**  
**DIELECTRIC STRENGTH OF GASES**

GAS	RELATIVE DIELECTRIC STRENGTH $E_{b,n} / E_{b,n} (\text{air})^*$
AIR	1.00
HYDROGEN ( $H_2$ )	0.67
HELIUM ( $He$ )	~ 0.2
CARBON DIOXIDE ( $CO_2$ )	0.9
SULFUR DIOXIDE ( $SO_2$ )	1.9
STEAM ( $H_2O$ )	~ 1.0
AMMONIA ( $NH_3$ )	~ 1.2
CHLOROFORM ( $CHCl_3$ )	4.2

•  $E_{b,n} (\text{air}) \approx 30,000$  volts/cm

**TABLE II**  
**CHARACTERISTICS OF ELECTROFLUIDDYNAMIC  
ENERGY CONVERSION PROCESSES**

- HIGH OUTPUT VOLTAGE  $\sim 10^5$  VOLTS AND HIGHER
- LOW ELECTRIC CURRENT DENSITY
- VERY HIGH NUMBER OF NEUTRAL MOLECULES PER ELEMENTARY CHARGE  $\sim 10^8$
- ELECTRIC POWER OUTPUT  $\sim 1 \text{ KW/cm}^2$
- FAVORABLE POWER-TO-WEIGHT RATIO
- BROAD RANGE OF POWER LEVELS
- NON-STRINGENT TEMPERATURE REQUIREMENTS
- VERY LOW TOTAL PRESSURE RATIO ACROSS CONVERSION SECTION

**TABLE III**  
**POTENTIAL APPLICATIONS OF EFD ENERGY**  
**CONVERSION PROCESSES**

POWER OUTPUT	CYCLE	ENERGY SOURCE	APPLICATION AREA	VOLTAGE	
FRACTION KW TO 0. MAGNITUDE 10 KW	RANKINE	<ul style="list-style-type: none"> <li>• SOLAR</li> <li>• ISOTOPE</li> <li>• CHEMICAL</li> </ul>	<ul style="list-style-type: none"> <li>• TELECOMMUNICATION</li> <li>• POWER FOR REMOTE AREAS</li> <li>• VEHICLE POWER</li> <li>• ELECTRIC PROPULSION (COLLOIDAL) FOR ATTITUDE CONTROL AND MINOR ORBITAL CORRECTIONS</li> </ul>	~10 <sup>5</sup> VOLTS	
					<ul style="list-style-type: none"> <li>• NUCLEAR REACTOR</li> </ul>
0. MAGNITUDE 100 KW TO 1000 KW	OPEN GAS TURBINE	<ul style="list-style-type: none"> <li>• CHEMICAL (NUCLEAR)</li> </ul>	<ul style="list-style-type: none"> <li>• MOBILE MILITARY POWER</li> <li>• POWER FOR REMOTE AREAS</li> <li>• STANDBY EQUIPMENT</li> </ul>	~10 <sup>5</sup> VOLTS	
	CLOSED CYCLE	<ul style="list-style-type: none"> <li>• FAN OR COMPRESSOR ACTUATED BY ELECTRICAL OR CHEMICAL ENERGY</li> </ul>			10 <sup>6</sup> to 10 <sup>7</sup> VOLTS
	OPEN GAS TURBINE	<ul style="list-style-type: none"> <li>• CHEMICAL (NUCLEAR)</li> </ul>			
0. MAGNITUDE 10 MW AND ABOVE	STORAGE BLOCKDOWN	<ul style="list-style-type: none"> <li>• CHEMICAL</li> </ul>	<ul style="list-style-type: none"> <li>• SHORT DURATION, HIGH POWER OUTPUT (HYPERSONIC FLOW SIMULATION)</li> </ul>	10 <sup>8</sup> VOLTS AND ABOVE	

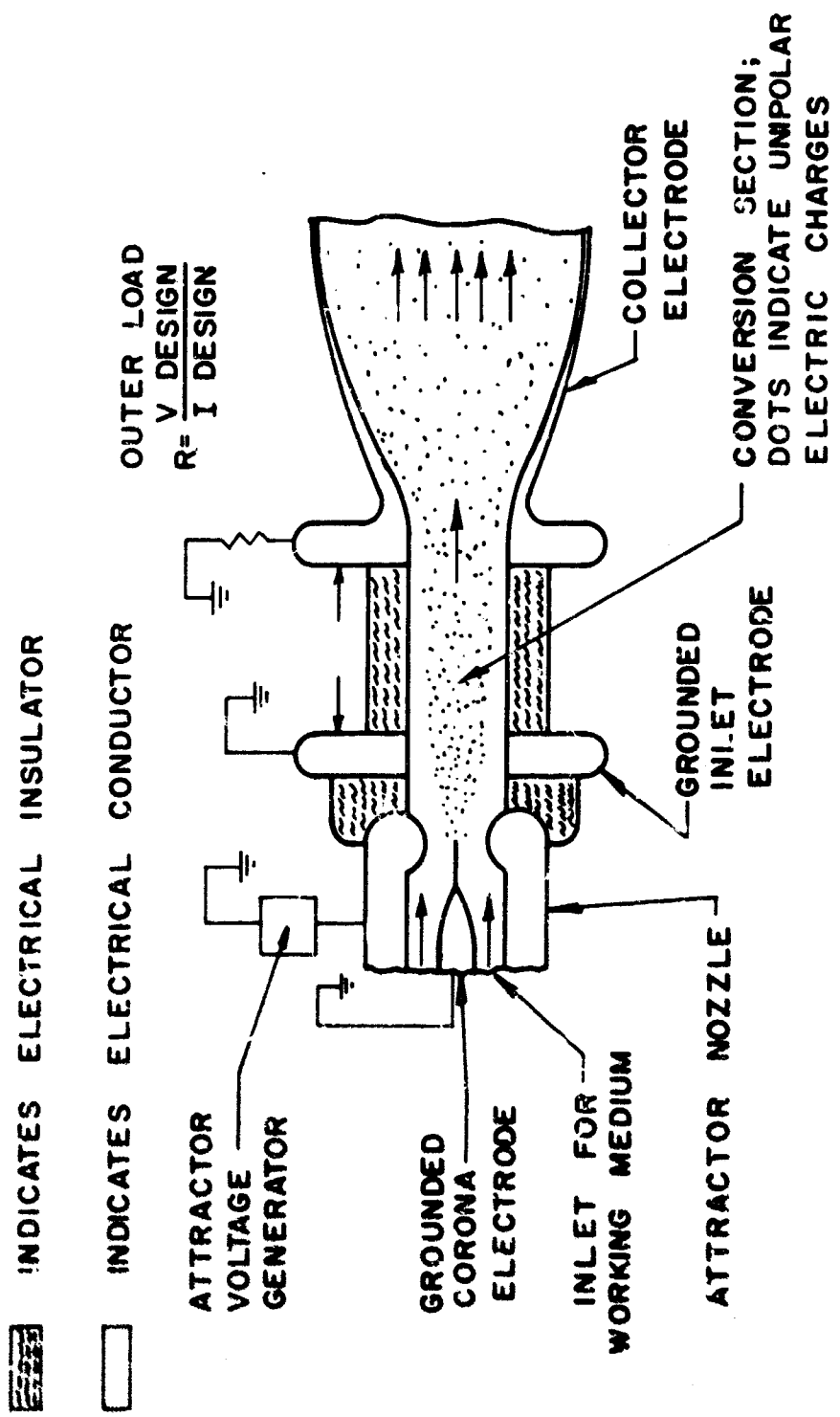
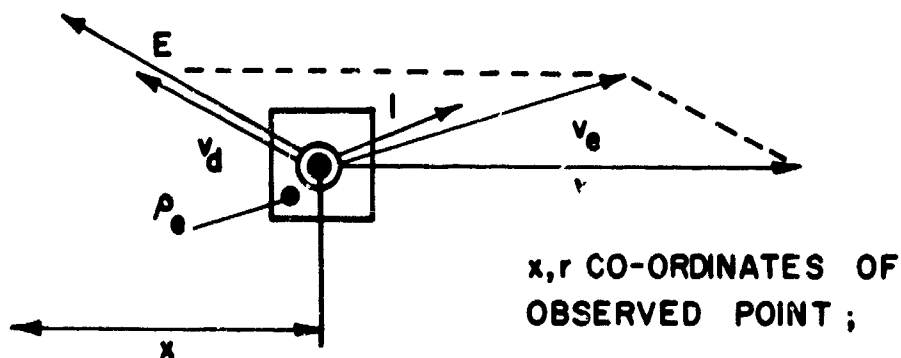


FIG. 1 ILLUSTRATION OF ELECTROFLUIDYNAMIC ENERGY  
 CONVERSION PROCESS  
 (FLUID DYNAMIC VAN DE GRAAFF)



$\vec{V}(x,r)$  = VELOCITY OF DIELECTRIC WORKING MEDIUM

$\vec{E}(x,r)$  = ELECTRIC FIELD STRENGTH DUE TO COLLECTOR POTENTIAL (V) AND SPACE CHARGE

$\vec{V}_d(x,r)$  = DRIFT VELOCITY OF CHARGED PARTICLES RELATIVE TO WORKING MEDIUM.  $k$  = MOBILITY

$\vec{V}_0(x,r) = \vec{V}(x,r) + \vec{V}_d(x,r)$  = TRANSPORT VELOCITY OF CHARGED PARTICLES

$\rho_0(x,r) = \epsilon \operatorname{div} \vec{E}(x,r)$  = ELECTRIC CHARGE DENSITY

$\vec{J}(x,r) = \rho_0(x,r) \cdot \vec{V}_0(x,r)$  = ELECTRIC CURRENT DENSITY

$V = \int_0^h \vec{E}(x,r) \cdot d\vec{x}$  = ELECTRIC POTENTIAL

THROUGHOUT THE CONVERSION SECTION;

$v_x(x,r) > kE_x(x,r)$  (CHARGES TRANSPORTED TO COLLECTOR)

$E(x,r) < E_0$  ( $E_0$  = BREAKDOWN FIELD STRENGTH)

$I = 2\pi \int_0^R \vec{J}(x,r) \cdot r dr$  = ELECTRIC CURRENT, INDEPENDENT OF  $x$   
(NO CHARGES DEPOSITED ON WALLS)

FIG. 2 RELATIONS BETWEEN ELECTRICAL AND VELOCITY FIELDS

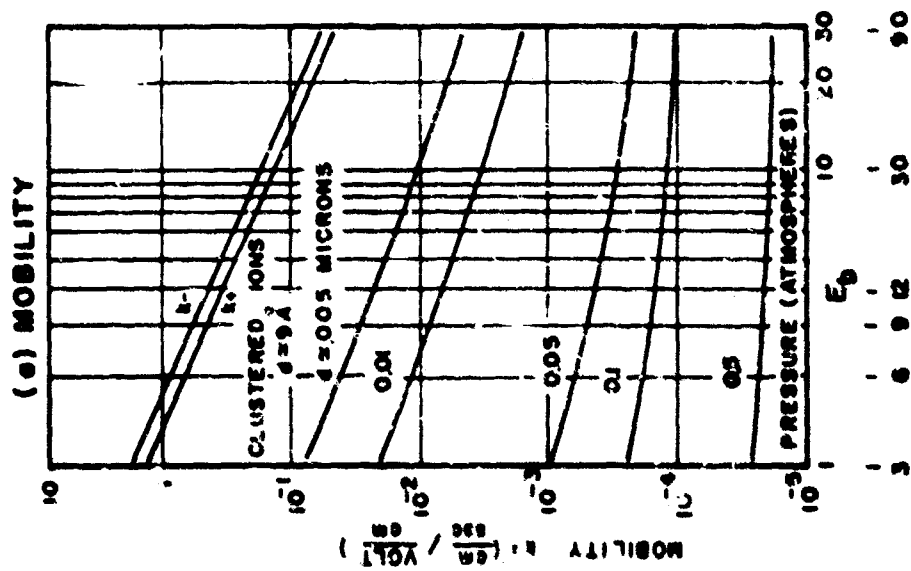
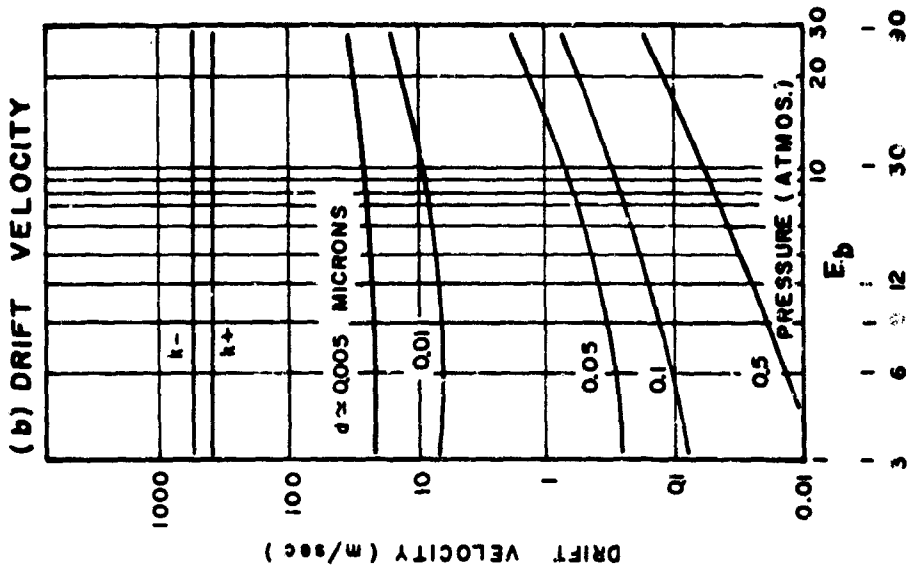


FIG. 3 MOBILITY AND DRIFT VELOCITY OF SINGLY CHARGED PARTICLES IN AIR AS A FUNCTION OF PARTICLE DIAMETER,  $d$ , AND PRESSURE ( $T = 228^\circ K$ )

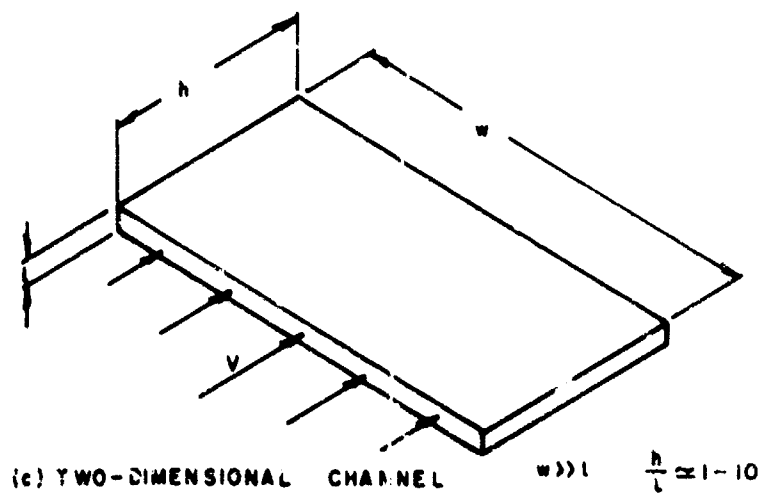
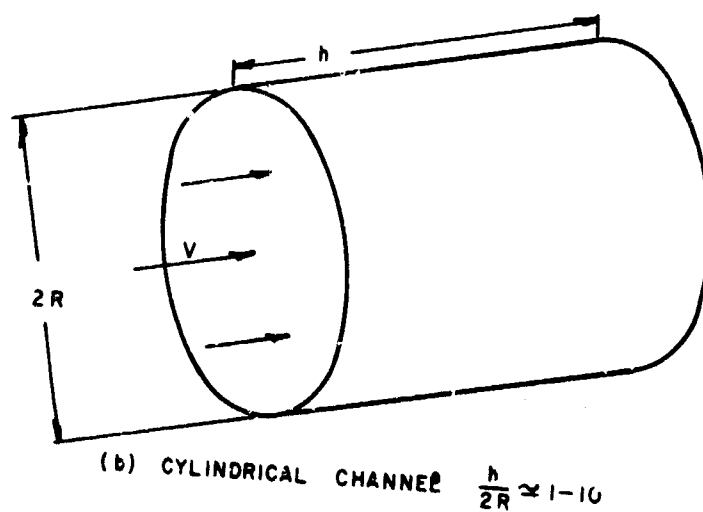
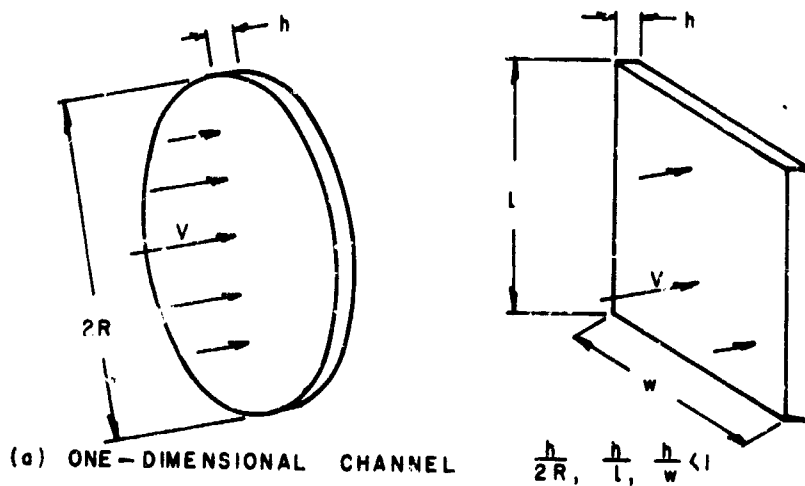


FIG. 4 EFD CONVERSION CHANNEL GEOMETRIES

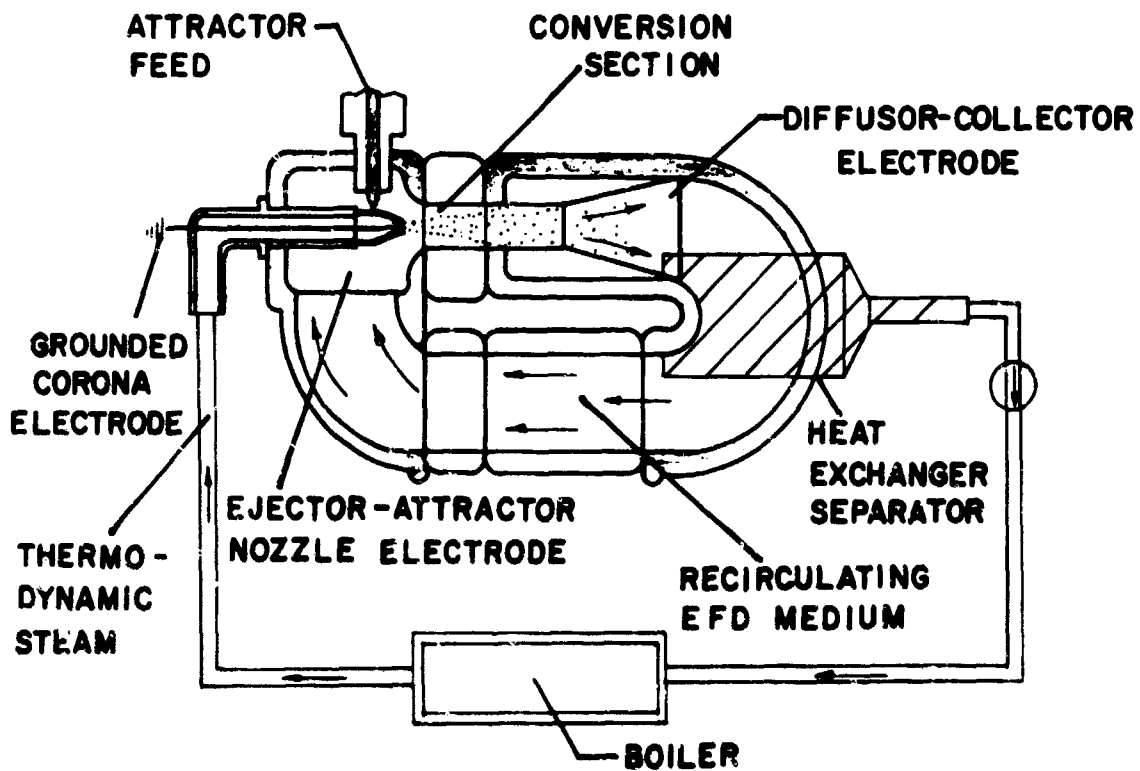


FIG. 5 ILLUSTRATION OF HIGH-PRESSURE-RATIO, TWO-FLUID CYCLE

RECIRCULATORY EFD GENERATOR,(CLOSED CYCLE SIMULATION)  
SCHEMATIC VIEW

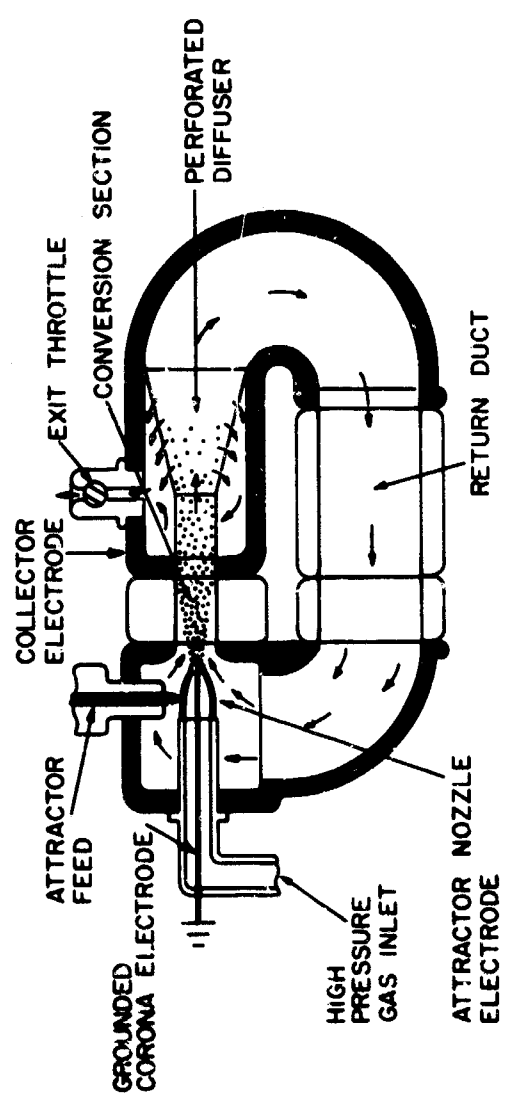


FIG. 6

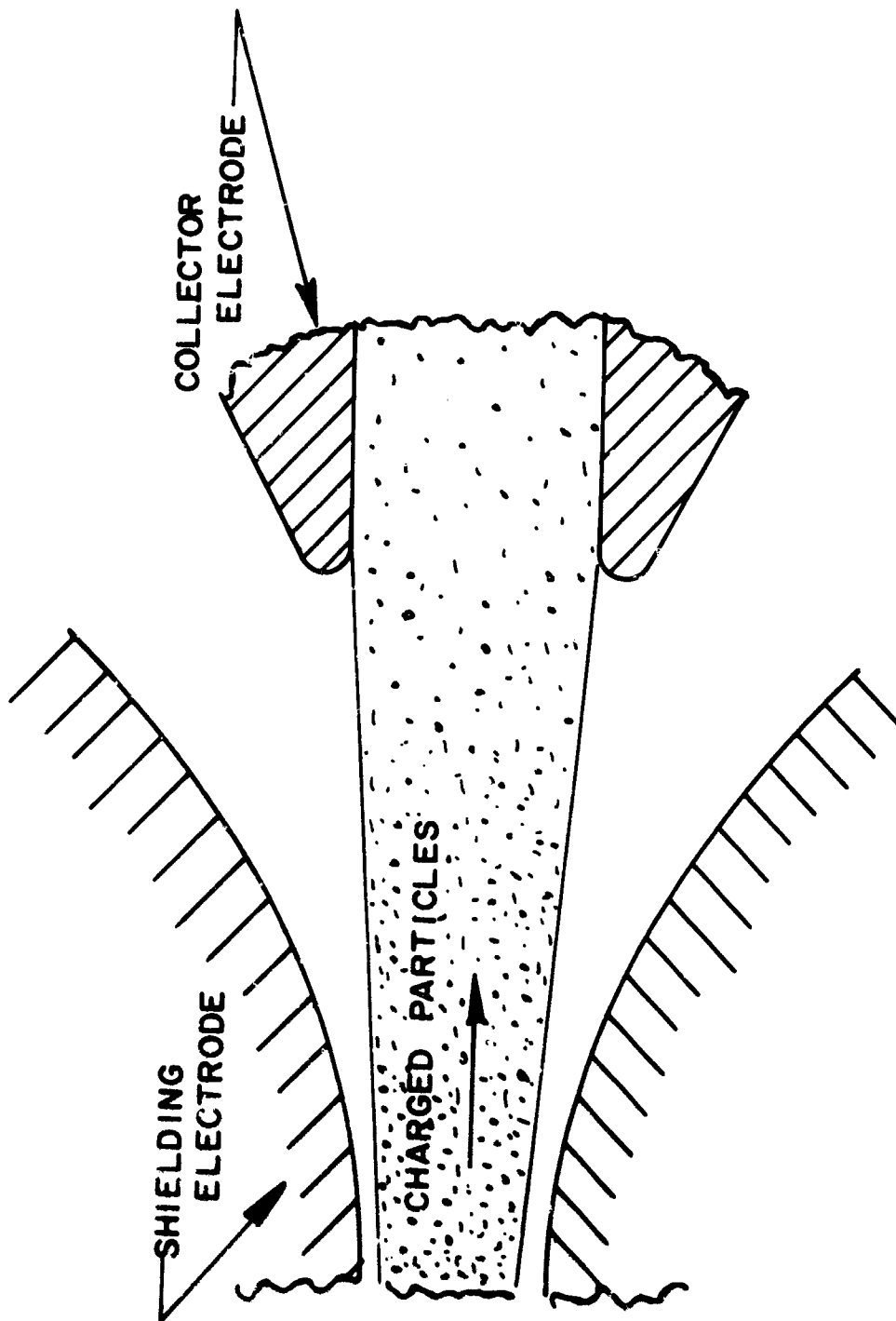


FIG-7 ELECTRODE SHIELDING REQUIREMENTS (Schematic)

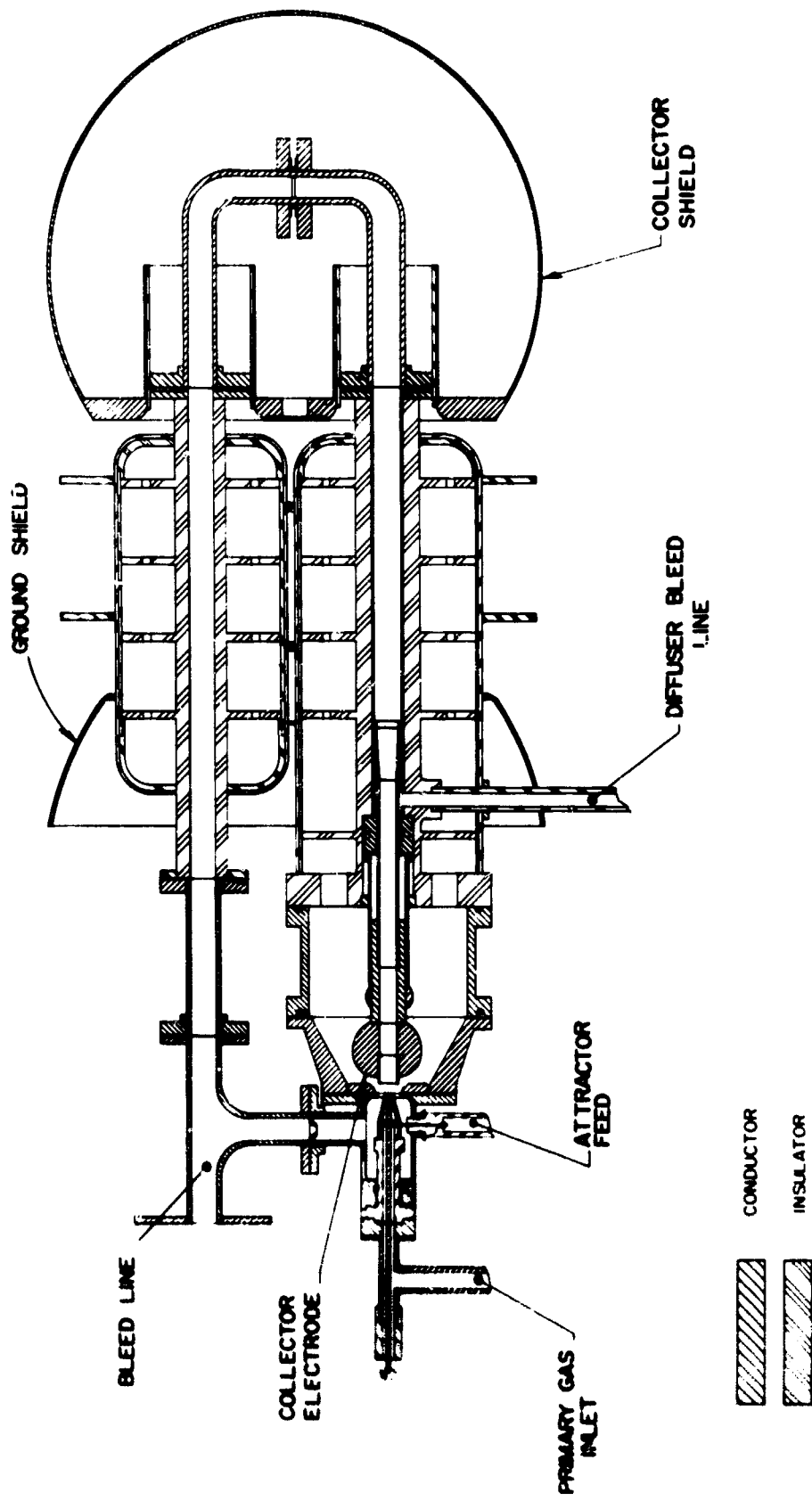


FIG. 8 ARL EXPERIMENTAL EFD GENERATOR

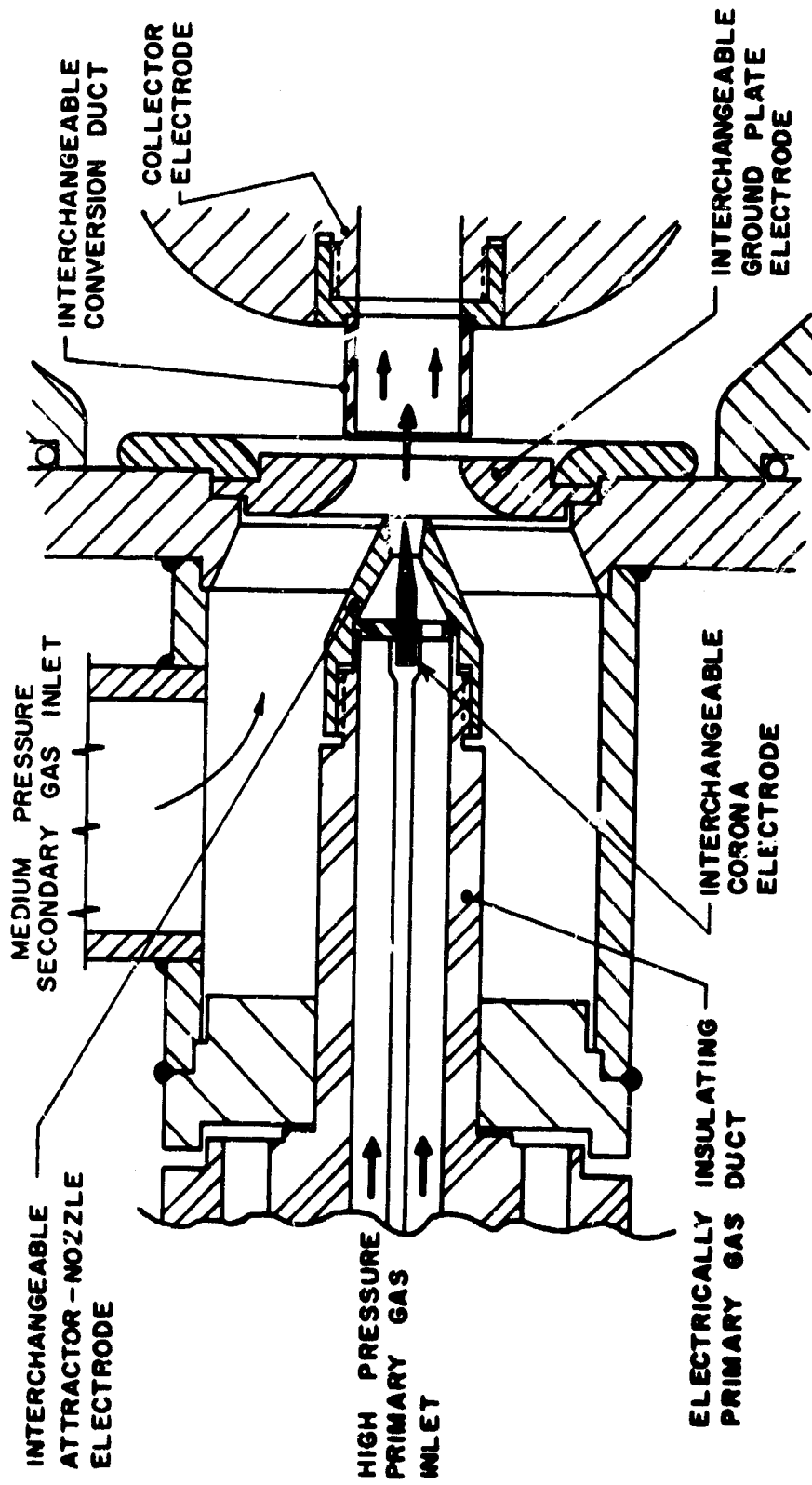


FIG. 9 TYPICAL ELECTRODE AND CHANNEL CONFIGURATION OF E.F.D. TEST GENERATOR

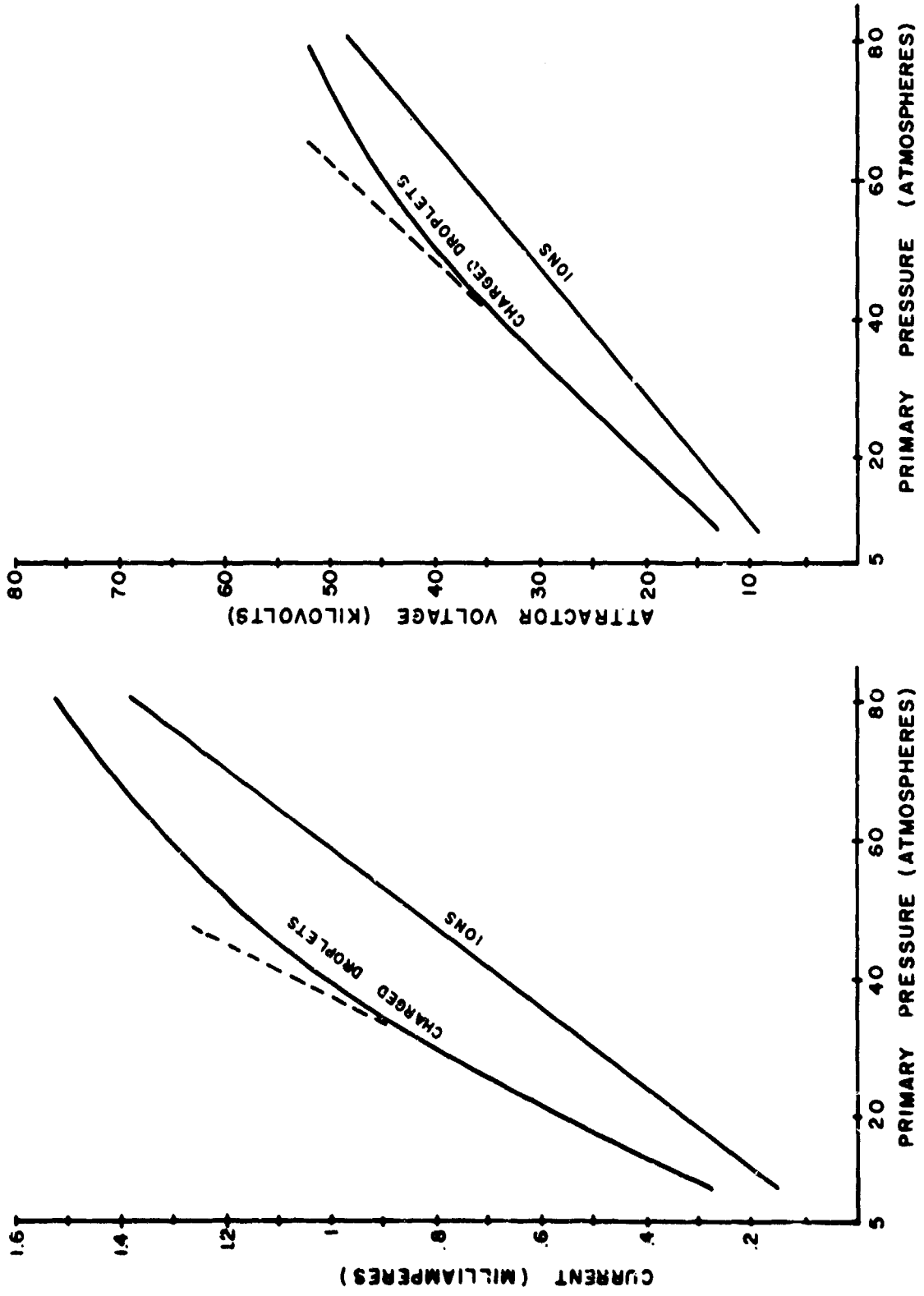


FIG.10 CORONA CURRENT AND VOLTAGE Vs. TOTAL PRESSURE

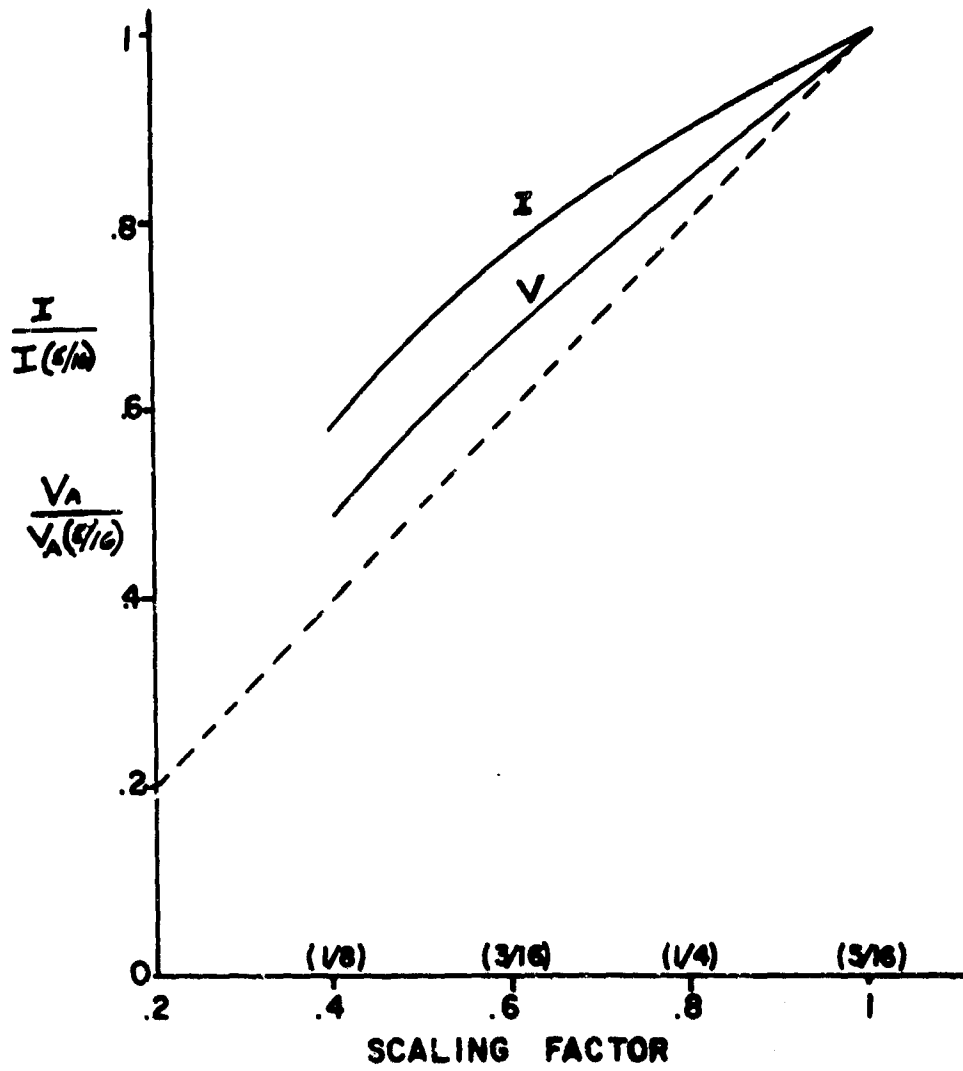


FIG. 11 TYPICAL CORONA CURRENT GEOMETRIC SCALING RESULTS

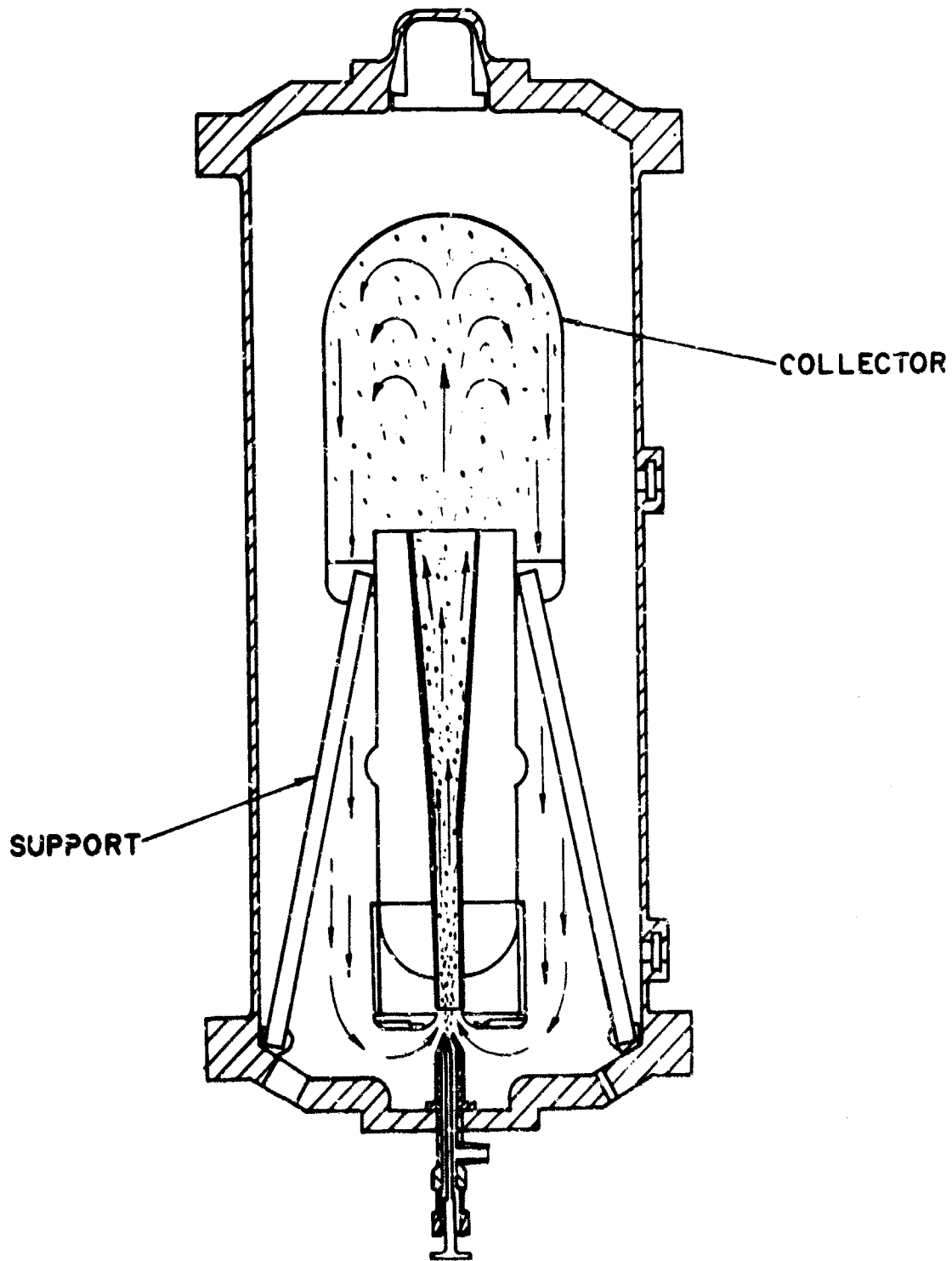


FIG. 12 ENCAPSULATED EFD TEST GENERATOR (Schematic)

# RADIAL OUTFLOW NOZZLE

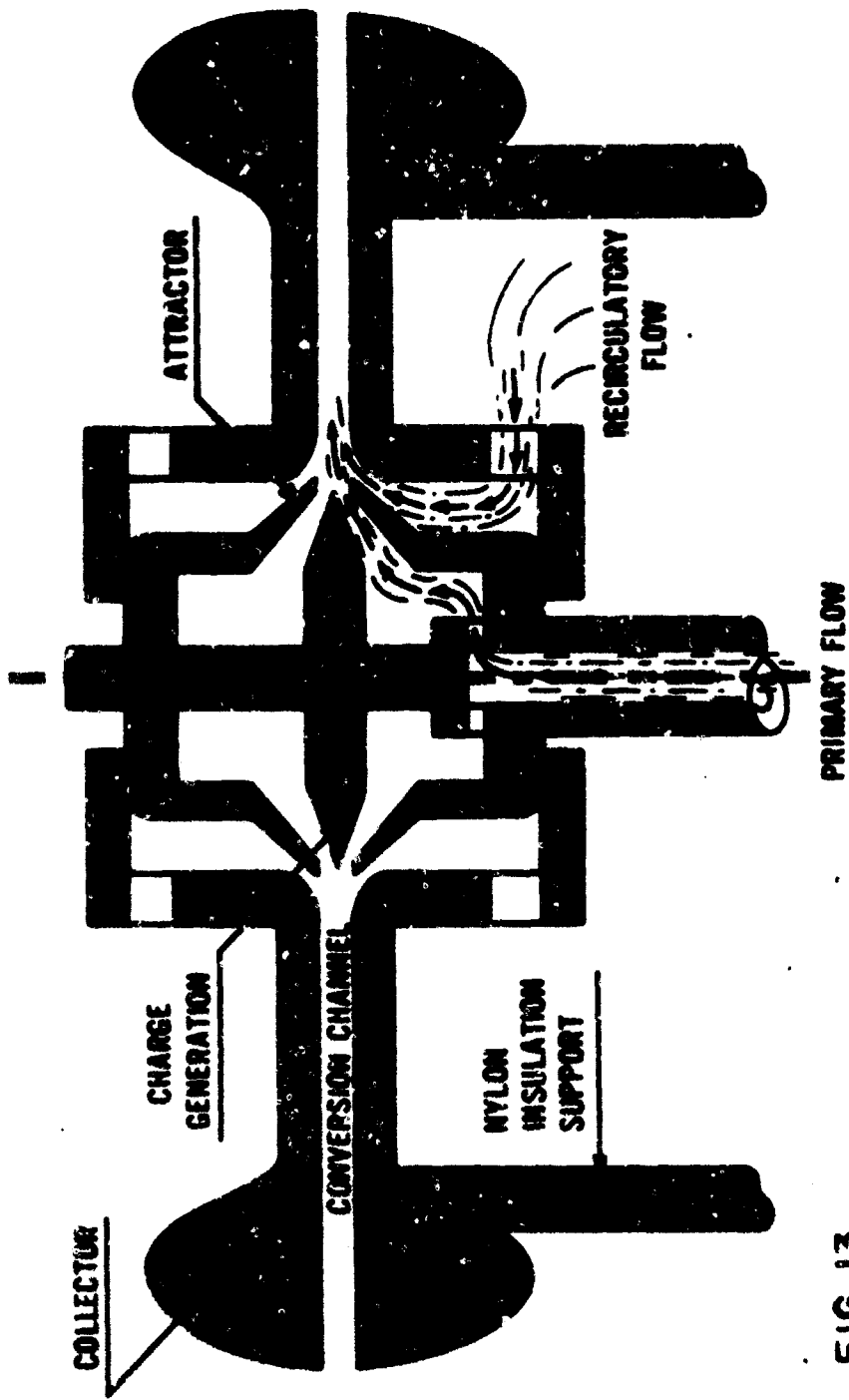


FIG. 13

**THE ISENTROPIC-COMPRESSION TUBE**

**F. J. Stoddard**

**Aerodynamic Research Department**

**Cornell Aeronautical Laboratory, Inc.**

**Buffalo, New York**

## THE ISENTROPIC-COMPRESSION TUBE

F. J. Stoddard

Aerodynamic Research Department  
CORNELL AERONAUTICAL LABORATORY, INC.  
Buffalo, New York 14221

### ABSTRACT

The isentropic-compression tube, which was conceived at CAL under ARL funding, is a recently proposed facility which can be operated in either of three modes to produce hypervelocity air flows with a wide range of properties. In two of the modes, an isentropically compressed and accelerated hypervelocity airflow is produced which possesses a desirable low dissociation level and a very high total pressure. The production in the laboratory of airflows with these characteristics is necessary for the realistic simulation of many aerodynamic and physical phenomena encountered in superorbital flight into the atmosphere of the earth. In the third mode, the facility produces a high-speed shocked flow, suitable for studies of plasmas, chemical kinetics, and some aerodynamic problems.

A discussion is presented of the status of the development of the isentropic-compression tube. The discussion includes a summary of recent theoretical work on the three modes of operation, a description of the pilot isentropic-compression tube, and the results of recent exploratory experiments which were performed in the pilot tube. In general, the experiments have verified the theoretical predictions. It has been confirmed that isentropic airflows were produced with speeds up to 10,000 ft/sec by using an uncontrolled-piston method which is one of the two operational modes for producing the isentropic flow. The second isentropic flow mode, called the braked-piston method, has not been tested as yet. Operation of the pilot tube in the third mentioned shock-tube mode has resulted in shock speeds of almost 30,000 ft/sec in air in spite of the 400 psia pressure limit of the pilot tube. This performance exceeds that obtainable in conventional shock tubes driven by hydrogen at 750°F and 30,000 psia.

Theoretical estimates of the potential of a high-performance facility have indicated that it should be possible to produce isentropically compressed and accelerated flows exceeding 30,000 ft/sec with dissociation levels of only a few percent. When operated in the shock-tube mode, such a facility could be capable of generating shock speeds in air exceeding 50,000 ft/sec. The techniques discussed in this paper provide a simple means of increasing the performance and versatility of shock tubes and tunnels while eliminating the explosive hazards associated with the use of hydrogen in these devices.

## I. INTRODUCTION

The shock tunnel<sup>1</sup> has been developed into an effective laboratory research tool for simulating hypersonic flight. However, further extension of conventional shock-tunnel techniques to the simulation of re-entry flight is not feasible in general because test air with little dissociation is required. As is well known, the test air in a conventional shock tunnel is accelerated and compressed by a shock wave and then expanded in a nozzle. The shocked air is necessarily very hot when high flow speeds are produced. As a result of the high air temperatures, significant dissociation and ionization are produced in the nozzle reservoir. The dissociation and ionization products are not removed during the subsequent expansion of the gas in the nozzle because of the action of complex chemical nonequilibrium processes. As a result, the test gas in general contains N, O, NO, electrons, and various ions in addition to the N<sub>2</sub> and O<sub>2</sub> of ordinary air<sup>2</sup>. While there are some problems of interest in which the free-stream composition would not be critically important, there are others in which effective simulation could not be achieved unless the test gas was normal air.

The effects of chemical nonequilibrium could be greatly reduced by accelerating and compressing the test air by a method which would generate less entropy than a shock compression would produce. In this respect, the isentropic-compression tube<sup>3-7</sup> is very promising. This facility could be operated in two different modes, the uncontrolled-piston and the braked-piston, in order to produce an isentropically compressed and accelerated flow. Calculations have shown that in such a facility flow speeds exceeding 30,000 ft/sec with dissociation fractions of only a few percent are theoretically possible<sup>4</sup>. The dissociation fraction for a corresponding shocked flow, which can also be produced in the isentropic-compression tube by operating in a third mode, is greater than 50%. This reduction in the dissociation level is achieved in principle by substituting nonsteady, isentropic wave processes for the shock wave. Nonsteady isentropic waves are capable of accelerating the test air to high flow speeds without producing the large temperatures found in the corresponding shocked flow.

In addition, with such a wave system it is possible to produce high-speed airflows which have much higher densities than can be obtained in a corresponding shocked flow. Thus, the isentropic-compression tube, when operated in either the uncontrolled-piston or braked-piston modes, would be capable of simulating high-speed flight at significantly lower altitudes than are currently possible in shock tunnels.

In the following section, the theory of three modes of operation of the isentropic-compression tube is discussed. That section is followed by sections giving a description of a pilot tube and summarizing the results of recent exploratory experiments. The last section contains a summary and conclusions concerning the present state of development of the isentropic-compression tube.

## II. THEORY OF THE ISENTROPIC-COMPRESSION TUBE

The fundamental theoretical concept of the isentropic-compression tube

and its potential usefulness in simulating re-entry flight was established in Refs 3-6. Recently, theoretical efforts have been directed toward the evaluation of various mechanical schemes for producing the desired isentropic flow. This phase of the study was begun in Ref 4 and was concluded in Ref 7 where two methods for producing the isentropic flow were emphasized: the braked-piston method and the uncontrolled-piston method. In both methods, a piston is used to compress the test gas in a large-diameter pump tube. The downstream end of the pump tube is connected to a smaller-diameter driven tube and a diaphragm is placed at the area contraction. The two methods are distinguished by the time at which the diaphragm is burst and by the type of piston motion occurring in the last foot or so of the piston stroke.

In the braked-piston method, the piston is decelerated by a large braking force acting over about the last foot of the piston trajectory which is otherwise uncontrolled. The braking force could be supplied by a tube of crushable material. The diaphragm burst time is controlled by the length of a spike mounted on the face of the piston. When the magnitude of the braking force is properly chosen and the diaphragm burst is properly timed, a close approximation to a focused isentropic compression wave is obtained in the driven tube. This process is illustrated in Fig. 1 which is a schematic wave diagram for the flow in the driven tube. Two isentropic test regions are identified. The flow in region 1, which follows the compression waves, has a high-Reynolds-number and high density. The flow in region 2, which follows the interface produced when the compression waves coalesce to form a shock wave, has a lower Reynolds number, but a significantly higher speed. There are potential advantages to being able to work in either region and both would be available with the braked-piston technique.

In the uncontrolled-piston method, there is no mechanical braking and the diaphragm is burst late in the compression stroke. In this case, the facility is operated as a free-piston shock tube<sup>8-10</sup> except that the test flow follows the interface rather than the shock wave. A schematic wave diagram of the resultant flow in the driven tube is shown in Fig. 2. A region 1 flow (Fig. 1) cannot be produced by this method.

The uncontrolled-piston method has more potential because no piston energy is expended in overcoming the braking force. On the other hand, the flow produced with the braked-piston method is likely to be much less influenced by diaphragm contamination than that produced by the uncontrolled-piston method. In the uncontrolled-piston method, the test air occupies a much smaller volume in the vicinity of the diaphragm and is much hotter when the diaphragm bursts. If diaphragm contamination of the test gas produced by the uncontrolled-piston technique should prove troublesome for some types of tests, the use of the braked-piston method would be desirable because the contamination should be very small.

The flow between the shock and the interface in Figs. 1 and 2 could also be used for testing purposes. In this case, the isentropic-compression tube is essentially a free-piston shock tube<sup>7-10</sup> with a large area contraction at the diaphragm station. In general, practical considerations dictate that helium should be used in the pump tube and compressed by the uncontrolled-piston method to produce a high sound speed driver. This would provide the means for driving strong shock waves into the test air which originally occupies the driven tube.

### III. DESCRIPTION OF THE PILOT ISENTROPIC-COMPRESSION TUBE

The pilot isentropic-compression tube has been constructed and tested in order to establish the feasibility of the theoretical concepts. A schematic drawing of the device is shown in Fig. 3. The pump tube is 20 ft long with a 17 in. internal diameter, while the driven tube is about 24 ft long and has internal dimensions of 1 1/2 x 2 1/2 in. The piston was machined from a Nylon casting and is equipped with Teflon piston rings. The piston weight is about 50 lbs. The design performance of this pilot isentropic-compression tube is limited to isentropic flow speeds below about 15,000 ft/sec by the 400 psia design operating pressure of the pump tube. A more detailed description of the pilot tube is given in Ref 7.

The tube is operated by first charging the driven tube and the portions of the pump tube ahead of and behind the piston to the desired pressures. The distance separating the piston from the rear end flange is about 30 in. The pressure behind the piston is typically about 20 to 35 psia while that ahead is typically a few mm Hg. The pressure difference is preserved because the piston rings enable the piston to act as a pressure seal. Once the desired pressures have been established, the piston is released by breaking the hollow weak link. This is accomplished by energizing a cartridge heater placed inside the weak link. The freed piston accelerates to a maximum speed not exceeding a few hundred ft/sec and then decelerates as the pressure in the gas ahead of the piston rises to a value, which for a few msec, greatly exceeds the initial pressure of the gas driving the piston. In the experiments which have been performed to date, the thin metal diaphragm separating the pump tube from the driven tube is burst by the spike on the face of the piston, thereby initiating the flow in the driven tube, at the time when the compressed-gas pressure is near its peak value. The mechanical operation of this pilot tube has been very successful and no difficulties have been encountered in the large number of experiments which have been conducted thus far.

### IV. EXPERIMENTAL STUDIES OF THE ISENTROPIC TEST FLOW

Two series of experiments have been performed with the objectives of examining the influence of nonideal effects, such as viscosity and heat transfer, on the isentropic flow. In the first series of experiments, the driven tube and transition piece (see Fig. 3) were removed and the piston motion and gas compression in the pump tube were studied. The result of these experiments confirmed that the compression process in the pump tube is isentropic and predictable using isentropic theory<sup>7</sup>. A peak temperature of about 3500°K was obtained in the compressed air.

In the second series, attempts were made at producing an isentropic region 2 flow using the uncontrolled-piston technique. These initial attempts were successful in the sense that flow speeds of about 10,000 ft/sec were produced and in general, theoretical predictions of the facility performance were confirmed<sup>7</sup>. The observed shock wave attenuation was nil during its transit of the driven tube.

The tests have shown that careful attention must be paid to boundary-layer phenomena, diaphragm-burst characteristics, and interface stability in order to realize the theoretical test time<sup>7</sup>. Difficulties associated with opening time of the diaphragm apparently can be minimized by using the lightest possible diaphragm for a given peak pressure in the pump tube. The use of helium in the driven tube would be expected to reduce the effects of any instability of the interface which separates the test air in the pump tube from the gas originally in the driven tube. In practice, the use of helium has been found to result in significantly improved pitot-pressure and stagnation-point heat-transfer histories when compared with those obtained with air in the driven tube. The test-time limitations imposed at a given test station by viscous effects can only be reduced by increasing the diameter of the driven tube.

An example of the pitot-pressure and the stagnation-point heat-transfer history of the flow produced in the driven tube when helium is used is shown in Fig. 4. It may be seen that the pitot pressure and the heat transfer tend to rise after an initial discontinuous jump which results from the passage of the shock wave. This behavior is caused by a viscous interaction in the shocked helium. After the arrival of the interface, both the pitot pressure and the stagnation-point heat transfer rise in accordance with the predictions of theory for the air flow in region 2 following the interface. The duration of pitot-pressure and heat-transfer plateaus, which constitutes the test time of the isentropic flow, is about 80  $\mu$  sec. Ideal wave-diagram calculations indicate that a uniform flow should have been obtained with a duration of about 400  $\mu$  sec. This discrepancy between the experimental and theoretical test times has been examined experimentally by probing the flow with a heat-transfer rake. The results of these experiments suggest that the test time was limited by the merging of the side-wall boundary layers along the centerline of the driven tube to form a complex, nonsteady, turbulent pipe flow<sup>7</sup>. The results also suggested that the test time might be considerably extended by changing the driven tube from a 1 1/2 x 2 1/2 in. rectangular cross section to a 2 1/2 in. i.d. round cross section. Accordingly, a new driven tube has been designed and additional tests are scheduled to determine the effect on the test time and the flow quality of the increased cross-sectional area of the driven tube.

## V. SHOCK-TUBE STUDIES

The pilot tube has also been operated in a shock-tube mode in which the piston is used to produce a reservoir of hot helium for the purpose of driving a shock wave into a low-pressure air in the driven tube\*. A series of experiments, with the pump tube alone, similar to those described above in which air was used, were performed with helium in order to assess the effects of heat transfer losses occurring from the compressed helium to the walls of the pump tube. The results of these experiments showed that substantial heat-transfer losses occurred but that peak helium temperatures as high as 6000°K

---

\* The shock-tube experiments were performed on CAL funds.

was obtained. It is anticipated that higher temperatures could be obtained in a larger pump tube working at higher pressures.

In spite of the performance limit imposed by the 400 psia design pressure, the peak temperatures in the compressed helium were sufficiently high that shock speeds of almost 30,000 ft/sec in air could be produced<sup>7</sup>. This performance was achieved by driving the piston with helium which had an initial pressure of only 35 psia. It may be noted that hydrogen at 30,000 psia and 750°F as used in conventional shock tubes is not able to match this performance. In addition to the higher performance potential, the adoption of the free-piston driver would eliminate the explosion hazard connected with hydrogen-driven shock tubes. Furthermore, it may prove possible to use the free-piston technique to extend significantly the performance of existing shock tunnels through its ability to achieve tailored-interface operation at incident shock Mach numbers exceeding 20.

Two representative shock trajectories are shown in Figs. 5(a) and (b). It may be seen that the shock wave accelerates until a peak velocity is attained and then it attenuates. Generally, it was found that the peak shock speed occurred further from the diaphragm when the maximum shock speed increased.

It should be possible to reduce the attenuation of the shock wave by using a pressure-regulating piston of the type described in Ref 7. This type of piston, which can be used in both isentropic-compression-tube and shock-tube applications, would reduce the shock attenuation by prolonging the duration of the peak conditions in the compressed helium after the diaphragm is burst.

Two representative histories of the radiation from the shocked air, as obtained with a photodiode, are shown in Figs. 6(a) and (b). The initial radiation overshoot is a nonequilibrium effect. The later rise, which appears when the duration of the shocked gas is sufficiently long, is caused by the interaction of the boundary layer with the inviscid core. These radiation records are similar to those obtained in conventional pressure-driven shock tubes and substantiate the quality of the test flow produced by this technique.

It has been found that reliable predictions of the shock-speed performance could be obtained in these experiments when allowance was made for the losses in the compressed helium and real gas effects in the shocked air. Accordingly, estimates were made of the shock speeds obtainable in a high-performance device based on the present design. It appears that shock speeds exceeding 50,000 ft/sec could be produced.

## VI. SUMMARY AND CONCLUSIONS

The results of recent research indicate that an isentropic region 2 flow was successfully produced in the pilot isentropic-compression tube by the uncontrolled-piston method. However, more development is required to increase the duration and quality of the test flow which appears to be influenced by the boundary layer. It is anticipated that the boundary-layer influence can be reduced by increasing the diameter of the driven tube. A series of

experiments are planned to evaluate the effects of an increased driven-tube diameter.

The braked-piston method has not been studied experimentally as yet. However, plans have been made to do so because it provides a means of producing two, rather than just one isentropic flow regions. Moreover, the method may prove valuable if undesirable contamination of the test gas by the diaphragm material results when the uncontrolled-piston technique is employed.

A high-performance isentropic-compression-tube facility is potentially a very versatile aerodynamic tool. When operated in either of two isentropic-flow modes, it would be capable of simulating and perhaps duplicating many aspects of re-entry flight into the earth's atmosphere at a small fraction of the cost of flight tests. In addition, it could be operated in a shock-tube mode to produce high-speed shock waves which, for example, would be suitable for the study of plasmas associated with re-entry flight. The potential of this type of shock tube is now well established by the work in Refs 7-10. The facility could also be operated as a shock tunnel which would be capable of higher performance, with significantly less danger, than currently operating, conventional, hydrogen-driven shock tunnels.

#### ACKNOWLEDGEMENTS

This work was performed on Contract AF 33(615)-5389 under the technical cognizance of Dr. Robert G. Dunn of ARL, and is an extension of a study initiated under Contract AF 33(657)-8860. The author is pleased to acknowledge the contributions of Dr. J. G. Hall and Mr. A. Hertzberg in the conception and subsequent investigation of the isentropic-compression tube.

## REFERENCES

1. A. Hertzberg, W. E. Smith, H. S. Glick and W. Squire, Modifications of the Shock Tube for the Generation of Hypersonic Flow, AEDC TN-55-15, March 1955.
2. J. G. Hall and C. E. Treanor, Nonequilibrium Effects in Supersonic Nozzle Flows, AGARDograph No. 124, also CAL Rept. No. 163, March 1968.
3. J. G. Hall, J. A. Lordi, B. H. Fetz, F. J. Stoddard and J. A. Bartz, Research on Advanced Gasdynamic Facilities, ARL Rept. No. 65-204, October 1965.
4. F. J. Stoddard, A. Hertzberg and J. G. Hall, The Isentropic Compression Tube: A New Approach to Generating Hypervelocity Flows with Low Dissociation, Proceedings of the Fourth Hypervelocity Techniques Symposium, Arnold Air Force Station, November 1965.
5. J. W. Daiber, F. J. Stoddard, H. M. Thompson and R. G. Rehm, Research on Advanced Gasdynamics Test Facilities, ARL Rept. No. 67-0069, April 1967.
6. R. G. Dunn, A New Method of Accelerating Flows for Hypersonic Wind Tunnels, OAR Research Review, Vol. 4, No. 4, pp. 8-11, June 1965.
7. F. J. Stoddard, Research on Advanced Gasdynamic Test Facilities: Part I - Theoretical and Experimental Studies of the Isentropic-Compression Tube, ARL Rept. No. 69-0001, May, 1968.
8. R. J. Stalker, A Study of the Free-Piston Shock Tunnel, AIAA Journal, pp. 2160-2165, December 1967.
9. J. W. Williard, Design and Performance of the JPL Free-Piston Shock Tube, Proceedings of the Fifth Hypervelocity Techniques Symposium, Univ. of Denver, March 1967.
10. R. J. Stalker and D. L. Plumb, Diaphragm-Type Shock Tube for High Shock Speeds, *Nature*, 218, 789-790, May 25, 1968.

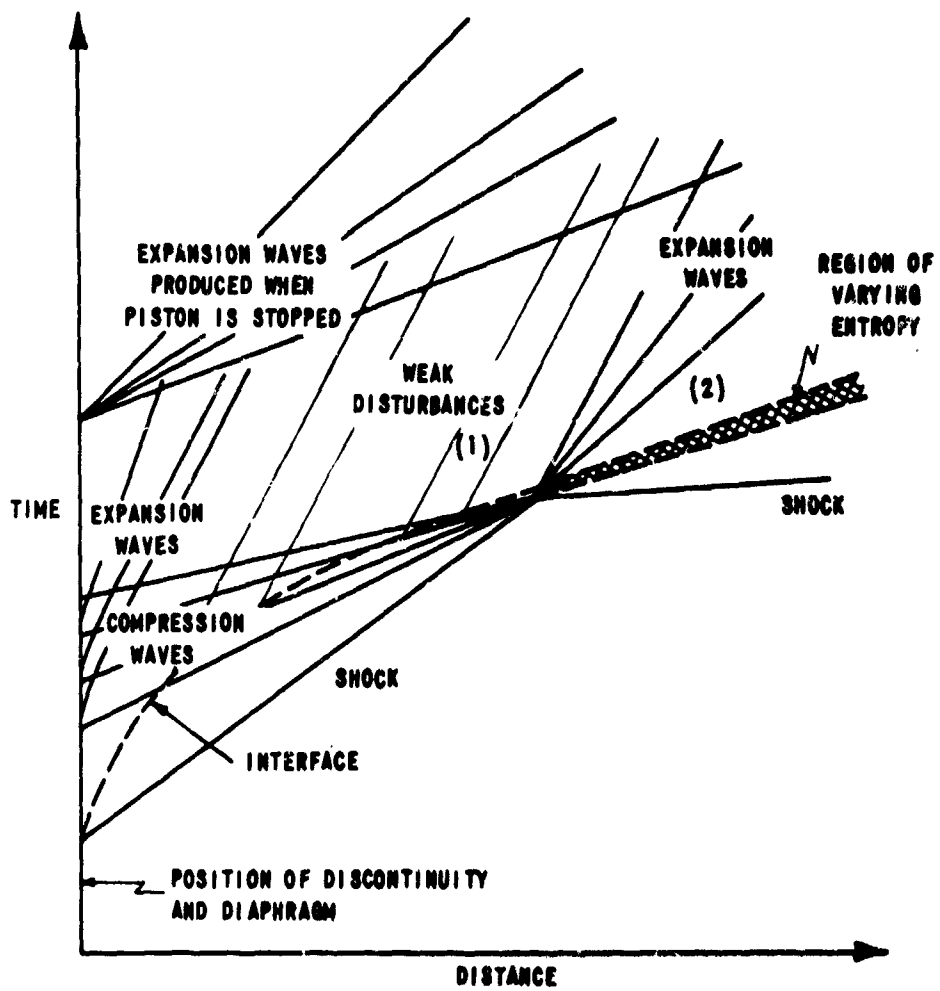


Figure 1 SCHEMATIC DRIVEN-TUBE WAVE DIAGRAM FOR THE BRAKED-PISTON METHOD WITH A DIAPHRAGM AT THE AREA CONTRACTION

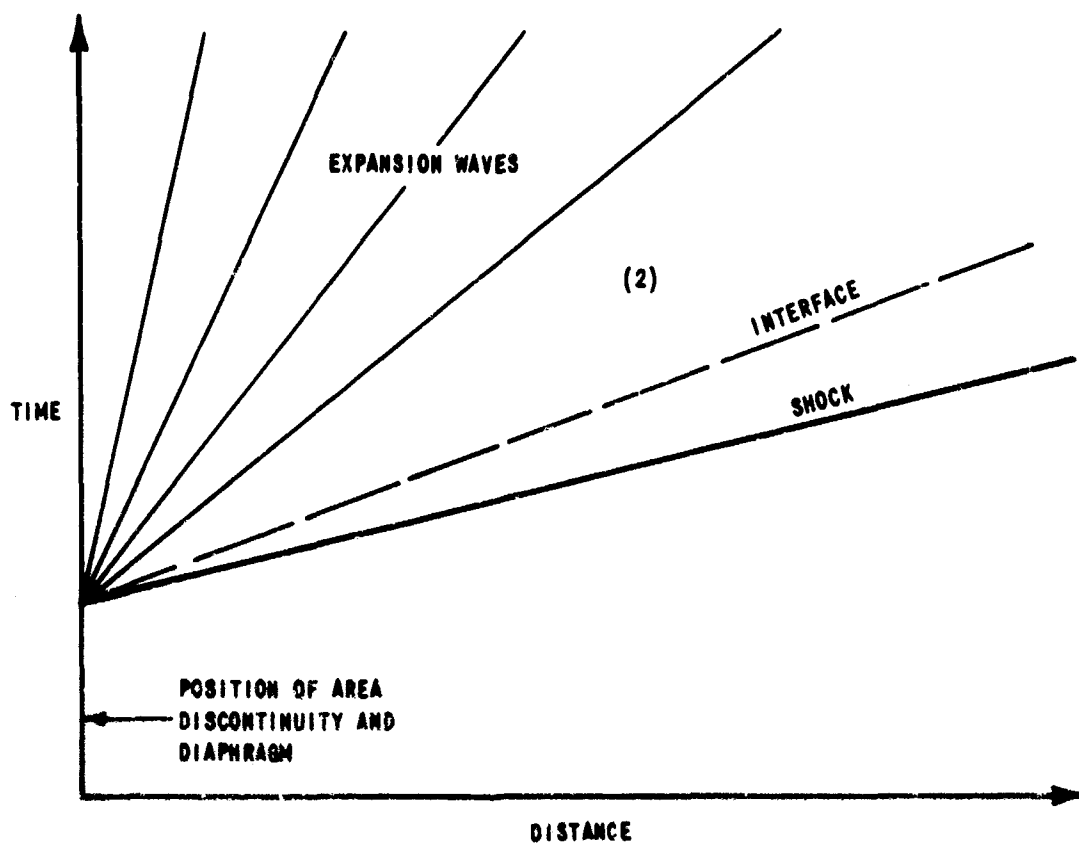


Figure 2 SCHEMATIC DRIVEN-TUBE WAVE DIAGRAM FOR THE FREE-PISTON METHOD

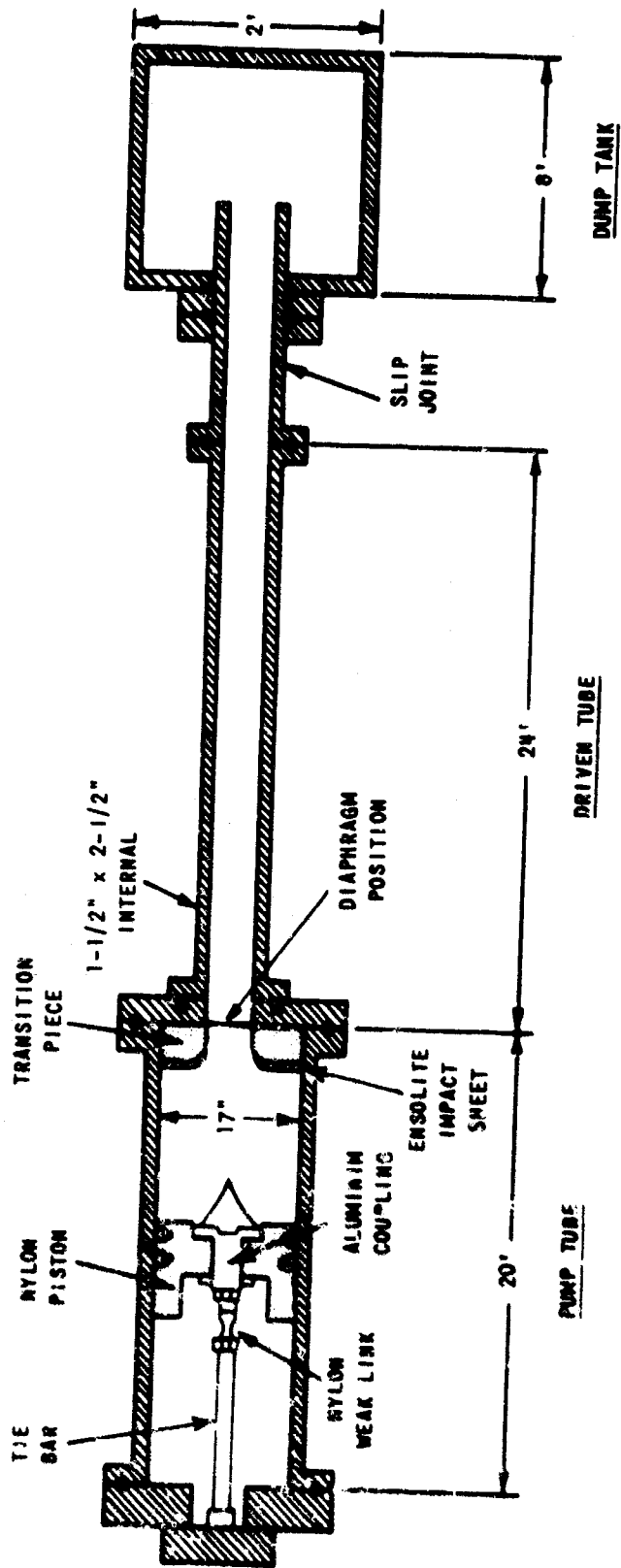


Figure 3 SCHEMATIC DRAWING OF THE PILOT ISENTROPIC-COMPRESSION TUBE

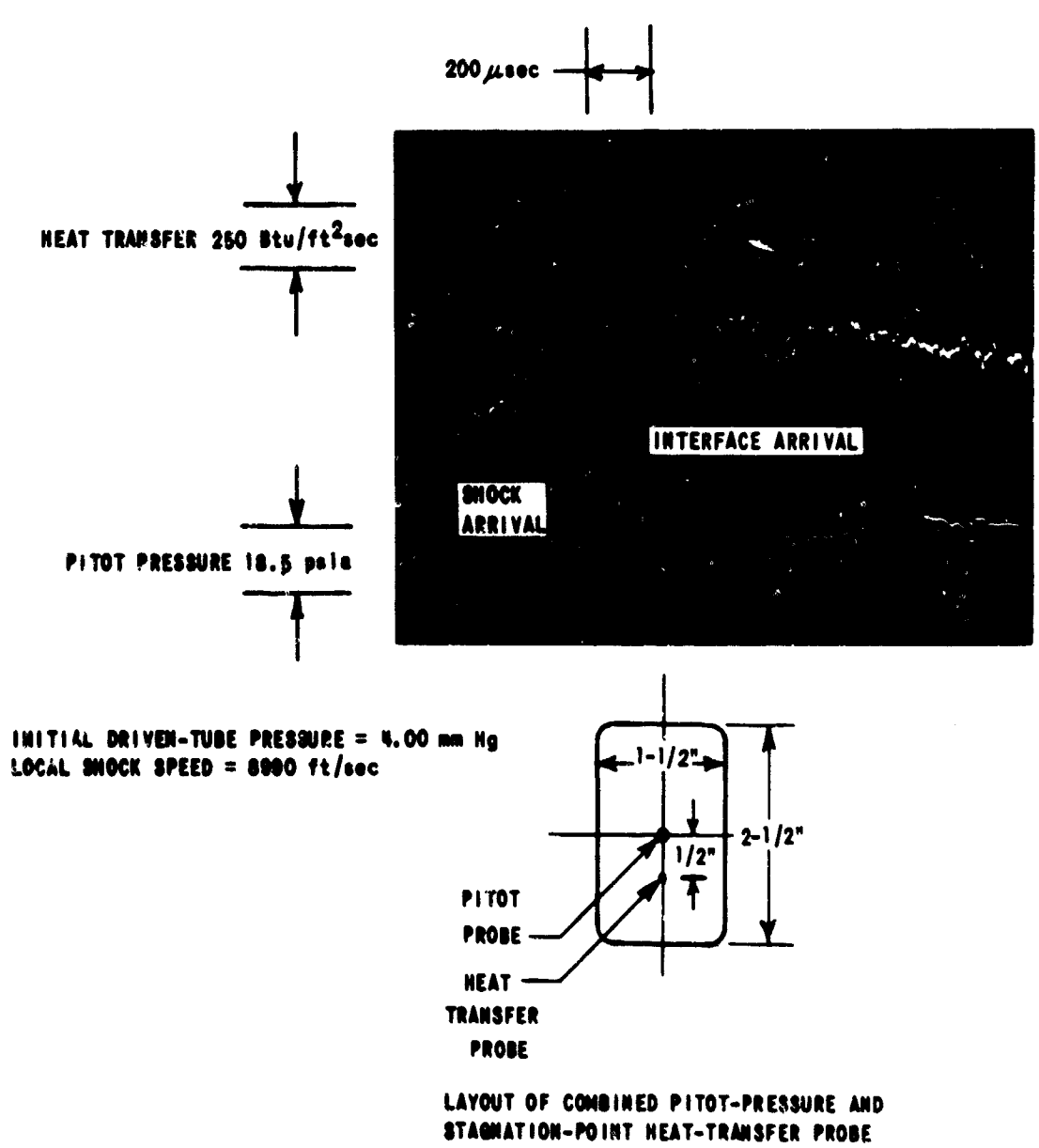


Figure 4 SIMULTANEOUS PITOT PRESSURE AND HEAT TRANSFER HISTORIES FOR HELIUM IN THE DRIVEN TUBE

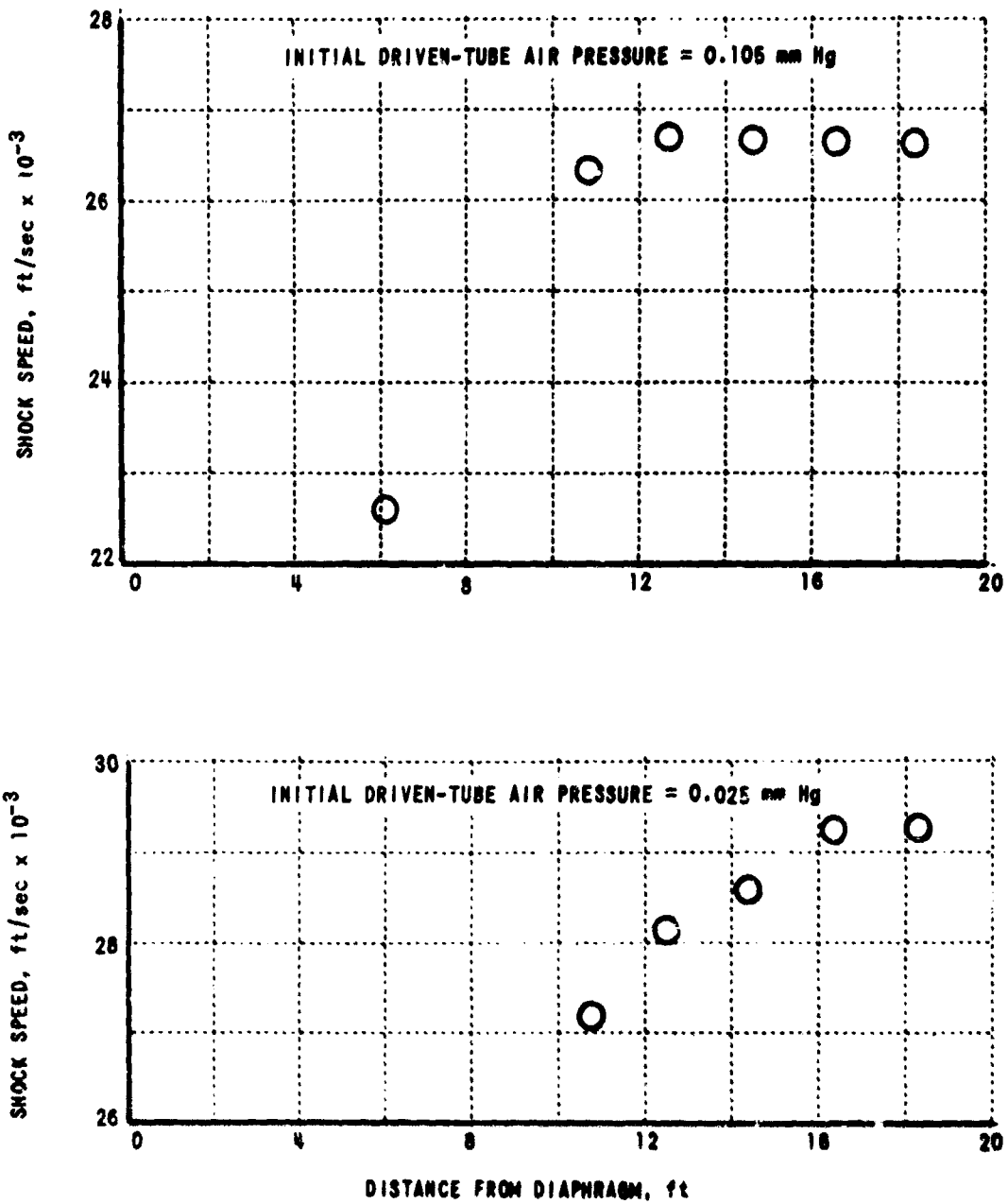


Figure 5 SHOCK-SPEED TRAJECTORIES PRODUCED IN FREE-PISTON SHOCK-TUBE TESTS

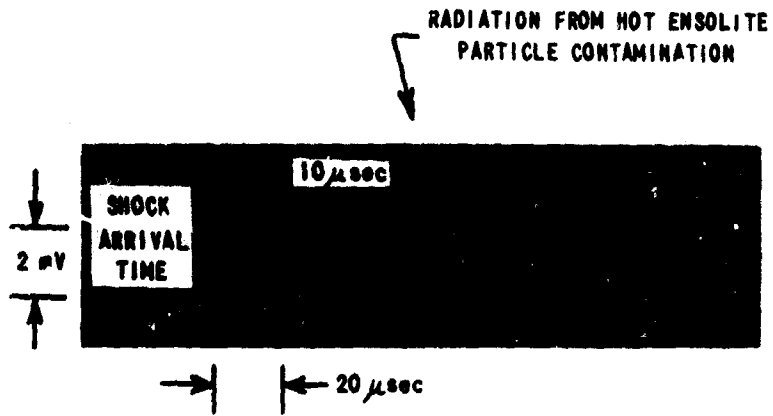


Figure 6(a) RADIATION HISTORY FOR A LOCAL SHOCK SPEED OF 29,300 ft/sec AND AN INITIAL DRIVEN-TUBE AIR PRESSURE OF 0.025 mm Hg

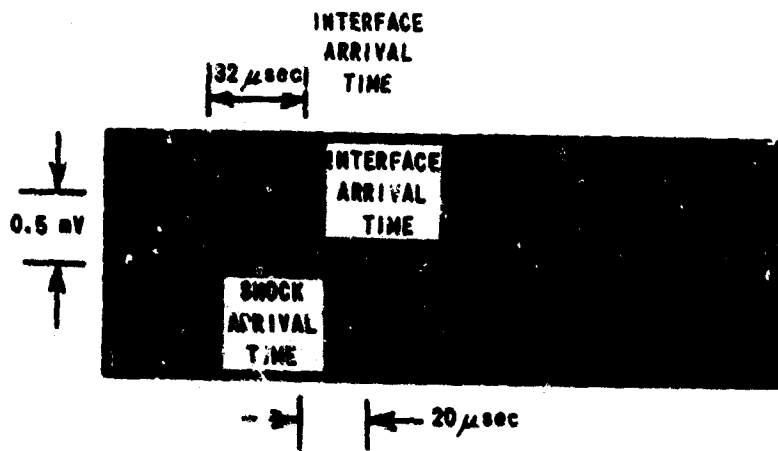


Figure 6(b) RADIATION HISTORY FOR A LOCAL SHOCK SPEED OF 16,500 ft/sec AND AN INITIAL DRIVEN-TUBE AIR PRESSURE OF 1 mm Hg

## SUPERSONIC COMPRESSOR RESEARCH

RONALD L. HAUGEN, Captain, USAF  
DR. ARTHUR J. WENNERSTROM

Fluid Dynamics Facilities Laboratory  
Aerospace Research Laboratories  
Office of Aerospace Research  
Wright-Patterson Air Force Base, Ohio

### ABSTRACT

Axial compressors are employed in many Air Force applications including the majority of aircraft engines, numerous types of ground-support equipment, and some environmental control systems. Supersonic compressors offer potential for reducing size, weight, and cost of these components. The Aerospace Research Laboratories are pursuing a research program in this area with the ultimate objective of developing satisfactory techniques for designing a supersonic compressor having adequate efficiency and useful operating characteristics.

The ARL program is composed of three coordinated efforts. An in-house effort involves experiments with two-dimensional supersonic cascades and theoretical work on prediction and analysis techniques for supersonic compressor stages. A joint effort is conducted with the Arnold Engineering Development Center. In this case the aerodynamic design of compressor stages, and analysis of experimental data, are accomplished at ARL. Compressor configurations are manufactured and tested at AEDC. The third effort is a contract with the von Karman Institute for Fluid Dynamics, in Belgium. This is administered by EOAR and the effort includes experimental work with both cascades and actual compressors.

Some recent research results are presented for all three efforts of this program. Data were obtained on six cascade configurations at ARL. From the joint ARL/AEDC effort some results are presented for an investigation of three annulus contours tested with one stage, a test of a new stage involving a larger scale twisted blade, and transient pressure measurements on the latter to determine shock wave patterns. The most significant recent result from the contract effort is a correlation for slot effectiveness for slotted airfoils.

## INTRODUCTION

One of the critical components of the turbojet or turbofan engine is the axial compressor. This is a type of compressor generally known for light weight, high through-flow capability, and low-pressure ratio per stage. It is more adaptable to staging than most other types and is usually employed in this form with as many as 20 stages. Figure 1 offers a rough idea of the configuration involved.

Axial compressors see service in many varied items within the Air Force inventory. The most conspicuous application is in the turbojet, turbofan, and turboprop engines which power most modern aircraft. However, a great many are employed in helicopter engines and ground-support equipment, such as starting carts, standby electrical generators, and aircraft environmental control systems. Practically all of this equipment is either flight or flight-transportable hardware. Thus, any research accomplishments leading to a reduction in the size and weight of axial compressors would be useful.

As compressor rotational speed is increased, both compression capability and, to some extent, flow-swallowing capability increase. Therefore, in terms of cost, size, and weight, the most economical method of achieving higher performance has been to increase speed. For example, one stage having a pressure ratio of four could replace two stages, each having a pressure ratio of two. Historically, the major objective of research in compressor aerodynamics has usually been the development of techniques for maintaining high compressor efficiencies while operating at increasingly higher speeds. Today, this objective remains unchanged but the frontier has risen into the supersonic regime.

As the rotational speed of a compressor rotor is increased, the velocity of flow relative to the moving blades becomes locally sonic long before current structural limitations are reached. In the vicinity of current structural limits, the relative flow can be supersonic over the entire radial span of the rotor. When this condition exists at the design-operating speed, a compressor is termed supersonic. Note that this definition has nothing to do with the speed of a vehicle in which it might be operating.

When operating supersonically, an axial compressor is potentially capable of producing at least twice the stage-pressure ratio of a modern transonic design. Alternatively, one supersonic stage can produce a pressure ratio equal to a series of many subsonic stages. Figure 2 illustrates the sort of compressor which might be achieved. However, the current state-of-the-art does not permit it to compete in terms of efficiency. Before a supersonic compressor can become a practical reality, ways must be found to raise its thermodynamic efficiency to a

level roughly comparable with current transonic designs. This is the broad objective of the ARL supersonic compressor research program. Quantitatively, we would like to arrive at a method of designing a single axial stage which is capable of producing a pressure ratio of at least three, with an adiabatic efficiency exceeding 82 percent. Further, the design must provide characteristics compatible with the over-all requirements of a gas-turbine engine.

### RESEARCH PROGRAM STRUCTURE

The ARL research program is composed of three closely related efforts. The major effort is conducted jointly by the Aerospace Research Laboratories and the Arnold Engineering Development Center. It involves a series of experiments conducted with full-scale operating supersonic compressor stages. These tests are selected to examine the influence of the variables available to the designer and to study in detail the various sources of inefficiency in the internal flow. ARL is responsible for the aerodynamic design and analysis of these experiments while AEDC is responsible for the complete execution of the experiments.

The second effort involves several exclusively in-house projects at ARL. On the theoretical side, design and analysis techniques are continually being refined. Experimentally, investigations have been conducted with two-dimensional stationary supersonic cascades. These experiments have proven a very economical method of making certain quantitative comparisons between different compressor-blade configurations.

The third effort is accomplished under contract. This contract, administered by the European Office of Aerospace Research, is with the von Karman Institute for Fluid Dynamics in Belgium. It is for research of a primarily experimental nature along the same general lines as the in-house program. Its emphasis has been on the rapid acquisition of data in new areas of exploration.

### ROTOR EXPERIMENTS

In the following figures some recent research results are presented which cover various facets of the over-all program. Figure 3 shows the evolution of performance achieved with one experimental rotor from the joint ARL-AEDC effort. In all three cases, the same rotor blades were used without modification; only the casing contour was changed and the tips of the blades machined to match. The original version, designated

Configuration No. 5, had a purely cylindrical annulus with no area change across the blade row. A striking feature is the very limited flow range which this version possessed.

The first modification (Configuration 8) employed a reduction in area across the rotor in a manner which placed most of the annulus convergence across the rear half of the blading. The principal effect of this change was to produce a striking increase in the flow range over which stable operation was possible. However, the increases achieved in pressure ratio and efficiency were relatively minor.

The next modification, designated Configuration No. 10, employed exactly the same annulus area reduction but distributed it differently. The rate of reduction in area was strongest at the rotor leading edge and tapered off gradually. The resulting performance was substantially increased. Not only was the broad flow range maintained, but significant gains were made in both pressure ratio and efficiency. Further theoretical work is planned emphasizing more satisfactory methods of predicting optimum annulus contours. This example illustrates some of the things which can be accomplished by inexpensive minor modifications to a limited number of test rotors and typifies the approach followed by this program. Although the three configurations shown would not represent an optimum design, a lot of useful information has been obtained at low cost.

The performance of the most recent rotor tested under the joint ARL-AEDC program is shown in Figure 4. This one, designed prior to the experiments just mentioned, also employs an annulus of constant area. However, a significantly different blade twist distribution and larger hydraulic diameter distinguish it from those tested earlier. The design speed performance shown here is the best achieved so far in this test series and represents an improvement of about 10 percentage points in efficiency.

To enhance our understanding of the internal flow in an operating rotor, several additional experiments were planned. The first of these, which has been completed, entailed measurement of the shock-wave patterns in the most recent rotor to see if the pattern assumed for design purposes corresponded to reality. Some typical results are shown in Figure 5. Special transducers were mounted in the compressor casing at nine locations and detected high frequency variations in pressure as the blades passed each transducer. A sharp increase in pressure between blades signified the presence of a shock wave. The most significant result of this experiment, shown in Figure 6, was that a multiple shock pattern, resembling a so-called "pseudo-shock," did indeed exist at the operating point of maximum efficiency. This condition was assumed for its design and the assumption was thereby verified. This experiment was the subject of a recent AGARD paper.

## CASCADE EXPERIMENTS

While experiments with full-scale operating compressor rotors are required to adequately define real performance characteristics, important and moreover economical comparisons of various blade configurations can be accomplished via stationary cascade experiments. A stationary cascade normally consists of several blade passages which, in an approximate manner, simulates a full-scale compressor. Figure 7 shows an example of the cascades tested at ARL. The blades are pin-supported between windows which are installed in the sides of a suitable wind tunnel.

Visual observation of flow conditions and shock-wave patterns is permitted by means of shadowgraph instrumentation. A typical shadowgraph photo is shown in Figure 8. The flow is from left to right in this illustration and dark lines which are prominent ahead of, and between, blades are shock waves. The pattern downstream of the blades gives an indication of the rate at which the flow again becomes uniform.

Of primary interest to the designer is the pressure rise accomplished by the blade design and the companion flow losses. Figure 9 shows typical static pressure distributions, measured within the blade passage. A knowledge of these is useful for determining the diffusion distribution through the passage. It is desirable to avoid local peaks in diffusion in order to minimize the effects of boundary layer separation.

The main objective of stationary cascade experiments is illustrated by Figure 10. In this figure the effectiveness of the blade design is represented by the total pressure recovery. Blade Configuration I exhibits a severe drop in pressure recovery for intermediate to high back-pressures. Shadowgraph photos show that the increased loss is due to early flow separation. Blade Configuration II represents a minor alteration in blade design and, as shown in Figure 10, the undesirable loss is avoided. A further increase in performance is exhibited by Configuration III.

Whereas the primary usefulness of stationary cascade experiments lies in comparing the relative merits of different geometric cascade configurations, cascade data is also of value in evaluating and developing compressor performance prediction techniques. A current objective within this area of interest concerns itself with the development of simple yet quantitatively correct methods applicable to forecasting cascade performance.

The prediction of compressor performance relies on a successful estimation of numerous and complicated flow processes. Of the various flow parameters, one must consider the blade shape, solidity, Mach number, angle of attack, turbulence

level, and Reynolds number. For conventional axial flow compressors the variation in these quantities is not extensive; but, the prediction of flow losses remains complex and, at best, inexact.

One method suggested applies a modification of the Lieblein diffusion correlation to the heavily loaded supersonic blading. Figure 11 shows typical cascade performance predicted by this method. Unaccounted shock losses may be a probable explanation of the lower values of experimental performance compared to the correlation. A second method, based upon shock and dump diffusion losses, is also presented in Figure 11. This method shows a better correlation with data for heavily loaded conditions. Further improvement to this method may be made by accounting for frictional losses.

Thus in the manner described, stationary cascade studies provide an insight into flow mechanisms occurring within the blade passages, provide an evaluation of performance prediction techniques, and furnish the designer with inexpensive quantitative comparisons between potential compressor blade designs.

#### CONTRACT EFFORT

One of the most useful recent contributions made by the von Karman Institute contract effort concerned a correlation for the effectiveness of slotted compressor airfoils. The incorporation of slots in a compressor blade is a technique selected to improve the aerodynamic efficiency or operating range of a heavily loaded blade row. Sometimes slots have performed as expected. However, there have also been notable examples where slots proved detrimental for reasons which are not clearly understood.

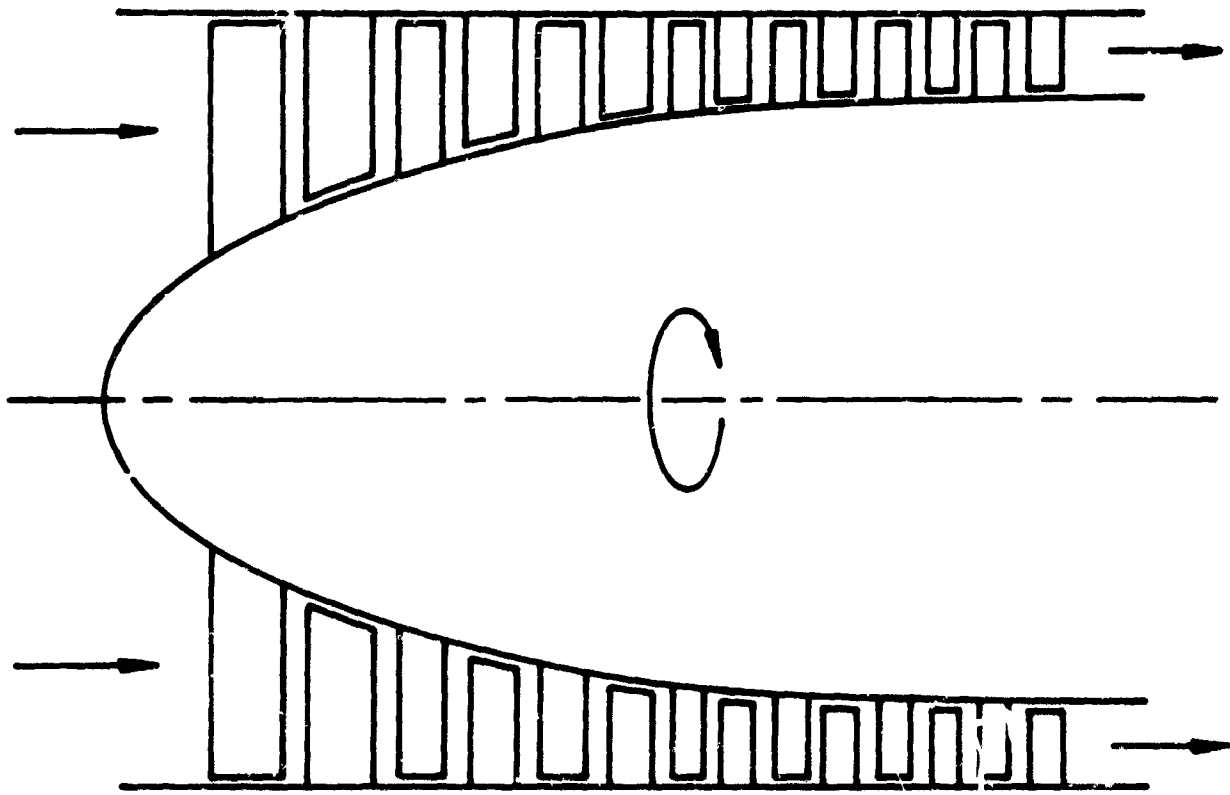
Various technical considerations led vKI to a correlation parameter, designated "A," which is a function of three geometric variables; namely, camber, aspect ratio, and solidity. The expression for "A" is shown for the abscissa in Figure 12. Each of the different curves corresponds to a different approach Mach number. As the Mach number increases the curves become more vertical. The ordinate indicates slot effectiveness. Positive values correspond to increases in aerodynamic efficiency and negative values to decreases. The correlation is still tentative since only limited data have been available for comparison. However, the correlation has provided a plausible explanation for some apparently conflicting experimental results and thus constitutes a welcome and valuable contribution.

## CONCLUSIONS

The examples presented represent some of the recent highlights of ARL's supersonic compressor research and were selected to give an indication of the over-all scope of the current research program. Most of the difficulties encountered in extracting better performance from supersonic compressors can be traced to accumulation and separation of various fluid boundary layers. As a result, the current emphasis of the program is on understanding how these boundary layers react and to what extent they may be controlled. Boundary-layer control is an old topic which has received much attention with respect to components such as wings and supersonic inlets. However, for various practical reasons, it has been largely ignored for the supersonic compressor. Our current opinion is that this line of research may ultimately lead to the sort of technical breakthrough necessary to realize the potential of the supersonic compressor.

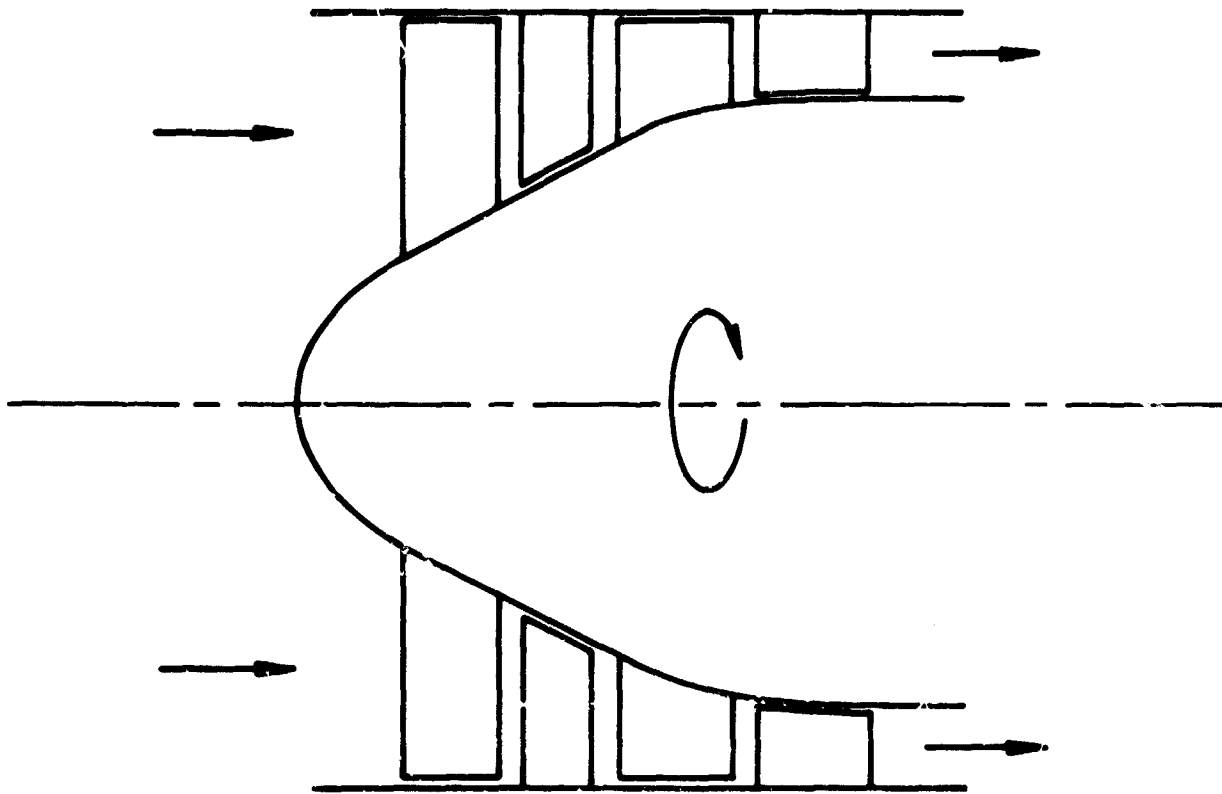
## REFERENCES

1. Wennerstrom, A. J. & Olympios, S., "A Theoretical Analysis of the Blunt-Trailing-Edge Supersonic Compressor and Comparison with Experiment," ARL 66-0236, 1966.
2. Carman, C. T., Myers, J. R., Wennerstrom, A. J., & Steurer, J. W., "Experimental Investigation of Two Blunt-Trailing-Edge Supersonic Compressor Rotors of Different Blade Thickness and with Circular Arc Camber Line," AEDC-TR-68-197, 1968.
3. Wennerstrom, A. J., Johnson, E. G., & Carman, C. T., "Experimentally Determined Shock Configurations in a High-Solidity Supersonic Rotor," Paper presented at the 32nd meeting of the AGARD Propulsion and Energetics Panel, September 1968, to be published 1969.
4. Haugen, R. L. & Steurer, J. W., "Cascade Testing of Supersonic Compressor Blade Elements," ARL 69- , 1969.
5. Chauvin, J., Breugelmans, F., & Griepentrog, H., "Application of the Blunt-Trailing-Edge Blade Concept to Low Hub Tip Ratio Transonic Supersonic Compressors," vKI IN 27 (ARL 68-0110), 1968.



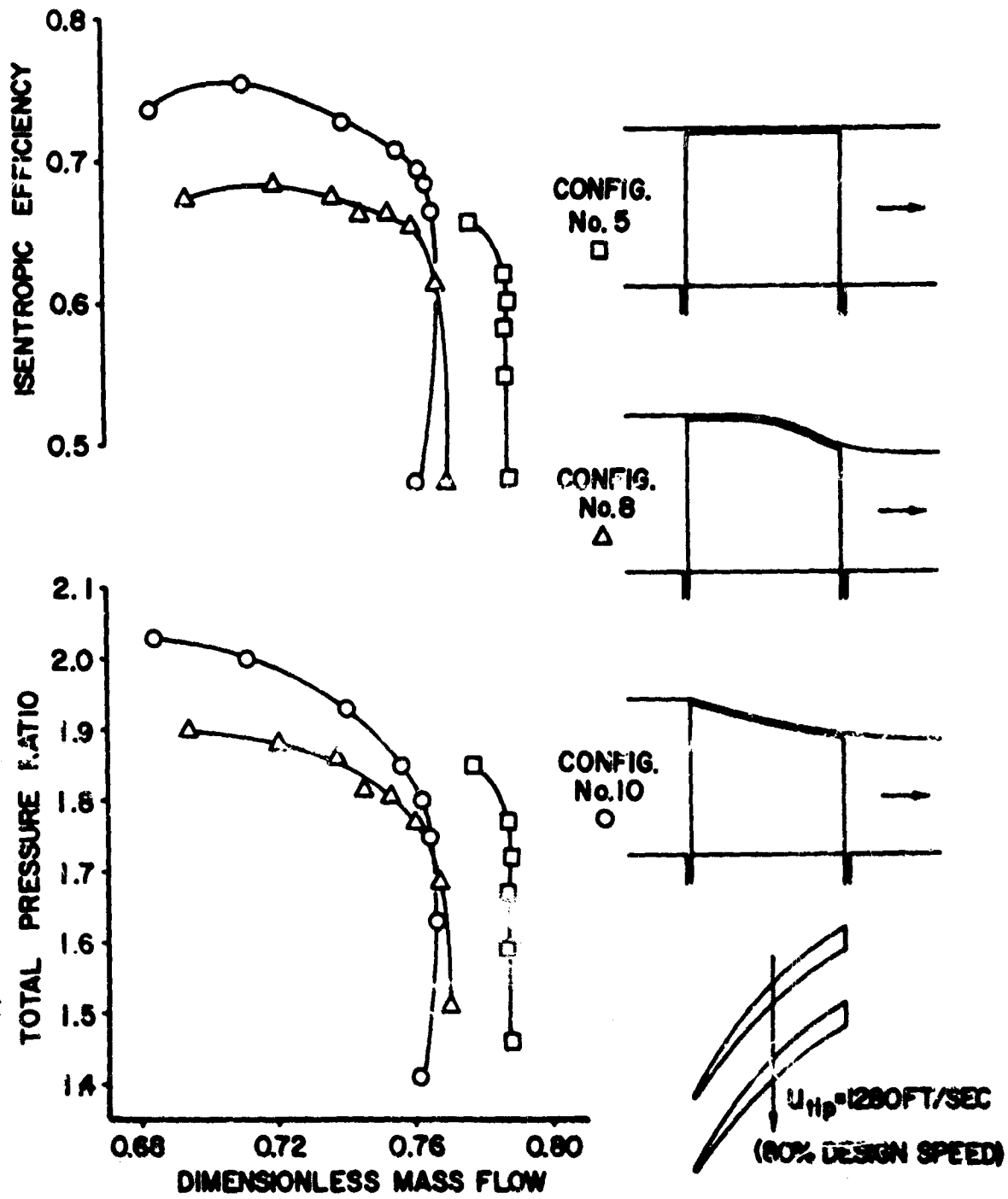
SCHEMATIC OF CONVENTIONAL AXIAL COMPRESSOR

FIG. 1



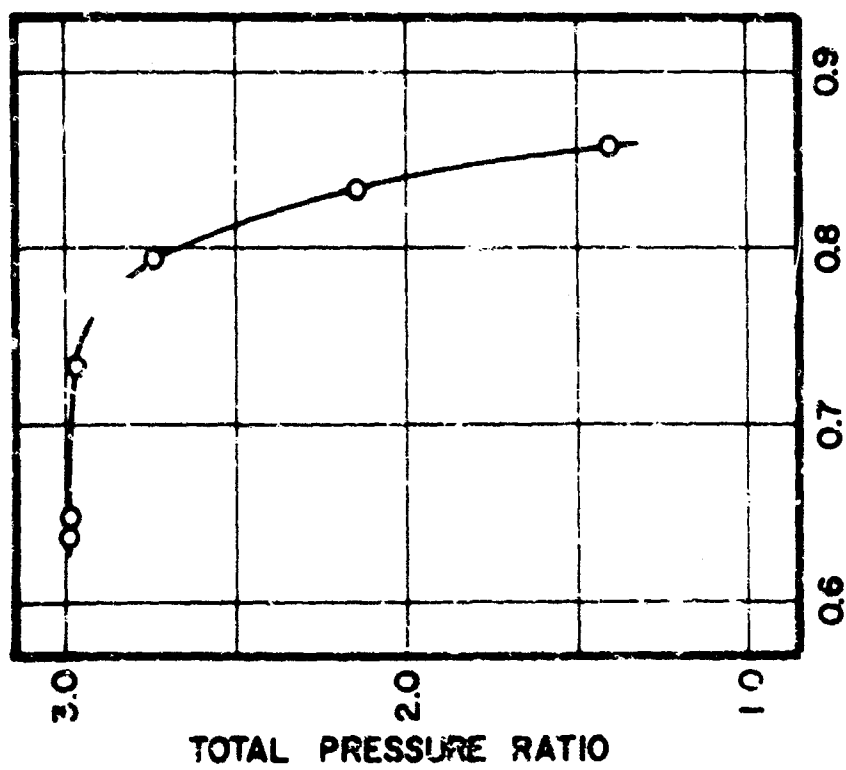
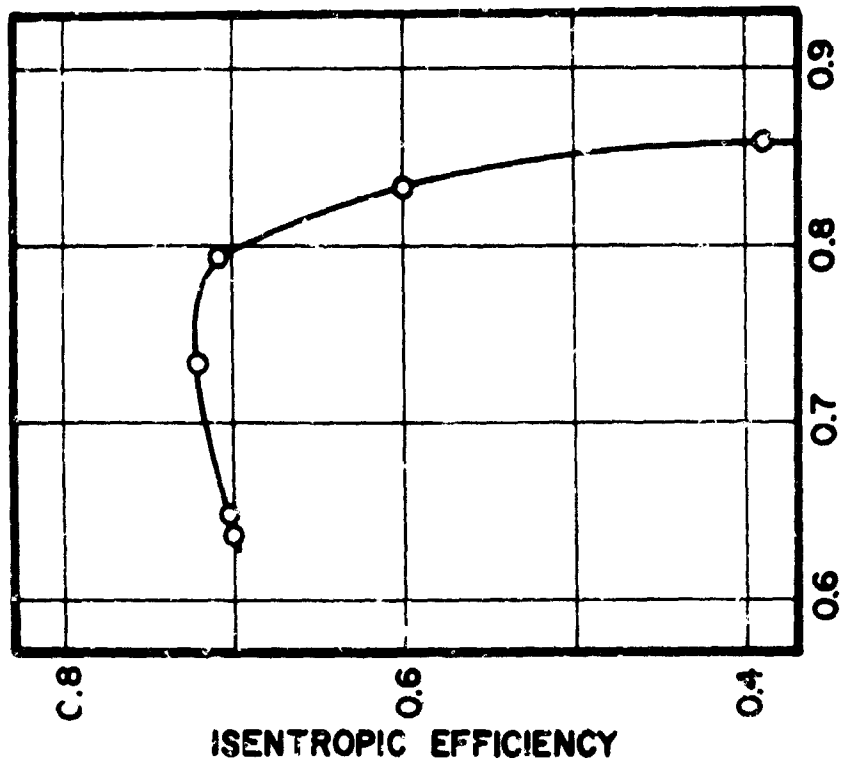
SCHEMATIC OF COMPRESSOR EQUIVALENT TO FIG. 1  
INCORPORATING A SUPERSONIC STAGE

FIG. 2



**SUPERSONIC COMPRESSOR PERFORMANCE EVOLUTION  
I BLADE CONFIGURATION; 3 ANNULUS CONTOURS**

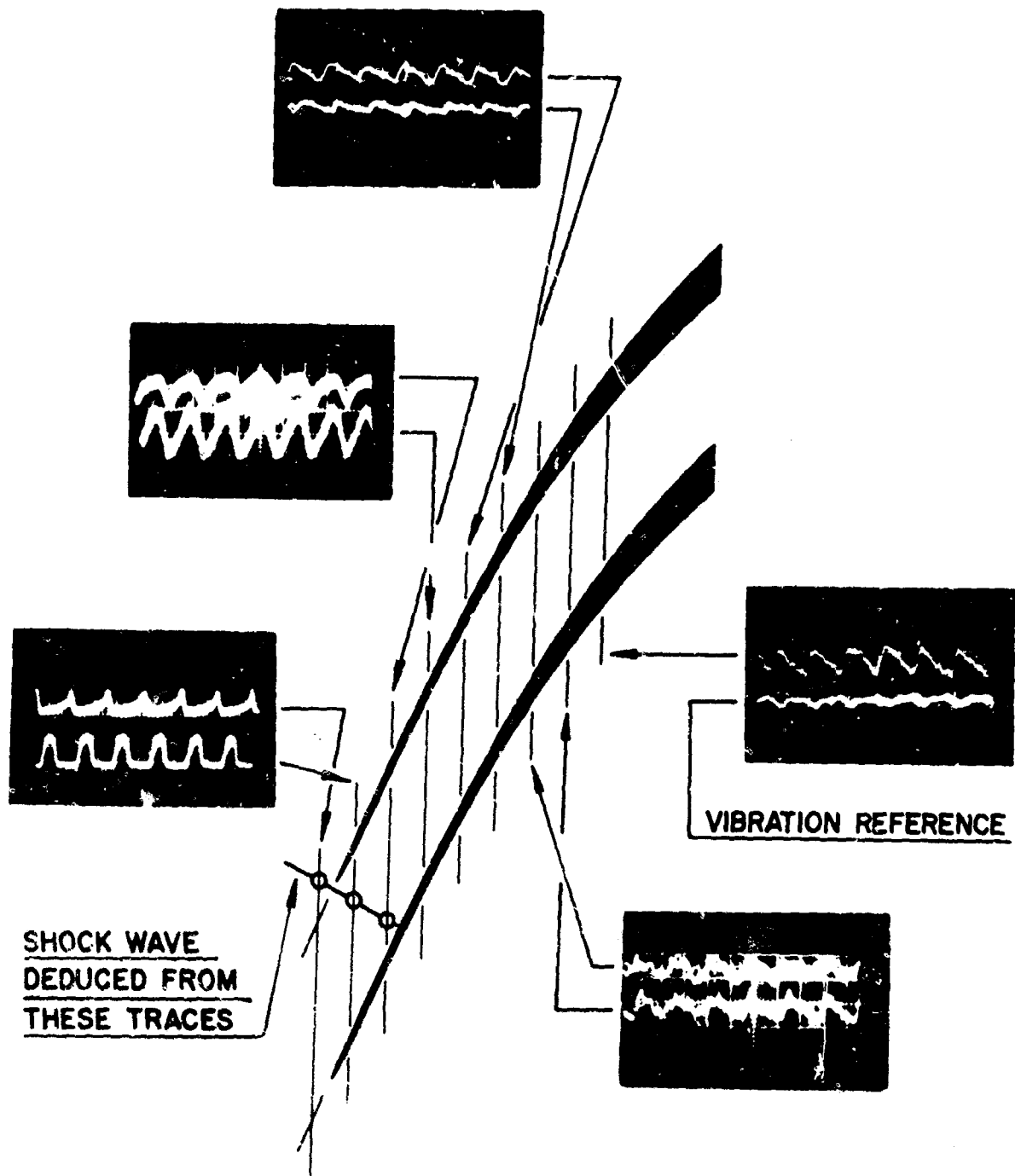
**FIG. 3**



(ACTUAL MASS FLOW) / (SONIC MASS FLOW)

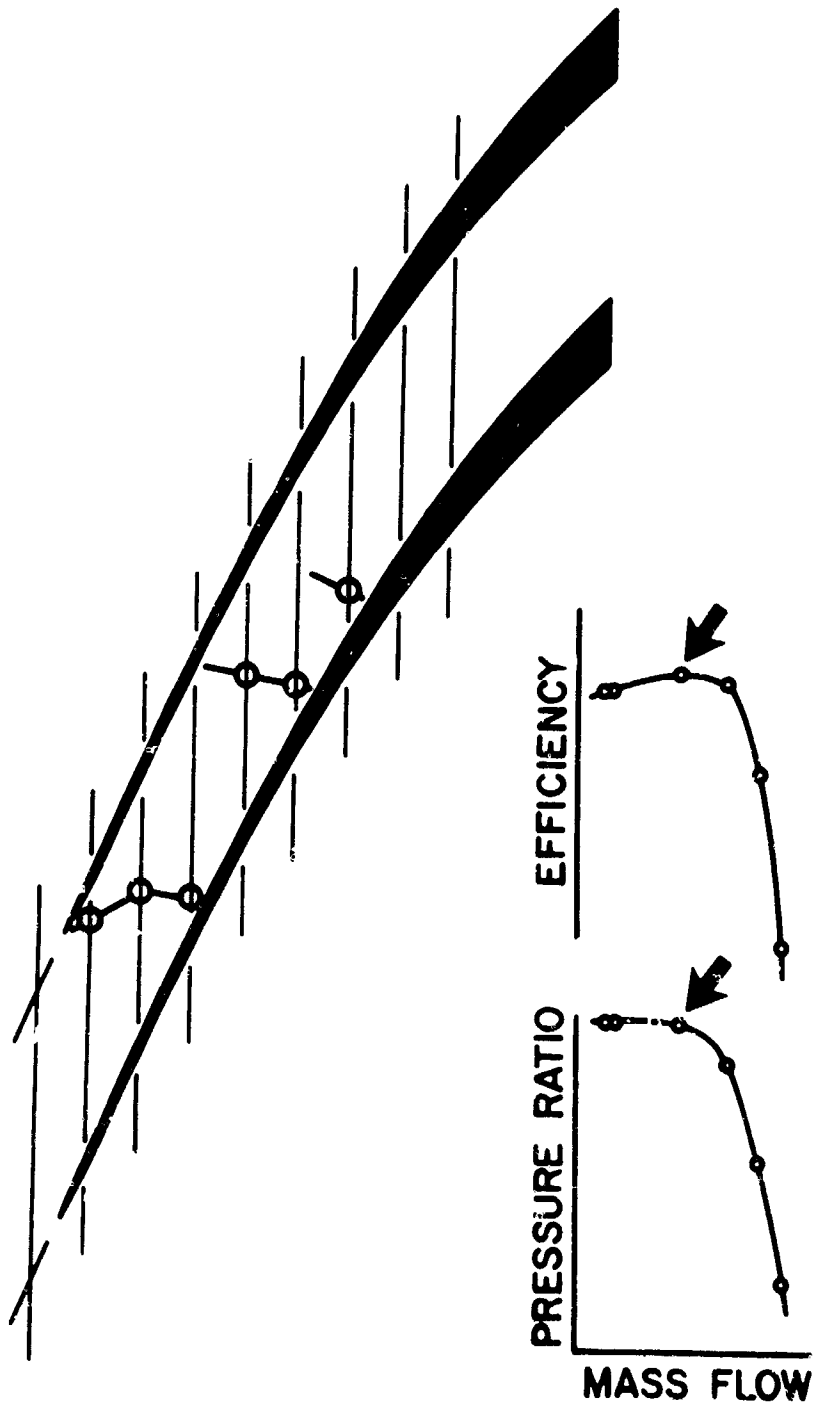
MASS-AVERAGED DESIGN-SPEED ROTOR PERFORMANCE

FIG. 4



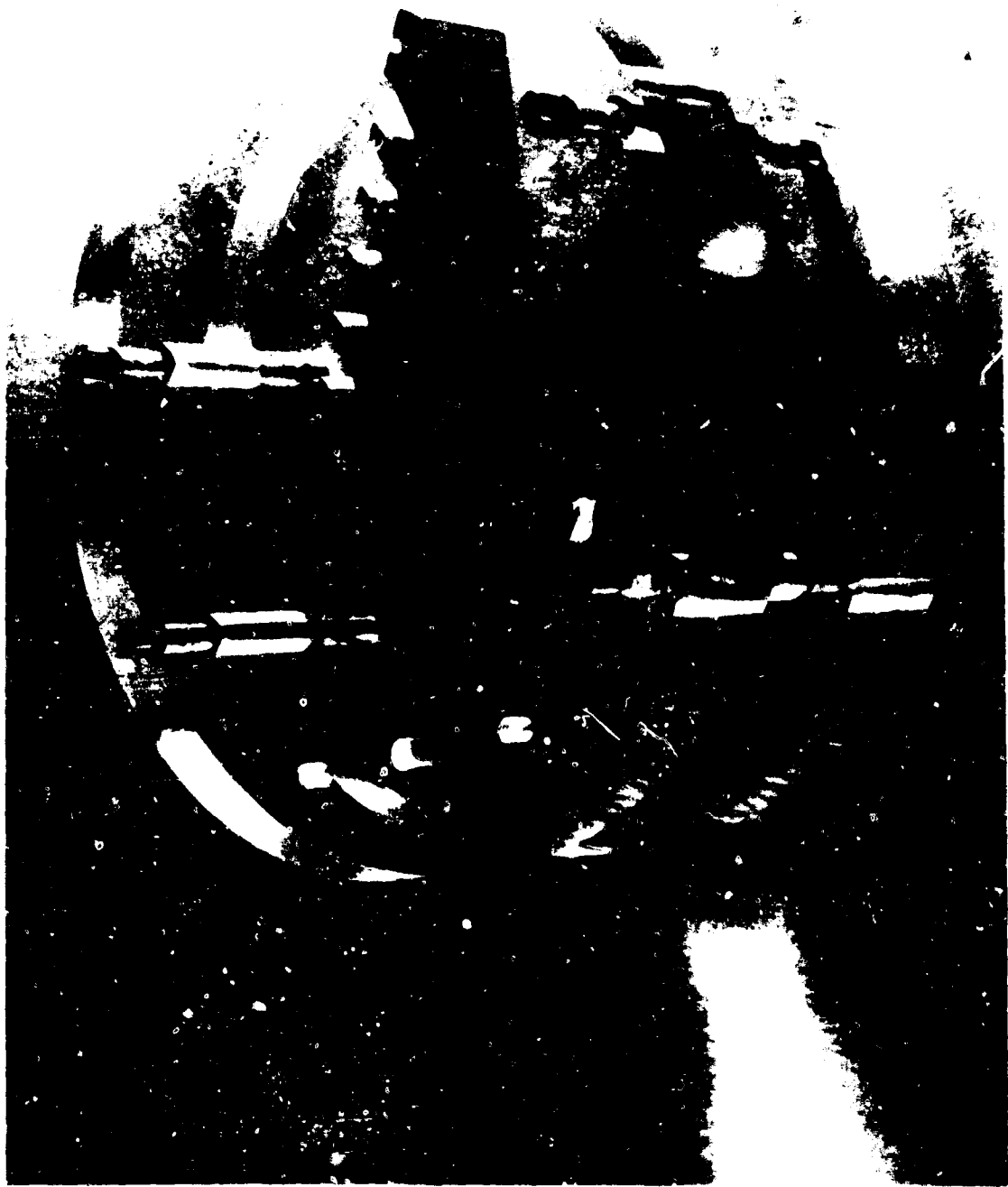
TYPICAL OSCILLOSCOPE TRACES  
OF CASING STATIC PRESSURE

FIG. 5

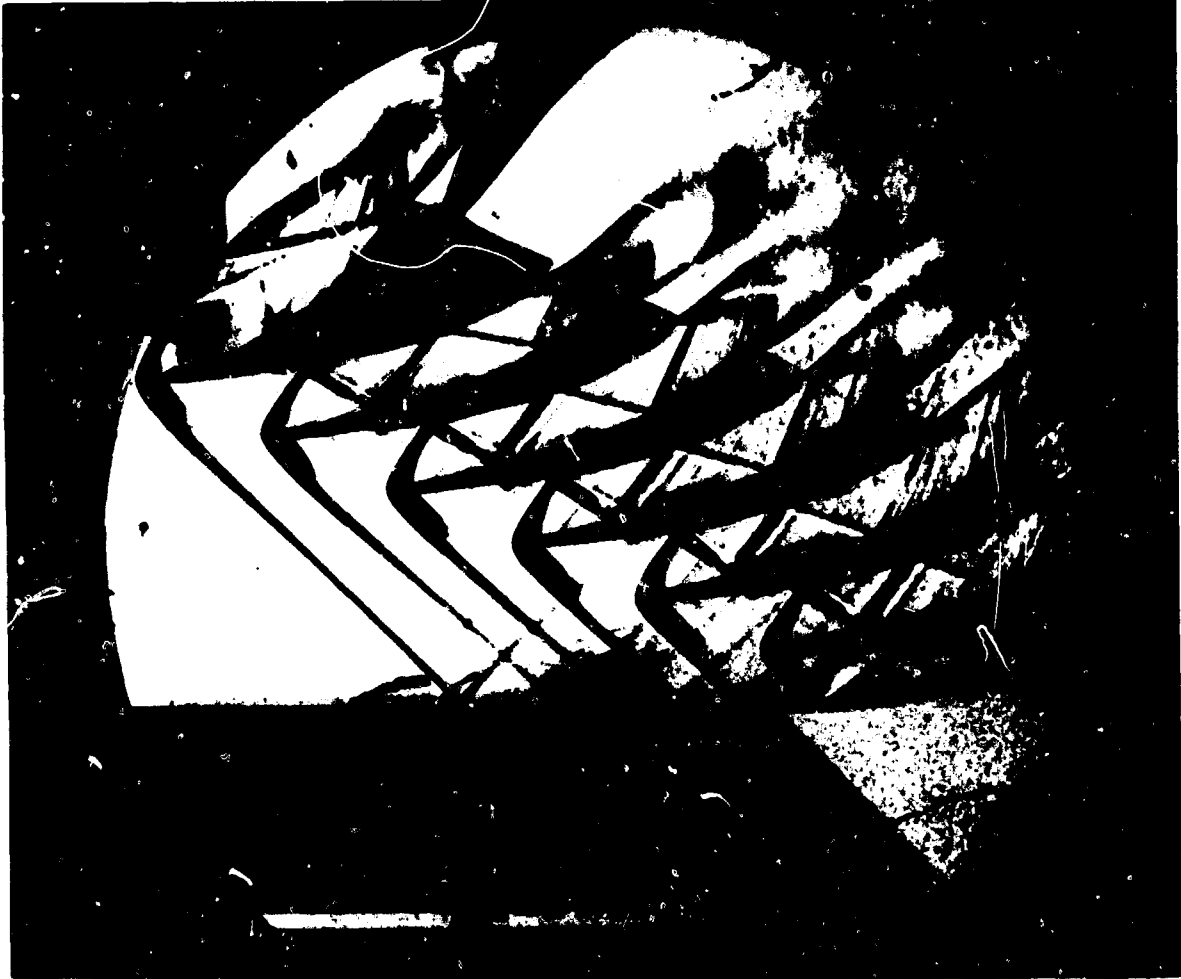


**SHOCK PATTERN, MAXIMUM EFFICIENCY**

**FIG. 6**

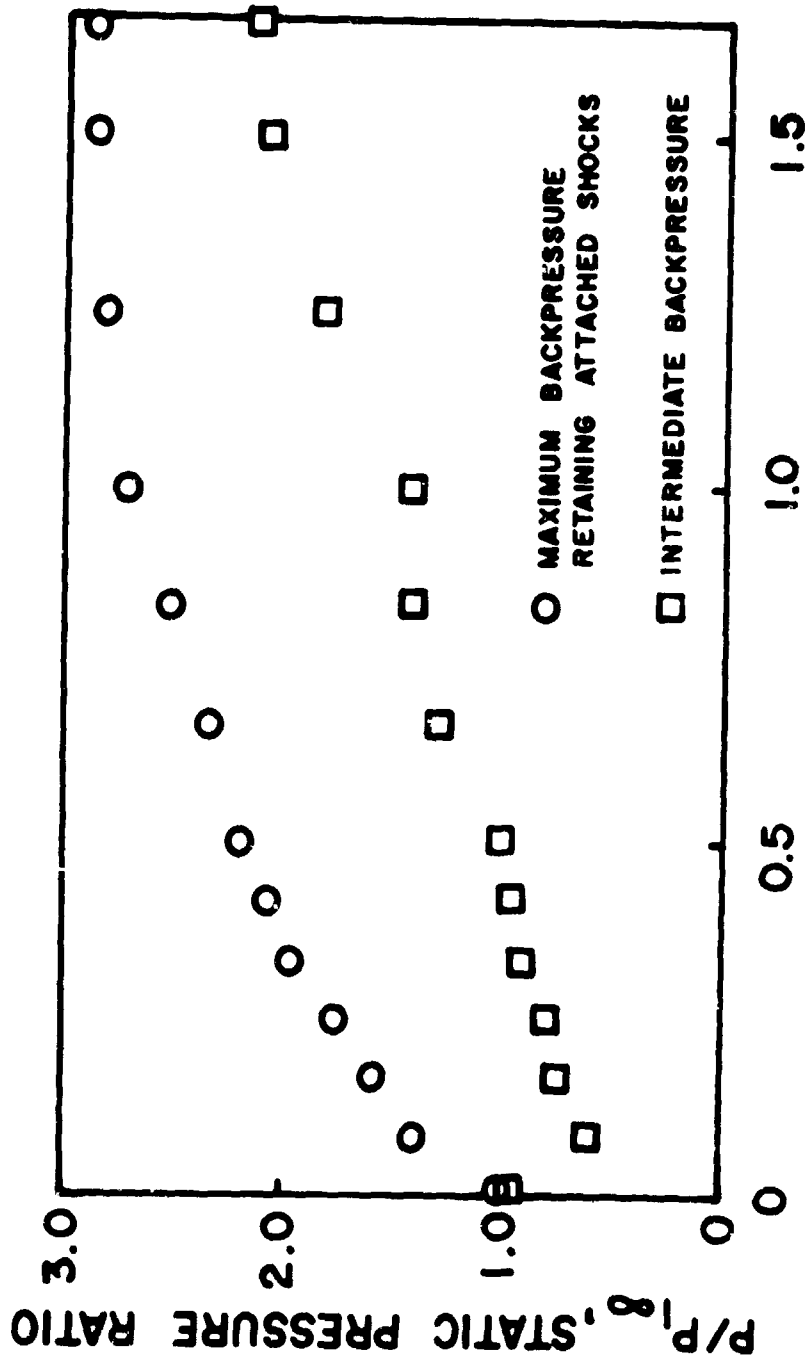


**CASCADE TEST FIXTURE  
FIG. 7**



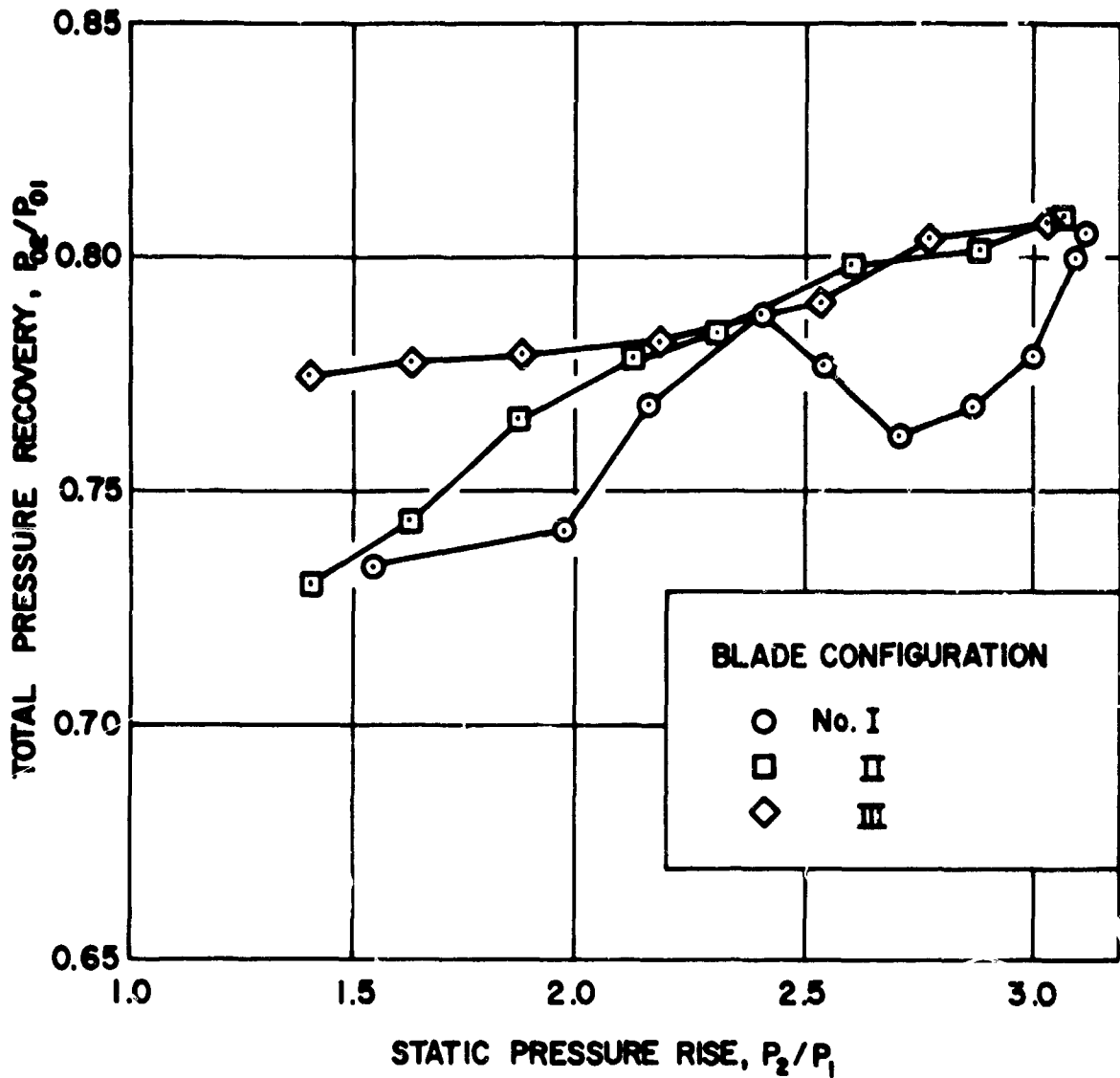
**SHADOWGRAPH OF SUPERSONIC CASCADE  
OPERATING AT LOW BACKPRESSURE**

**FIG. 8**



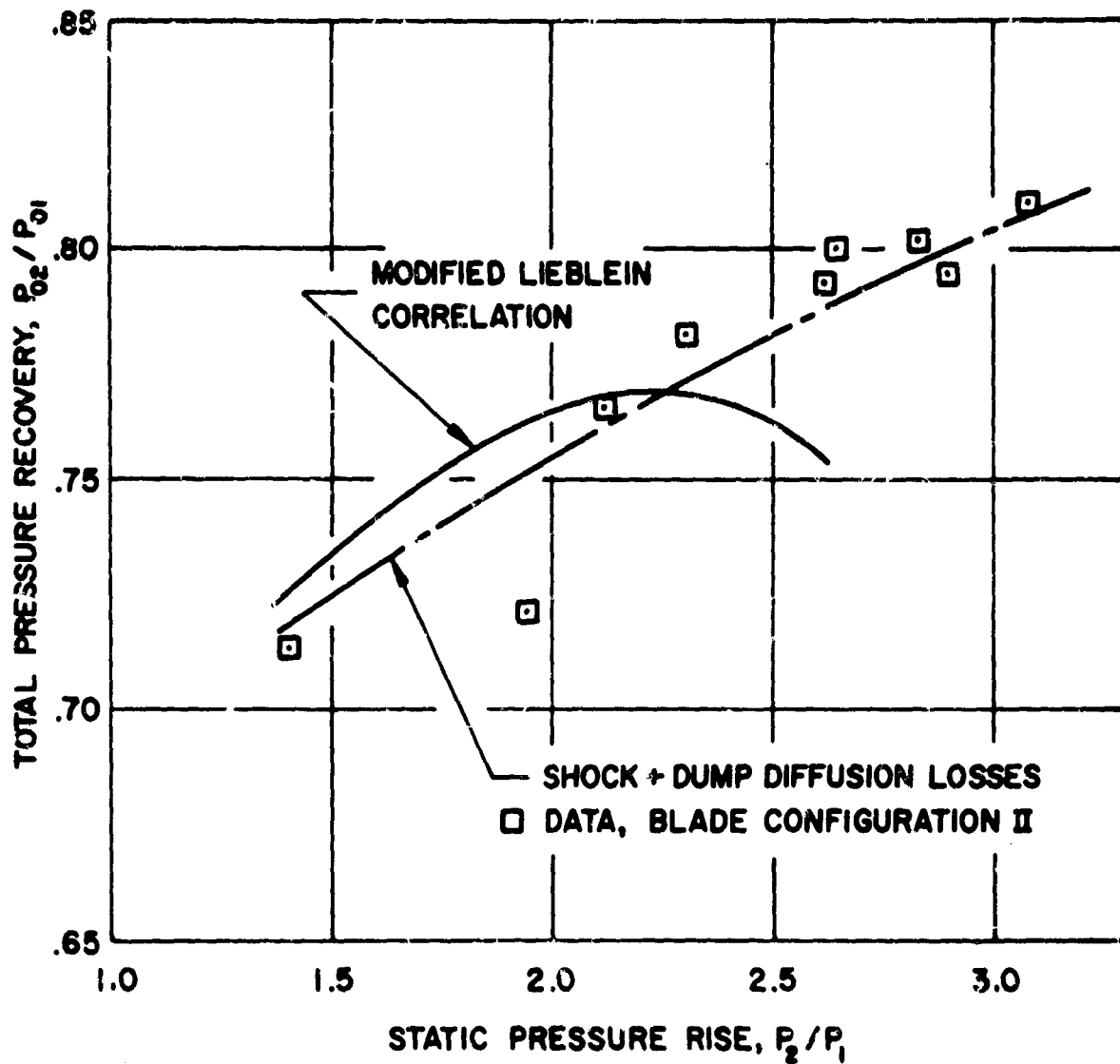
FRACTIONAL DISTANCE THROUGH BLADE ROW  
 PASSAGE CENTERLINE STATIC PRESSURE DISTRIBUTION

FIG. 9



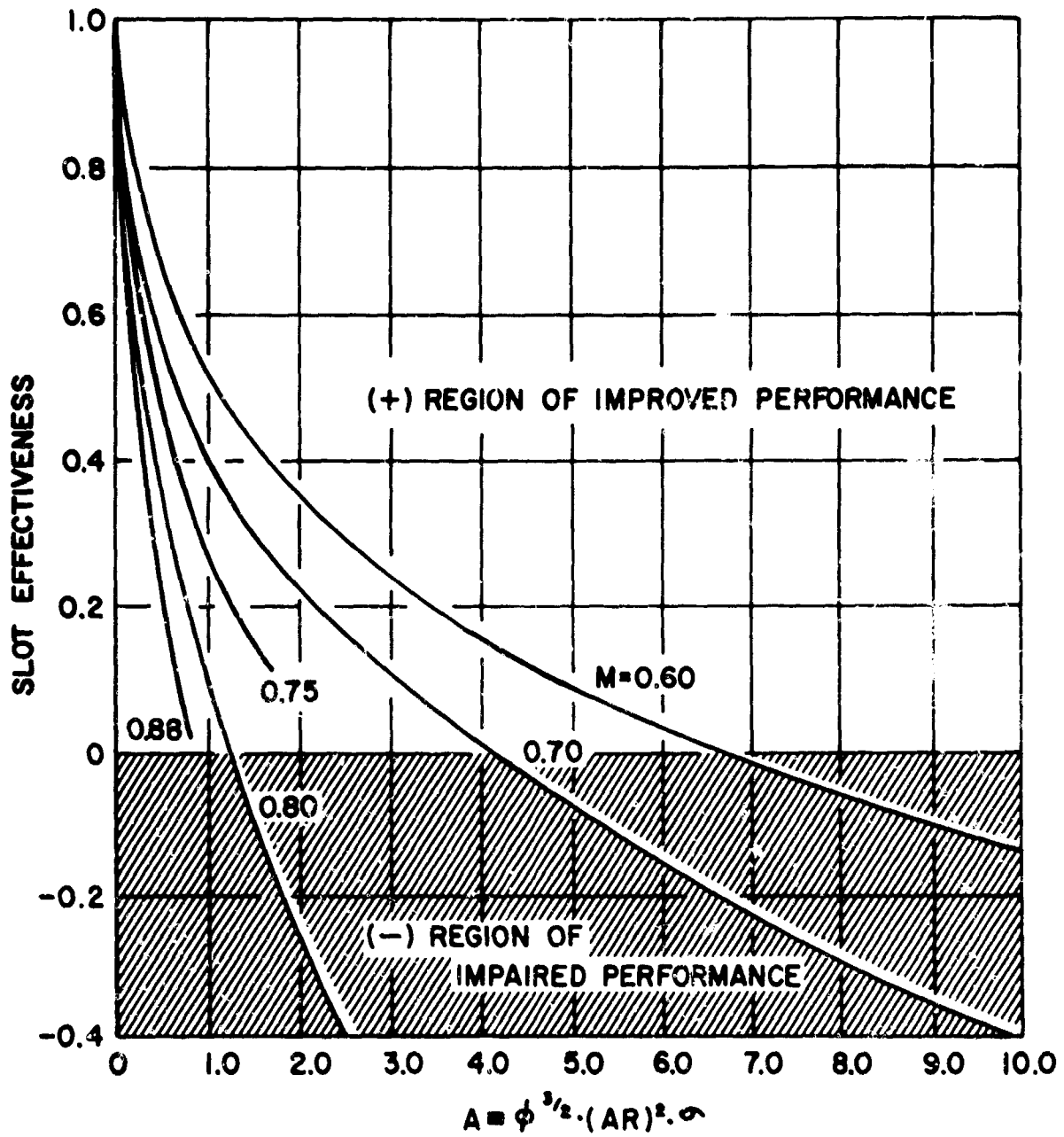
**CASCADE PERFORMANCE OF**  
**THREE VARIATIONS OF SUPERSONIC COMPRESSOR BLADING**

FIG. 10



CASCADE PERFORMANCE PREDICTIONS

FIG. 11



TENTATIVE LOSS CORRELATION  
FOR SLOTTED COMPRESSOR BLADES (vKIFD)

FIG. 12

UNCLASSIFIED

Security Classification

DOCUMENT CONTROL DATA - R & D		
<i>(Security classification of title, body of abstract and indexing annotation must be entered when the overall report is classified)</i>		
1. ORIGINATING ACTIVITY (Corporate author) Hq Office of Aerospace Research 1400 Wilson Blvd. Arlington, Va. 22209		2. REPORT SECURITY CLASSIFICATION UNCLASSIFIED
		3. GROUP N/A
3. REPORT TITLE <u>PROCEEDINGS OF THE OAR RESEARCH APPLICATIONS CONFERENCE, 13 March 1969</u>		
4. DESCRIPTIVE NOTES (Type of report and inclusive dates) Scientific Annual 1969		
5. AUTHOR(S) (First name, middle initial, last name)  N/A		
6. REPORT DATE June 1969	7a. TOTAL NO. OF PAGES 330	7b. NO. OF REFS N/A
8a. CONTRACT OR GRANT NO.  N/A	8b. ORIGINATOR'S REPORT NUMBER(S)  N/A	
9. PROJECT NO.  N/A	9b. OTHER REPORT NO(S) (Any other numbers that may be assigned this report) OAR 69-0011      AD 692500	
10. DISTRIBUTION STATEMENT 1. This document has been approved for public release and sale; its distribution is unlimited.		
11. SUPPLEMENTARY NOTES  N/A	12. SPONSORING MILITARY ACTIVITY Hq OAR (RRO) 1400 Wilson Blvd. Arlington, Va. 22209	
13. ABSTRACT  The papers presented at this Conference reflect some of the current or potential applications resulting from OAR research. The included papers are: "Application of High Magnetic Fields" by Benjamin Lax, D. Bruce Montgomery and Henry H. Kolm; "New Developments in Supersonic Combustion Research" by J. Swithenbank; "Negative Ion Reactions of Significance to the Atmosphere" by Thomas O. Tiernan and B. Mason Hughes; "New Atomic Spectroscopic Methods for Trace Analysis" by J.D. Winefordner; "Plan Shear Indicator for Real-Time Doppler Radar Identification of Hazardous Storm Winds" by Graham M. Armstrong and Ralph J. Donaldson, Jr.; "Stress Corrosion Cracking of 6-4 Titanium Alloy" by William E. Craven; "The Spectrum-Analysis Radar" by J.L. Poirier; "Nondestructive Evaluation of Metal Fatigue" by W. Lyle Donaldson, J.R. Barton and F.N. Kusenberger; "Application of the Statistics of Ionospheric Scintillation to VHF and UHF Systems" by Richard S. Allen; "Electrochemical Behavior of a Molten Aluminum-Chloride/Sodium-Chloride Electrolyte" by L.A. King and D.W. Seigmiller; "The Magnetic Wind-Tunnel-Model Suspension and Balance System" by Eugene E. Convert and Fred L. Daum; "Research in Electrofluidynamic Power Generation" by John A. Decaire and Maurice O. Lawson; "The Isentropic-Compression Tube" by F.J. Stoddard; "Supersonic Compressor Research" by Ronald L. Haagen and Arthur J. Wennerstrom.		

DD FORM 1473

UNCLASSIFIED

Security Classification

UNCLASSIFIED

Security Classification

14. KEY WORDS	LINK A		LINK B		LINK C	
	ROLE	WT	ROLE	WT	ROLE	WT
High Magnetic Fields Supersonic Combustion Negative Ion Reactions Atomic Spectroscopy Trace Analysis Plan Shear Indicator Doppler Radar Identification Hazardous Storm Winds Stress Corrosion Cracking 6-4 Titanium Alloy Spectrum Analysis Radar Nondestructive Evaluation Metal Fatigue Statistics Ionospheric Scintillation VHF, UHF Systems Electrochemical Behavior Aluminum-Chloride/Sodium-Chloride Electrolyte Magnetic Wind-Tunnel-Model Suspension and Balance System Electrofluiddynamic Power Generation Isentropic Compression Tube Supersonic Compressor						

UNCLASSIFIED

Security Classification